UNIVERSITÀ
DEGLI STUDI
DI PADOVA

Head Office: Università degli Studi di Padova

Department of Industrial Engineering

PH.D. COURSE IN: INDUSTRIAL ENGINEERING

CURRICULUM: ELECTRICAL ENERGY ENGINEERING

CYCLE: XXXI

Dynamic Wireless Charging of Electric Vehicles

Thesis written with the financial contribution of the Interdepartmental Centre for Energy Economics and Technology “Giorgio Levi Cases”

Coordinator of the Ph.D. Course: Prof. Paolo Colombo

Coordinator of the Curriculum: Prof. Roberto Turri

Supervisor: Prof. Manuele Bertoluzzo

Ph.D. Student : Mattia Forato

Contents

List of Figures

List of Tables

Abstract

This thesis deals with the Wireless Power Transfer (WPT) for the dynamic charging of Electric Vehicles (EVs). Dynamic WPT is an emerging technology that can accelerate the transition from conventional to electrical mobility. Dynamic Wireless Power Transfer Systems (WPTSs) exploit the principle of electromagnetic induction to power EVs during their motion without the need for a galvanic contact between the vehicles and a stationary supplying system. Since a portion of the power required by the EVs for the charging and for the propulsion is provided by an external grid, the size of the on-board batteries can be shrunk with the consequent benefits in terms of cost and weight of the EVs. An infrastructure of widespread public dynamic WPTSs can contribute to maintain the EVs always charged thus providing them with an ideal infinite range.

After a detailed introduction of the fundamental principles that govern the WPT technology and after a thorough description of a general WPTS, the focus of the thesis moves to dynamic WPTSs. The variations of the magnetic parameters caused by the EV movement make the study, the design, and the control of dynamic WPTSs very challenging. In the thesis, various dynamic WPTSs are studied under steady-state condition. This analysis shows that the LC compensation in the track side is particularly suited for such systems since it provides the track with the current source capability. This feature greatly simplifies the control and the power transfer regulation of dynamic WPTSs.

The attention of this thesis is focused mainly on the modeling and on the control of dynamic WPTSs. As regards the modeling, a novel method called Modulated Variable Laplace Transform (MVLT) is proposed. The method is used for the base band modeling of systems, such as dynamic WPTSs, where modulated quantities are involved. The accuracy of the MVLT is verified through the application of the method for the study of the dynamic of various circuits. In particular, MVLT method is adopted to find the dynamic model of an LC-compensated dynamic WPTS. With the aid of the obtained model the regulator that controls the track current of the system is designed. The performance of the regulator is tested by simulations, obtaining results in good agreement with the expected ones.

The thesis investigates also the dc/dc converter installed on-board the EVs responsible for the battery charging control. The operation of this converter is analyzed in conjunction with the type of compensating network used for the pickup. A novel topology for the pickup circuitry is proposed together with a new control strategy for the switch of the dc/dc converter. This topology allows for the pickup size reduction and it shows high performance in terms of efficiency.

Sommario

Questa tesi si occupa della tecnologia del trasferimento wireless di potenza (dall'inglese *Wireless Power Transfer - WPT*) per la ricarica dinamica dei Veicoli Elettrici (VE). Il trasferimento dinamico di potenza è una tecnologia innovativa che può accelerare la transizione da una mobilità convenzionale, basata su veicoli azionati da motore a combustione interna, verso una mobilità elettrica incentrata sui VE. I sistemi per il trasferimento wireless dinamico di potenza (dall'inglese *Dynamic Wireless Power Transfer systems - DWPT systems*) sfruttano il principio dell'induzione elettromagnetica per alimentare i VE mentre sono in movimento, senza la necessità di utilizzare un contatto galvanico tra i veicoli e un sistema di alimentazione stazionario. Poiché parte della potenza richiesta dai VE per la ricarica e per la propulsione è fornita da una rete elettrica esterna, le dimensioni delle batterie a bordo dei veicoli possono essere ridotte con i conseguenti benefici in termini di costo e peso dei VE. Una estesa infrastruttura di sistemi DWPT può contribuire a mantenere le batterie dei VE sempre cariche, consentendogli di avere un'autonomia idealmente illimitata.

Dopo una dettagliata introduzione dei principi fondamentali che governano la tecnologia WPT e dopo un'accurata descrizione di un sistema WPT generico, il fulcro della tesi si sposta verso i sistemi DWPT. Le variazioni dei parametri magnetici causate dal movimento dei VE rendono lo studio, il dimensionamento e il controllo dei sistemi DWPT molto impegnativo. In questa tesi, vari sistemi DWPT sono studiati in condizione di regime stazionario. Questa analisi mostra che la compensazione del *track* fatta con una rete LC è particolarmente adatta per tali sistemi poiché essa conferisce al track la caratteristica di generatore di corrente. Questa proprietà semplifica di molto il controllo e la regolazione della potenza nei sistemi DWPT.

L'attenzione di questa tesi è focalizzata principalmente sulla modellizzazione e sul controllo dei sistemi DWPT. Per quanto riguarda la modellizzazione, un nuovo metodo chiamato *Modulated Variable Laplace Transform (MVLT)* è presentato in questo lavoro. Questo metodo è usato per la modellizzazione dei sistemi, come ad esempio i sistemi DWPT, in cui sono coinvolte grandezze modulate. L'accuratezza del metodo MVLT è verificata attraverso la sua applicazione nello studio della dinamica di diversi circuiti. In particolare, il metodo MVLT è utilizzato per trovare il modello dinamico di un sistema DWPT in cui il track è compensato con una rete LC. Con l'ausilio del modello ottenuto viene progettato il regolatore che controlla la corrente del track del sistema. Le prestazioni di questo regolatore sono testate attraverso delle simulazioni, ottenendo risultati molto prossimi a quelli attesi.

Nella tesi è studiato anche il convertitore dc/dc installato a bordo dei VE

responsabile del controllo del processo di ricarica. Il funzionamento di questo convertitore è analizzato in modo congiunto con il tipo di compensazione del *pickup*. Una nuova topologia di circuito per il pickup è proposta assieme ad una nuova strategia di controllo per il convertitore dc/dc. Questa topologia permette una riduzione delle dimensioni del pickup e mostra elevate prestazioni in termini di efficienza.

I don't know anything, but I do know that
everything is interesting
if you go into it deeply enough.

— Richard Feynman, Nobel Prize, 1965

Acknowledgments

First of all, I would like to thank Prof. Giuseppe Buja for accepting me in the Electric Systems for Automation and Automotive laboratory.

I would like to express my gratitude to the Interdepartmental Center for Energy Economics and Technology "Giorgio Levi Cases" that supported my Ph.D. grant. In particular, I would like to thank the director of the center Prof. Alberto Bertucco for the opportunity that he gave to me to present my research topic in the intriguing showcase of the Galileo Festival.

A special thank goes to my supervisor Prof. Manuele Bertoluzzo who wisely and carefully guided me during my Ph.D. period. Thanks to him and his enlightening advice I could better myself from the personal and the working perspective. Without him, my Ph.D. would have been really disappointing.

Many thanks go to all my lab colleagues. First of all I would like to acknowledge the Indian group: Kundan, Syam, Hemant and Rupesh. I spent memorable moments with them and I have also learned a lot from people having a different culture but, at the same time, an open-minded attitude. Many thanks to Christian and to Stefano who made the laboratory environment very delightful. The habitual coffee breaks passed in pastry shop with them have been enjoyable, also thanks to the patient and the pleasantness of Luana.

I would like to thank all the master students that decided to pursue their thesis in our lab: Filippo, Christian, Tommaso and especially Elena who made me proud choosing me as her co-advisor.

Many thanks to my colleagues at the Department of Industrial Engineering in particular Mattia with whom I spent all the eight years of my academic life.

I would like to thank Giulia for the countless hours spent in train to commute. Our frequent discussions and complaints helped me to overcome all the tough moments of my Ph.D. life. I wish her all the best for her future academic career.

I am grateful to Elena who is always ready to give me the right advice and to lift my spirits when I feel sad. I really appreciate the gifts that she gave to me in particular the Swiss chocolate.

I would like to thank all my friends with whom I used to spend the weekends. They saved me from an inevitable insanity caused by plenty of hours spent to study in front of books.

Finally, I would like to express my gratitude to my family: my parents Marisa and Ivano who always supported me, my brother Samuele and my sister Beatrice.

Padova, September 2018

Mattia Forato

Chapter 1

Introduction

The effects of climate change, caused by human activities and predicted by scientists years ago, are now perceived by the aware community. The major manifestation of these effects on the Earth is the global warming of the planet's surface whose temperature has risen about 1 °C since the late 19th century [1]. Most climate experts agree that the main cause of the current global warming trend is the expansion of the greenhouse gases (such as CO_2) emissions. A large part of the CO_2 emissions generated by the humans arises from the road transport sector [2] which heavily relies on vehicles propelled by Internal Combustion Engines (ICE vehicles). Besides the emission of substantial amounts of carbon dioxide, these vehicles are responsible for the air pollution that can pose severe problems to the humans' health [3]. Furthermore, the fuels used to propel the ICE vehicles originate from petroleum that is a fossil fuel thus it is prone to the depletion [4]. In the sight of these evidences, novel solutions are required to provide a more sustainable future for the road transport and Electric Vehicles (EVs) constitute a promising alternative to the fossil-fueled vehicles.

Although the EV sales are increasing year by year, Plug-in Hybrid Electric Vehicles (PHEVs) and Battery Electric Vehicles (BEVs) remain a small fraction among the road transport fleet. In 2017, the only two countries where the market share of EVs exceeded the 3% of the total were Norway and Sweden [5]. Notwithstanding this percentage, PHEVs seem to be a feasible solution for the consumers in the car market, whereas the widespread adoption of BEVs is still hindered by some issues that worry the drivers. Probably, the biggest challenge to the commercialization of the EVs is the battery. Even though the performances of the batteries are increasing more and more, they still need large improvements to make the EVs effectively competitive with the ICE vehicles. The main drawbacks of the nowadays batteries are:

1. **Low Energy Density**
   The energy density of the state-of-art Li-ion batteries is 90-100 Wh/kg (for the battery pack) which is much less than the energy density of the gasoline (12 000 Wh/kg) [6]. To achieve ranges comparable with those of ICE vehicle, EVs need to be equipped with large and heavy batteries.

2. **High Initial Cost**
   The actual Li-ion battery cost is around 500 \$/kW h that in a favorable

scenario can be reduced to a value less than 100 \$/kW h by the 2030 [7]. The battery cost represents the 75% of EVs powertrain cost.

3. **Long Charging Time**
   The battery charging rate is limited due to internal electrochemical processes. A fast charge can accelerate the deterioration of the batteries performance [8].

Besides improving the batteries performance, a key factor for the widespread adoption of the EVs is the broad deployment of charging equipment of different power levels in public or semi-public areas.

The uptake of EVs can be fostered by the proposal of novel technologies and ideas. One innovative solution that can solve the problems related to the on-board energy storage of the EVs is the Wireless Power Transfer (WPT) technology. With this technology, the power required by the battery charging process is transferred to the vehicle wirelessly, by means of an inductive coil coupling[1]. By wirelessly transferring energy to the EV, the charging becomes an easier task. In Wireless Power Transfer Systems (WPTSs) the coil coupling, formed by an external transmitting coil and a receiving coil installed underneath the EV, replaces the charging cable of a conventional battery charger. Therefore, users do not need to handle a power connector anymore. This increases convenience and, more importantly, it eliminates the safety concerns related to the high-power electrical equipment.

WPTSs for EVs charging application can be classified mainly into two categories: *static* and *dynamic* WPTSs. Static WPTSs refer to a situation in which cars are stationary, whereas dynamic WPTSs are intended to charge the EVs during their motion. For a static WPTS, the drivers just need to park their car over a specific place where the transmitting coil is deployed, and the charging can be automatically launched (for example through a particular app installed in the smartphone). The static WPTSs could be even fully autonomous, thus allowing for the opportunity charging since the users often forget or choose not to charge when the vehicle is parked for short periods of time. Automatic operation encourages more frequent and reliable charging of EVs in a larger number of venues at high power levels. A static WPTS can be installed in a private home or in a public parking area (see Fig. 1.1(a)). As regard the public transportation, a static WPTS can be installed in a bus stop (cf. Fig. 1.1(b)) and the power can be transferred to the vehicle while the passengers embark/disembark. More frequent charging (every bus stops) reduces the batteries' depth of discharge, which extends battery lifetime [10].

In dynamic WPTSs, a portion of the traction and the charging power are wirelessly delivered to the moving EVs from an external stationary grid. Dynamic WPT technology can be envisaged as an extreme form of hybridization [11]. Since part of the required power is provided by the external grid, the capacity of the batteries on-board the EVs can be reduced with the consequent benefits in terms

[1] Wireless power transfer systems in which the power is transferred by means of a coil coupling are also called Inductive Power Transfer (IPT) systems. Although power can be wirelessly transferred also through a capacitive coupling [9], IPT technology seems to be the best solution for the EV charging application.

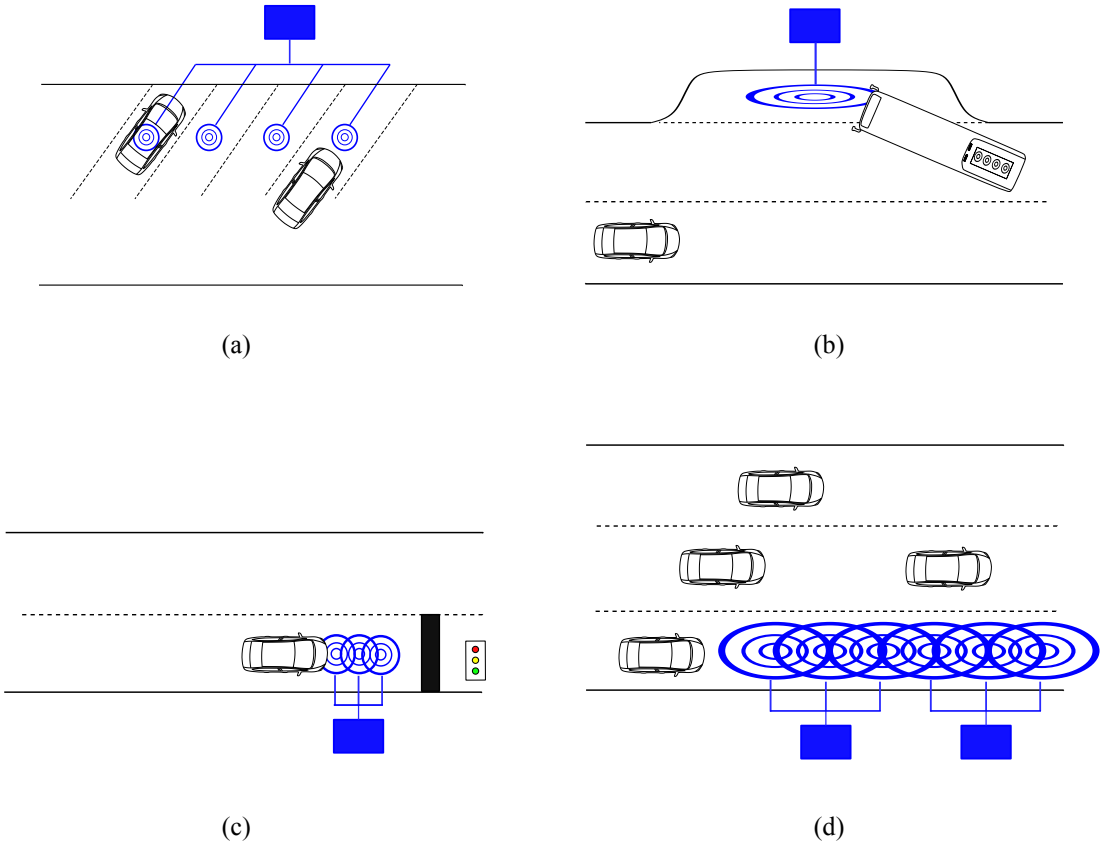

Fig. 1.1: WPTSs for vehicle application: (a) WPTS in a parking area, (b) WPTS at a bus stop, (c) semidynamic WPTS in proximity of a traffic light, (d) dynamic WPTS in a highway line.

of cost and weight. This last point brings also a reduction of the EVs' energy consumption.

The ideal placement of a dynamic WPTS is along a dedicated highway line (see Fig. 1.1(d)). One or more transmitting coil/s is/are buried under the highway pavement to form a structure called *track*. The track properly energized is used to create a magnetic field in the surrounding space. As in the static WPTSs, EVs are equipped with a receiving coil that in case of dynamic WPTSs is called *pickup*. When the EVs move along the designated highway line, the pickup coil links the magnetic flux produced by the track and converts the energy stored in the magnetic field into electrical energy that is used to charge the battery (or for the vehicle propulsion). Using the designated highway line, the EVs drivers allow the range of their cars to be extended.

Besides the installation on the highways, another solution for the employment of dynamic WPTSs is to create a compact network of chargers deployed on the roads that would keep the vehicle batteries charged at all times. It has been demonstrated [12] that if only a small percentage of the roadway is powered in urban environments, most vehicle types can easily meet the 480-km target range with a relatively small battery pack. The dynamic WPTSs can be installed in proximity of the traffic lights (see Fig. 1.1(c)) or at taxi ranks, where the vehicles could be stacked head to tail for a considerable amount of time. In the case of slow

moving traffic dynamic WPTSs are also referred to as semidynamic WPTSs [13].

The typical structure of a WPTS is common for both the static and the dynamic case. As shown in detail in Sec. 2.1, to properly supply the transmitting coil on one side and to condition the energy collected by the receiving coil on the other side, different types of power converters are necessary. Furthermore, to enhance the power transfer capability and to reduce the VA rating of the power supply, the transmitting coil/s and the receiving coil are equipped with compensating networks. They consist in electrical circuits formed by reactive components that, in addition to provide the reactive power required by the coil coupling, are used to change the electrical behaviors of the power supply.

The main difference between a static and a dynamic WPTS is in the coil coupling. In static WPTSs usually both the transmitting and the receiving coils are built in form of pad. The magnetic parameters of the coil coupling are almost fixed during the charging. On the contrary, the magnetic parameters of a dynamic WPTS are anything but constant during the EV motion and their variation depends also on the geometry and the topology of the coils. While the pickup coil of a dynamic WPTS is equivalent to the receiving coil of a static WPTS, the structure of the track can be different. According to the track structure, dynamic WPTSs can be classify into *stretched* track and *lumped* track systems. A stretched track system employs a track coil having the longitudinal dimension, or length, i.e. the dimension along the EV motion direction, much longer than the pickup coil; a lumped track system, instead, is made up of a set of coils having the longitudinal dimension comparable with that of the pickup coil. A stretched track system is more easily implementable with respect to a lumped track system, since the involved magnetic parameters are less prone to changing during the EV motion. However, stretched track systems suffer from poor coupling that brings efficiency and electromagnetic interference (EMI) issues. These problems can be overcome with a lumped track system. The intrinsic pulsating nature of the power transmitted with lumped truck systems makes their implementation challenging.

1.1 Aim and Contributions of the Thesis

The aim of this thesis is the study of dynamic WPTSs. Although static WPTSs are very similar to dynamic WPTSs with a lumped track structure, the variations of the magnetic parameters caused by the EV movement make the study, the design, and the control of dynamic WPTSs much more challenging.

The attention of this work is focused mainly in the control of dynamic WPTSs with a lumped track structure. Usually, for such systems, the power transfer regulation is carried out both in the grid side and in the car side. The power converters in the grid side, in particular a high-frequency inverter, are controlled to supply the track coil with a sinusoidal current of constant amplitude. In the car side, a dc/dc converter downstream a rectifier is used to regulate the battery charging process. Both the track-side control and the pickup-side control are faced in this thesis.

To increase the efficiency of the system and to reduce the unwanted stray field, a track coil of lumped track dynamic WPTSs should be supplied only when the

pickup is directly coupled to it. For this reason, the coils of the track should be switched on and off with a fast transient, in order to maximize the effective power transfer period and the amount of energy transferred to the moving EV. A good regulator for the grid-side inverter is mandatory to minimize the start-up transient period and to make the system robust against the variation of the parameters. The design of an effective controller calls for finding a good dynamic model of the system.

The ability to maintain the track current constant irrespective of the parameters variations could be a good intrinsic quality of a dynamic WPTS. This feature relieves the task of the control system, thus allowing a loosening of the regulator requirements. Among other things, compensating networks can provide this ability to the system. For this reason, part of the thesis is devoted to study various topologies of compensating networks. In particular, the LC compensating network in the track side is thoroughly analyzed since it is considered the best solution for lumped track dynamic WPTSs.

As regards the regulation of the battery charging in the EV side, usually, the standard topologies of non-isolated dc/dc converters are employed to fulfill this task. The particular topology used in dynamic WPTSs depends also on the type of compensating networks connected to the pickup. In this work, an accurate study is performed that takes into account both the pickup compensation and the dc/dc converter in a combined way and an attempt to simplify the scheme of the dc/dc converter by integrating part of it in the compensating network is made.

The main contribution of this thesis is the development of a novel method for the base band modeling of systems where modulated quantities are involved. The method is called Modulated Variable Laplace Transform (MVLT) and in this thesis it is applied to find the dynamic model of WPTSs. However, in general MVLT method can be applied to study the dynamic of a large variety of resonant converters. Here, the model obtained with the MVLT method of an LC-compensated dynamic WPTS is used to design the regulator that controls the track current.

Another important result of this thesis is the proposal of an unconventional topology for the pickup compensating network that tries to integrate also part of the dc/dc converter responsible for the battery charging. In the proposed topology, the large dc inductance used to sustain the rectifier output current in the parallel-compensated pickup has been moved in the ac side as part of the compensating network. The advantage of doing this is that the required value for the inductance in the ac side is lower than the value of the inductance in the dc side with the consequent reduction in weight and size of the pickup.

1.1.1 Scientific Contributions

The results reported in this thesis and also other scientific contributions have been published or will be published in some conference proceedings. The publications are listed below.

[1] **M. Forato** and M. Bertoluzzo, "A modified LCC-compensated pickup topology for dynamic wireless power transfer systems," presented at the IECON

2018 – 44th Annual Conference of the IEEE Industrial Electronics Society, Washington DC, USA, 2018.

[2] M. Bertoluzzo, **M. Forato** and E. Sieni, "Optimization of the compensation networks for WPT systems," presented at the IECON 2018 – 44th Annual Conference of the IEEE Industrial Electronics Society, Washington DC, USA, 2018.

[3] M. Bertoluzzo, G. Buja and **M. Forato**, "Transferred power leveling/energy maximization in dynamic WPT systems," presented at the IECON 2018 – 44th Annual Conference of the IEEE Industrial Electronics Society, Washington DC, USA, 2018.

[4] **M. Forato**, M. Bertoluzzo and G. Buja, "Dynamic EV charging WPT system control based on Modulated Variable Laplace Transform," in *Proc. 2018 IEEE PELS Workshop on Emerging Technologies: Wireless Power Transfer (Wow)*, Montréal, QC, Canada, 2018, pp. 1-6.

[5] **M. Forato** and M. Bertoluzzo, "Modified series-series compensation topology for WPT systems," in *Proc. 2018 IEEE PELS Workshop on Emerging Technologies: Wireless Power Transfer (Wow)*, Montréal, QC, Canada, 2018, pp. 1-6.

[6] **M. Forato**, M. Bertoluzzo and G. Buja, "Modeling of the dynamics of a resonant wireless power transfer circuit," in *Proc. 2017 IEEE 26th International Symposium on Industrial Electronics (ISIE)*, Edinburgh, 2017, pp. 472-477.

1.2 Outline of the Thesis

With the goal of providing the reader with a fundamental understanding of the topic, the main results are presented towards the end of the thesis in favor of a detailed introduction. This thesis consists of eight chapters and one appendix whose content is briefly explained in the following.

Chapter 2 presents the general scheme of a WPTS and describes in detail each part that forms it. A particular section is dedicated to the core element of a WPTS, i.e. the coil coupling, and the possible ways to model it are thoroughly illustrated.

An individual chapter (Chapter 3) is reserved to the compensating networks. In this chapter, the importance of the reactive power compensation in both the transmitting and the receiving side of WPTSs is highlighted. The common compensating networks, i.e. series, parallel and LC, are introduced and analyzed.

Chapter 4 studies the steady-state operation of various WPTSs. First of all, a WPTS with a series-series compensation is analyzed in order to show the limits of this compensating network when it is used in dynamic WPTSs. In the light of these limitations, the LC network for the compensation of the track side of dynamic WPTSs is introduced. The steady-state operation of an LC-series compensated dynamic WPTS is analyzed. To this scope, Appendix A can be very helpful since it provides a formulary that describes the steady-state operation of various WPTSs having the LC compensation in the transmitting side.

Chapter 5 deals with the dynamic modeling of WPTSs and presents the major contribution of this thesis, namely the MVLT method. At first, the effectiveness of the proposed method is verified through a simple test case in order to become acquainted with it. Afterward the MVLT method is applied to a series-compensated receiver of a WPTS, where it is shown that the method produces very accurate results.

In Chapter 6, the dynamic model of an LC-compensated dynamic WPTS obtained with the MVLT method is used to design the regulator that maintains the track current constant irrespective of the variations of the magnetic parameters caused by the EV motion. The faithful dynamic model allows for a good design of the regulator which provides a fast and stable start-up of the coil current of the considered lumped track dynamic WPTS.

The second main achievement of this thesis is presented in Chapter 7. In this chapter a novel pickup topology is proposed with the aim of reducing the size of the pickup circuitry. The particular control strategy adopted for the dc/dc converter responsible for the battery charging brings the pickup to work with the maximum efficiency. The operation of the pickup is carefully explained and a design procedure for the proposed topology is provided.

Chapter 8 summarizes the obtained results and concludes this work.

Chapter 2

Wireless Power Transfer Systems

In this chapter the main components of a Wireless Power Transfer System (WPTS) will be introduced and described in detail. First of all, a glance at the entire WPTS is given. Successively, each stage is explained in detail, starting from the coil coupling which is the core element of a WPTS. Battery charging process, receiver rectifier as well as transmitter-side inverter are exhaustively analyzed, at least from the WPTS perspective. The chapter concludes with the introduction of an equivalent scheme that is widely employed in the literature to study the electrical behavior of WPTSs.

2.1 Wireless Power Transfer Circuit

The typical WPTS for battery charging applications can be envisaged as in Fig. 2.1. It is constituted essentially by two galvanically isolated parts: the transmitting-side stage, stationary and located outside the EV, is used to transfer power, wirelessly by mean of an inductive coupling, to the receiving stage circuitry which resides on board the car.

The power required by the battery charging process is supplied by the utility grid through several stages. First, the low-frequency grid voltage v_G is rectified by an ac/dc converter with the power factor correction [14], [15]. The rectified

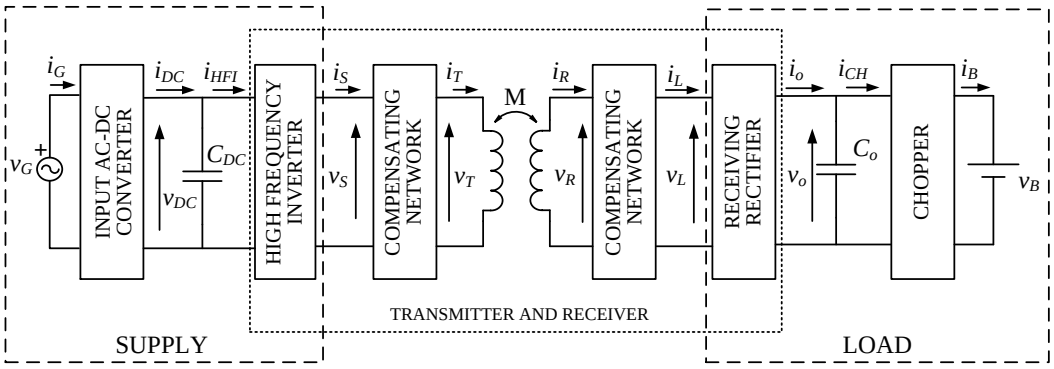

Fig. 2.1: Typical scheme of a Wireless Power Transfer System (WPTS).

current is then filtered by the capacitor C_{DC} which has the twofold purpose of: 1) eliminate the ripple in the voltage v_{DC}, 2) reduce the Electromagnetic Interference (EMI) in order to guarantee that the current i_{HFI}, absorbed by the system, does not affect the grid voltage quality. In this thesis, the capacitance C_{DC} is considered large enough to assume the voltage v_{DC} constant and equal to its average value V_{DC}. This voltage is used to feed an High Frequency Inverter (HFI) which, in turn, supplies the transmitting-side circuit. The HFI is typically a single-phase inverter[1] whose switching frequency ranges between 20 kHz and 150 kHz depending on the specific application [6], [17]–[19]. For the case of EV battery charging the Society of Automotive Engineers (SAE), in the J2954 Task Force [20], sets the interval 81.39-90 kHz in which the system supply frequency (the inverter switching frequency) has to lay. This relatively high frequency has been the crucial point that made the WPT feasible, allowing a reduction of the system size and an increment of the power transfer efficiency, which posed serious obstacles to the early WPTS commercialization [21], [22].

The high-frequency current i_T which flows in the transmitting coil creates an high-frequency magnetic field in the surrounding space. When the receiving coil, installed under the vehicle chassis, is moved in close proximity to this area, it is invested by the magnetic flux and, thanks to the Faraday's law, an ac voltage v_R appears across its terminals. Substantially, the electrical energy provided by the grid is first transformed into magnetic energy by the transmitting coil and then it is converted back into electrical by the receiving coil. Electrical energy is well suited to be conditioned to properly supply the battery v_B. Since the recharge of an EV battery requires a dc voltage and a dc current i_B, the alternating receiving coil current i_R is rectified by the a ac/dc converter. The rectified current i_o is first filtered and then it passes through a chopper which manages the charging process.

The large amount of reactive power involved in the coil coupling would not permit a conspicuous level of active power to be transferred while maintaining an acceptable efficiency and devices bulkiness. For this reason, WPTSs adopt compensating networks in both the transmitting and the receiving side. They are formed by inductors and capacitors which have to be tuned to resonate at the supply frequency. The simplest compensating networks are formed by a single capacitor which can be connected in series or in parallel with both the transmitting and the receiving coils [23]–[27]. Despite their simplicity the one-element compensating networks cannot meet different requirements. For this reason, several more complex topologies have been proposed [28]–[33].

2.2 Coil Coupling

The core element of a WPTS is unarguably the coil coupling. In this section, an overview of the various topologies and geometries of the coils will be presented first and then a thorough analysis of the possible ways for modeling the mutual coupling will by given.

[1] In [16], the authors have studied the possibility of supplying the system with a three-phase inverter.

2.2.1 Topologies and Geometries

To transfer power wirelessly, via inductive power transfer method, there should be at least two coils. One or more transmitting coils are laid outside the EV and they are stationary, while a receiver coil is installed underneath the EV and moves with it. As regards the stationary WPTSs, both the transmitter and the receiver coils are always made in form of pads, sometimes called couplers [34]. In dynamic WPTSs, the receiving coils are the same as in static WPTSs, whereas the transmitting coils, which are buried into the road, can assume different shapes. Usually the transmitting coils are deployed on an highway with a framework that resembles a *track*. For this reason, the transmitting coil/s of a dynamic WPTS is usually referred as track and the receiving coil, which is responsible to "collect" the magnetic flux produced by the track, is called *pickup*.

All the coils, being them employed in the track or in the pickup, typically consist of:

- a coil winding which is responsible for the magneto motive force (mmf) that produces the flux in the surrounding space;
- some magnetic cores that guide the flux toward the opposite coil by lowering the reluctance of the magnetic path;
- a shield that screens from the unwanted stray field. Usually it is made of a metallic sheet, but other methods are possible [35];
- a plastic case which protects the coil and confers on it stiffness and resilience properties[2].

Among the key points that have to be considered in the design of the coils, constraints on dimensions and efficiency are crucial. The couplers need to have high power density to fit the EV size and have to be as much efficient as possible in order to simplify the thermal management on-board the vehicle. Moreover, better designed coils allow more power to be transferred, the dimension and the efficiency being equal. The "quality" of a coil coupling is quantified through two parameters: the coupling coefficient k and the coil quality factor Q_L. The former is an indication of how much power can be transfer from the transmitter to the receiver, whereas the latter affects more the efficiency of the power transfer, although both efficiency and power are influenced by k and Q_L, in conjunction. The coupling coefficient will be investigated further in the next section, while a better insight into the coil quality factor is given here. The quality factor is given by the ratio between the *VA* rating of a coil and the power lost in it [36]:

$$Q_L = \frac{VA}{P_{loss}} = \frac{VA}{P_{Fe} + P_{Cu} + P_{sh}} \tag{2.1}$$

The *VA* rating of the coil is given by the product between the nominal RMS voltage across its terminals and the nominal RMS current that flows on it. The

[2]The plastic case which is always present in the receiver coupler on board the vehicle can be omitted in the transmitter construction when the coils are buried into the road.

power losses P_{loss} in (2.1) account for the copper losses P_{Cu} and for the hysteresis losses and the losses due to the eddy currents in the magnetic material collected in the term P_{Fe}. Since the shield that protects the pedestrians and the drivers from the stray field is made of metal, eddy currents flow also through it and they are responsible for the functioning of the shield itself. Unfortunately, even if the shield is made up with an high-conductivity material (e.g. aluminum), losses P_{sh} are unavoidable.

To improve the power transfer and the power transfer efficiency, WPTSs adopt frequencies in the kHz range. At these frequencies, both the copper losses and the losses in the magnetic material would be very high if the proper precautions were not taken. The higher the frequency is, the higher is the ac parasitic resistance of the coil. In fact, due to skin and proximity effects, the distribution of the high-frequency current is not constant throughout the cross sectional area of the wires forming the winding, but rather the current density is higher near the surface. These phenomena reduce the effective cross section available for the current flow, thus increasing the ohmic losses. Also the losses in the magnetic material increase with the frequency, according to the Steinmetz's law [37]. To reduce the copper losses, the wires that form the winding are made up of several self-isolated strands. In this way, the skin and the proximity effects are avoided. These particular wires are known as *Litz* wires. To reduce the magnetic losses, ferrite cores are employed to guide the flux between the coils. Ferrite cores are ceramic materials having very low conductivity and hence low eddy current losses. Unfortunately, ferrites have low saturation flux density (250÷500 mT) as compared with other magnetic material, e.g. silicon steels (1.5÷2 T) [38]. This fact has to be taken into consideration during the coil design. For the same flux, having an higher flux density permits the dimension of the magnetic structure to be shrunk, but a too high magnetic induction leads to saturation.

A different equation for the coil quality factor can be obtained introducing the equivalent series resistance of the coil r_L that account for the overall losses above mentioned. Equation (2.1) can be rewritten as:

$$Q_L = \frac{VA}{P_{loss}} = \frac{\omega L I * I}{r_L I^2} = \frac{\omega L}{r_L} \tag{2.2}$$

where L is the self-inductance of the coil and ω is the angular frequency of the nominal current that flows through it. From (2.2), it is noticeable that a coil with an high quality factor has the reactive part ωL much greater than the resistive part. In case of an ideal component, where $r_L = 0$, the quality factor tends to infinity.

Besides the quality factor and the coil coupling coefficient, another important parameter that is crucial for the WPTS coils is the tolerance to misalignment. Indeed, the transmitter and the receiver coils in static WPTSs, and even more so in the dynamic WPTSs, are never perfectly aligned. If the coils are too much sensitive to the coil coupling variations, the transmitted power can drastically reduce as soon as the EV position differs from the optimal one only by few centimeters [39].

A good magnetic design of the coil coupling may lead to a 50%-100% improvement, in terms of coil coupling, quality factor, transmitted power and efficiency and tolerance to misalignment, compared with some non-optimal designs [6].

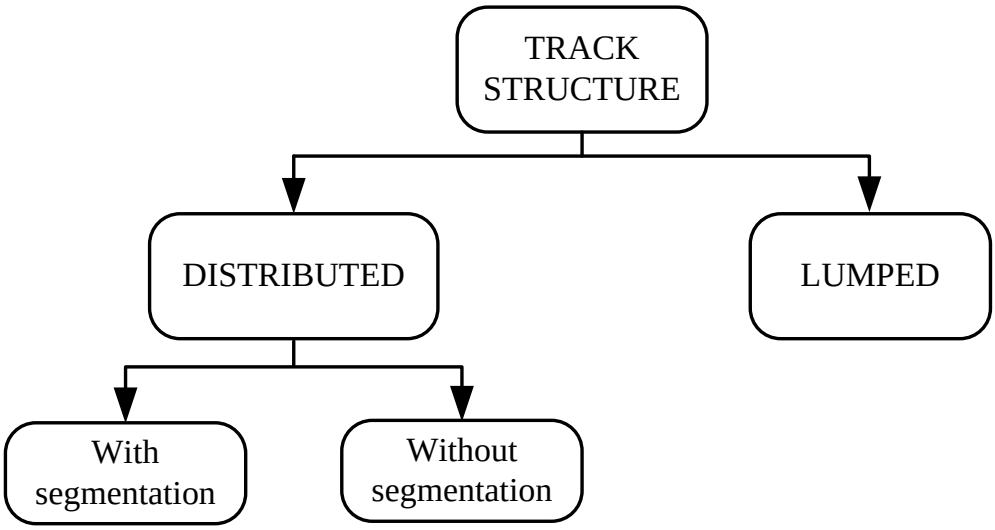

Fig. 2.2: Different topologies for the track structure.

Magnetic design is the fundamental step for the coil design, but cares must be given also to safety concerns. The parasitic current circulating in the metallic shield gives rise to ohmic losses P_{sh} that produce heat. If the heat is not conveniently drained away, the temperature of the coils can raise above admissible values. The same situation can arise when a metallic object is interposed between the transmitter and the receiver. Furthermore, a WPTS for EV charging should complies with the guidelines from the International Commission on Non-Ionizing Radiation Protection (ICNIRP) [40], [41]. These guidelines have been established to limit human exposure to time-varying electromagnetic field with the aim of preventing adverse health effects. ICNIRP stipulates that the general public should not be exposed to body average rms flux densities greater than 27 µT in the frequency range of 3 kHz–10 MHz, although above 100 kHz RF specific reference levels need to be also considered. Local spot measurements are allowed to exceed this 27 µT limit provided that the spatial average remains within the guidelines [42].

The first thing that one has to consider when is designing the coils of a WPTS is the particular configuration of the coil coupling that can be selected to transfer the required power on board the vehicle. In a static WPTS the only possible choice is in the couplers geometry, whereas in the dynamic WPTSs design, a fundamental point is the selection of the track topology. The track of a dynamic WPTS can be build according to various possibilities in terms of shapes and sized. The possible track structures can be classified as shown in Fig. 2.2. The track structure is distributed when the track is constituted by an elongated coil whose dimension in the EV-moving direction is much longer than the pickup coil. Since the pickup covers only a small portion of the track, the coupling coefficient of a WPTS with a distributed track is very small. The poor coupling brings efficiency and electromagnetic interference (EMI) issues. To reduce the EMI issue, the track can be built by segments with a single transmitter power converter and a set of switches to

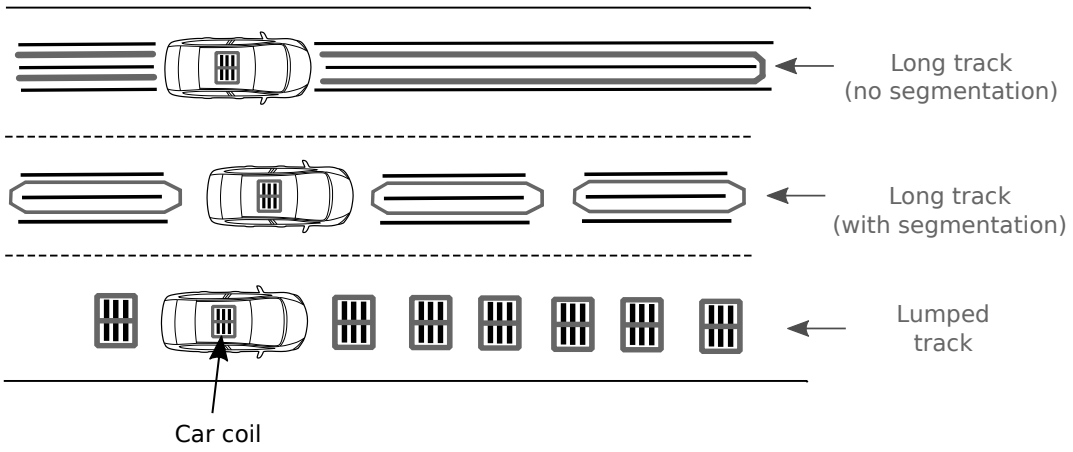

Fig. 2.3: Different topologies for the track structure.

alternately power the track [43]. A track segment is excited only when it is coupled with the pickup. In this way, the electromagnetic field above the inactive segments is reduced significantly. Even with this segmentation technique, a dynamic WPTS with a distributed track cannot attain the performance of a static WPTS.

When each segment is short enough and its size approaches the one of the pickup, the track structure is said to be lumped. In this topology the coils that form the track resemble the pads of a static WPTS and similar coils geometries can be employed. The different track structures are sketched in Fig. 2.3.

In a WPTS with a lumped track structure, ideally, there is one inverter for each coil of the track. In this situation, efficiency and EMI performance can be as good as in static WPTS. Unfortunately, this method is unaffordable since the system would become too expensive. Thus, the idea is to use one inverter for supplying few coils and the current in each pad can be controlled based on the position of the pickup. To do this, several sensors to estimate the car speed and position are needed. To avoid the use of a large number of sensors and the implementation of complex algorithms for controlling the track current, Luckic *et al.* proposed the reflexive field containment idea [44]. By carefully design the track and the pickup parameters, the primary current automatically raises in the track coil directly coupled with the pickup, thanks to the reflexive field of the pickup.

Distributed Track: Coil Geometries

The distributed track structure has been employed by researchers of Korea Advanced Institute of Science and Technology (KAIST) in the On-Line Electric Vehicle (OLEV) project [45]. OLEV is a project started in the 2009 with the target of making the dynamic WPT feasible, both from a technical and economical point of view. Since then, various generations of OLEV cars and busses have been developed and each generation has its own peculiar characteristics and improvements respect to the previous one [22].

The long track coils in a distributed track structure can assume different shapes imposed especially by the the ferrite core employed. With the succession of OLEV generations, various track structures have been implemented and tested, each one

with its particular ferrite core shape. The different track structures in the various generations of OLEV project are illustrated in Fig. 2.4 on the following page. Here, only a brief description of the track structures shown in Fig. 2.4 will be given. For a detailed overview of OLEV generations, one can refer to [22], [46], [47].

First Generation (1G) First generation of OLEV proofs the dynamic WPT concept in a golf car. In the 1G OLEV both the track and the pickup employ E-shaped ferrite cores (E stands for the shape of the cross-sectional area of the ferrite cores). The air-gap between the track and the pickup is 1 cm and, furthermore, the pickup coil is mechanically aligned with the track. The track length is 45 m.

Second Generation (2G) To increase the air-gap up to 17 cm in the 2G OLEV an U-shaped ferrite core has been deployed under the road in the KAIST Munji Campus to form the track and ten I-shaped pickup cores have been installed under a bus. The track length is 240 m and the track width is 1.4 m. The width of the track is large because two external wires have been employed to mitigate the magnitude of the magnetic flux density in the outer space.

Third Generation (3G) The main issues observed in the 2G OLEV have been the large width of the track structure, the inherently weak structure of the track, where the core separates the concrete into two parts and the significant stray field in the pickup coil due to the I-shaped ferrite cores. To solve this problems, various improvements have been adopted in the 3G OLEV. First of all, W-shaped track and flat pickups have been employed. Thus, the upward magnetic leakage flux from the pickup of 2G OLEV have been drastically mitigated by using the flat pickup core, which prohibits the magnetic flux between the power supply rail and pickup from leaking. Secondly, the bone structure of the track have been proposed. The W-shaped ferrite cores are placed far one from each other and the distance between them has been optimized. In this way, the concrete used in the construction of the track can percolate down through the bone structure, making it stronger against mechanical solicitations and without impairing its magnetic characteristics. The W-shaped cores have permitted to halve the width of the track with respect to the 2G OLEV.

Third Generation (3^+G) The efficiency obtained in the 3G OLEV had been too low and for this reason the researchers at KAIST decided to redesign all the power converting stages of the system. From this process, the 3^+G OLEV generation have arisen. Track and pickup geometries remain the same as 3G. Some 3^+G buses have been commercialized.

Fourth Generation (4G) In the 4G OLEV, thanks to the innovative I-shaped core, the track width have been reduced to 10 cm, whereas the air-gap and the tolerance to misalignment have increased to 20 cm and 24 cm, respectively. The track structure in the 4G OLEV is modular and so the deployment time, which was the drawback of the bone structure, have been reduced to

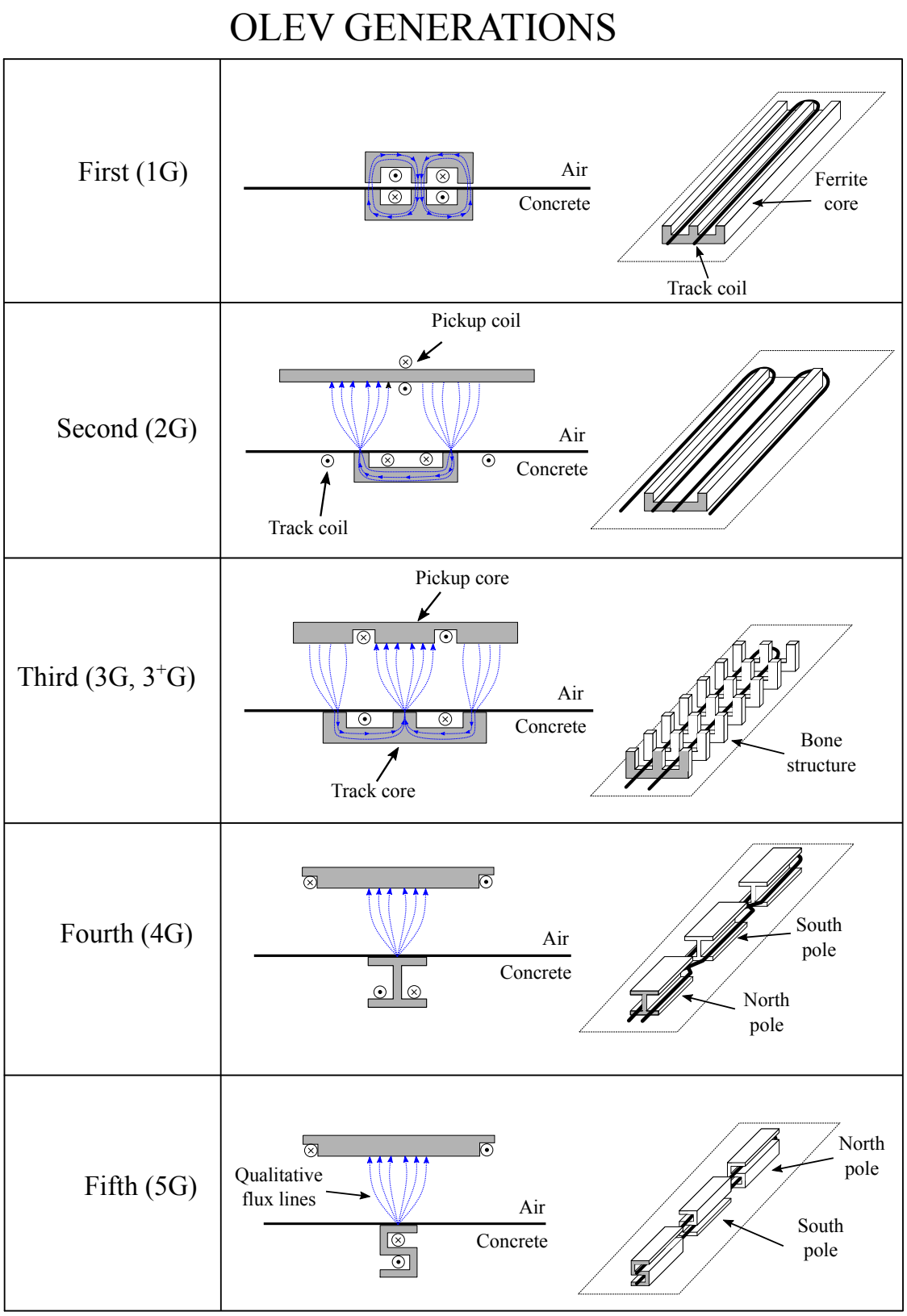

Fig. 2.4: Track structures in various generations of OLEV project.

few hours. The magnetic poles of the I-shaped track alternate along the track length, thus significantly reducing the lateral stray field.

Fifth Generation (5G) In the 5G OLEV, the I-shaped cores that form the track structure of the 4G OLEV are replaced with the same amount of ultra slim S-shaped cores. The S-shaped cores allow to reach a track structure width of 4 cm. The 5G OLEV still adopts modular track concept, where each module is self-compensated with a bank of capacitors connected in series. The high flexibility of S-shaped modules makes the track structure easy to bury.

Lumped Track: Coil Geometries

When the coils of the track become commensurable in size with the pickup coil, the track structure is said to be lumped. The coils of a lumped track assume almost the same geometry as the pickup and they resemble the couplers employed in the static WPT. The couplers of the static WPTSs usually are made in form of pads that embed the windings, the ferrite cores and the metallic shields all inside a case usually made of plastic. The good features required by well designed couplers are:

- high coupling coefficient k;
- high quality factor Q_L;
- high efficiency η;
- small size;
- high tolerance to misalignment.

When designing the couplers it is not easy to achieve the target for all the attributes at the same time. Designers of the coil coupling are often struggling with trade-offs: for example design the coils for having an high quality factor with large pads, rather than focusing on small pads with a limited attainable coupling coefficient. As stated, the above mentioned qualities are usually contrasting.

The characteristics of the couplers are mainly yielded by their geometries. First couplers for EVs consisted in coils wound around pot cores [48], [49]. After that, several design options have been proposed with their own advantages and disadvantages. In [35] the authors have described their developments over twenty years of research in couplers design and they have classified the couplers according to the scheme of Fig. 2.5.

Besides the above mentioned features, another interesting quality for the couplers of a WPT EV charging system is the possibility to approach the transmitting coil from any direction. This can be helpful in the parking operation of the vehicle, without a mechanism that assists the drivers. Based on this characteristic couplers can be classified into *polarized* and *non-polarized*. The particular symmetry of the geometry makes the polarized couplers sensitive to the orientation of the pads. The coupling coefficient between the transmitter and the receiver varies differently depending on the approaching direction. In a non-polarized pad the flux distribution

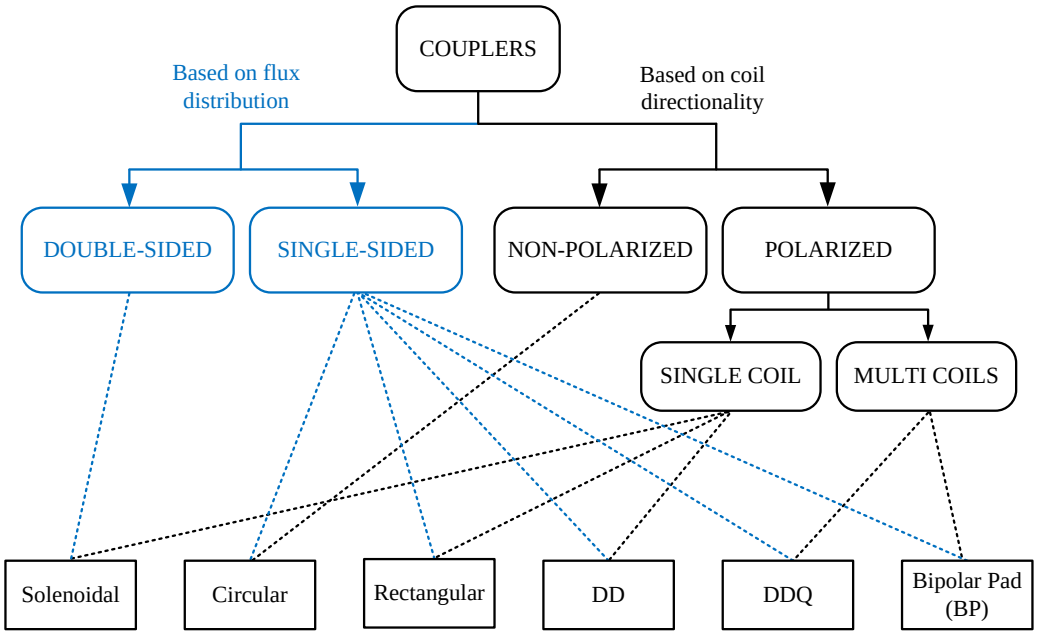

Fig. 2.5: Classification of the couplers valid both for static WPT and for dynamic WPT with lumped track structure.

around the transmitting coil is axisymmetric and so the direction from which the receiver coil approaches the transmitter does not influence the coupling coefficient.

From the scheme of Fig. 2.5, couplers can also be divided into *double-sided* and *single-sided* according to the flux distribution around the coils. The main flux of single-sided couplers exits the coil only by the right direction, i.e. the direction towards the opposite pad. On the contrary, the flux of double-sided couplers exists in both the side around the coil and so a large amount of flux is "wasted". The flux in the wrong side has to be screened through a metallic shield and this operation can reduce significantly the quality factor of the coil.

To date, the most common coupler used for EV charging is by far the circular pad, which origins directly from the early pot core topology. It consists of a spiral winding wound on a ferrite disk which lays in a plastic case that can contain the metallic shield for screening the stray fields [50], [51]. Ferrite is fragile and expensive and for this reason the authors in [52] have introduced an optimized version of the circular coupler. Ferrite disk has been substituted with commercial I-type cores laid under the winding as the spokes of a wheel. The layout of this coupler is shown in Fig. 2.6(a). In Fig. 2.6(a) (on the right) are depicted also the qualitative path of the magnetic flux density. It can be noticed that, from the symmetry of the coil and from the distribution of the field, the circular pad is single-sided and non-polarized. Since the flux is present only in the space between the coils, with circular pad high quality factor and low losses can be obtained. The circular pad designed in [52] has a native Q_L of 291 at 20 kHz and an inductance of 542 µH. The 700 mm diameter pad, designed to transfer 2 kW of power with an air-gap of 200 mm, dissipates 124 W, an so fans cooling is not necessary.

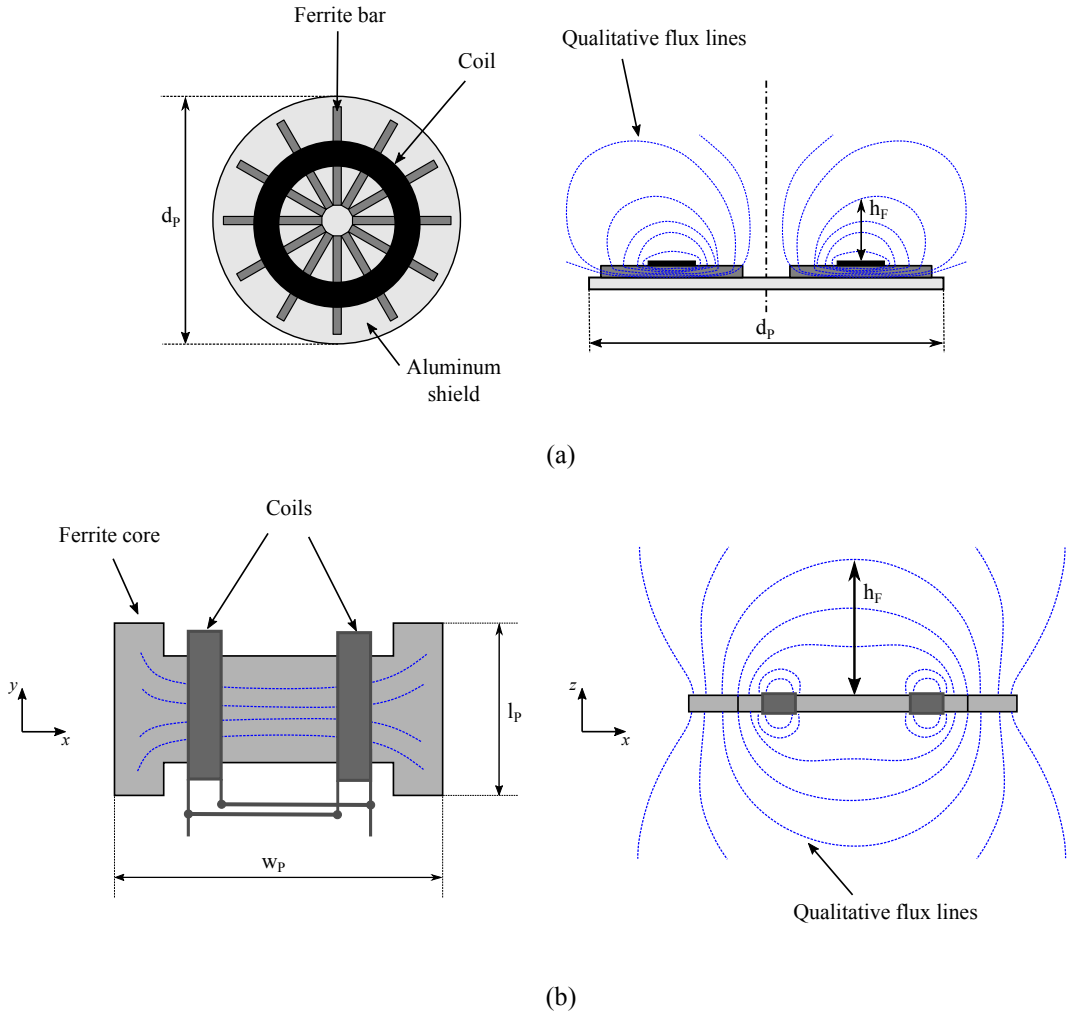

Fig. 2.6: Top (on the left) and front (on the right) views of: circular pad (a) and solenoidal coupler (b).

The circular couplers have also some drawbacks. When the circular pads are not properly aligned the power transferred to the receiver drops significantly. The maximum allowable misalignment is found to be 40% of the coil diameter and beyond this value no power is transferred.

Another issue of the circular pads is that for transferring the power required by EV applications with an air gap that must meet the automotive compliance, the pad size becomes very large. In fact, the transferred power depends on the coupling coefficient that, in turn, depends on the mutual flux between the transmitting and the receiving coils. The mutual flux depends on the capability of the transmitting pad to "launch" the flux toward receiver. An indication of the capability to launch the flux to the opposite pad is given by the quantity h_F, illustrated in Fig. 2.6, which is the *flux height*. It represents the height of the flux line corresponding to the minimum significant value of the magnetic flux density. For a circular pad the flux height is one quarter of the pad diameter ($h_F = \frac{d_P}{4}$) [34]. It is easy to understand that to transfer the same amount of power with a larger air-gap, the couplers has to be scaled up a lot.

A coupler similar to the circular pad, which loses the symmetry around the central axis, is the rectangular coil [53]. Rectangular coils show better tolerance to misalignment [54]. Typically, they constitute one of the coil for the multi coils couplers.

In the attempt to increase the power transfer capability of the circular couplers, authors in [34] designed the pad illustrated in Fig. 2.6(b). It consists of two flattened solenoids that are wound around a shaped ferrite bar. The two coils are connected magnetically in series to increase the mmf and electrically in parallel to limit the inductance value. With the same current rating, the higher the inductance is, the higher is the voltage rating of the pad. The advantage brought by the solenoidal pad is that the flux height h_F (see Fig. 2.6(b)) is half the pad width ($h_F = \frac{w_P}{2}$). A solenoidal pad with the same dimensions of a circular pad has a better coupling coefficient. Unfortunately, the solenoidal coupler is double-sided and the amount of flux coming out of the front of the pad is similar to that coming out of the back. For this reason, high losses arise due to eddy currents when a metallic shield is added to screen the backward field. The presence of the shield in [34] makes the quality factor Q_L of the coupler decrease from 260 to 86.

A coupler that combines both the advantages of the circular pad and of the solenoidal pad is the so called DD coil [42]. The layout of the DD coupler can be seen in Fig. 2.7. DD coupler is formed by two coils with D shape connected in such a way to produce the flux lines of Fig. 2.7(b). The two coils can lay on a ferrite plate, but as in a circular pad, only few properly arranged ferrite bars are enough for channeling the flux in order to avoid the unwanted rear field. Both the coils and the ferrite strips are arranged in a plastic case that possibly contains also the metallic shield.

As for the solenoidal coupler, with DD pad the gain in flux height is essentially a factor of two times higher than for a circular coil with the same linear dimension, corresponding to a coupling factor k that may be 20%-25% higher [36]. In [42] a DD coil with an inductance value of 589 µH and with a quality factor of 392 at 20 kHz have been designed.

Unlike the circular pad, the DD coil is polarized: the coupling coefficient varies differently based on the approaching direction. As concerns the tolerance to misalignment, according to Fig.2.7, the DD pad performs better in the y-direction with respect to the x-direction. In fact, with a misalignment of 34% in the x-direction with respect to the pad width w_P, there is a null point in the coupling coefficient and consequently in the transferred power. At this position, flux enters and exits the same coil, resulting in no induced voltage.

To improve the capability of the DD coil along the x-direction, multi coils couplers have been proposed for the receiving-side pad. The first version of a multi coils coupler is the DDQ which is shown in Fig. 2.8(a). DDQ pad employs a third coil in "quadrature" with the two D coils. The quadrature coil Q is a rectangular coil which is electrically independent from the D coils and magnetically it captures the flux that is spatially shifted of 90° from the flux coupled with the DD coils. The Q coil is self-compensated and the voltage that appears at its terminals is rectified through its own ac-dc converter as explained in [55]. Since the quadrature coil couples the vertical flux produced by the transmitting coupler and the DD coils intercept the horizontal flux, the DD and the Q coils can be considered independent.

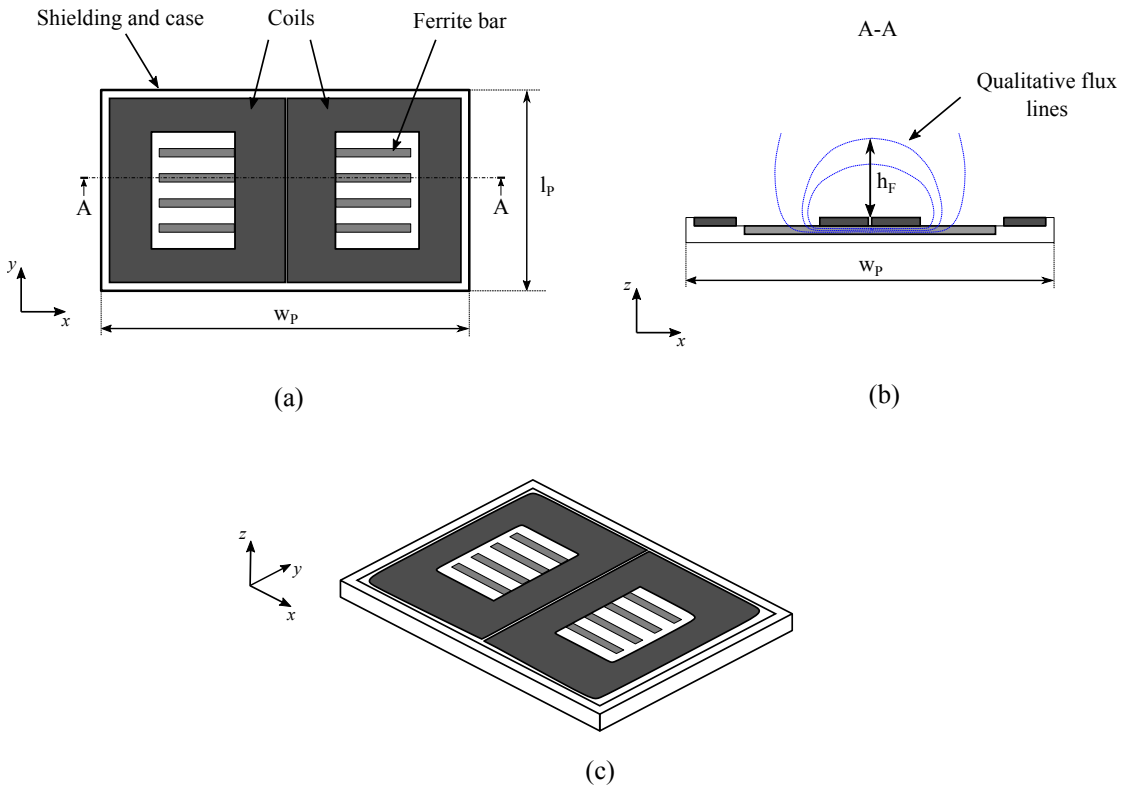

Fig. 2.7: Top (a), front (b) and 3D (c) views of DD coupler.

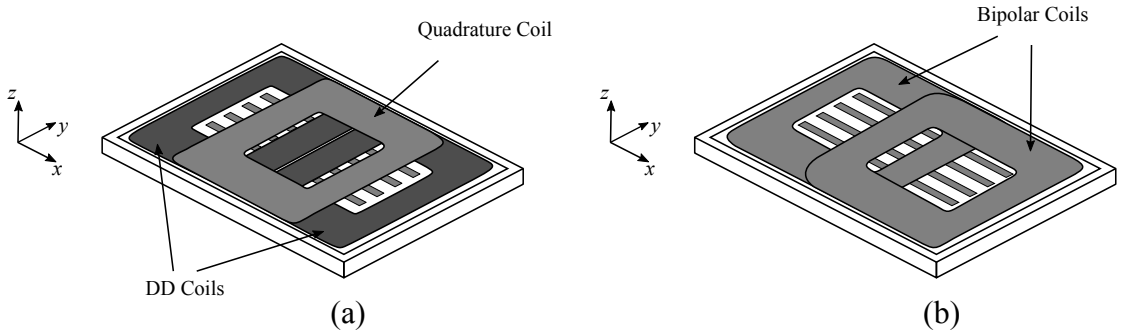

Fig. 2.8: 3D view of: DDQ pad (a) and bipolar pad (b).

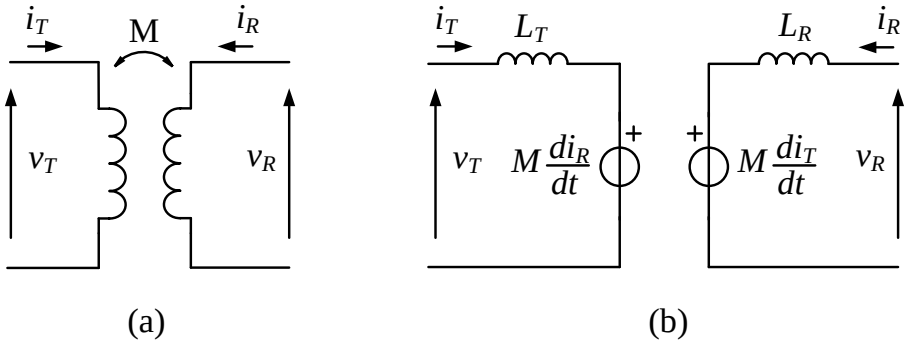

Fig. 2.9: Circuital symbol of the mutual inductance (a). Its equivalent electrical scheme (b).

In case of a DD transmitter coupled with a DDQ receiver, when the two couplers are aligned the output power is provided mainly by the DD coils of the receiver, while in case of misalignment along x-axis the output power is sustained by the quadrature coil. The charging zone of DD-DDQ couplers, defined as the physical operating region where the desired power can be delivered with a particular air gap, is almost three times larger of the charging zone of two circular pads [36].

Another multi coils receiving pad is the Bipolar Pad (BP) [56]. Its structure resembles the one of DD coupler, but the two D coils are overlapped in the x-direction (see Fig. 2.8(b)). In DDQ receiver the tolerance to misalignment along x-direction is achieved adding the quadrature coil to the DD pad. The BP obtains this tolerance to horizontal displacement by virtue of its overlapped coil design. The overlapped coil design achieves this tolerance because, as the induced power in one coil starts to drop down due to the relative horizontal misalignment from the transmitter, the induced power in the other coil starts to increase and starts providing sufficient power to the load before the first coil's output hits the null point. In addition, in a DDQ receiver the DD structure is naturally mutually decoupled from the Q coil due to their relative physical position, which enables the independent tuning and control of the DD and the Q coils. On the other hand, the overlap between the two coils constituting the BP, is designed to ensure zero mutual coupling between them. This mutual decoupling between the two coils enables the two BP coils to be independently tuned and controlled as well [56].

The output power attained from a BP coupled with a DD pad (and also the relative charging zone) is almost identical to the one obtained with a DD transmitter and a DDQ receiver. The advantage of using the BP as receiver pad is that it uses 25%-30% less copper than the DDQ pad [36].

2.2.2 Modeling

Two magnetically coupled coils can be represented from a circuital point of view by a two-port element whose symbol is shown in Fig. 2.9(a).

The equations that govern the relation between currents and voltages at the

two ports are given by:

$$\begin{cases} v_T = L_T \frac{di_T}{dt} + M \frac{di_R}{dt} \\ v_R = M \frac{di_T}{dt} + L_R \frac{di_R}{dt} \end{cases} \tag{2.3}$$

where L_T and L_R are the self-inductances of the coils and M is the mutual inductance between them. For physical reason, the parameters L_T and L_R are always positive, whereas M can be positive or negative depending on the sign convention adopted [57]. Henceforth, M will be considered positive, unless the contrary will be explicitly stated.

Equation (2.3) can be written in matrix form by:

$$\begin{bmatrix} v_T \\ v_R \end{bmatrix} = \begin{bmatrix} L_T & M \\ M & L_R \end{bmatrix} \cdot \frac{d}{dt} \begin{bmatrix} i_T \\ i_R \end{bmatrix} \tag{2.4}$$

which in a more compact notation is:

$$\mathbf{v} = \mathbf{Z} \cdot \frac{d}{dt}\mathbf{i} \tag{2.5}$$

where $\mathbf{v}$ is the vector of the voltages across the two-port, $\mathbf{i}$ is the vector of the currents and $\mathbf{Z}$ is the matrix that represents the relation between them (usually called *impedance matrix*).

The equations in (2.3) can be described with the circuit of Fig. 2.9(b), which is the widest used model of the coil coupling in the WPTS papers [44], [58]–[62]. It should be noted that the sign convention for both the ports is the passive element sign convention.

The infinitesimal electrical work that enters the two-port is given by:

$$dw = p\,dt = (p_T + p_R)\,dt = (v_T i_T + v_R i_R)\,dt \tag{2.6}$$

Using (2.3), equation (2.6) becomes:

$$\begin{aligned} dw &= \left(L_T \frac{di_T}{dt}\, i_T + M \frac{di_R}{dt}\, i_T + M \frac{di_T}{dt}\, i_R + L_R \frac{di_R}{dt}\, i_R \right) dt = \\ &= L_T\, d\left(\frac{i_T^2}{2}\right) + M\, d(i_T i_R) + L_R\, d\left(\frac{i_R^2}{2}\right) \end{aligned} \tag{2.7}$$

Equation (2.7) shows that the electrical work absorbed by the mutual inductance is a state function which depends only by the instantaneous values of the currents i_T and i_R. Thus, the total work absorbed in the interval which starts at the time t_0, when the currents are both equal to 0, and ends at time t_1, where $i_T(t_1) = i_T$ and $i_R(t_1) = i_R$, is given by:

$$w = \int_{t_0}^{t_1} p\,dt = L_T \frac{i_T^2}{2} + M\, i_T i_R + L_R \frac{i_R^2}{2} \tag{2.8}$$

which corresponds to the energy stored in the coil coupling at time t_1 (provided that $w(t_0) = 0$). Using the notation introduced in (2.5), equation (2.8) can be written as:

$$w = \frac{1}{2}\,\mathbf{i}^T\,\mathbf{Z}\,\mathbf{i} \tag{2.9}$$

where $\mathbf{i}^T$ indicates the transpose of the current vector. Since the two-port mutual inductance is a passive element, equation (2.8) and then (2.9) should be non-negative. Being (2.9) a quadratic form, it is always greater than or equal to zero if and only if matrix $\mathbf{Z}$ is positive semi-definite. This observation yields the following constrain:

$$L_T L_R \geq M^2 \Longrightarrow \sqrt{L_T L_R} \geq |M| \tag{2.10}$$

One important parameter which defines the "degree" of coupling between two coils is the coupling coefficient k which is equal to:

$$k \triangleq \frac{M}{\sqrt{L_T L_R}} \tag{2.11}$$

Parameter k is dimensionless and, by (2.10), can vary between -1 and 1; when $|k| = 1$ the two coils are *perfectly coupled*, if $|k| > 0.5$ the two coils are said to be *tightly coupled* and if $|k| < 0.5$ the two coils are said to be *loosely coupled*. In WPTSs the coupling coefficient is usually less than 0.3 and the power is transferred from primary to secondary by means of two loosely coupled inductors.

To give physical insight to the parameters of the two-port mutual inductance, we can refer to the Fig. 2.10. In Fig. 2.10(a), the magnetic flux lines for two circular coupled coils are depicted. It can be seen that part of the flux of the magnetic field (Φ_M) produced by the current i_T and i_R links both the transmitting and the receiving coils and is responsible of the mutual coupling between them, whereas the fluxes which link only one coil $\Phi_{T\sigma}$ and $\Phi_{R\sigma}$ gives rise to the leakage inductances. This situation can be approximately analyzed considering the equivalent magnetic circuit depicted in Fig. 2.10(b).

The parameters of the matrix in (2.4) are related to the magnetic flux thanks to the following equations:

$$L_T \triangleq \left.\frac{\varphi_{TT}}{i_T}\right|_{i_R=0} = \left.\frac{N_T\Phi_T}{i_T}\right|_{i_R=0} \tag{2.12}$$

$$L_R \triangleq \left.\frac{\varphi_{RR}}{i_R}\right|_{i_T=0} = \left.\frac{N_R\Phi_R}{i_R}\right|_{i_T=0} \tag{2.13}$$

$$M \triangleq \left.\frac{\varphi_{TR}}{i_T}\right|_{i_R=0} = \left.\frac{N_R\Phi_R}{i_T}\right|_{i_R=0} \tag{2.14}$$

where the variable φ_{ij} represents the flux produced by the coil i which links the coil j, thus, for instance, φ_{TT} means the flux produced and linked by the transmitting coil. These fluxes can be derived from the ones in Fig. 2.10(b) as indicated from the second equalities of (2.12), (2.13) and (2.14), in which N_T and

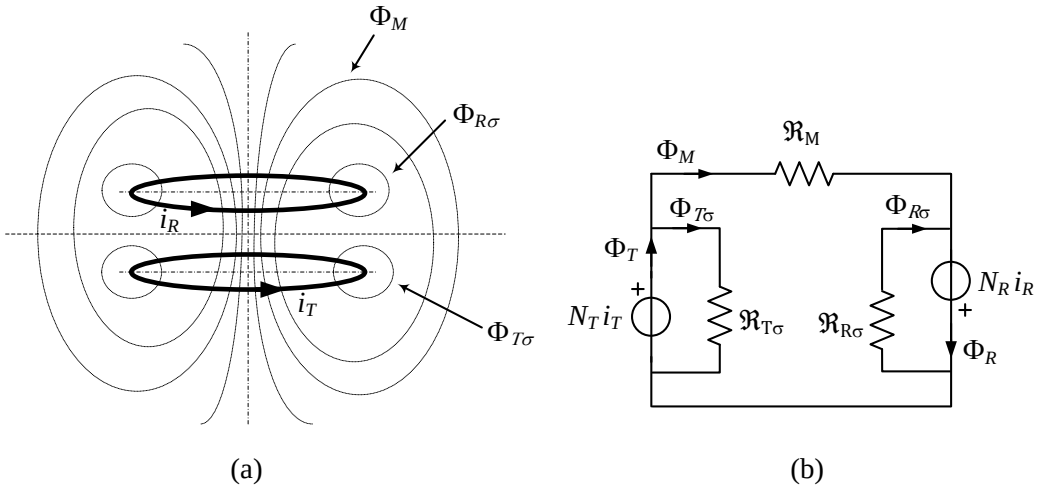

Fig. 2.10: Magnetic flux lines for a simple coil coupling structure (a) and its related magnetic circuit (b).

N_R are the number of turns of the transmitting and receiving coil, respectively[3]. Equations (2.12)-(2.14) can be further expanded, applying the Hopkinson's law and the superposition principle to the circuit of Fig. 2.10(b):

$$L_T = \left.\frac{N_T \Phi_M}{i_T}\right|_{i_R=0} + \left.\frac{N_T \Phi_{T\sigma}}{i_T}\right|_{i_R=0} = \frac{N_T^2}{\Re_M} + \frac{N_T^2}{\Re_{T\sigma}} = L_{TM} + L_{T\sigma} \tag{2.15}$$

$$L_R = \left.\frac{N_R \Phi_M}{i_R}\right|_{i_T=0} + \left.\frac{N_R \Phi_{R\sigma}}{i_R}\right|_{i_T=0} = \frac{N_R^2}{\Re_M} + \frac{N_R^2}{\Re_{R\sigma}} = L_{RM} + L_{R\sigma} \tag{2.16}$$

$$M = \left.\frac{N_R \Phi_M}{i_T}\right|_{i_R=0} = \frac{N_T N_R}{\Re_M} \tag{2.17}$$

In the previous equations $\Re_M$, $\Re_{T\sigma}$ and $\Re_{R\sigma}$ are the reluctances [38] for the magnetic path of the mutual flux, the transmitting coil leakage flux and the receiving-side leakage flux, respectively. For a configuration of flux as in Fig. 2.10(a) or in more complex magnetic structures, in which the flux pipes are not well defined, it is very difficult to calculate the reluctances analytically, and usually Finite Element Method (FEM) commercial software are employed [51], [53], [63]. Equations (2.15) and (2.16) show that both the self-inductances can be split in two contributions: the part of the self-inductance caused by the common flux and the part due to the leakage fluxes. It is worth noting that the parameters L_{TM}, L_{RM} and M constitute a perfectly coupled coil[4]. So, $L_{T\sigma}$ and $L_{R\sigma}$ represent additional inductances

[3] These equations are derived assuming that all the turns of the transmitting and the receiving coils link the same flux. This approximation can be not realistic in case of a distributed coils, like for example the spiral coils.

[4] Indeed, the fictitious parameter k defined as the ratio between M and the square root of the product L_{TM} times L_{RM} is equal to 1, as can be ascertained from equation (2.15) and (2.16).

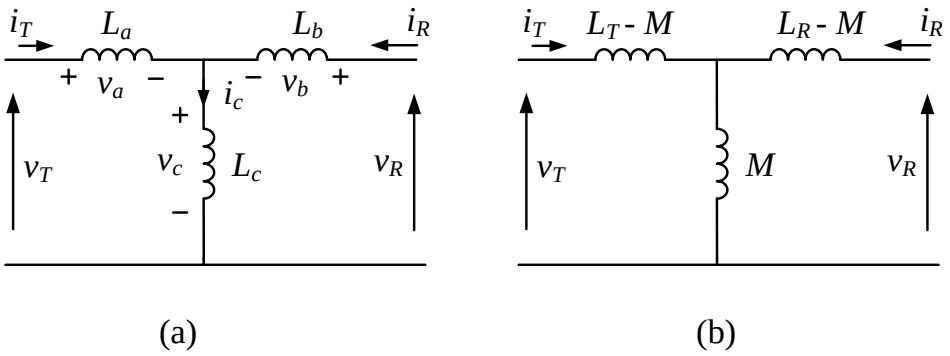

Fig. 2.11: T circuit with generic inductances (a). Equivalent T-circuit of a coil coupling (b).

to put in series with two perfectly coupled coils (L_{TM} and L_{RM}), but they do not contribute in the energy exchange between transmitter and receiver.

Coming back to (2.3) or (2.4), it can be noticed that only three parameters are necessary to completely define the coil coupling. For this reason, the equations in (2.3) can be represented with the T topology circuit shown in Fig. 2.11(a).

The equivalence of the circuit in Fig. 2.11(a) and the one in Fig. 2.9(b) is guaranteed if the generic inductances L_a, L_b and L_c are equal to:

$$L_a = L_T - M \tag{2.18}$$
$$L_b = L_R - M \tag{2.19}$$
$$L_c = M \tag{2.20}$$

Indeed, being $i_c = i_T + i_R$, $v_T = v_a + v_c$ and $v_R = v_b + v_c$, the voltages at the two ports can be written as:

$$\begin{cases} v_T = L_a \frac{di_T}{dt} + L_c \frac{di_c}{dt} = (L_a + L_c) \frac{di_T}{dt} + L_c \frac{di_R}{dt} \\ v_R = L_b \frac{di_R}{dt} + L_c \frac{di_c}{dt} = (L_b + L_c) \frac{di_R}{dt} + L_c \frac{di_T}{dt} \end{cases} \tag{2.21}$$

Since the circuit in Fig. 2.11(a), by definition, represents the coil coupling, equation (2.21) has to be equal to (2.3) and this is valid when equations (2.18)-(2.20) are satisfied. The equivalent T-circuit of a coil coupling is drawn in Fig. 2.11(b) and it is quite employed in WPTS literature [10], [64]–[67].

Further considerations about the circuit in Fig. 2.11(b) can be done by applying a voltage source v_s in the transmitting side and measuring the open-circuit voltage in the receiving side. In this situation, since $i_R = 0$, equation (2.21) in addition with (2.18)-(2.20) becomes:

$$\begin{cases} v_s = L_T \frac{di_T}{dt} \\ v_{OC} = M \frac{di_T}{dt} \end{cases} \tag{2.22}$$

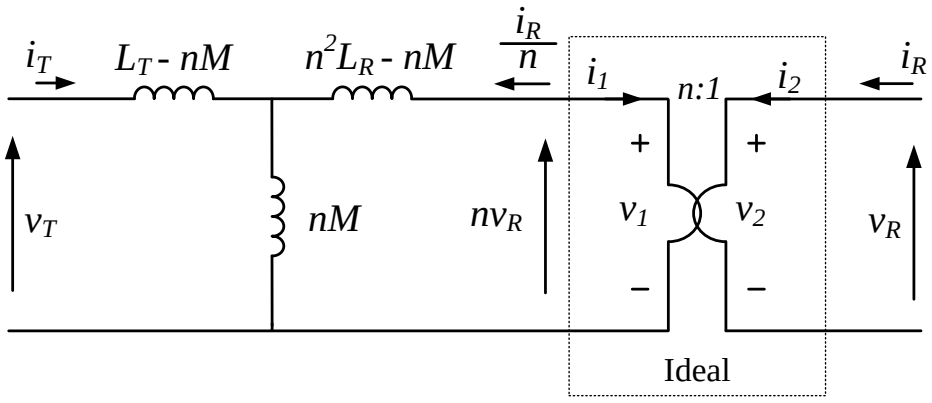

Fig. 2.12: Equivalent T-circuit of the coil coupling with an ideal transformer in cascade.

If the receiving-side open-circuit voltage v_{OC} is greater than the voltage v_s, i.e. the coil coupling is amplifying the input voltage, from (2.22), it is easy to derive the condition $M > L_T$ and so the inductance L_a of Fig. 2.11 becomes negative[5]. The meaning of a negative inductance in time-domain analysis is not clear. Anyway, this situation can be avoided by inserting in cascade to the network of Fig. 2.11(b) an amplifying element: the ideal transformer. The result is shown in Fig. 2.12.

The parameters of the Fig. 2.12 is calculated starting from the equations of the ideal transformer:

$$\begin{cases} v_1 = n\, v_2 \\ i_1 = -\frac{1}{n}\, i_2 \end{cases} \tag{2.23}$$

As a consequence, the T-network upstream the ideal transformer in Fig. 2.12 can be envisaged like the equivalent circuit of a two-port mutual inductance having v_T and i_T as electrical quantities in the primary port and $n\, v_R$ and $\frac{i_R}{n}$ in the secondary port. At the same time, the relations (2.3) for the outermost ports must hold to guarantee the equivalence of the circuit in Fig. 2.12 with the circuit of Fig. 2.11(b). In other words, to find the values of the impedances for the T-network of Fig. 2.12 that make the two circuits equal, it is necessary to maintain the relations (2.3) unaltered using the variable $\frac{i_R}{n}$ and $n\, v_R$ for the second port. This is accomplished as follows:

$$\begin{cases} v_T = L_T \frac{di_T}{dt} + nM \frac{d}{dt}\left(\frac{i_R}{n}\right) \\ n\, v_R = nM \frac{di_T}{dt} + n^2 L_R \frac{d}{dt}\left(\frac{i_R}{n}\right) \end{cases} \tag{2.24}$$

It is easy to proof that the impedance matrix of the coil coupling changes according to:

[5]The same consideration can be done applying the voltage source in the receiving side. If the open-circuit transmitting-side voltage is greater than v_s the condition $M > L_R$ arises.

$$\mathbf{Z} = \begin{bmatrix} L_T & nM \\ nM & n^2 L_R \end{bmatrix} \tag{2.25}$$

which yields the equivalent T-network sketched in Fig. 2.12. It is worth to note that the turns ratio n of the ideal transformer can be chosen arbitrarily, provided that $L_T - nM$ and $n^2 L_R - nM$ remain positive. The classical choice, made especially in case of tightly coupled inductors with an iron core which guides the flux, i.e. in the real transformers, is to set n equal to the ratio between the number of turns of the transmitting coil N_T and the number of turns of the receiving coil N_R. In this case, referring to (2.15)-(2.17), we have:

$$n \triangleq \frac{N_T}{N_R} = \frac{L_{TM}}{M} = \frac{M}{L_{RM}} \quad \Rightarrow \quad n = \sqrt{\frac{L_{TM}}{L_{RM}}} \tag{2.26}$$

With the relations in (2.26), the inductance $n^2 L_R - nM$ of Fig. 2.12, for example, assumes the form:

$$n^2 L_R - nM = n^2 \left(L_R - \frac{M}{n} \right) = n^2 \left(L_R - L_{RM} \right) = n^2 L_{R\sigma} \tag{2.27}$$

In the same way, the inductances $L_T - nM$ and nM can be treated. The resulting equivalent scheme is shown in Fig. 2.13(a). In the figure, the inductance calculated with (2.27) has been referred to the receiving side with the standard rule valid for the ideal transformer of dividing by n^2. This model is employed for example in [29], [47], [68].

Another possible and feasible solution is to choose n equal to:

$$n = n_e = \sqrt{\frac{L_T}{L_R}} \tag{2.28}$$

Such value of n is an effective turns ratio that tends to become equivalent to $\frac{N_T}{N_R}$ only when the coupling between the coils is high, namely when $L_{T\sigma}$ and $L_{R\sigma}$ approach zero.

With this selection of n, the inductance nM can be written as:

$$nM = n_e M = \sqrt{\frac{L_T}{L_R}}\, k \sqrt{L_T L_R} = k L_T \tag{2.29}$$

in which (2.11) has been used. As in (2.29), all the other inductances of Fig. 2.12 can be inferred. This selection of n originates the scheme in Fig. 2.13(b), which in literature can be found in [32].

All the circuits derived in this section are valid because they have been obtained by mathematical manipulations of the equations governing the coil coupling. In any case, as concern WPTSs, the model of Fig. 2.9(b) seems to be the best one. This is simply because the self-inductances of the coils are easy measurable (unlike for example L_{TM} and L_{RM}) and they are almost constant against the coupling coefficient variation.

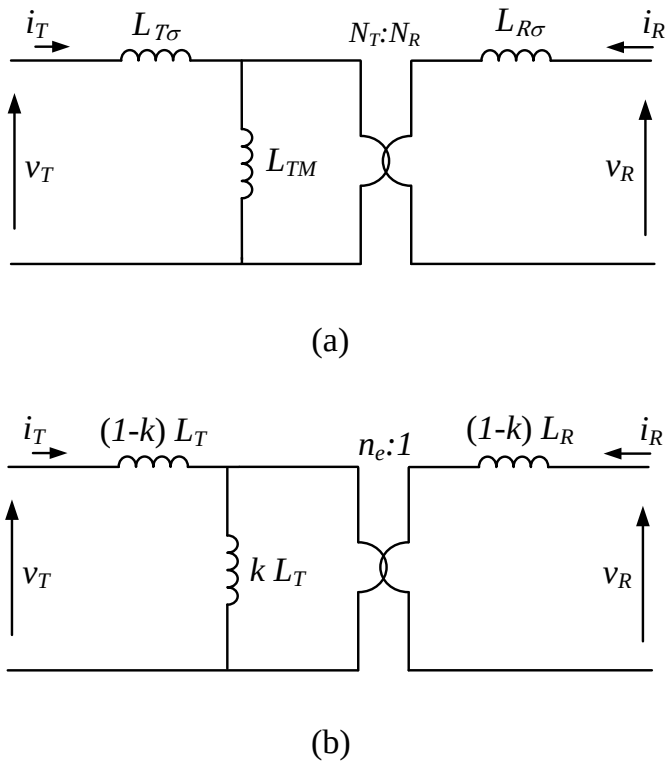

Fig. 2.13: Equivalent T-circuit of the coil coupling with an ideal transformer in cascade. The turns ratio of the ideal transformer is $\frac{N_T}{N_R}$ in (a) and n_e in (b).

Parameters Measurement

In a standard single-phase transformer, where the two coils are tightly coupled, the most convenient way to model the coil coupling is the one depicted in Fig. 2.13(a). In fact the parameters of the equivalent circuit are easily evaluated by two simple measurements. The short-circuit test can be used to measure the leakage inductances, whereas with the open-circuit test, L_{TM} is obtained [69]. These two tests are based on the fact that for a transformer the inductance L_{TM} is significantly higher than $L_{T\sigma}$ and $L_{R\sigma}$. If the two coils are loosely coupled, as it happens in WPTSs, finding L_{TM} and $L_{T\sigma}$ separately is not so easy. For this reason, in this case it is more advisable to calculate the parameters L_T, L_R and M. If the equivalent T-circuit of the coil coupling is still required, it can be obtained starting from the one in Fig. 2.12.

The two self-inductances and the mutual inductance of a coil coupling can be obtained using an RLC meter and performing the measurements illustrated in Fig. 2.14. The RLC meter works by supplying a sinusoidal voltage v_m with a fixed frequency and sensing the current i_m. Depending on the phase displacement between v_m and i_m and the ratio between their amplitude, this instrument is able to provide the resistive and the reactive parts of the impedance for the circuit under measurement.

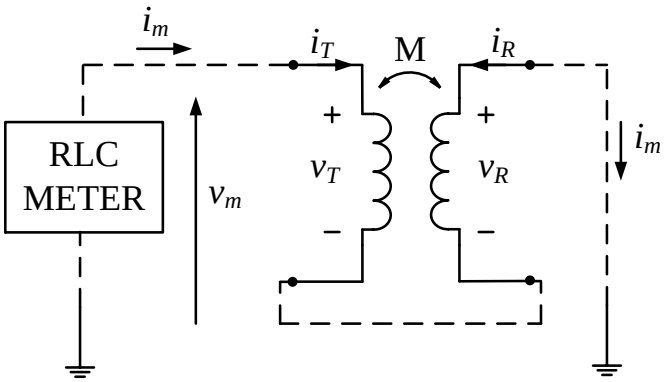

(a)

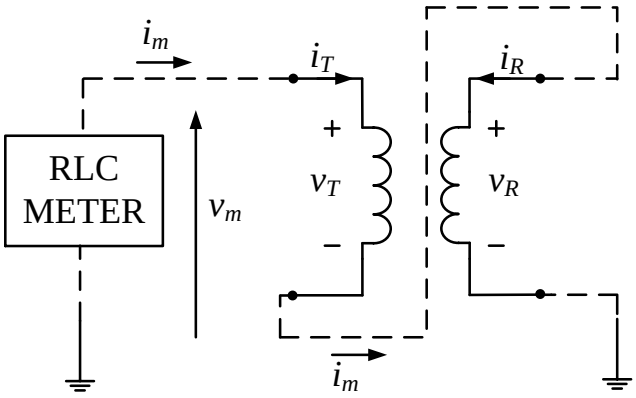

(b)

Fig. 2.14: Simple setup to measure L_T, L_R and M of a coil coupling.

Connecting the two windings of a coil coupling as in Fig. 2.14(a), the voltage supplyed by the RLC meter can be written as the difference between v_T and v_R, which is given by (cf. (2.3)):

$$v_m = v_T - v_R = (L_T - M)\frac{di_T}{dt} + (M - L_R)\frac{di_R}{dt} \tag{2.30}$$

Since from Fig. 2.14(a) it comes out that $i_T = i_m$ and $i_R = -i_m$, equation (2.30) can be written as:

$$v_m = v_T - v_R = (L_T + L_R - 2M)\frac{di_m}{dt} \tag{2.31}$$

It is easy to see that with the setup of Fig. 2.14(a), the RLC meter measures an inductance whose value is $(L_T + L_R - 2M)$.

Likewise, the inductance measured by the RLC meter with the configuration of Fig. 2.14(b) is found to be:

$$L_m = (L_T + L_R + 2M) \tag{2.32}$$

The circuit in Fig. 2.14(b) is obtained from the setup of Fig. 2.14(a), swapping the role between the ground terminal of the RLC meter and the auxiliary wire, in the receiving coil.

Summing up and subtracting the above measures of inductance, we get:

$$L_m^{(1)} + L_m^{(2)} = 2\,(L_T + L_R) \quad \Rightarrow \; L_T + L_R = \frac{L_m^{(1)} + L_m^{(2)}}{2} \tag{2.33}$$

$$L_m^{(2)} - L_m^{(1)} = 4M \quad \Rightarrow \qquad M = \frac{L_m^{(2)} - L_m^{(1)}}{4} \tag{2.34}$$

where the superscript numbers stand for first or second configuration of Fig. 2.14. As can be seen, from (2.34) the mutual inductance is found, whereas (2.33) can be used to obtain the sum of the two self-inductances.

The self-inductance, say L_T, can be measured connecting the RLC meter across the transmitting coil, while letting the receiving coil open.

These three measurements are enough to find the parameters that define the coil coupling.

Effects of the Receiver on the Transmitting Side

One of the main reason why the models derived from the circuit of Fig. 2.12 have been introduced is due to the fact that they replace the troublesome current-controlled voltage sources of Fig. 2.9(b) with a network made by impedances. Consequently, the effect of a load connected to the receiver can be examined throughout the well-known methods of analysis for the passive networks.

In the study of WPTSs, though, as it will be lighten in the next chapters, it is more convenient to adopt the model in Fig. 2.9(b). Therefore, it is useful to understand how to evaluate the impact of the receiver on the transmitting side. These effects are not so trivial to be studied since the transmitter, in turn, affects the receiving stage, giving rise to a reciprocal interaction.

For the purpose of studying the effects of a load connected to the receiving side, it is convenient to analyze the coil coupling and the load itself in the s-domain. The situation is sketched in Fig. 2.15, where it can be observed that the behavior of the load is represented via an equivalent impedance $Z_L(s)$.

The equations of the coil coupling, written in s-domain are given by:

$$\begin{cases} V_T(s) = sL_T\, I_T(s) + sM\, I_R(s) \\ V_R(s) = sM\, I_T(s) + sL_R\, I_R(s) \end{cases} \tag{2.35}$$

An inspection of Fig. 2.15 allows the voltage V_R to be written as:

$$V_R(s) = -Z_L(s)\, I_R(s) \tag{2.36}$$

which, substituted in the second of (2.35), yields the current $I_R(s)$:

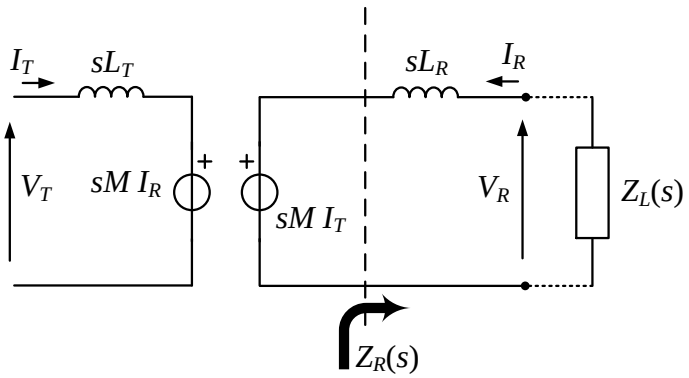

Fig. 2.15: Load connected in the transmitting side of a coil coupling. Circuit studied in s-domain.

$$I_R(s) = -\frac{sM}{Z_R(s)}\, I_T(s) \tag{2.37}$$

where, as indicated in Fig. 2.15, $Z_R(s)$ is the impedance seen by the current-controlled voltage source of the receiving side and it is given by $Z_R(s) = sL_R + Z_L(s)$. Using (2.37), the first equation of (2.35) becomes:

$$V_T(s) = sL_T\, I_T(s) + \left(-\frac{s^2M^2}{Z_R(s)}\right)\, I_T(s) \tag{2.38}$$

Equation (2.38) states that the effect of the receiving-side circuit on the transmitter can be represented via an equivalent *reflected* impedance given by

$$Z_{ref}(s) = -\frac{s^2M^2}{Z_R(s)} \tag{2.39}$$

In the study of WPTSs, since the quantities involved in the coil coupling at steady-state are approximately sinusoidal, it is quite common to introduce the phasors to analyze the circuit. Relations (2.35)-(2.39) remain valid also in the phasor-domain, provided that the Laplace variable s is substituted with the imaginary quantity $j\omega$. As an example, the reflected impedance in the phasor-domain is given by:

$$\dot{Z}_{ref} = \frac{\omega^2M^2}{\dot{Z}_R} \tag{2.40}$$

2.3 Battery Charging Process

The battery charging process depends upon the type of the battery that has to be charged. Although different batteries have their inherent characteristics, the charging methods for the EV batteries are standard. Typically, the battery charging process is controlled through a dc/dc converter that adjusts the energy

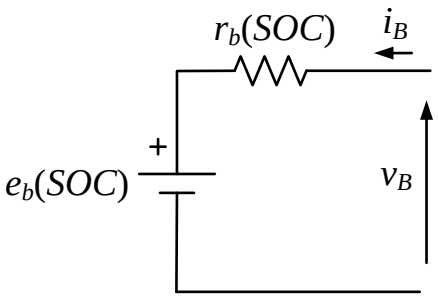

Fig. 2.16: Equivalent Thévenin circuit for a battery.

source features to the battery requirements. These voltage and/or current requirements remain unaltered for long time as compared with the time period of the ac quantities involved in a WPTS. For this reason, as concern the study of the power transfer between transmitter and receiver, battery and dc/dc converter can be modeled with an equivalent resistance.

2.3.1 Charging Methods

Despite the different chemistries, all the batteries can be characterized by their electrical behavior at terminals. At a first glance, a battery, being it lead-acid rather than Li-ion, can be conceived as a voltage source in series with a resistor (cf. Fig. 2.16) [70]. In Fig. 2.16 the parameter e_b is the internal voltage, also known as open-circuit voltage or e.m.f., of the battery which is produced by the internal chemical reactions at the two electrodes. It depends on several conditions, especially from the State Of Charge (SOC) of the battery. The nominal open-circuit voltage for the common cells employed in the EVs batteries ranges from 1.2 V for the NiMH batteries to 2 V of the lead-acid batteries, up to 3.7 V typical of the Li-ion batteries. The process of charging/discharging of the batteries is not 100% efficient. There are some internal losses that are modeled through the resistance r_b and depend upon the temperature, SOC and the State Of Health (SOH) of the battery. The rough model of Fig. 2.16 is oversimplified and cannot give any detailed and accurate information about the battery operation and performance such as the battery SOC, thermodynamics, etc [71], [72]. However, it is a good starting point to examine in broad terms how batteries behave during the charging process.

For EV batteries, there are the following common charging methods:

1. **Constant Voltage (CV)** Constant voltage method charges the battery at a constant voltage set to the full charging voltage reached by the battery at the end of the charging process. This method is suitable for all kinds of batteries and probably is the simplest charging scheme. The battery charging current varies along the charging process. Since at the beginning of the charging the battery e.m.f. is low, the charging current can be large at the initial stage and gradually decreases to zero when the battery is fully charged, namely

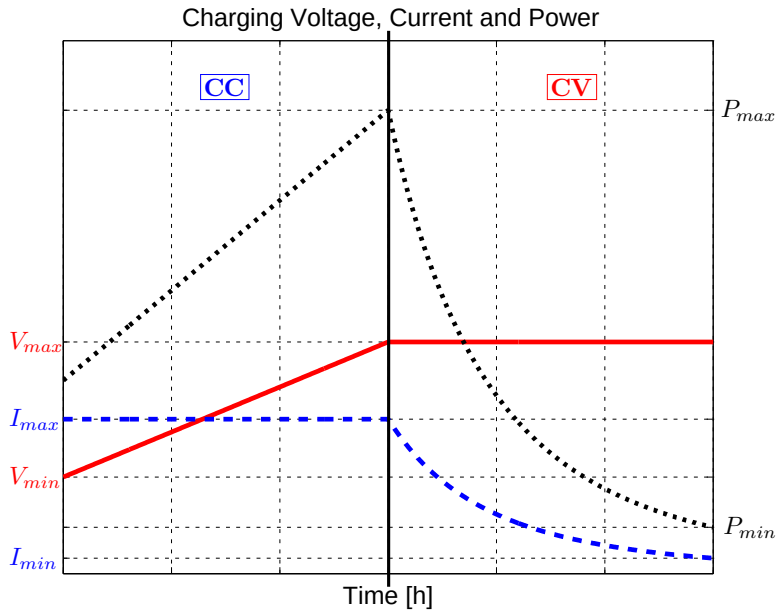

Fig. 2.17: Battery charging waveforms: charging current (blue dashed line), battery voltage (red solid line) and charging power (black dotted line).

when the battery e.m.f. reaches the full charging voltage. The drawback in this method is the requirement of very high power in the early stage of charging.

2. **Constant Current (CC)** In this charging scheme, the charging voltage applied to the battery is controlled to maintain a constant current through the battery. The SOC will increase linearly versus time for a constant current method. The challenge of this method is how to determine the completeness of a charge with SOC 100%.

3. **CC-CV** . This method is the combination of constant voltage and constant current methods. During the charging process of a battery, normally both the methods are used.

In Fig. 2.17 the voltage, the current and the power waveforms during the CC-CV charging process of a generic battery are illustrated. At the initial stage, the battery is charged with a constant current. Usually the current in the CC stage is set to be the highest possible (I_{max}) compatibly with the manufacturer specifications; this permits the charging process to be hastened. Meantime, the voltage across the battery terminals, which starts from the minimum value V_{min} in case of completely discharged batteries, tends to boost. In Fig. 2.17 this growth is approximated with a linear raise, though usually the voltage in the CC stage assumes different shapes [73]. When the voltage reaches the maximum value V_{max}, the charging process enters the CV stage. During this phase, the voltage across the battery terminals is maintained constant and equal to V_{max}, whereas the battery e.m.f. continues to grow. Subsequently, the charging current starts to decrease.

The charging process ends when the current reaches the minimum value I_{min}, which is usually given as a percentage of I_{max} (e.g. 1%, 5%, 10%).

The parameters which define the charging process, i.e. V_{min}, V_{max} and I_{max} are specified in the battery datasheet, whereas I_{min} can be rationally chosen. Typically, the charging current I_{max} is given by the manufacturer in terms of *C-rate*. The *C*-rate expresses the charging current (and also the discharging one) in a normalized way, thus allowing a comparison between batteries with different capacities. It is defined as the ratio between the actual discharging current and the current that ideally discharges the battery in 1 h. For example, if the capacity of a battery is $10\,\mathrm{A}\cdot\mathrm{h}$, the current that completely discharges the battery in 1 h is 10 A and, by definition, its *C*-rate is equal to $1C$. Therefore, a charging/discharging current of 20 A has a *C*-rate equal to $2C$. In the same way, the *C*-rate for a current of 5 A is $0.5C$, which is preferably written as $C/2$ or in more compact notation as $C2$. Batteries with high *C*-rate can be charged faster.

Besides voltage and current, in Fig. 2.17, it is displayed the power absorbed by the battery during the charging process[6]. It can be seen that the power is maximum in the transition point between CC and CV stages. The maximum power P_{max} is considered the nominal value in the design of the battery chargers. At the end of the charging the power absorbed by the battery is minimum and equal to P_{min}.

The charging of a battery requires long time. For this reason, from the WPTSs point of view, where the involved quantities have very fast dynamics, the battery can be considered a resistance. This resistance is given by the ratio of the battery voltage and current shown in Fig. 2.17, at any given time:

$$R_B = \frac{V_B}{I_B} \tag{2.41}$$

Since the time scale of the Fig. 2.17 is very long, the battery voltage V_B and the battery current I_B are denoted with capital letters to highlight that they remain constant for several periods of the ac quantities involved in the compensating networks of a WPTS. The situation is illustrated in Fig. 2.18 on the next page.

2.3.2 Dc/dc Converter

To regulate the battery charging process in a WPTS, usually a dc/dc converter is inserted between the diode rectifier and the battery (see Fig. 2.1). The widest used dc/dc converters are buck and boost converters and their selection, among other things, depends on the type of the receiving-side compensating network [6]. Some other dc/dc converter topologies utilizable in WPTSs are found in [74] and in [75], where in this last paper the authors proposed a tristate boost converter. Regardless of the type, the function of the dc/dc converter is to adapt the average value V_o of the rectifier output voltage or the average value I_o of the rectifier output current to the battery demands. Indeed, the voltage and the current required by the battery during the charging process, as shown in Fig. 2.17, are fixed instant by instant. On the contrary, the voltage and the current at the output of the rectifier may change for instance due to a variation of the coupling coefficient

[6] In Fig. 2.17, current, voltage and power are plotted with different scales.

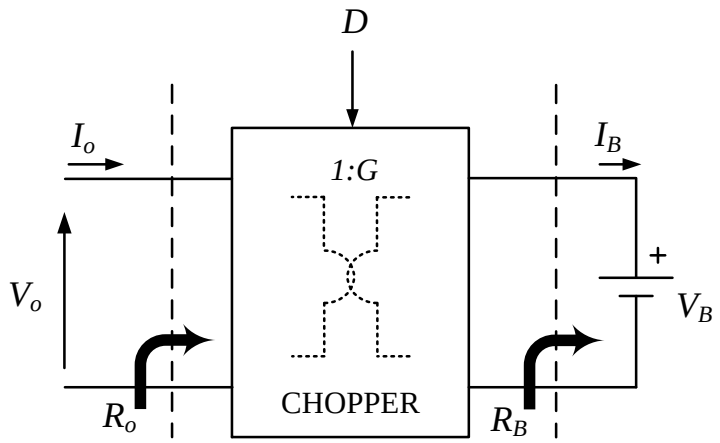

Fig. 2.18: Equivalent resistances of the battery and of the dc/dc converter of a WPTS.

between the transmitting and the receiving coils and in any case unlikely matches with the battery quantities. The control system of the chopper has to modify the control quantity accordingly, to cope with the input variations and with the different values of the battery voltage and current during the different stages of the charging process. The switching operation of the dc/dc converter can be slow [18], but for EV charging, fast controllers are preferable [76]. However, in both the cases, the switching period of the chopper is significantly smaller than the time scale of the charging process. The regulation performed by the dc/dc converter on the average value of the voltage v_o to obtain V_B (see Fig. 2.18), can be expressed with the following relation:

$$V_B = G\,V_o \tag{2.42}$$

In (2.42), the quantity G represents the voltage gain. If the dc/dc converter operates in the Continuous Conduction Mode (CCM), as it usually happens in WPTSs, the voltage gain is a constant that does not depends on the load but only on the control variable of the converter, which is typically the duty cycle D of the switch. The voltage gain and the the duty cycle are indicated with the capital letter to point out that they are slow variables with respect to the WPTS operational period. The voltage gains for the basic dc/dc converter topologies are listed in Tab. 2.1.

If the dc/dc converter is ideal, with an efficiency of 100%, the battery charging power P_B, which is shown in Fig. 2.17 and which is obtained with the product of the battery current I_B and the battery voltage V_B, should be equal to the chopper input power. Neglecting the small power arisen from the harmonics, the power at the input of the dc/dc converter is given by the product between the average values V_o and I_o. By imposing the equality of the input and output powers, a relation for the average value of the input and output current in found in the form:

$$V_B I_B = V_o I_o \quad \Rightarrow \quad I_B = \frac{1}{G} I_o \tag{2.43}$$

Tab. 2.1: Comparison of the basic dc/dc converter topologies [74].

Topology	Voltage Gain (G)	Equivalent resistance (R_o)	R_o (range)
Buck	D	$\frac{R_B}{D^2}$	$(R_B \div \infty)$
Boost	$\frac{1}{1-D}$	$(1-D)^2 R_B$	$(0 \div R_B)$
Buck-Boost	$\frac{-D}{1-D}$	$\frac{(1-D)^2}{D^2} R_B$	$(0 \div \infty)$
Ćuk	$\frac{-D}{1-D}$	$\frac{(1-D)^2}{D^2} R_B$	$(0 \div \infty)$
SEPIC	$\frac{D}{1-D}$	$\frac{(1-D)^2}{D^2} R_B$	$(0 \div \infty)$

In (2.43), the equation (2.42) has been used. From the relations (2.43) and (2.42), it is easy to recognize that the dc/dc converter in CCM behaves like an ideal transformer with a variable transfer ratio given by $1 : G$. This fact is depicted in Fig. 2.18.

Dividing (2.42) by I_B and using (2.43) for the Right Hand Side (RHS), we have:

$$\frac{V_B}{I_B} = G^2 \frac{V_o}{I_o} \quad \Rightarrow \quad R_o = \frac{1}{G^2} R_B \tag{2.44}$$

Equation (2.44) states that, from the rectifier output terminals, the cascade of the chopper and the battery can be envisaged as an equivalent resistance R_o which is proportional to R_B given by (2.41). The constant of proportionality is equal to $\frac{1}{G^2}$ which depends on the duty cycle D of the dc/dc converter in a different way for the different topologies. The equivalent input resistance for the basic dc/dc converter topologies can be found in Tab. 2.1, where it is also specified the range of values that it can assume.

The voltage gain G, which in the above discussion has been considered constant, actually varies during the battery charging process. In fact, let us suppose that the chopper input voltage is regulated somehow to have a constant average value. Consequently, the voltage gain G has to adjust its value to provide the battery voltage charging profile at the output of the dc/dc converter. For this reason, in the battery charging time scale, the profile of the chopper equivalent resistance differs from the profile of the battery equivalent resistance not simply by a constant. This fact can be evident considering that the equivalent resistances can be obtained with:

$$\begin{aligned} R_B &= \frac{V_B^2}{P_B} \\ R_o &= \frac{V_o^2}{P_o} \end{aligned} \tag{2.45}$$

Since, for the hypothesis of having an ideal dc/dc converter, $P_o = P_B$, it means that the two equivalent resistances deviate for the different profile of the voltage V_o and V_B. The battery and the chopper equivalent resistances during the charging period are plotted in Fig. 2.19.

In Fig. 2.19, the various resistances are calculated with (2.45). The graph reports the profile of the battery equivalent resistance (blue solid line), the equivalent

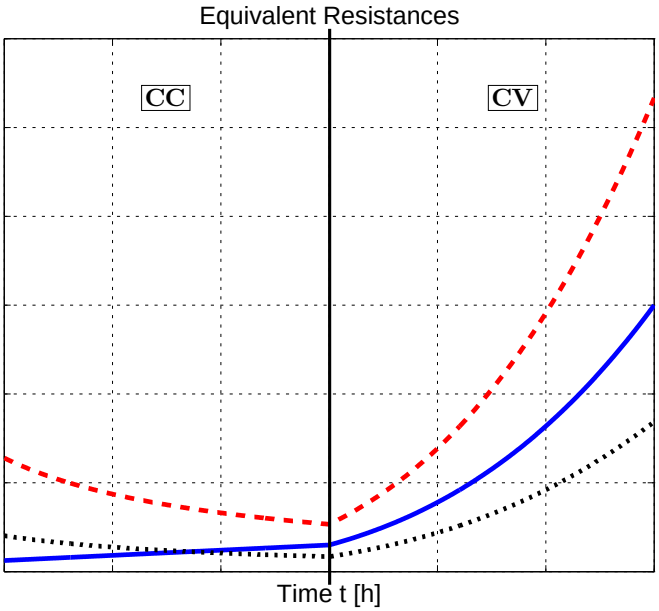

Fig. 2.19: Equivalent resistances: battery (blue solid line), chopper step-down (red dashed line) and chopper step-up (black dotted line).

resistance at the input of a step-down chopper (red dashed line) and the equivalent resistance at the input of a step-up chopper (black dotted line). It can be noticed that, while in the CV stage all the resistances continuous to grow, in the CC stage the chopper equivalent resistances and the battery equivalent resistance behave differently. Since the battery voltage increases linearly and the battery current remains constant, the battery equivalent resistance increases as well as the voltage. Instead, the chopper equivalent resistances, regardless the type of the dc/dc converter, in the CC stage decrease their value.

2.4 Receiving-side Rectifier

To transfer the power between the transmitter and the receiver with a magnetic coupling it is necessary to have a time-varying magnetic field. This magnetic field, which is produced by an high frequency current that flows in the transmitting coil, induces an alternated voltage across the terminals of the receiving coil. The dc component in the transmitting coil current is "blocked" by the coil coupling and it is also undesirable because it can saturate the ferrite core used to enhance the coil coupling coefficient. Based on these considerations, it is clear that the quantities involved in the coil coupling and in the compensating networks are alternated and most of the time almost sinusoidal.

As explained in the previous section, the battery of an EV needs both dc current and dc voltage to be charged. For this reason in WPTSs, a rectifier has to be employed to convert the ac quantities of the receiving-side compensating network into quantities that have a significant dc component.

The receiving-side ac/dc converter employed in WPTSs is usually a single-

phase H-bridge rectifier. The rectifier can be full active [60], [77]–[81], i.e made up of 4 switches. In any case, when the bidirectional power flow is not necessary, this solution adds complexity and cost. Some authors introduced a semi-active rectifier to regulate the unidirectional power flow from the receiving coil toward the battery [59], [64], [82], [83]. However, the widest used receiving-side ac/dc converter in WPTSs is the passive bridge rectifier [84]–[87].

A diode-passive bridge can operate mainly in two ways: in Continuous Conduction Mode (CCM) or in Discontinuous Conduction Mode (DCM). In the first mode of operation, the resonant current of the compensating network at the input of the rectifier flows continuously through its diodes. When the load connected to the rectifier output terminals is light, i.e. it absorbs small power, it may happen that the rectifier input current ceases to flow and the diodes of the passive bridge become reverse biased, blocking the power flow for some time within the resonant period. This situation is known as DCM. Typically, WPTSs are designed in order to operate the receiving-side rectifier in CCM.

The behaviors of the diode rectifier in CCM strongly depend on the type of the compensating network which can force either a sinusoidal current or a sinusoidal voltage at the rectifier input. The rectifier output filter is another element that defines the characteristics of the currents and the voltages of the ac/dc converter. If the filter is capacitive it force the output voltage to be constant, the small ripple being disregarded. On the contrary, an inductive network at the rectifier output filters all the harmonics of the output current, sustaining a constant dc component. According to the type of compensating network and to the type of output filter, we can have the following suitable combination [88]:

- current-fed diode rectifier with capacitive filter;
- voltage-fed diode rectifier with inductive filter.

These topologies are illustrated in Fig. 2.20(a) and Fig. 2.20(c), whereas figures 2.20(b) and 2.20(d) report their typical waveforms. From Fig. 2.20(b) it can be seen that a current-fed diode rectifier with capacitive filter (cf. Fig 2.20(a)) has a sinusoidal input current i_L which is usually forced by the upstream resonant compensating network. This current is rectified and then filtered in order to extract the dc component I_o from the rectifier output current i_o. The value of I_o is given by the average value of the current i_o over a resonant period[7]:

$$I_o = \frac{1}{\pi}\int_0^{\pi} I_L \sin(\theta)\, d\theta = \frac{2}{\pi} I_L \tag{2.46}$$

In the derivation of (2.46) the rectifier input current i_L has been supposed purely sinusoidal with an amplitude equal to I_L. With this assumption, the average value of the rectifier output current is found to be proportional to its peak value which coincides with I_L.

In Fig. 2.20(b), the voltage waveforms are also shown. The large capacitor that forms the output filter maintains the output voltage constant and equal to $R_o\, I_o$.

[7] Figures 2.20(b) and 2.20(d) express the waveforms in terms of an angular coordinate $\theta = \omega t$ that simplifies the calculations of the average value and of the Fourier series coefficients.

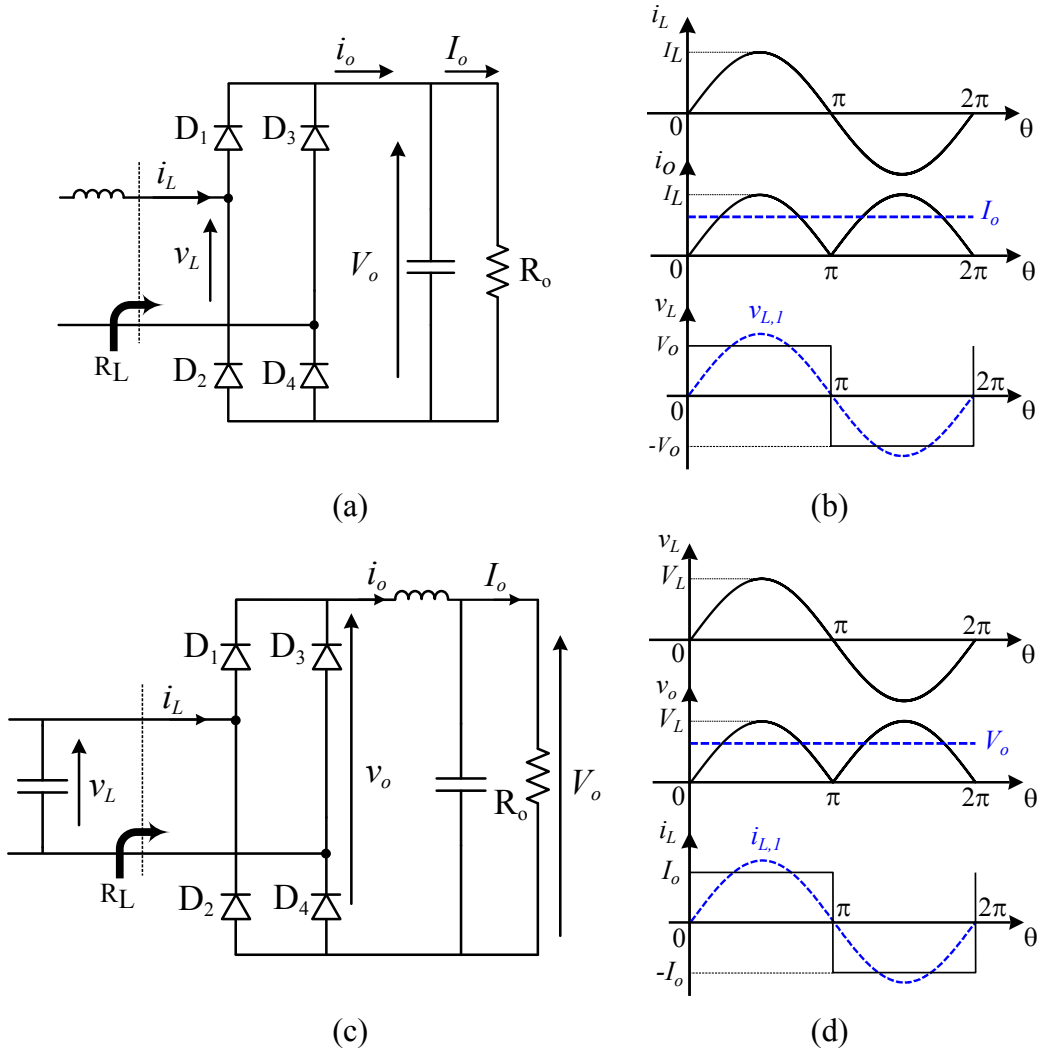

Fig. 2.20: Waveforms (b) and (d) of different topologies (a) and (c) for the diode rectifier. Figures (a) and (b) refer to a current-fed diode rectifier with capacitive filter, whereas figures (c) and (d) are for voltage-fed diode rectifier with inductive filter.

The rectifier input voltage depends on the sign of i_L. In fact, when the current i_L is positive, the diodes D_1 and D_4 conduct and the rectifier input voltage is equal to V_o, the voltage drops being disregarded. When i_L is negative, diodes D_2 and D_3 conduct and the the rectifier input voltage becomes equal to $-V_o$. Thus, the resulting rectifier input voltage is a square wave.

From the resonant compensating network side, it is possible to neglect all the harmonics in v_L and consider only its fundamental $v_{L,1}$. This approximation is called Fundamental Harmonic Approximation (FHA) and it is quite commonly applied in the analysis of the resonant converters like WPTSs [89]. It permits the analysis of the system to be simplified, making it linear, and it provides good results, especially when the rectifier operates in CCM. After applying FHA, all the quantities involved in the ac side of the system become sinusoidal and the circuit can be studied in phasor domain.

The fundamental of the voltage v_L, indicated in Fig. 2.20(b) with $v_{L,1}$, is in phase with the current i_L and it is given by:

$$v_{L,1} = V_L \sin(\theta) = \frac{4}{\pi} V_o \sin(\theta) \tag{2.47}$$

The amplitude V_L of the fundamental in (2.47) is the 1-st Fourier coefficient of the square wave v_L. Since i_L and $v_{L,1}$ are in phase, it means that the rectifier and the downstream load appear as an equivalent resistance for the compensating network. This equivalent resistance is illustrated in Fig. 2.20(a) with the symbol R_L and its value can be calculated dividing the amplitude of $v_{L,1}$ by the amplitude of the current i_L:

$$R_L = \frac{V_L}{I_L} = \frac{8}{\pi^2} \frac{V_o}{I_o} = \frac{8}{\pi^2} R_o \tag{2.48}$$

To obtain (2.48), (2.47) and (2.46) have been used. The equivalent resistance seen by the rectifier input terminals is proportional to the equivalent resistance seen by the chopper input terminals, which is given by (2.44), with a constant of proportionality equal to $\frac{8}{\pi^2}$.

Figure 2.20(c) illustrates the circuit of a voltage-fed diode rectifier with inductive filter. This topology, as can be noticed also from Fig. 2.20(d), is the dual of the current-fed diode rectifier with capacitive filter. In this topology, the resonant network forces the rectifier input voltage v_L to be sinusoidal, whereas the large output inductor maintains the output current i_o almost constant and equal to the load current I_o. When the voltage v_L is positive, the diodes D_1 and D_4 are forward biased and, in an ideal situation, the output voltage v_o coincides with v_L. When $v_L < 0$, the constant output current flows through the diodes D_2 and D_3 and the output voltage v_o is equal to the input voltage rectified. The ripple in the output voltage is filtered by the output inductor and the average value of v_o is applied to the load. The rectifier input current i_L is a square wave in phase with the rectifier input voltage. Applying once again the FHA, a voltage-fed rectifier with an inductive output filter, from the ac side, can be conceived as a resistance R_L. With a process similar to the one used to find the equivalent ac resistance for a current-fed rectifier with a capacitive output filter, the equivalent resistance for a voltage-fed rectifier with an inductive output filter is found to be:

$$R_L = \frac{V_L}{I_L} = \frac{\pi^2}{8} \frac{V_o}{I_o} = \frac{\pi^2}{8} R_o \tag{2.49}$$

The various equations for the two topologies of receiving rectifier above mentioned are summarized in Tab. 2.2.

In Fig. 2.20(c) it is illustrated the output LC filter which is inserted upstream the equivalent load R_o representing the cascade of the chopper and the battery. Very often, the voltage-fed rectifier with inductive output filter is used in conjunction with a boost dc/dc converter. In this situation, the input inductor of the boost converter can be exploited as output filter for the rectifier to implement the receiving stage in an integrated way [90], [91].

Tab. 2.2: Characteristic equations for the two topologies of diode rectifier shown in Fig. 2.20.

Current-fed Rectifier with Capacitive Output Filter	Voltage-fed Rectifier with Inductive Output Filter
$i_L(\theta) = I_L \sin(\theta)$	$v_L(\theta) = V_L \sin(\theta)$
$v_{L,1}(\theta) = \frac{4}{\pi} V_o \sin(\theta)$	$i_{L,1}(\theta) = \frac{4}{\pi} I_o \sin(\theta)$
$I_o = \frac{2}{\pi} I_L$	$V_o = \frac{2}{\pi} V_L$
$R_L = \frac{8}{\pi^2} R_o$	$R_L = \frac{\pi^2}{8} R_o$

2.5 Transmitting-side Inverter

Although the early WPTSs employed push-pull inverters to feed the transmitting coil [18], nowadays the widest used topology for the HFI of the transmitting side is the single-phase full bridge inverter [19], [59], [76].

The inverter of a WPTS is used to force a sinusoidal current into the transmitting coil and, through its control, it is responsible to regulate the power transferred from the transmitter to the receiver. Traditionally, to impose a sinusoidal adjustable current into a circuit, inverters are controlled with the well-known PWM technique [92]. With PWM modulation the inverter switching frequency must be several times higher than the operating frequency of the current that has to be imposed. This method results unfeasible for WPTSs, where the operating frequency should be high to permit the transfer of power. Controlling the inverter of a WPTS with PWM technique would result in excessive switching losses. For this reason, in WPTSs the inverter switching frequency is set to be equal to the operating frequency of the signals in the compensating network. With a full-bridge voltage-fed inverter, the output voltage can assume only three values; the output voltage can be equal to plus or minus the voltage of the input dc bus V_{dc}, or it can be clamped to zero. Usually, the inverter is controlled to have a periodic signal as output voltage but, as can be deduced by the previous statement, it cannot be sinusoidal. Its frequency spectrum contains harmonics with frequencies multiples of the operational one. Nevertheless, the band-pass filtering behavior of the transmitting-side compensating network guarantees that the current flowing in the transmitting coil is almost sinusoidal. The amplitude of the injected transmitting coil current can be controlled operating the inverter either at variable frequency or at fixed frequency [93]. In the first case, the inverter output voltage is a square wave whose frequency is adjusted in order to control the the transmitting coil current amplitude. Both the amplitude and the phase of the transmitting coil current depend on the supply frequency, which can be modified in order to control the power flow between transmitter side and receiving side. When a variable frequency control is implemented, designers have to take care about the *bifurcation phenomenon* [94]. Furthermore, variable frequency control cannot be used when multiple receivers

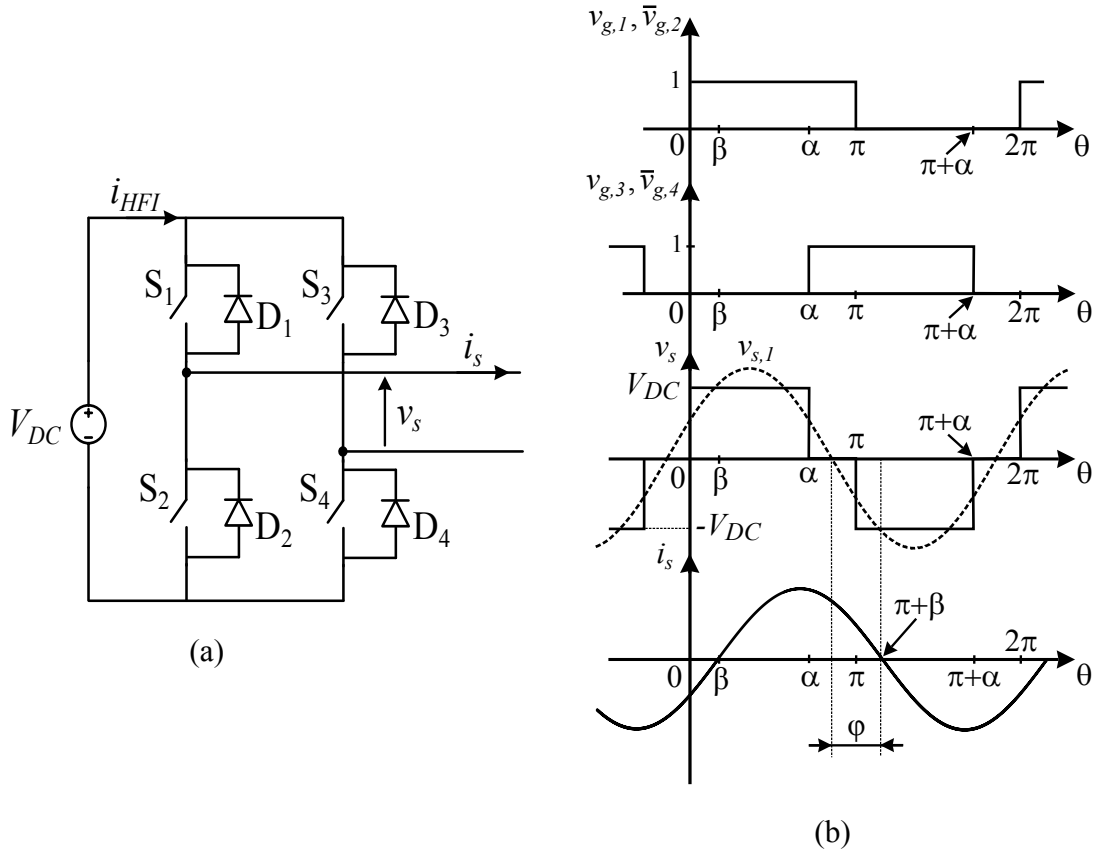

Fig. 2.21: Scheme of a voltage-fed single-phase full bridge inverter (a) and its typical waveforms when it is controlled with the phase-shift technique (b).

are present above a single transmitter. Controlling the power transfer between the transmitter and a single receiver makes the supply frequency of the transmitter change, thus mistuning all the other receivers. In this situation, fixed frequency control is preferred. When the switching frequency is fixed, the amplitude of the transmitting current can be controlled by changing the amplitude of the fundamental of the inverter output voltage. This can be done by varying the voltage of the dc bus [67] or, more commonly, operating the inverter legs with the *phase-shift* technique. The scheme of a voltage-fed single-phase full bridge inverter and its typical waveforms when it is controlled with the phase-shift technique are depicted in Fig. 2.21.

In Fig. 2.21(a), the inverter switches S_i are considered ideal and unidirectional. For this reason, the freewheeling diodes D_i are put in parallel to them to allow the circulation of negative currents. Figure 2.21(b) shows the typical waveforms arising from the phase-shift control. From top to bottom, the figure reports the following plots: command signal $v_{g,1}$ of the switch S_1, command signal $v_{g,3}$ of the switch S_3[8], inverter output voltage v_s and its fundamental $v_{s,1}$ and inverter output current i_s. The phase-shift technique derives its name form the fact that the gate signals of the second leg switches are shifted of an angle α with respect to the gate signals

[8]The gate signal for the lower switches S_2 and S_4 are the logical complements of the signal $v_{g,1}$ and $v_{g,3}$, respectively.

for the first leg switches. The resulting inverter output voltage is a quasi-square wave (cf. third plot of Fig. 2.21(b)), whose fundamental can be modified changing the phase-shift angle α. The 1-st complex Fourier coefficient of the voltage v_s is given by:

$$c_1 = \frac{2}{\pi} V_{DC} \sin\left(\frac{\alpha}{2}\right) e^{-j\frac{\alpha}{2}} \tag{2.50}$$

The fundamental of the voltage v_s is related to the complex Fourier coefficient c_1, according to:

$$v_{s,1} = 2|c_1| \cos(\theta + \varphi_{c_1}) = 2|c_1| \sin\left(\theta + \varphi_{c_1} + \frac{\pi}{2}\right) \tag{2.51}$$

where $|c_1|$ and φ_{c_1} are the modulus and the phase of c_1. Substituting (2.50) into (2.51), the fundamental of the inverter output voltage is found to be:

$$v_{s,1} = \frac{4}{\pi} V_{DC} \sin\left(\frac{\alpha}{2}\right) \sin\left(\theta + \frac{\pi - \alpha}{2}\right) \tag{2.52}$$

From (2.52) it can be noticed that the amplitude of the fundamental of the inverter output voltage can be adjusted by varying the phase-shift angle α. The variable α affects also the phase of the fundamental which is found to be $\frac{(\pi-\alpha)}{2}$, when the command signal of the switch S_1 is taken as reference.

The amplitude of $v_{s,1}$ has a direct implication on the amplitude of the inverter output current, which as illustrated in Fig. 2.21(b), can be considered sinusoidal. The phase of the current, indicated with β in Fig. 2.21(b), depends both on the phase of $v_{s,1}$ and on the load connected to the inverter output terminals. The phase displacement between $v_{s,1}$ and i_s is given by:

$$\varphi = \frac{\pi - \alpha}{2} + \beta \tag{2.53}$$

which is greater than $\frac{\pi-\alpha}{2}$ when the inverter sees an inductive load, less than $\frac{\pi-\alpha}{2}$ when the load connected to the inverter is capacitive. The type of load, i.e. inductive or capacitive, affects the soft-switching capabilities of the inverter.

2.5.1 Soft-Switching

The inverter switching losses are caused by the simultaneous presence of currents and voltages in the switches during the turn on or the turn off and they are proportional to the switching frequency. Since the inverter of a WPTS works with an high switching frequency, it is very important to guarantee either the Zero Current Switching (ZCS) at turn off or the Zero Voltage Switching (ZVS) at turn on for the switches S_i [95]. Turning the switches on and off with no current flow through (ZCS) or zero voltage (ZVS) across them allows for an high efficiency of the HFI to be achieved. With single-phase full bridge inverters it is possible to achieve both ZCS and ZVS but not at the same time. For IGBTs is better to have a ZCS turn off, whereas for MOSFETs a ZVS turn on is preferred [38].

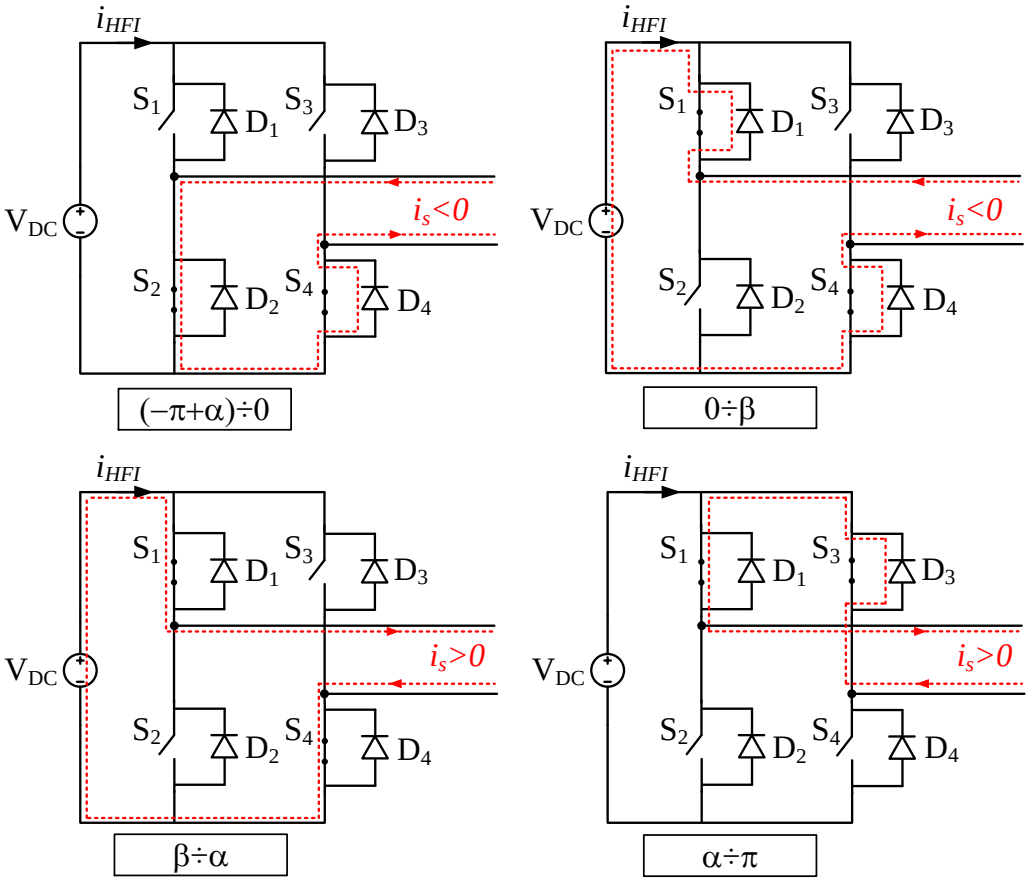

Fig. 2.22: Components under conduction for the full-bridge inverter with the waveforms of Fig. 2.21(b).

To investigate the soft-switching capabilities of a full-bridge inverter with an inductive load, figure 2.21(b) has to be further analyzed bearing in mind the conducting components throughout the various intervals. Figure 2.22 helps in solving this task.

An inspection of Fig. 2.21(b) and 2.22 is necessary to see that just before $\theta = 0$, switch S_2 and S_4 are in the on state. Since the current i_s is negative, it flows through S_2 and through freewheeling diode D_4. At $\theta = 0$, S_2 is turned off and, at the same time, S_1 is tuned on[9]. The switch S_2 is turned off in a hard way, whereas, since the current i_s is still negative thus circulating in the diode D_1, the switch S_1 is turned on with ZVS. At $\theta = \beta$ the current becomes positive flowing in the switches S_1 and S_4. This state persists until $\theta = \alpha$ when the switch S_4 is turned off and S_3 is turned on. The switch S_4 turns off with a current flowing into it, while the switch S_3 turns on with ZVS since the voltage is clamped to zero by the forward biasing of diode D_3. In the interval $[\pi \div 2\pi]$, the situation is the same as in the interval $[0 \div \pi]$ except that the lower diodes and switches assume the

[9]This analysis is done neglecting the *dead time*, when both the switches of a single leg are simultaneously in the off state.

Tab. 2.3: Components under conduction for the full-bridge inverter with the waveforms of Fig. 2.21(b).

	$[0,\beta]$	$[\beta,\alpha]$	$[\alpha,\pi]$	$[\pi,(\pi+\beta)]$	$[(\pi+\beta),(\pi+\alpha)]$	$[(\pi+\alpha),2\pi]$
First Leg	D_1	S_1	S_1	D_2	S_2	S_2
Second Leg	D_4	S_4	D_3	D_3	S_3	D_4

roles of the upper components, and vice versa. The components under conduction throughout various intervals are summarized in Tab. 2.3.

From the previous analysis arises that the switches of the inverter with the waveforms of Fig. 2.21(b) are softly commutated during the turn on, but they have to turn off with currents. This situation, which is advantageous when the inverter switches are MOSFETs, is characterized by the fact that the inverter output current is lagging the fundamental of the inverter output voltage. In other words the load seen at the inverter output terminals is inductive. Having an inductive load is not enough to achieve ZVS. In fact, the load should be as much inductive as necessary to have a negative current at $\theta = 0$ (when the switch S_1 is turned on). This means to have $\beta > 0$ in Fig. 2.21(b) and according to (2.53) it is necessary that:

$$\varphi > \frac{\pi - \alpha}{2} \tag{2.54}$$

From (2.54) it can be noticed that in case of small phase-shift angle α, to guarantee the ZVS, the phase displacement between $v_{s,1}$ and i_s should be close to $\frac{\pi}{2}$[10]. This entails the circulation of an high reactive current that the inverter switches have to treat but that does not contribute to the active power transfer. From this point of view, it is better to operate the inverter with square-wave, i.e. $\alpha = \pi$, and control the amplitude of $v_{s,1}$ by changing the dc bus voltage V_{DC} (cf. (2.52)). In this way, according to (2.54), the ZVS can be achieve with $\varphi > 0$. Ideally, if the load connected to the inverter is pure resistive, i.e. $\varphi = 0$, the inverter switches can be commutated with both the ZVS and the ZCS. Practically, since MOSFETs have parasitic output capacitances C_{oss} there should be a minimum negative current at $\theta = 0$, to charge $C_{oss,2}$, related to S_2, and to discharge $C_{oss,1}$, related to S_1, during the dead time of the first leg [96]. Same considerations can be done for the second leg at the different switching instants. In conclusion, the inverter output load should be a little bit inductive to permit the ZVS.

Let us return to the case when the fundamental of the inverter output voltage is controlled through phase-shift technique. When condition (2.54) is not satisfy, the ZVS of the switches of the first leg is lost. The situation is depicted in Fig. 2.23 for various types of load.

All the graphs of Fig. 2.23 present the zero-crossing of the current i_s before $\theta = 0$, thus having $\beta < 0$. In this case, being the current i_s positive just before $\theta = 0$, it is circulating in the diode D_2 and in the switch S_4. At $\theta = 0$, switch S_2

[10] The phase displacement φ cannot be greater that $\frac{\pi}{2}$, otherwise the load should deliver power to the inverter dc side.

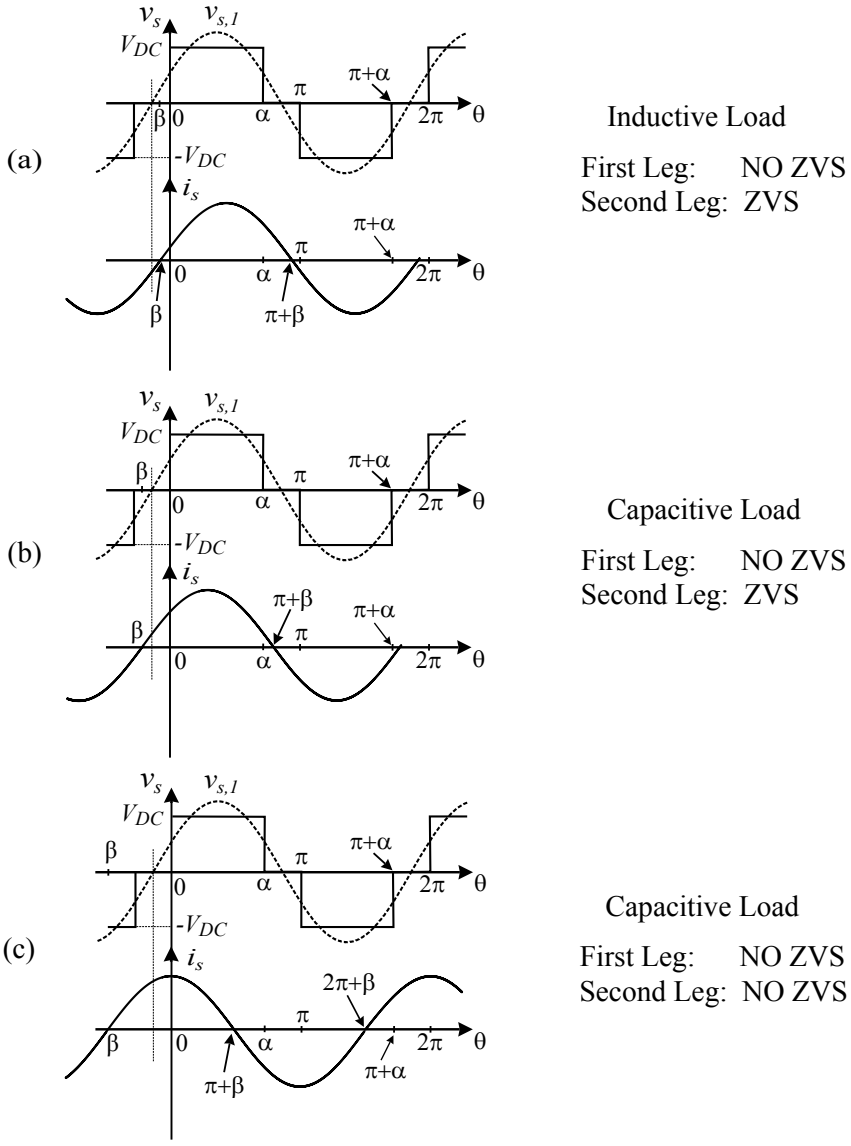

Fig. 2.23: Analysis of the soft-switching capabilities of a phase-shift controlled inverter for various types of load.

is turned off and S_1 is turned on. Since the current i_s was flowing through D_2, S_2 turns off with ZCS. When the gate signal is provided to the switch S_1, the current in the diode D_2 starts to decrease and correspondingly the current in the switch S_1 starts to increase. Diode D_2 remains in conduction until its current reaches 0 and during this period it maintains the voltage across the switch S_1 clamped to V_{DC}. Consequently, S_1 turns on with both voltage and current that correspond to power losses in the switch. As stated before, the same considerations can be done at $\theta = \pi$ when S_1 turns off with ZCS and S_2 is hardly turned on.

As illustrated in Fig. 2.23, the soft-switching capabilities for the switches of the second leg depend on the type of load connected to the inverter output terminals. As rule of thumb, to have ZVS of the switches S_3 and S_4 the current i_s should be positive at $\theta = \alpha$ (and for symmetry reason $i_s < 0$ at $\theta = \pi + \alpha$). Differently, the switches would turn off with ZCS, but with an hard turn on.

The value of the current i_s at $\theta = \alpha$ depends on the load. In case of inductive load (cf. 2.23(a)), the current i_s at $\theta = \alpha$ is always positive. For this reason, the ZVS of the switches S_3 and S_4 is guaranteed. If the load is capacitive, the ZVS of the second leg switches can or cannot be achieved, depending on the extent of the phase displacement between the current i_s and the fundamental of the inverter output voltage $v_{s,1}$. The condition that allows the ZVS for the second leg switches in case of capacitive load is

$$\beta > -(\pi - \alpha) \tag{2.55}$$

which substituted in (2.53) yields to:

$$\varphi > -\frac{\pi - \alpha}{2} \tag{2.56}$$

When (2.56) is satisfied the current i_s at $\theta = \alpha$ is greater than zero, as shown in Fig. 2.23(b). This entails that the switches S_3 and S_4 turn on with ZVS. If the phase displacement φ is less then the value expressed by (2.56), the ZVS of the second leg switches is lost (see Fig. 2.23(c)).

To avoid the introduction of a large reactive power in the WPTSs, usually the inverter output current i_s is maintained in phase (or slightly lagging) with the fundamental of the inverter output voltage. Therefore, the second leg switches always turn on softly, whereas the ZVS for the first leg switches is not guaranteed for the whole operating conditions.

2.6 Equivalent WPT Circuit

The general scheme of a WPTS, introduced in Fig. 2.1, is very complicated and involves a lot of conversion stages. The discussions done in the previous sections permit a reduction of the complexity and they lead to the simplified equivalent WPT circuit of Fig. 2.24. Figures 2.24(a) and 2.24(b) refer to a receiving rectifier with a capacitive output filter, whereas Fig. 2.24(c) and Fig. 2.24(d) refer to a receiving rectifier with inductive output filter.The circuit in Fig. 2.24(b) and Fig. 2.24(d) models the behavior of the part of the system downstream the receiving rectifier.

The simplifications of the circuits of Fig. 2.24 with respect to the scheme presented in Fig. 2.1 are based on the following assumptions:

1. The compensating networks behave as band pass filters that eliminate the harmonics introduced in the ac/ac power stage by the inverter and by the rectifier;

2. the battery charging process is slow;

3. the transmitting-side dc-bus voltage V_{DC} is considered constant.

Hypothesis 1. permits us to substitute the inverter with a voltage source whose value is given by the fundamental of the inverter output voltage. It permits also the receiving rectifier to be modeled, from the ac side perspective, with a sinusoidal

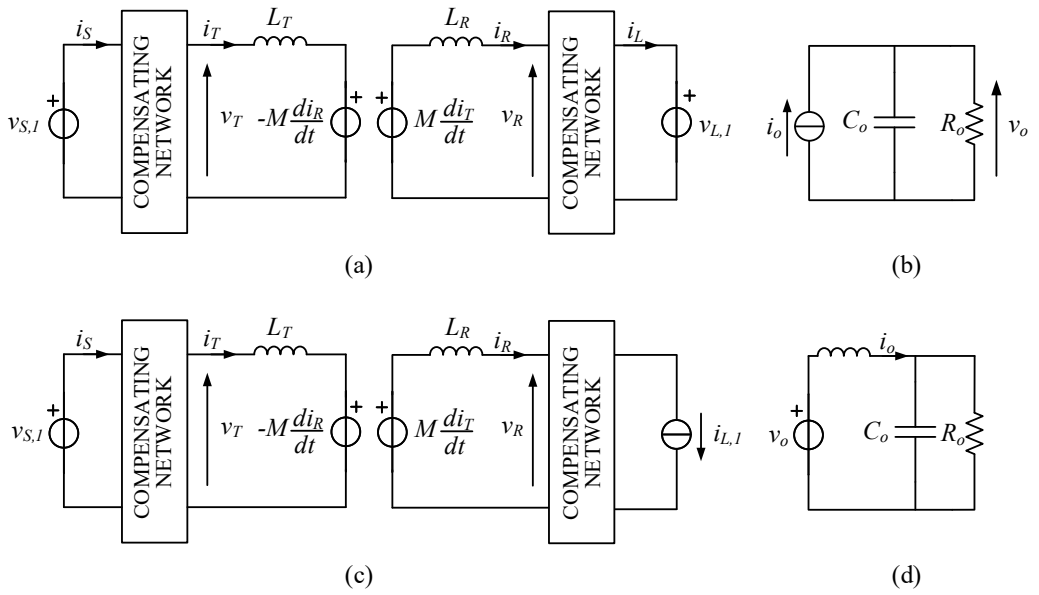

Fig. 2.24: Equivalent WPT model. Model for the ac/ac power transfer stage (a) and (c). Model for the dc quantities downstream the receiving rectifier (b) and (d). Figures (a) and (b) refer to a receiving rectifier with a capacitive output filter. Figures (c) and (d) refer to a receiving rectifier with an inductive output filter.

voltage source or with a sinusoidal current source, depending on the type of the output filter cascaded to the rectifier. The amplitudes of the sinusoidal sources are the values shown in Tab. 2.2. Hypothesis 2. allows us to model the chopper and the battery on board the EV through the equivalent resistance R_o. Hypothesis 3. permits us to disregard, in the analysis, the system upstream the transmitting-side inverter. In Fig. 2.24 the coil coupling is modeled as explained in Sec. 2.2.2.

Circuits in Fig. 2.24 are valid both in steady-state and also in the transient conditions. In dynamic conditions the quantities involved in the ac/ac power stage are high-frequency sinusoidal signals amplitude-modulated through low frequency signals. The filtered quantities downstream the rectifier are proportional to some modulating signals of the ac/ac power stage and usually they dominate the transient behavior with their overdamped responses. When the transients are extinguished, all the quantities of Fig. 2.24(a) and 2.24(c) become sinusoidals with a constant amplitude. Consequently, the system can be studied in phasor domain with the equivalent circuit shown in Fig. 2.25.

Despite the different types of filter connected to the receiving rectifier output terminals, in steady-state conditions, a single equivalent circuit can be used to study different types of WPTS. The rectifier under the steady-state conditions of the ac/ac power stage can be envisaged as a resistance R_L, whose value can be found, once again, in Tab. 2.2.

Different WPTSs differ for the various compensating networks they employ. In any case, the circuit in Fig. 2.25 can be used to find the relations between

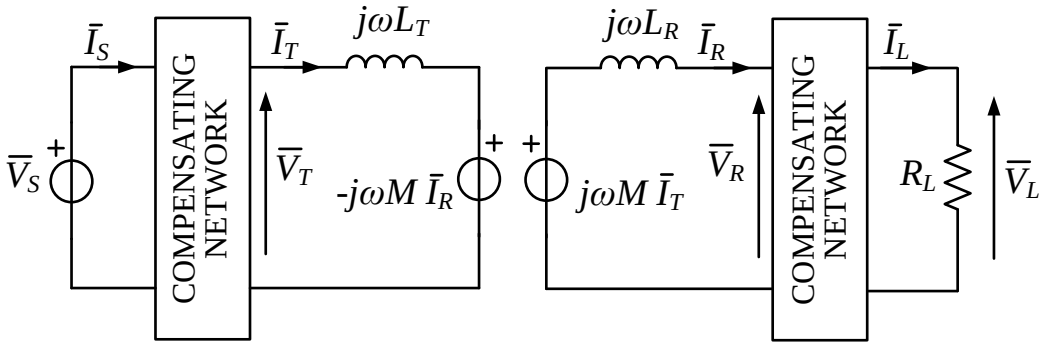

Fig. 2.25: Equivalent circuit for the study of WPTSs in steady-state conditions.

the amplitudes of the phasors involved in any WPTSs[11]. For this reason, it is extensively used during the design phase of the power transfer stage.

[11] It can happen that, with certain compensating networks, it is necessary to employ a current-fed inverter and thus the voltage source $\bar{V}_s$ has to be replaced with a sinusoidal current source.

Chapter 3

Compensating Networks

Compensating networks are crucial for improving performance of WPTSs. With proper compensation at some specific frequencies, a WPTS can achieve load-independent constant output voltage or current, near zero reactive power and soft switching of power inverter, resulting in simplified control circuitry, reduced component ratings and improved power conversion efficiency.

Compensating networks can be as simple as one capacitor connected in series or in parallel with both the transmitting and the receiving coil, but often these two-capacitors compensating networks do not allow WPTS to meet all the design requirements simultaneously. To increase the degrees of freedom, designers can use higher order compensating networks formed by capacitors and inductors connected in a suitable way. Despite the topology, resonant networks consist of resonant tanks tuned to resonate somehow at the inverter supply frequency.

This chapter begins with the review of series and parallel resonant tanks. Then, in a similar way, LCL circuit is introduced and analyzed.

Using the established background, the chapter concludes explaining the importance of the compensation for the WPTSs.

3.1 Series Resonant Tank

As illustrated in Fig. 3.1, series resonant tank circuit is formed by an inductor, a capacitor and a resistance connected in series. The circuit of Fig. 3.1 can be envisaged as the receiving stage of a WPTS, where the voltage source v_s represents the induced voltage, the inductor L is the receiving coil, the resistance R is the equivalent battery resistance and the capacitor C forms the compensating network. Since the capacitor C is connected in series with the coil inductor, this type of compensation is called series compensation.

As stated in Ch. 2, quantities in the ac-side of a WPTS can be considered sinusoidal with a good approximation. It is very important to characterize the frequency behavior of the series resonant tank in steady-state conditions when the RLC circuit is supplied with a sinusoidal voltage source. For this analysis, we can refer to the phasor domain circuit of Fig. 3.1(b). The input impedance of the circuit $\dot{Z}$ depends on the frequency of the voltage source and it is given by:

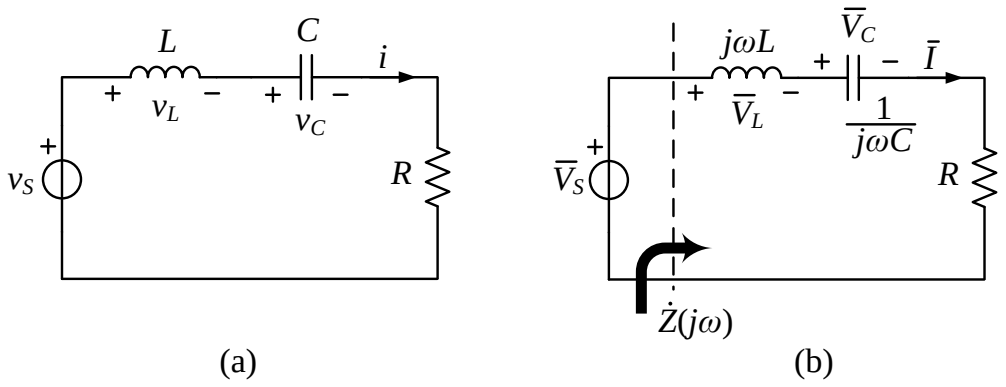

Fig. 3.1: Series resonant tank analyzed in: time domain (a), phasor domain (b).

$$\dot{Z} = R + j\left(\omega L - \frac{1}{\omega C}\right) = \frac{1 - \omega^2 LC + j\omega RC}{j\omega C} \tag{3.1}$$

Most important is the equivalent admittance of the series which can be derived from (3.1) and it is found to be:

$$\begin{aligned} \dot{Y} &= \frac{1}{\dot{Z}} = \frac{j\omega C}{1 - \omega^2 LC + j\omega RC} \\ &= \frac{1}{(1 - \omega^2 LC)^2 + \omega^2 R^2 C^2}\left[\omega^2 RC^2 + j\omega C(1 - \omega^2 LC)\right] \end{aligned} \tag{3.2}$$

Considering the voltage source $\bar{V}_s$ as reference, the current of the circuit is proportional to the admittance by $\bar{I} = \dot{Y}\bar{V}_s$ and it assumes the same frequency behavior as $\dot{Y}(\omega)$. The magnitudes and the phases of the impedance and the admittance versus the angular frequency of the supply voltage source are depicted in Fig. 3.2. As can be seen from the figure, the behavior of the series resonant tank changes a lot when the supply frequency changes. From the graph of the phases, we can see that at low frequencies the input impedance is capacitive ($\angle\dot{Z}$ tends to $-\frac{\pi}{2}$) whereas the inductive reactance becomes significant at higher frequencies. It is easy to notice that it exists one particular frequency ω_o where the impedance is purely resistive ($\angle\dot{Z} = 0$). At this frequency, called *resonant frequency*, the magnitude of the inductive reactance and of the capacitive reactance are equal and the input impedance reaches its minimum value given by R. At the same frequency the admittance and also the current that flows in the RLC series are maximum. The resonant frequency can be found as follows:

$$\omega L - \frac{1}{\omega C} = 0 \quad \rightarrow \quad \omega_o = \frac{1}{\sqrt{LC}} \tag{3.3}$$

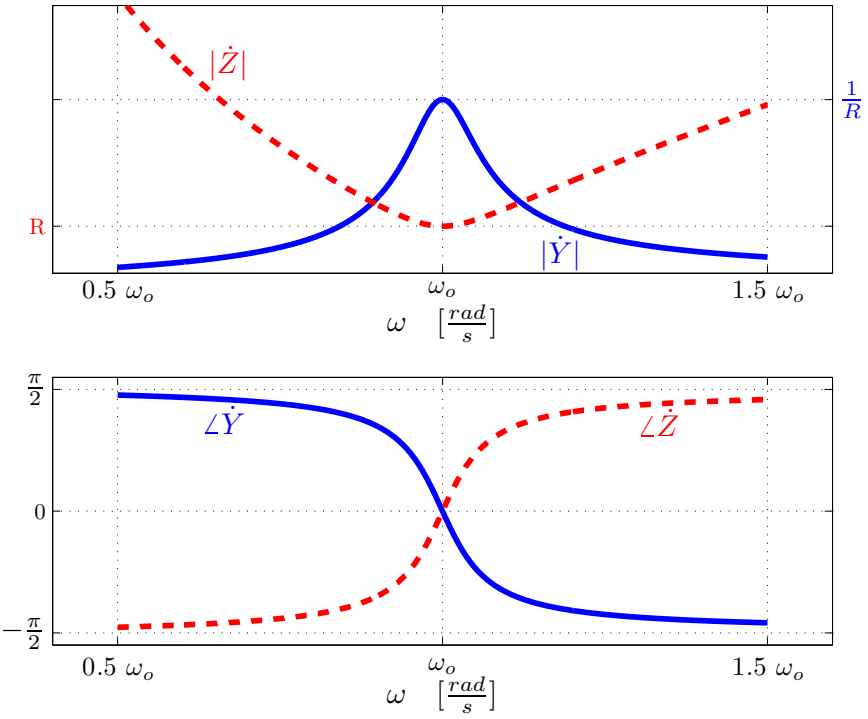

Fig. 3.2: Magnitude (upper plot) and phase (lower plot) of the impedance and the admittance of a series resonant tank.

3.1.1 Resonant Operation

In resonance, the series of the inductor L and the capacitor C can be envisaged as a short circuit. For this reason the voltage across the load resistance is exactly equal to the voltage source $\bar{V}_s$ and the state of the system is given by:

$$\begin{cases} \bar{I} = \frac{\bar{V}_s}{R} \\ \bar{V}_C = -j\frac{1}{\omega_o C}\bar{I} = -j\frac{1}{\omega_o C}\frac{\bar{V}_s}{R} \end{cases} \tag{3.4}$$

In time domain, Eq. (3.4) becomes:

$$\begin{cases} i = I\sin(\omega_o t) = \frac{V_s}{R}\sin(\omega_o t) \\ v_C = V_C \sin\left(\omega_o t - \frac{\pi}{2}\right) = -\frac{I}{\omega_o C}\cos(\omega_o t) \end{cases} \tag{3.5}$$

The short circuit formed by the LC series is only fictitious and inductor and capacitor continuously exchange energy between them. Since the instantaneous power absorbed by the inductor is equal to the instantaneous power delivered by the capacitor the total net power is null at the terminals of the series. The situation is shown in Fig. 3.3. Together with the instantaneous powers depicted in the central graph, the figure shows the waveforms of the current, of the voltage across the capacitor C and of the voltage across the inductor (cf. upper plot). Furthermore, in the lowest graph, the energies stored in the reactive components

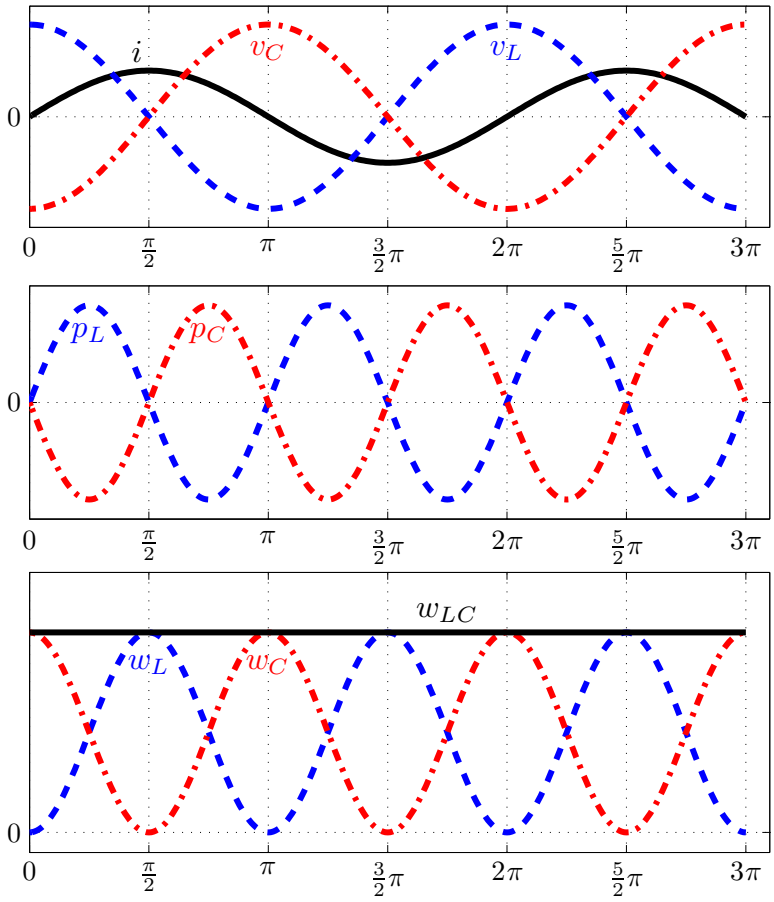

Fig. 3.3: Characteristic waveforms of a series resonant tank in resonance conditions.

are illustrated.[1] The total energy stored in the resonant tank is given by:

$$w_{LC} = \frac{1}{2} L\, i^2 + \frac{1}{2} C\, v_c^2 \tag{3.6}$$

Using (3.5), equation (3.6) becomes:

$$w_{LC} = \frac{1}{2} L\, I^2 \sin^2(\omega_o t) + \frac{1}{2} C\, \frac{I^2}{\omega_o^2 C^2} \cos^2(\omega_o t) = \frac{1}{2} L I^2 \tag{3.7}$$

where relation (3.3) has been used for rewrite $\omega_o^2 C$. It can be noticed from (3.7) that the energy stored in the resonant tank is constant and equal to the energy stored in an inductor L flown by a constant current I.

The energy delivered by the voltage source v_s to the load resistance R over a resonant period T_o can be calculated multiplying the active power absorbed by R times T_o and it results:

$$w_R = \frac{1}{2} R\, I^2\, T_o \tag{3.8}$$

[1] All the waveforms are plotted versus the angular coordinate $\theta = \omega_o t$.

In addition to the resonant frequency, an important parameter that defines the characteristic of the resonant tank is the *quality factor* Q which is proportional to the ratio between the energy stored in the resonant components and the energy delivered to the load R over a resonant period:

$$Q = 2\pi \frac{w_{LC}}{w_R} \tag{3.9}$$

Using (3.7) and (3.8), the quality factor Q for a series resonant tank is found to be:

$$Q = 2\pi \frac{\frac{1}{2} L I^2}{\frac{1}{2} R I^2 T_o} = \frac{\omega_o L}{R} \tag{3.10}$$

In (3.10), relation $\frac{2\pi}{T_o} = \omega_o$ has been used. Quality factor can be written in different ways, exploiting the formula for the resonant frequency:

$$Q = \frac{\omega_o L}{R} = \frac{1}{\omega_o C R} = \sqrt{\frac{L}{C}} \frac{1}{R} \tag{3.11}$$

The quality factor Q of the resonant tank does not have to be confused with the quality factor of the coil Q_L defined with (2.2). In fact, here, the quality factor is simply a parameter that characterizes the resonant circuit and it can be defined also in case of ideal inductors. On the contrary, the quality factor of the coil accounts for the inductor losses and for this reason it is necessary to consider the parasitic resistances for its calculation. Another difference between them is that the quality factor of the coil is frequency-dependent, whereas the quality factor of the resonant tank, as can be seen from (3.11), is independent from the frequency, once the parameters R, L and C have been assigned.

It can be noticed from Fig. 3.3 that, in resonant condition, the voltage across the resonant capacitor v_C and the voltage across the inductor v_L are equal and 180° shifted. According to the second of (3.4) and to the definition of the quality factor, their amplitude can be written as:

$$V_C = V_L = \frac{1}{\omega_o C} \frac{V_s}{R} = Q\, V_s \tag{3.12}$$

Since usually Q is greater than 1, it is easy to see that in the series resonant tank the voltages across the reactive components are amplified by a factor Q with respect to the source voltage. This fact has to be taken into account in the components selection.

3.1.2 Frequency Domain Analysis: Transfer Functions

Equations (3.1) and (3.2) have been derived from the phasor domain analysis and they have been plotted in Fig. 3.2 versus the angular frequency of the supply voltage source. A better way to analyze the frequency response of the series resonant tank is to consider the s-domain circuit and to plot the Bode diagrams of the relevant transfer functions. Equation (3.2) can be written in s-domain as:

$$Y(s) = \frac{sC}{1 + sRC + s^2LC} \tag{3.13}$$

Dividing (3.13) by its maximum value ($\frac{1}{R}$), the normalized admittance can be obtained. If the voltages of the circuit are normalized with V_s as base voltage, the normalized admittance can be envisaged as the transfer function which links the normalized voltage source to the normalized current of the circuit. It can be written as:

$$Y_N(s) = \frac{sCR}{1 + sRC + s^2LC} \tag{3.14}$$

Using the definitions (3.3) and (3.10), equation (3.14) becomes:

$$Y_N(s) = \frac{1}{\omega_o Q} \frac{s}{1 + \frac{s}{\omega_o}\frac{1}{Q} + \frac{s^2}{\omega_o^2}} \tag{3.15}$$

The transfer function consists of a zero in the origin and two poles. The placement of the poles depends on the quality factor and on the resonant frequency. They are given by the following equation:

$$s_{1,2} = \frac{\omega_o}{2Q}\left[-1 \pm \sqrt{1 - 4Q^2}\right] \tag{3.16}$$

The poles can be two real stable poles when $Q < \frac{1}{2}$ (when $R > 2\,\omega_o L$). When the quality factor is very small the two poles can be approximated as:

$$\begin{cases} s_1 \approx -\frac{\omega_o}{Q} = -\frac{R}{L} \\ s_2 \approx -\omega_o Q = -\frac{1}{RC} \end{cases} \tag{3.17}$$

The response of the normalized current of a series resonant tank with a low quality factor is well overdamped.

In case of $Q > \frac{1}{2}$, the two poles become complex conjugates. The standard way to express the denominator of a transfer function in Bode's form in case of complex conjugate poles pair is:

$$D(s) = 1 + 2\xi\,\frac{s}{\omega_o} + \frac{s^2}{\omega_o^2} \tag{3.18}$$

where the variable ξ is the *damping ratio*. When the damping ratio is less than 1, the zeros of $D(s)$ are complex conjugate and ξ gives an indication of the intensity of the oscillations of the system output response, when a step is applied as input of the system. A comparison between (3.18) and the denominator of (3.15) permits us to find:

$$Q = \frac{1}{2\xi} \tag{3.19}$$

The quality factor of the resonant tank is inversely proportional to the damping ratio of the system.

The complex conjugate poles can be derived from (3.16) and they are given by:

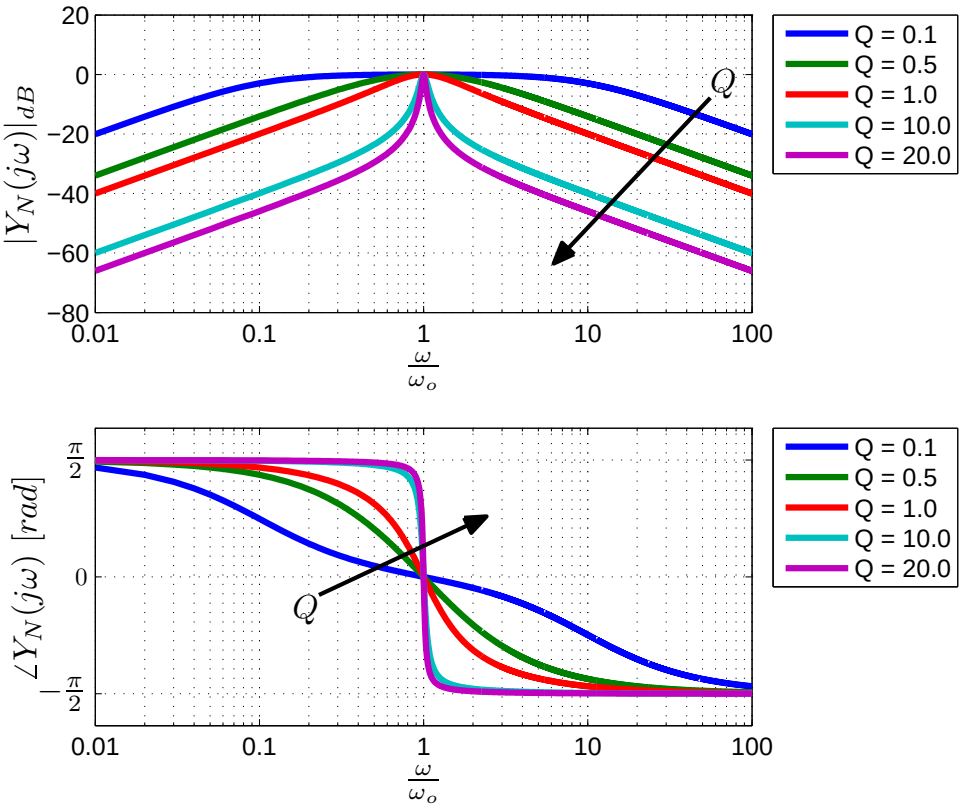

Fig. 3.4: Bode diagram of the normalized admittance for various values of Q.

$$\begin{aligned} s_{1,2} &= \frac{\omega_o}{2Q}\left[-1 \pm j\sqrt{4Q^2-1}\right] \\ &= \omega_o\left[-\xi \pm j\sqrt{1-\xi^2}\right] \end{aligned} \tag{3.20}$$

When the quality factor becomes very high (ξ tends to 0) the two complex conjugate poles become imaginary and the system becomes undamped.

The quality factor of the system affects also the Bode diagram of Y_N, and consequently all the transfer functions that can be assessed from the system. In Fig. 3.4, the Bode diagram of the normalized admittance can be observed. As explained before, when Q is very low the poles of the transfer function are real and separated. When Q increases the poles start to move closer and closer, reaching the value $s_{1,2} = -\omega_o$. A further increment of Q makes the poles complex conjugate with an amplitude of ω_o and a phase equal to: $\mp\arctan(\sqrt{4Q^2-1}) \pm \pi$.

All the curves of Fig. 3.4 have a unitary magnitude (0 dB) and a phase equal to 0 rad at $\omega = \omega_o$. The quality factor affects the graphs governing how smooth is the transition of the system from a capacitive behavior (low ω) to the inductive behavior (high ω). If the system is tuned to resonate at the supply frequency ω_s and the system has a very high Q, a small deviation of ω_s from the resonant frequency can cause a significant variation of the admittance. Systems with very high Q are very difficult to tune. This fact and the meaning of the quality factor

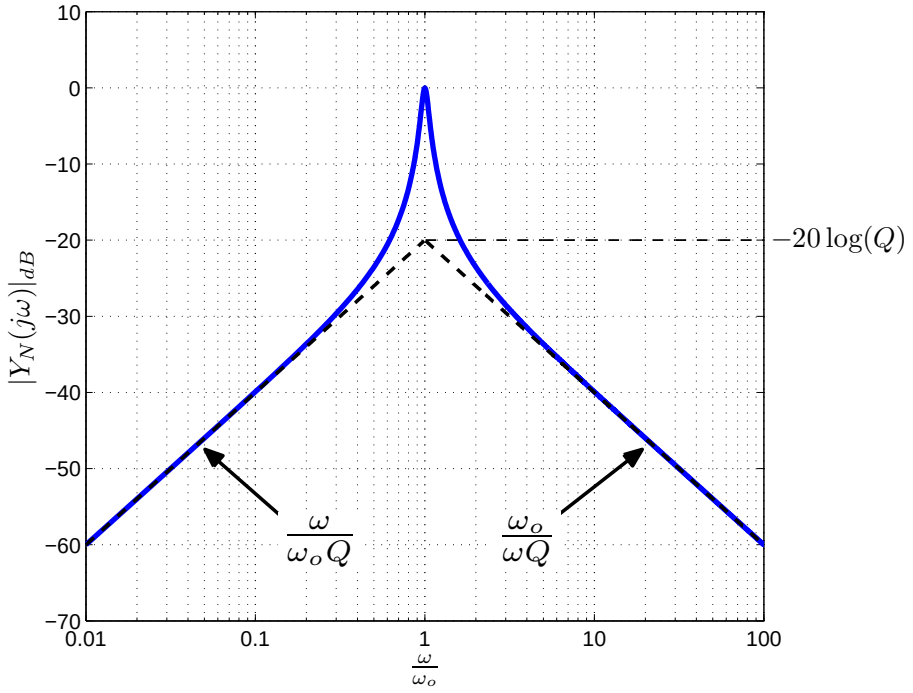

Fig. 3.5: Bode magnitude plot of the normalized admittance with $Q = 10$.

in the Bode magnitude plots can be grasped looking at the Fig. 3.5. In the figure, the Bode magnitude of the normalized admittance for a single value of $Q > \frac{1}{2}$ is plotted. Figure also shows the asymptotic behavior of the admittance. The two asymptotes can be obtained from the formula of $|Y_N(j\omega)|$:

$$|Y_N(j\omega)| = \frac{1}{\omega_o Q} \frac{\omega}{\sqrt{\left(1 - \frac{\omega^2}{\omega_o^2}\right)^2 + \frac{\omega^2}{\omega_o^2}\frac{1}{Q^2}}} \tag{3.21}$$

The asymptotes are defined from the magnitude of the admittance as follows:

$$\begin{cases} asym_1(\omega) = \left|Y_N(j\omega)\right|_{\omega<<\omega_o} = \frac{\omega}{\omega_o Q} \\ asym_2(\omega) = \left|Y_N(j\omega)\right|_{\omega>>\omega_o} = \frac{\omega_o}{\omega Q} \end{cases} \tag{3.22}$$

and they are depicted in Fig. 3.5 with dashed lines. It can be noticed that the two asymptotes intersect at $\omega = \omega_o$ where they are equal to $\frac{1}{Q}$. Concurrently, the actual value of the magnitude of the admittance is 1. For this reason, it can be stated that the quality factor represents the gain which has the real Bode plot with respect to the asymptotic Bode plot at the resonant frequency.

The higher the quality factor is, the narrower is the bandwidth of the series resonant tank. The bandwidth is defined as $BW = \omega_2 - \omega_1$, where ω_2 and ω_1 are the angular frequencies at which the normalized admittance is equal to $\frac{1}{\sqrt{2}}$[2]. Using (3.21), this condition becomes:

[2]Usually, the frequencies that determine the bandwidth are defined as the frequencies where the output power becomes half of the power delivered at $\omega = \omega_o$, so the frequencies where

$$\frac{1}{\omega_o Q}\frac{\omega}{\sqrt{\left(1-\frac{\omega^2}{\omega_o^2}\right)^2+\frac{\omega^2}{\omega_o^2}\frac{1}{Q^2}}}=\frac{1}{\sqrt{2}} \tag{3.23}$$

Solving it for ω, the two sought frequencies are found:

$$\begin{cases}\omega_2=\omega_o\left[\sqrt{\frac{1}{4Q^2}+1}+\frac{1}{2Q}\right]\\ \omega_1=\omega_o\left[\sqrt{\frac{1}{4Q^2}+1}-\frac{1}{2Q}\right]\end{cases} \tag{3.24}$$

And the bandwidth is given by:

$$BW=\omega_2-\omega_1=\frac{\omega_o}{Q} \tag{3.25}$$

Equation (3.25) shows that an high quality factor reduces the bandwidth of the system and this makes the system very sensitive to the supply frequency.

3.1.3 Current Response

Usually in WPTSs the compensating networks are tuned to resonate at the supply frequency. For this reason, it is interesting to investigate the current response of the series resonant tank after the turn on of the sinusoidal input voltage source with a frequency equal to the resonant one. The current response of the series resonant tank can be obtained from the convolution product between the impulse response and the input. An easier way to evaluate it, is to used the Laplace transform. The Laplace transform of the normalized current is given by the product of $Y_N(s)$ and the Laplace transform of the input voltage. For a sinusoidal input with a unitary amplitude, $I_N(s)$ is given by:

$$I_N(s)=Y_N(s)\frac{\omega_o}{s^2+\omega_o^2} \tag{3.26}$$

which, using (3.15), the definition of the damping ratio and considering $\xi<1$, it can be written as:

$$I_N(s)=\frac{2\xi\,\omega_o s}{(s+\xi\,\omega_o)^2+\omega_o^2\,(1-\xi^2)}\frac{\omega_o}{s^2+\omega_o^2} \tag{3.27}$$

After the application of the partial fraction decomposition to (3.27), the Laplace Transform of the normalized current can be written as:

$$I_N(s)=-\omega_o\frac{1}{(s+\xi\,\omega_o)^2+\omega_o^2\,(1-\xi^2)}+\omega_o\frac{1}{s^2+\omega_o^2} \tag{3.28}$$

With the Laplace transform of the normalized current written in this way, it is easy to apply the inverse Laplace transform to find the time response of the normalized current that is found to be:

the magnitude of the circuit current is $\frac{1}{\sqrt{2}}$ of the magnitude of the current when the circuit is in resonance. It can be proved that this condition is the same as the condition posed in the normalized admittance.

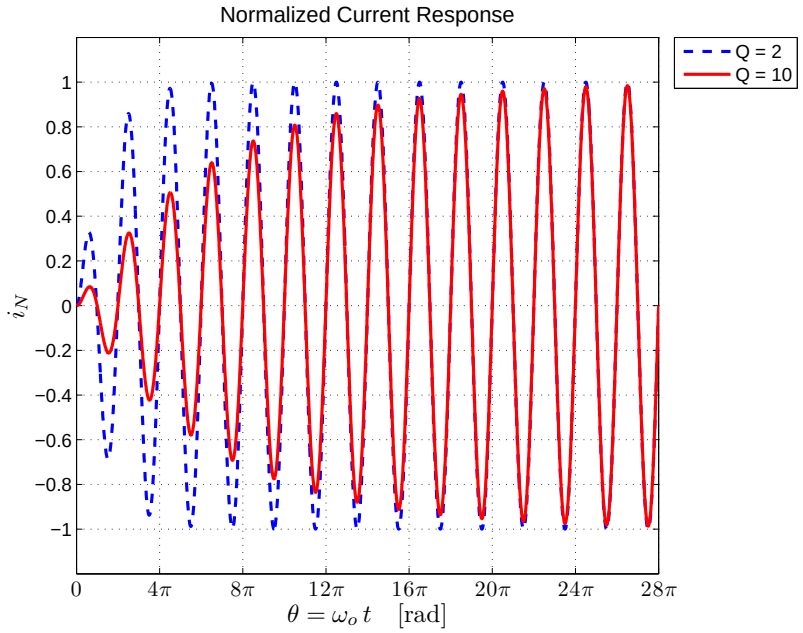

Fig. 3.6: Normalized current responses for two series resonant tanks with a different quality factor.

$$i_N(t) = -\frac{\omega_o}{\omega_r} e^{-\xi \omega_o t} \sin(\omega_r t) + \sin(\omega_o t) \tag{3.29}$$

in which $\omega_r = \omega_o \sqrt{1-\xi^2}$. The normalized current response is given by the sum of a transient term (the one multiplied by $e^{-\xi \omega_o t}$) and a steady-state term which as expected from the Bode diagram of $Y_N(s)$ is a sinusoidal signal with the same amplitude and the same phase of the input. Two different current responses for two systems with a different quality factor can be observed in Fig. 3.6. It can be seen that systems with lower Q (higher ξ) reach the steady-state faster than systems with high Q, but in any case the envelope of the response does not exhibit oscillation. This fact can be directly observed by (3.29). Indeed, when ξ is relatively low, the quantity ω_r is very similar to ω_o and (3.29) can be approximated as:

$$i_N(t) \approx \left(1 - e^{-\xi \omega_o t}\right) \sin(\omega_o t) \tag{3.30}$$

The normalized current is an amplitude-modulated signal whose carrier has a frequency ω_o and whose modulating-signal is $\left(1 - e^{-\xi \omega_o t}\right)$. The exponential behavior of the modulating-signal is easily recognizable in Fig. 3.6 as the envelopes of the alternating normalized currents.

3.2 Parallel Resonant Tank

Another simple type of compensating network is the parallel compensation, which is called in this way because the compensating capacitor is connected in parallel across the coil terminals. Figure 3.7(a) shows the phasor domain circuit of

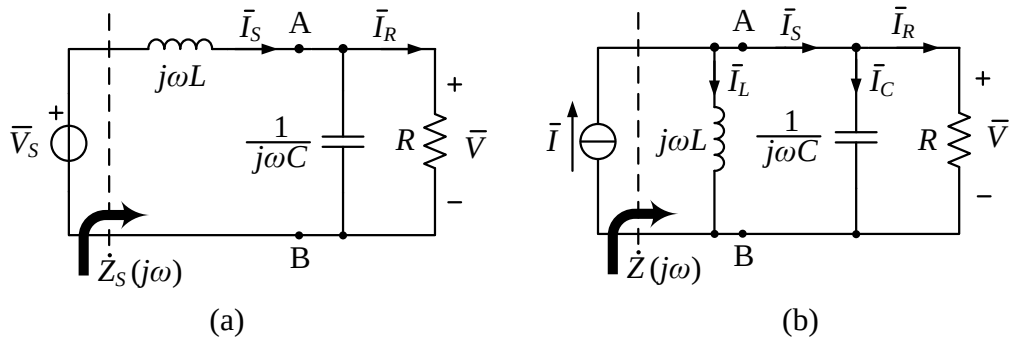

Fig. 3.7: Phasor domain circuit of a parallel compensation (a) and the parallel resonant tank obtained applying the Norton's theorem at port AB (b).

a parallel compensation conceived to be used for example in the receiving side of a WPTS. While in the following sections this circuit will be extensively analyzed, here the attention is given to the parallel resonant tank of Fig. 3.7(b). The circuit of Fig. 3.7(b) can be obtained from the circuit of Fig. 3.7(a) applying the Norton's theorem at port AB. The equivalent current source $\bar{I}$ is given by $\frac{\bar{V}_s}{j\omega L}$. It is important to study the parallel resonant tank because, as concern the behavior of the system connected downstream the port AB, it is exactly equivalent to the circuit of Fig. 3.7(a).

The parallel resonant tank is the dual of the series resonant tank. The results obtained in the previous section are still valid provided that currents are substituted with voltages and vice versa. Similarly, impedances take the place of the admittances. Applying the duality property for instance to (3.1), the equivalent input admittance of the parallel resonant tank is found to be:

$$\dot{Y} = \frac{1}{R} + j\left(\omega C - \frac{1}{\omega L}\right) = \frac{R(1-\omega^2 LC) + j\omega L}{j\omega L} \tag{3.31}$$

and consequently the input impedance is:

$$\begin{aligned} \dot{Z} &= \frac{j\omega L}{R(1-\omega^2 LC) + j\omega L} \\ &= \frac{1}{R^2(1-\omega^2 LC)^2 + \omega^2 L^2}\left[\omega^2 RL^2 + j\omega R^2 L(1-\omega^2 LC)\right] \end{aligned} \tag{3.32}$$

Once the input impedance of the parallel resonant tank is known, the voltage $\bar{V}$ of the circuit can be obtained with $\bar{V} = \dot{Z}\bar{I}$. If the current source is considered as reference for the phase, the profile of the input impedance versus the angular frequency is proportional to the profile of the output voltage.

The admittance and the impedance versus the supply angular frequency of the parallel resonant tank have the same profile of the curves in Fig. 3.2 with the difference that the curves are interchanged. The input impedance is inductive for low value of angular frequency, whereas at higher value of ω the reactance of the

capacitor becomes dominant. The input impedance assumes its maximum at the resonant frequency ω_o which is still found with (3.3). At this frequency the angle of the input impedance is zero and it means that the current source supplies only active power.

3.2.1 Resonant Operation

In resonant condition the susceptance of the inductor and the susceptance of the capacitor are equal and opposite. Under this condition the parallel of the inductance and of the capacitance is an open circuit. For this reason, the current fed by the current source goes entirely to the load resistance R. The output voltage is given by:

$$\bar{V} = R\,\bar{I} \tag{3.33}$$

And the current in the inductor is:

$$\bar{I}_L = \frac{\bar{V}}{j\omega_o L} = -j\frac{R}{\omega_o L}\,\bar{I} \tag{3.34}$$

Equation (3.34) shows that, even if the current that flows into the parallel between L and C is zero (the parallel is equivalent to an open circuit), the current that flows into the single component is not null an can reach high values.

Since the current of the parallel is zero, the instantaneous power absorbed by it is also zero. This entails that the energy stored in the reactive components, given by the integral of the instantaneous power, is constant. The energy stored in the system is constant, but the energies individually stored in the inductor and in the capacitor oscillates from zero to their maximum value with a frequency twice the supply one as it happens for the series resonant tank (cf. Fig. 3.3). To calculate the total energy stored in the parallel it is necessary to take the sum of the energy stored in the inductor and in the capacitor. It is possible to evaluate this sum when for example the energy in the inductor is zero and correspondingly when the energy stored in the capacitor is maximum. So the constant value of the total energy is given by:

$$w_{LC} = \frac{1}{2}\,C\,\max\left(v^2\right) = \frac{1}{2}C\,V^2 \tag{3.35}$$

The active power absorbed by the load is:

$$P_R = \frac{1}{2}\frac{V^2}{R} \tag{3.36}$$

which multiplied by the resonant period T_o yields the energy delivered by the current source to the load.

The quality factor of the circuit can be determined also for the parallel resonant tank and it is defined as in (3.9). Substituting the energies previously calculated, it becomes:

$$Q = 2\pi\,\frac{w_{LC}}{P_R\,T_o} = \frac{2\pi}{T_o}\,\frac{\frac{1}{2}C\,V^2}{\frac{1}{2}\frac{V^2}{R}} = \omega_o\,RC \tag{3.37}$$

Again, it can be written in different ways, using the formula $\omega_o = \frac{1}{\sqrt{LC}}$:

$$Q = \omega_o RC = \frac{R}{\omega_o L} = \sqrt{\frac{C}{L}}\, R \tag{3.38}$$

It can be observed that the quality factor of the parallel resonant tank circuit is the inverse of the quality factor for the series resonant tank circuit[3].

Using the definition (3.38), equation (3.34) can be rewritten in the following manner:

$$\bar{I}_L = \frac{\bar{R}}{j\omega_o L}\,\bar{I} = -jQ\,\bar{I} \tag{3.39}$$

Since the quality factor is typically greater than 1, the current in the reactive components of a parallel resonant tank is amplified by a factor Q with respect to the source current.

It is interesting for the parallel compensation of Fig. 3.7(a) to calculate the current $\bar{I}_s$ that the voltage source has to supply. It can be evaluated from the circuit of Fig. 3.7(b) according to:

$$\bar{I}_s = \bar{I} - \bar{I}_L = \bar{I}\,(1 + jQ) = \frac{\bar{V}_s}{\omega_o L}\,(Q - j) \tag{3.40}$$

It is easy to see that the current is not in phase with the voltage source which has to provide also a part of reactive power. The input impedance $\dot{Z}_s$ of the parallel resonant compensation circuit can be found dividing the input voltage by the input current and it is found to be:

$$\dot{Z}_s = \frac{\bar{V}_s}{\bar{I}_s} = \frac{1}{1+Q^2}\,(R + j\omega_o L) \tag{3.41}$$

The input impedance is ohmic-inductive and this fact, as we will see later, influences the reflected load into the primary side making it slightly capacitive.

3.2.2 Frequency Domain Analysis: Transfer Functions

The frequency behavior of the normalized input impedance can be studied in s-domain and it is equal to the transfer function that links the normalized output voltage to the normalized input current. Using the current source I and the value of the output voltage in resonant condition ($V = RI$) as base quantities, the normalized input impedance of the parallel resonant tank is given by:

$$Z_N(s) = \frac{V_N(s)}{I_N(s)} = \frac{Z(s)}{R} = \frac{L}{R}\,\frac{s}{1 + s\frac{L}{R} + s^2 LC} \tag{3.42}$$

Using definitions (3.38) and (3.3), equation (3.42) can be written as:

[3] Quality factor is again proportional to the ratio between the energy stored in the resonant tank and the energy delivered to the load over a resonant period. It is worth nothing that the energies stored in the system of Fig. 3.7(a) and the one stored in the parallel resonant tank circuit are different. For the parallel compensated circuit of Fig. 3.7(a) the stored energy is not constant (as in the circuit of Fig. 3.7(b)) but a fictitious quality factor is still defined using (3.38).

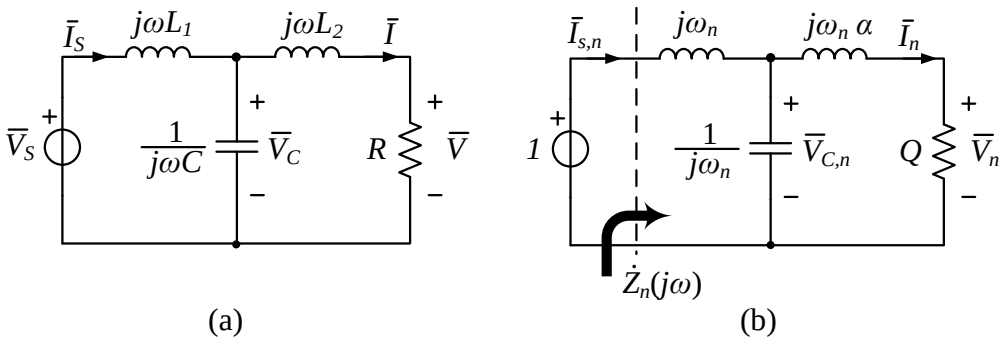

Fig. 3.8: LCL circuit in phasor domain (a) and its equivalent circuit used for the normalized analysis (b).

$$Z_N(s) = \frac{1}{\omega_o Q} \frac{s}{1 + \frac{s}{\omega_o Q} + \frac{s^2}{\omega_o^2}} \tag{3.43}$$

A comparison between (3.43) and (3.15) is useful to see that the normalized input impedance for the parallel resonant tank can be written in the same way as the normalized input admittance of the series resonant tank. The analysis done in Sec. 3.1.2 can be repeated word for word here.

3.3 LCL Resonant Tank

Besides the series compensation and the parallel compensation, another common compensation for WPTSs is the LC network derived from the LCL circuit [97]. It uses more than a simple capacitor for the reactive power compensation, but this drawback is counterbalanced by other interesting features that it owns and they will be introduced in this section.

The LCL circuit is shown in Fig. 3.8(a). Between the voltage source $\bar{V}_s$ and the load R, it is inserted the LCL network formed by an inductor L_1 in series with the voltage source, a resonant capacitor C and another inductor L_2 in series with the load.

In order to compare easily different designs for the LCL circuit, it is convenient to study the frequency behavior of the circuit with an analysis conducted with normalized quantities. The amplitude of the voltage source V_s and the characteristic impedance $Z_o = \sqrt{\frac{L_1}{C}}$ can be chosen as base quantities for the normalization process. Furthermore, other parameters can be defined: the resonant frequency $\omega_o = \frac{1}{\sqrt{L_1 C}}$, the ratio between the inductances $\alpha = \frac{L_2}{L_1}$ and an equivalent quality factor $Q = \frac{R}{\omega_o L_1}$. All the currents, the voltages and impedances of the circuit of Fig. 3.8(a) can be normalized according to the previous definitions. For instance, the normalization process of the impedance $j\omega L_2$ yields:

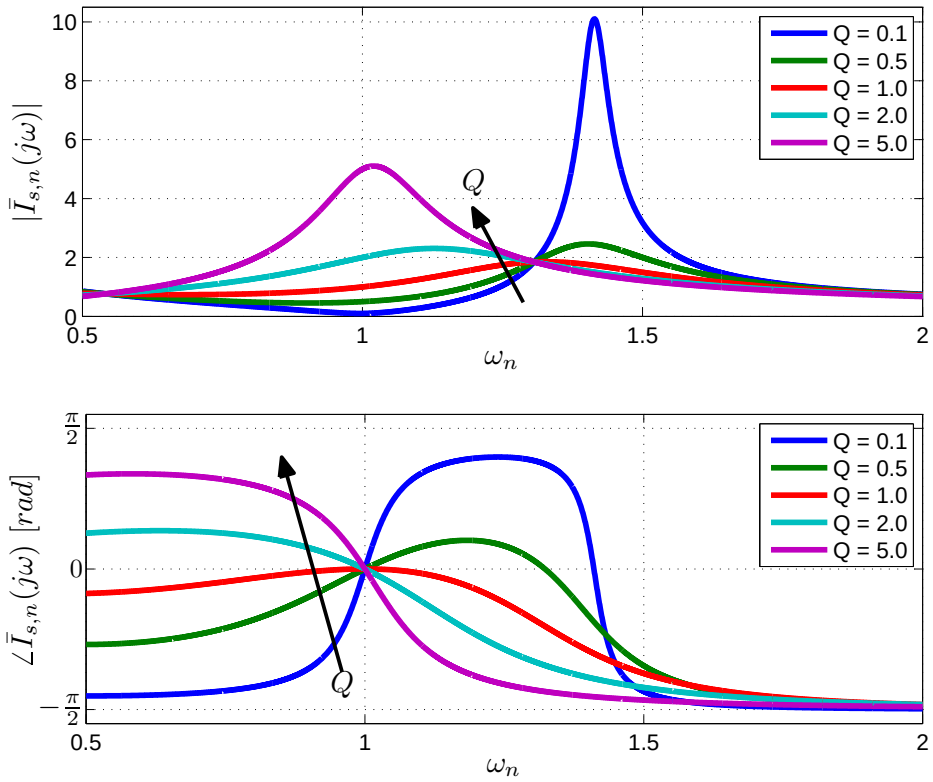

Fig. 3.9: Normalized input current of the LCL circuit versus the normalized angular frequency of the voltage source: magnitude (upper plot) and phase (lower plot). The curves refer to an LCL circuit with $\alpha = 1$.

$$\dot{Z}_{L_2,n} = \frac{j\omega L_2}{\sqrt{\frac{L_1}{C}}} = \frac{j\omega\alpha L_1}{\omega_o L_1} = j\omega_n\,\alpha \tag{3.44}$$

where $\omega_n = \frac{\omega}{\omega_o}$ is the normalized angular frequency.

The application of the normalization procedure to the circuit of Fig. 3.8(a) leads to the normalized circuit of Fig. 3.8(b). Studying the normalized circuit, one can find for example the normalized input impedance:

$$\dot{Z}_n = \frac{Q\,(1-\omega_n^2) + j\omega_n\,[1+\alpha\,(1-\omega_n^2)]}{1-\omega_n^2\,\alpha + j\omega_n Q} \tag{3.45}$$

and consequently the normalized input current, which is equal to the normalized input admittance, is found as follows:

$$\bar{I}_{s,n} = \frac{1}{\dot{Z}_n} = \frac{1-\omega_n^2\alpha + j\omega_n Q}{Q\,(1-\omega_n^2) + j\omega_n\,[1+\alpha(1-\omega_n^2)]} \tag{3.46}$$

The input current depends on the frequency of the voltage source ω_n and on the load quality factor. These dependencies can be assessed from the graph of Fig. 3.9. Both the amplitude and the angle of $\bar{I}_{s,n}$ vary changing the supply frequency. The load also affects the input current, but the effect that it produces strongly depends

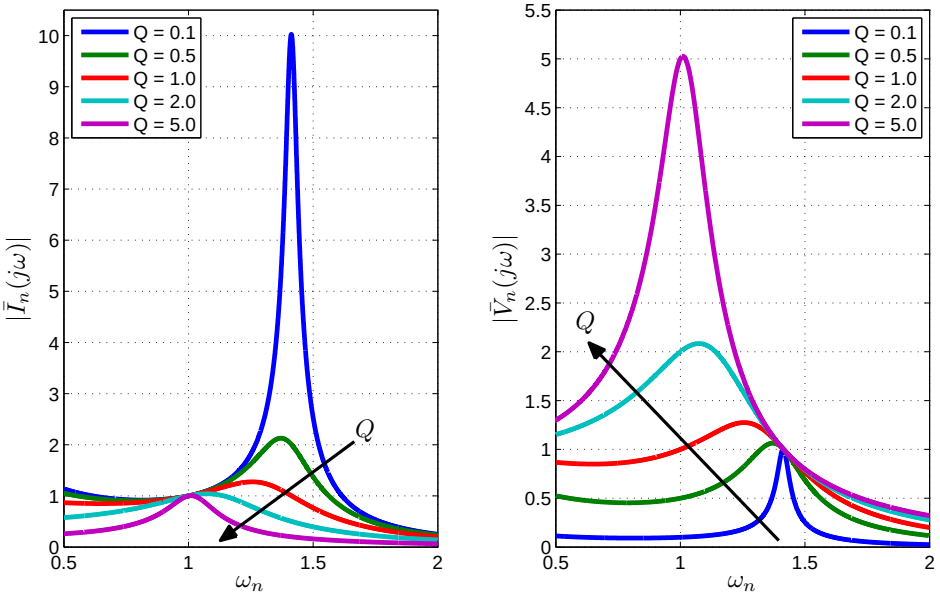

Fig. 3.10: Amplitude of the normalized load current (left) and of the normalized load voltage (right) of the LCL circuit versus the normalized angular frequency of the voltage source. The curves refer to an LCL circuit with $\alpha = 1$.

on ω_n. Let us consider the phase of the input current: when $0.5 < \omega_n < 1$, with high Q the current tends to be capacitive and vice versa it is inductive with low Q. The opposite situation occurs when the supply frequency is slightly greater than ω_o. When the supply frequency is exactly equal to ω_o the phase of the input current is zero independently from the load and this is due also to the fact that $\alpha = 1$.

From the circuit of Fig. 3.8(b), it is possible to derive also the normalized load current $\bar{I}_n$ and the normalized load voltage $\bar{V}_n$. They are given by:

$$\bar{I}_n = \frac{1}{Q\,(1-\omega_n^2) + j\omega_n\,[1+\alpha(1-\omega_n^2)]} \tag{3.47}$$

$$\bar{V}_n = \frac{1}{(1-\omega_n^2) + j\,\frac{1}{Q}\,\omega_n\,[1+\alpha(1-\omega_n^2)]} \tag{3.48}$$

Their amplitudes which correspond to the current and voltage gains of the circuit are plotted in Fig. 3.10. It can be noted that the LCL circuit can work as a current source when $\omega_n = 1$, or as a voltage source (see the voltage gain graph where all the curves are equal to 1 for $\omega_n \approx 1.41$). The correct frequencies that the voltage source has to supply to make the LCL circuit either current source or voltage source can be found from (3.47) and (3.48). In fact, the load current is independent from the load when Q disappears from the formula (3.47) and this happens when $\omega_n = 1$. In the same way, it can be found that the voltage gain is independent from Q when:

$$\begin{aligned} 1+\alpha\left(1-\omega_n^2\right)&=0\\ \Downarrow&\\ \omega_n&=\sqrt{\frac{1+\alpha}{\alpha}} \end{aligned} \tag{3.49}$$

that is equal to $\sqrt{2}\approx 1.41$ when $\alpha=1$.

In WPTSs it is interesting to have a compensating network with the current source behavior and for this reason the LCL network, usually, is designed with $\omega_n=1$.

3.3.1 Resonant Operation

Looking at the definition of ω_o, the condition $\omega_n=1$ is equivalent to say that the capacitor C is in resonance with the inductor L_1. Applying the Norton's theorem as it has been done for the parallel compensation circuit, it is easy to see that in this condition the converter behaves as a current source. In fact, since the parallel of L_1 and C can be envisaged as an open circuit, the equivalent current source of the Norton's equivalent circuit entirely feeds the load R.

The load current and all the other quantities that can be calculated from the circuits in Fig. 3.8 are reported in Tab. 3.1. The equations show once again the current source characteristic of the LCL cirucit when $\omega=\omega_o$.

It is interesting to calculate the equations of the circuit when $\alpha=1$, namely when $L_1=L_2$. In this situation, the input impedance becomes:

$$\dot{Z}=\frac{\omega_o^2 L_1^2}{R} \tag{3.62}$$

The input impedance is purely resistive and is proportional to the inverse of the load. Having a real input impedance is a good feature that permits the LC network to be exploited both in the transmitting and in the receiving side of a WPTS.

The input current is given by:

$$\bar{I}_s=\bar{V}_s\frac{R}{\omega_o^2 L_1^2} \tag{3.63}$$

Equation (3.63) shows that when there is no load ($R=0$) the input current of the LCL circuit is ideally zero, whereas the load current remains constant.

3.3.2 Frequency Domain Analysis: Transfer Functions

As it has been done for the series and the parallel resonant tanks, the frequency analysis in s-domain is carried out also for the LCL circuit. Assuming $\alpha=1$, the transfer function that links the normalized input current to the normalized supply voltage can be written as:

$$I_{s,n}(s)=\frac{\omega_o L_1}{R}\frac{1+RC\,s+L_1C\,s^2}{1+2\frac{L_1}{R}\,s+L_1C\,s^2+\frac{L_1^2C}{R}s^3} \tag{3.64}$$

Tab. 3.1: Equations of the LCL circuit when $\omega_n = 1$.

Normalized	$\dot{Z}_n = \frac{1}{(1-\alpha)^2 + Q^2}\left[Q + j\,(1-\alpha)\right]$	(3.50)
	$\angle\dot{Z}_n = \arctan\left\{\frac{1-\alpha}{Q}\right\}$	(3.51)
	$\bar{I}_{s,n} = Q - j\,(1-\alpha)$	(3.52)
	$\bar{I}_n = -j$	(3.53)
	$\bar{V}_n = -jQ$	(3.54)
	$\bar{V}_{C,n} = \alpha - jQ$	(3.55)
Not Normalized	$\dot{Z} = \frac{1}{\left(\frac{L_1-L_2}{L_1}\right)^2 + \frac{R^2}{\omega_o^2 L_1^2}}\left[R + j\,\omega_o(L_1 - L_2)\right]$	(3.56)
	$\angle\dot{Z} = \arctan\left\{\frac{\omega_o(L_1-L_2)}{R}\right\}$	(3.57)
	$\bar{I}_s = \frac{\bar{V}_s}{\omega_o L_1}\left[\frac{R}{\omega_o L_1} + j\left(\frac{L_1-L_2}{L_1}\right)\right]$	(3.58)
	$\bar{I} = -j\frac{\bar{V}_s}{\omega_o L_1}$	(3.59)
	$\bar{V} = -j\bar{V}_s\frac{R}{\omega_o L_1}$	(3.60)
	$\bar{V}_C = \bar{V}_s\left[\frac{L_2}{L_1} - j\frac{R}{\omega_o L_1}\right]$	(3.61)

Considering the definition for the quality factor Q and for ω_o, equation (3.64) becomes:

$$I_{s,n}(s) = \frac{1}{Q}\,\frac{1 + \frac{Q}{\omega_o}\,s + \frac{1}{\omega_o^2}\,s^2}{1 + \frac{2}{\omega_o Q}\,s + \frac{1}{\omega_o^2}\,s^2 + \frac{1}{\omega_o^3 Q}s^3} \tag{3.65}$$

The Bode diagram for the normalized input current of an LCL circuit with $\alpha = 1$ is shown in Fig. 3.11. A good insight into the plot can arise from the approximation of the transfer function (3.65) in case of very low and very high Q. To do this, the method explained in [38, p. 289] for roughly finding the roots of a polynomial can be employed. In case of high Q the transfer function for the normalized input current can be written as:

$$I_{s,n}(s) \approx \frac{1}{Q}\,\frac{1 + \frac{Q}{\omega_o}\,s}{1 + \frac{2}{\omega_o Q}\,s + \frac{1}{\omega_o^2}\,s^2} \tag{3.66}$$

in which the zero and the pole $\left(1 + \frac{1}{\omega_o Q}\,s\right)$ have been canceled out. The transfer

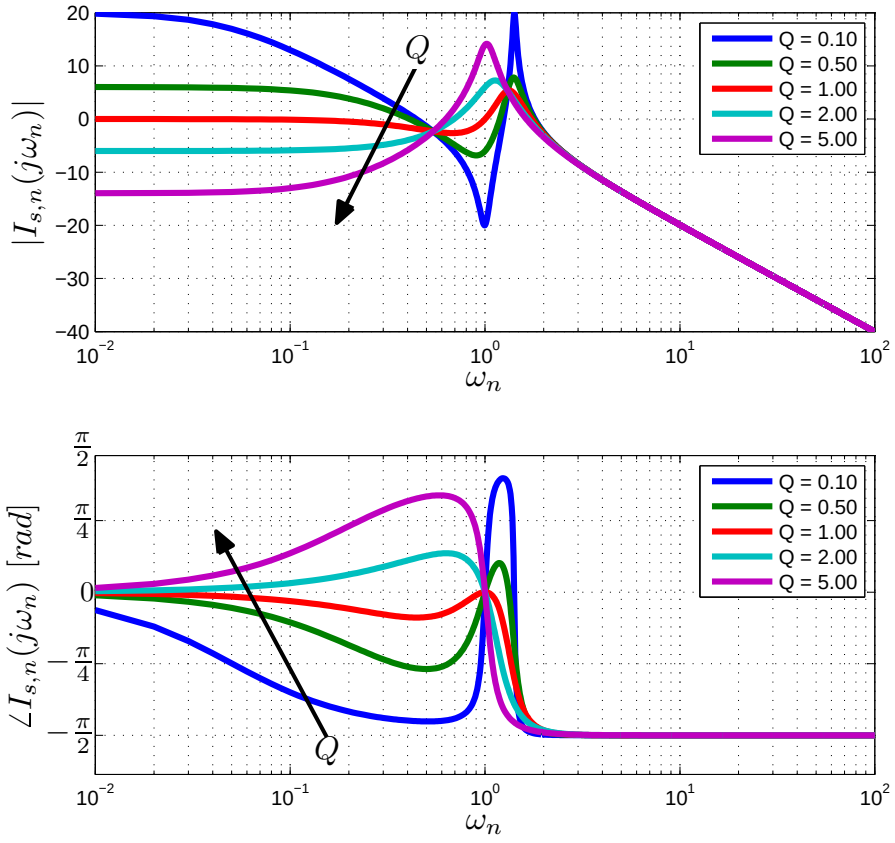

Fig. 3.11: Bode diagram for the normalized input current of an LCL circuit with $\alpha = 1$.

function has one zero at the cut-off frequency $\omega_c = \frac{\omega_o}{Q}$ which is clearly less than ω_o for the approximation made. It has also a complex conjugate poles pair with a natural frequency of ω_o. This situation is illustrated by the curve with $Q = 5$ in Fig. 3.11.

When the load resistance is small and Q is small as well, the transfer function (3.65) can be approximated with:

$$I_{s,n}(s) \approx \frac{1}{Q} \frac{1 + \frac{Q}{\omega_o} s + \frac{1}{\omega_o^2} s^2}{\left(1 + \frac{2}{\omega_o Q} s\right)\left(1 + \frac{Q}{2\omega_o} s + \frac{1}{2\omega_o^2} s^2\right)} \tag{3.67}$$

The complex conjugate poles pair, which in case of high Q has a natural frequency of ω_o, for low Q is shifted at a natural frequency $\omega_o\sqrt{2}$. At frequency ω_o the transfer function of the normalized input current has two complex conjugate zeros that are very close to the imaginary axis. The LCL circuit with low Q possesses also a real pole with a very low cut-off frequency given by $\frac{\omega_o Q}{2}$. An example of Bode diagram for the approximate transfer function described by (3.67) is shown in Fig. 3.11 and it is identified with the label $Q = 0.10$. It can be seen from the graph that, since the complex poles are underdamped, at $\omega = \omega_o\sqrt{2}$ the Bode diagram has an high resonant peak. If the LCL circuit is fed by an inverter controlled with

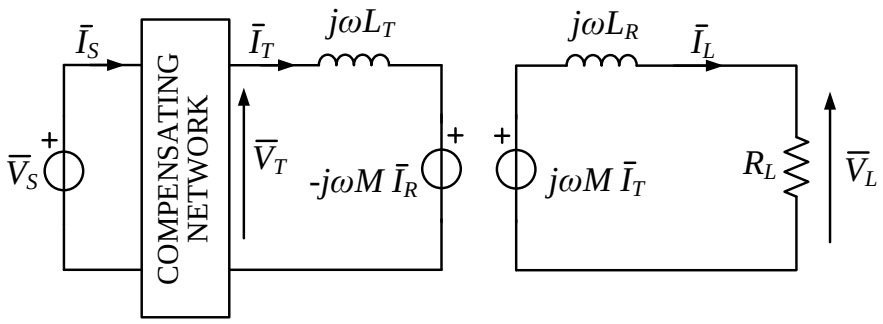

Fig. 3.12: WPTS with constant transmitting current and an uncompensated receiver.

the phase-shift technique, the harmonic content of the input voltage includes all the odd frequencies multiple of ω_o. The resonant peak at $\omega_o\sqrt{2}$ makes the higher order harmonics of the input current of an LCL circuit with low Q greater than the fundamental. Thus, when the load resistance is small, the fundamental harmonic approximation is no more valid as explained in [98], where the authors took into account the higher order harmonics of the input current for evaluating the inverter ZCS capabilities.

3.4 Aim of the Compensating Networks

After having introduced the series, the parallel and the LCL resonant tanks and the parameters used to analyze them, now it is time to explain why they are employed in WPTSs.

Let us suppose to have a constant current in the transmitting coil. This result can be obtained employing in the transmitting side a compensating network with a current source behavior (parallel or LCL) or by controlling the inverter to maintain the transmitting coil current constant irrespective of the load and mutual inductance variations.

When the transmitting coil current is maintained constant, two important parameters that define the coil coupling are:

- the open-circuit receiving-side voltage $\bar{V}_{OC} = j\omega M \bar{I}_T$;
- the short-circuit receiving-side current $\bar{I}_{SC} = \frac{\bar{V}_{OC}}{j\omega L_R} = \frac{M}{L_R}\,\bar{I}_T$.

Let us consider an uncompensated receiver as shown in Fig. 3.12 and suppose, hereafter in this section, that the amplitudes of the phasors are the rms of the quantities. The power absorbed by the load is given by:

$$P_L = \frac{R_L}{R_L^2 + \omega^2 L_R^2} V_{OC}^2 \tag{3.68}$$

Deriving it for R_L and equating the derivative to zero, the maximum power that can be transferred to the load in case of uncompensated receiver can be found when $R_L = \omega L_R$ and it is given by:

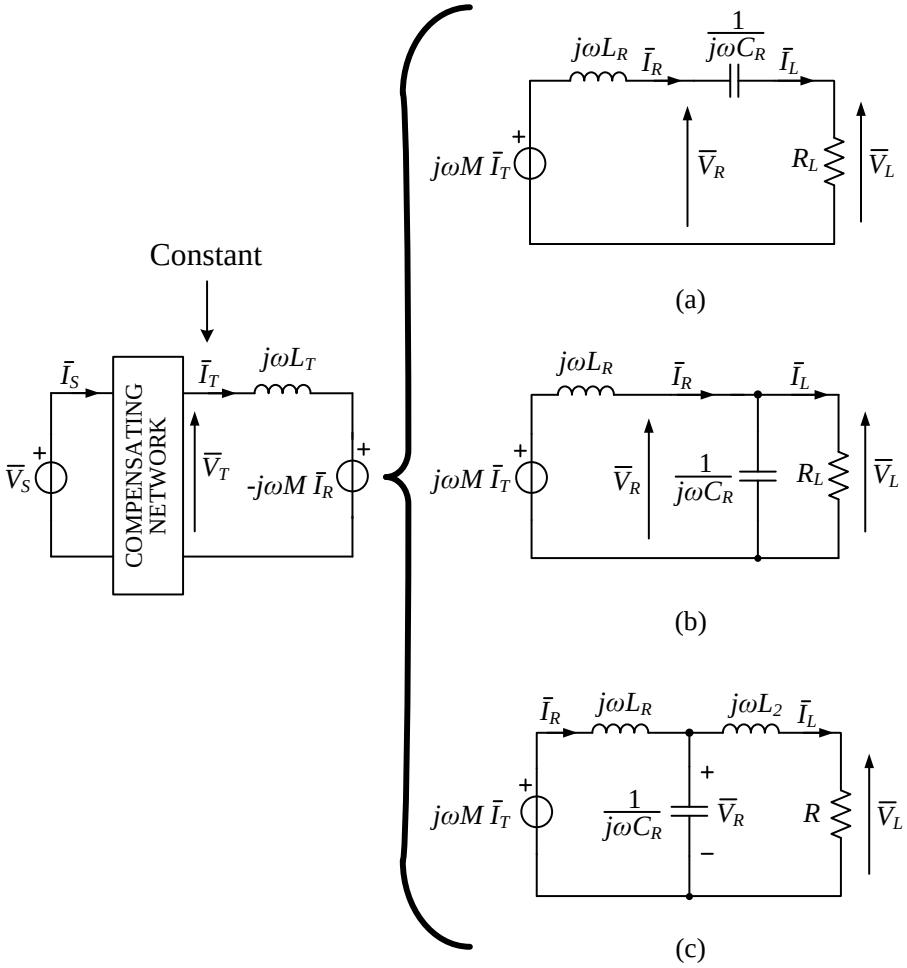

Fig. 3.13: Different receiver compensations for a WPTS with constant transmitting current. Series compensation (a), parallel compensation (b) and LC compensation (c).

$$P_L = \frac{1}{2}\frac{V_{OC}^2}{R_L} = \frac{1}{2}\frac{V_{OC}^2}{\omega L_R} = \frac{1}{2}V_{OC}I_{SC} = \frac{1}{2}S_u \tag{3.69}$$

The maximum power that can be transferred in case of an uncompensated receiver is then equal to one half of the product between the open-circuit receiving-side voltage and the receiving-side short-circuit current (this product has been denoted as S_u). This power is generally not sufficient and compensating networks in the receiving side are used to increase it [39].

Let us consider now the effect of the various compensations in the receiving side. Figure 3.13 can be used for this purpose. For this analysis we assume that the frequency of the transmitting coil current is exactly equal to the resonant frequency ω_o of the compensating networks.

Series Compensation

When the receiver is series-compensated the voltage across the load is equal to the open-circuit voltage V_{OC}. The load current instead is given by:

$$\bar{I}_L = \frac{\bar{V}_{OC}}{R_L} = \frac{\bar{V}_{OC}}{j\omega_o L_R} \frac{j\omega_o L_R}{R_L} = j\,\bar{I}_{SC}\,Q_R \tag{3.70}$$

where Q_R is the quality factor of the receiving-side series resonant tank. It can be noticed that the load current is amplified by a factor Q_R with respect to the short-circuit receiving-side current.

The power that can be transferred to the load when the receiver is series compensated is equal to:

$$P_L = \frac{V_{OC}^2}{R_L} = V_{OC} \frac{V_{OC}}{\omega_o L_R} \frac{\omega_o L_R}{R_L} = V_{OC} I_{SC}\,Q_R = S_u\,Q_R \tag{3.71}$$

It is easy to see that the load power is increased by a factor $2\,Q_R$ with respect to the maximum power that can be transferred with an uncompensated receiver.

The rms of voltage and the rms of the current that the receiving coil has to sustain are given by:

$$V_R = V_{OC}\sqrt{1+Q_R^2} \approx V_{OC}\,Q_R \tag{3.72}$$

$$I_R = I_L = I_{SC}\,Q_R \tag{3.73}$$

Since usually $Q_R > 1$, both the coil voltage and the coil current are greater than the open-circuit receiving-side voltage and than the short-circuit receiving-side current, respectively.

The *VA* rating of the coil as defined in (2.2) is equal to:

$$VA_R = \omega_o L_R I_R^2 = \omega_o L_R I_{SC}^2\,Q_R^2 = V_{OC} I_{SC}\,Q_R^2 = S_u\,Q_R^2 \tag{3.74}$$

Please note that the *VA* rating of the coil as defined before is different from the product between the voltage across and the current flowing through the coil. This is simply because the definition (2.2) does not consider the voltage induced in the receiver coil, but it takes into account only the voltage drop $\omega_o L_R I_R$ across the inductance L_R. However, when the quality factor of the receiving-side circuit is sufficiently high, the two definitions are almost equivalent.

Parallel Compensation

Looking at the Fig. 3.13(b), one can derive the power that can be transmitted by a WPTS with a parallel-compensated receiver.

Contrary to what happens in case of a series compensation, in the parallel compensation the load current is equal to I_{SC}[4]. The load voltage instead is given by:

[4] This can be seen applying the Norton's theorem to the receiver of Fig. 3.13(b).

$$\bar{V}_L = R_L \bar{I}_L = \frac{R_L}{j\omega_o L_R}\, j\omega_o L_R\, \bar{I}_{SC} = -j\, Q_R\, \bar{V}_{OC} \tag{3.75}$$

Then, the power is obtained with:

$$P_L = V_L I_L = V_{OC} I_{SC}\, Q_R = S_u\, Q_R \tag{3.76}$$

Power can be written in the same way as for the series compensation. The only difference between (3.76) and (3.71) is in the definition of the quality factor.

The design of the receiving coil has to take into consideration the voltage across its terminal and the current that flows through it which can be written as:

$$V_R = V_L = V_{OC}\, Q_R \tag{3.77}$$

$$I_R = I_{SC} \sqrt{1 + Q_R^2} \approx I_{SC}\, Q_R \tag{3.78}$$

Equation (3.78) has been derived from (3.40).

The *VA* product of the coil for a parallel-compensated receiver is:

$$VA_R = \omega_o L_R I_R^2 = V_{OC} I_{SC}\, (1 + Q_R^2) = S_u\, (1 + Q_R^2) \approx S_u\, Q_R^2 \tag{3.79}$$

The *VA* rating of the coil in case of parallel compensation can be written in an approximated way as the *VA* rating of the coil of a series compensation.

LC Compensation

The LC receiving-side compensation of Fig. 3.13(c) is very similar to the parallel compensation. Both of them have a current source output characteristic and both have the load current equal to I_{SC}. The load voltage of an LC-compensated receiver can be written as (3.75). Being the load current and the load voltage of the LC compensation equal to the ones of the parallel compensation, it means that the load power is also equal and can be found with (3.76). Some differences appear in the equations of the voltage across the coil terminals and in the current that flows through the coil. For an LC-compensated receiver they are equal to:

$$V_R = V_{OC} \sqrt{1 + Q_R^2} \approx V_{OC}\, Q_R \tag{3.80}$$

$$I_R = I_{SC}\, Q_R \tag{3.81}$$

Equations (3.80) and (3.81) are obtained from (3.55) and (3.52), respectively.

Since the current I_R of the receiving coil is equal to $I_{SC}\, Q_R$, as it happens for the coil current of a series compensated receiver, the *VA* rating of the coil can be written as in (3.74).

In this section, it has been shown that, despite the topology of the receiving-side compensation network, the active power that can be transferred to the load can

Tab. 3.2: Equations summary for different receiver topologies.

	Series Compensation	Parallel Compensation	LC Compensation
Q_R	$\frac{\omega_o L_R}{R_L}$	$\frac{R_L}{\omega_o L_R}$	$\frac{R_L}{\omega_o L_R}$
I_L	$I_{SC}\, Q_R$	I_{SC}	I_{SC}
V_L	V_{OC}	$V_{OC}\, Q_R$	$V_{OC}\, Q_R$
P_L	$S_u\, Q_R$	$S_u\, Q_R$	$S_u\, Q_R$
V_R	$V_{OC}\sqrt{1+Q_R^2}$	$V_{OC}\, Q_R$	$V_{OC}\sqrt{1+Q_R^2}$
I_R	$I_{SC}\, Q_R$	$I_{SC}\sqrt{1+Q_R^2}$	$I_{SC}\, Q_R$
VA_R	$S_u\, Q_R^2$	$S_u\,(1+Q_R^2)$	$S_u\, Q_R^2$
$V_R * I_R$	$S_u\, Q_R\sqrt{1+Q_R^2}$	$S_u\, Q_R\sqrt{1+Q_R^2}$	$S_u\, Q_R\sqrt{1+Q_R^2}$

be written in a common manner and it is given by the uncompensated apparent power S_u times the quality factor of the compensating network. The different topologies have different voltage and current ratings. The results of this section are summarized in Tab. 3.2. It is possible to see that the parallel and the LC topologies boost the load voltage with respect to the open-circuit receiving-side voltage, whereas the series compensation boosts the load current with respect the the short-circuit receiving-side current. Although the VA of the coils are different for the various compensations and they are different from the product between the coil voltage V_R and the coil current I_R, when the quality factor of the receiving-side circuit is high they can be approximated with the same formula:

$$VA_R \approx V_R * I_R \approx S_u\, Q_R^2 = P_L\, Q_R \tag{3.82}$$

It is worth noting that the VA rating of the receiving coil in first approximation is proportional to the load power and to the receiver quality factor which, for this reason, cannot be too high.

Expanding the formula for the load power found in Tab. 3.2, another interesting form of the equation is obtained:

$$P_L = S_u\, Q_R = V_{OC} I_{SC}\, Q_R = \omega_o I_T^2\, \frac{M^2}{L_R}\, Q_R = \omega_o I_T^2\, k^2 L_T\, Q_R \tag{3.83}$$

where in the last equivalence, the mutual inductance M has been replaced by its definition that includes the coupling coefficient k.

The factor $\omega_o L_T I_T^2$ in (3.83) can be identified as the VA rating of the transmitting coil (cf. definition (3.74)) and (3.83) can be rewritten as follows:

$$P_L = \omega_o L_T I_T^2\, k^2\, Q_R = VA_T\, k^2\, Q_R \tag{3.84}$$

By using (3.84) and (3.82), a relation between the VA rating of the transmitter and of the receiver can be found:

$$VA_T = \frac{VA_R}{k^2 Q_R^2} \tag{3.85}$$

The rating of the transmitting coil can be greater or less than the rating of the receiving coil and this is based on the value of the product kQ_R.

The *VA* rating of the transmitting and of the receiving coils permits the losses of the WPTS system to be assessed. According to (2.1) and assuming that the power is dissipated mainly in the coil windings, the losses of the system can be written as:

$$P_{Loss} = \frac{VA_T}{Q_{L,T}} + \frac{VA_R}{Q_{L,R}} \tag{3.86}$$

where $Q_{L,T}$ and $Q_{L,R}$ are respectively the coil quality factor of the transmitter and of the receiver. Using (3.82) and (3.85), equation (3.86) becomes:

$$\begin{aligned} P_{Loss} &= \frac{VA_R}{k^2\, Q_R^2\, Q_{L,T}} + \frac{VA_R}{Q_{L,R}} \\ &= P_L \left[\frac{1}{k^2\, Q_R\, Q_{L,T}} + \frac{Q_R}{Q_{L,R}} \right] \end{aligned} \tag{3.87}$$

The two terms inside the square brackets represent the losses in the transmitting coil (first term) and in the receiving coil (second term). Taking the derivative of (3.87) with respect to Q_R and equating it to zero, it is found that the losses are minima when:

$$Q_R = \frac{1}{k} \sqrt{\frac{Q_{L,R}}{Q_{L,T}}} \tag{3.88}$$

Under condition (3.88), the losses are shared equally in the transmitting and in the receiving coil and they are equal to:

$$P_{Loss,min} = P_L \frac{2}{k\sqrt{Q_{L,T}\, Q_{L,R}}} \tag{3.89}$$

Once the equation of the minima losses is found, it is easy to calculate the maximum efficiency of the WPTS that is given by:

$$\eta_{max} = \frac{P_L}{P_L + P_{Loss,min}} = \frac{1}{1 + \frac{P_{Loss,min}}{P_L}} = \frac{1}{1 + \frac{2}{k\sqrt{Q_{L,T}\, Q_{L,R}}}} \tag{3.90}$$

To increase the maximum allowable power efficiency it is important to maximize the figure of merit $k\sqrt{Q_{L,T}\, Q_{L,R}}$. In other words, building coils with high self quality factors permits the required power to be transferred with high efficiency even if the coupling coefficient is low.

In conclusion, when the transmitting coil current is maintained constant, it is convenient to use compensating networks in the receiving side for increasing both the transmitted power and the efficiency. The compensation of the transmitting side can be employed for helping the controller of the transmitting coil current to maintain it constant. This result is accomplished when compensating networks with current source behavior such as parallel and LC are exploited. In any case, the compensation of the transmitter is used to reduce the power sizing of the inverter.

In fact, with compensating networks it is possible to achieve a unity power factor at the inverter output terminals. For the same output power P_L, if the voltage and the current are in phase, it means that the inverter does not have to manage the reactive power and it has to be rated only for the active power.

Chapter 4

WPTSs Under Steady-State

This chapter analyzes the WPTSs from the steady-state viewpoint. The WPTS with series compensation both in the transmitting and in the receiving side is the simplest one and it has very good performance. For this reason it is presented as first, deriving the fundamental relations for the circuital voltages and currents. Based on these relations, a possible way to design a series-series WPTS is explained.

The main shortcoming of series-series compensation is that it is very difficult to control the transmitting current in case of load and coil coupling variations. This is a drawback especially when series-series compensation has to be employed in dynamic WPTSs. After having analyzed the steady-state of the series-series compensation, the chapter continues with the study of the LC-series compensation, with the goal of moving towards the dynamic WPTSs. It will be shown that when the track is LC-compensated the current that flows through it, is inherently constant. This fact allows a reduction of the control system complexity. A possible way to design a dynamic WPTS with LC-series compensation is proposed considering a very simple situation.

The steady-state equations useful for the design of the LC-series, the LC-parallel and the LC-LC WPTSs are derived with the assumption of having the receiver always in resonance and they are collected in the appendix A.

4.1 Series-Series WPTS

Among the simplest possible two-elements compensated WPTSs [26], the Series-Series (SS) compensated WPTS seems to be the best solution for the EV battery charging [99]. For this reason a brief review of this topology is provided in this section, even though the more-elements compensations are preferred especially in dynamic WPTSs.

The steady-state analysis of the SS-compensated WPTS can be conducted with the aid of Fig. 4.1. The circuit shown in the figure is equivalent to the generic WPTS scheme of Fig. 2.25 in which the compensating network blocks are replaced with two simple capacitors connected in series with the transmitting and the receiving coils.

Instead of finding the relations between the real quantities of the SS WPTS, in order to compare different designs, it is more convenient to operate with nor-

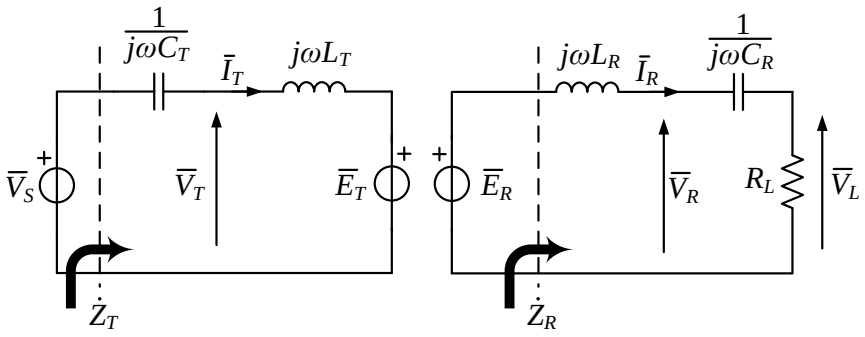

Fig. 4.1: Scheme for the steady-state analysis of a WPTS with series-series compensation.

malized quantities. Furthermore, to simplify the analysis, some parameters can be introduced. They are summed up in the following list:

- $\alpha = \frac{L_R}{L_T}$ ratio between the inductances;
- $\beta = \frac{C_R}{C_T}$ ratio between the capacitances;
- $\omega_T = \frac{1}{\sqrt{L_T C_T}}$ resonant frequency of the transmitter;
- $\omega_R = \frac{1}{\sqrt{L_R C_R}} = \frac{\omega_T}{\sqrt{\alpha\beta}}$ resonant frequency of the receiver;
- $\omega_n = \frac{\omega}{\omega_T}$ normalized angular frequency;
- $M = kL_T\sqrt{\alpha}$ mutual inductance;
- $Q_R = \frac{\omega_R L_R}{R_L} = \sqrt{\frac{\alpha}{\beta}}\frac{\omega_T L_T}{R_L}$ quality factor of the receiving circuit.

The employed based quantities are:

- $V_b = V_s$
- $Z_b = \omega_T L_T$
- $I_b = \frac{V_b}{Z_b}$
- $P_b = \frac{V_b^2}{Z_b}$

Considering the base quantities and the parameters above mentioned all the impedances, voltages and currents that appear in the circuit of Fig. 4.1 can be replaced by their respective normalized values. For example, the normalized load resistance can be obtained as follows:

$$R_{L,n} = \frac{R_L}{\omega_T L_T} = \sqrt{\frac{\alpha}{\beta}}\frac{1}{Q_R} \tag{4.1}$$

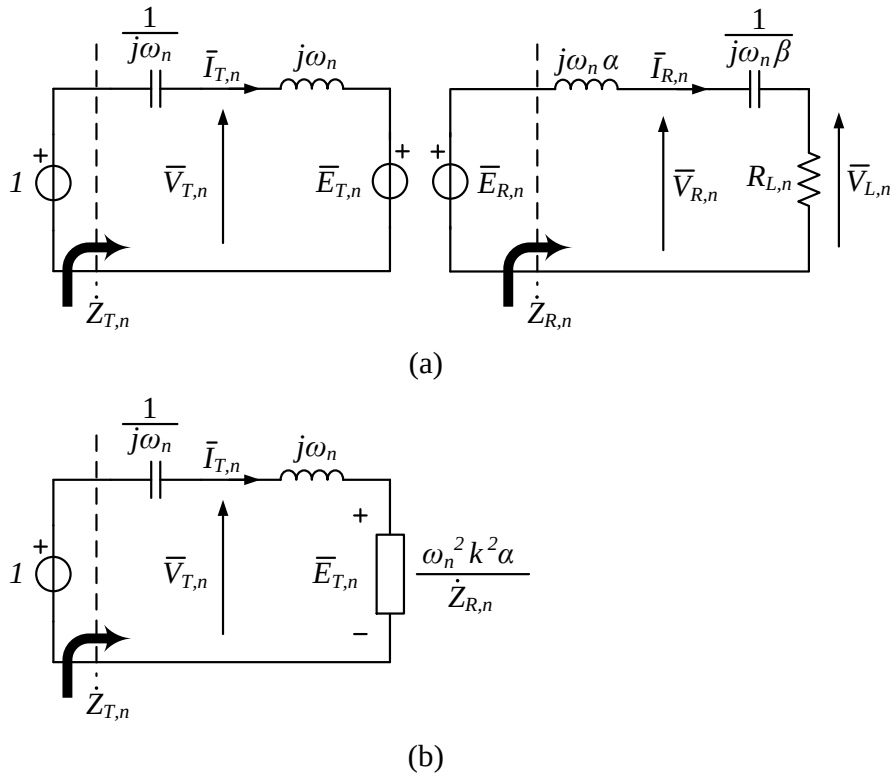

Fig. 4.2: Scheme for the normalized steady-state analysis of a WPTS with SS compensation (a). Transmitting-side equivalent circuit (b).

According to definition (2.40) the normalized reflected impedance can be obtained with:

$$\dot{Z}_{ref,n} = \frac{1}{\omega_T L_T}\frac{\omega^2 M^2}{\dot{Z}_R} = \frac{1}{\omega_T^2 L_T^2}\frac{\omega^2 M^2}{\dot{Z}_{R,n}} = \frac{\omega_n^2 k^2 \alpha}{\dot{Z}_{R,n}} \tag{4.2}$$

And a similar approach can be used for all the other quantities. When the normalization process has been completed, the circuit of Fig. 4.2 is found.

The first thing that is worth finding is the normalized input impedance $\dot{Z}_{T,n}$ of the transmitting circuit. Once $\dot{Z}_{T,n}$ is found, all the quantities of the circuit in Fig. 4.2 are immediately derivable. To calculate the normalized input impedance it is necessary to have the normalized reflected impedance $\dot{Z}_{ref,n}$, which in turn depends on the normalized receiving-side impedance $\dot{Z}_{R,n}$ (see Fig. 4.2). The normalized receiving-side impedance is given by:

$$\dot{Z}_{R,n} = \sqrt{\frac{\alpha}{\beta}}\frac{1}{Q_R} + j\left(\frac{\omega_n^2\alpha\beta - 1}{\omega_n \beta}\right) \tag{4.3}$$

Substituting (4.3) into (4.2), the normalized reflected impedance is found in the form:

$$\dot{Z}_{ref,n} = \frac{1}{\omega_n^2 + Q_R^2\,\alpha\beta\,\left(\omega_n^2 - \frac{1}{\alpha\beta}\right)^2}\left[\sqrt{\alpha\beta}\,k^2 Q_R\,\omega_n^4 - j\,\alpha\beta Q_R^2\,\omega_n^3 k^2\left(\omega_n^2 - \frac{1}{\alpha\beta}\right)\right] \tag{4.4}$$

An inspection of Fig. 4.2(b) permits us to see that the real part of the transmitting-side input impedance coincides with the real part of the reflected impedance, while the imaginary part is found to be:

$$\Im\{\dot{Z}_{T,n}\} = \frac{\omega_n^2\left(\frac{\omega_n^2-1}{\omega_n}\right) + Q_R^2\,\alpha\beta\left(\frac{\omega_n^2-1}{\omega_n}\right)\left(\omega_n^2 - \frac{1}{\alpha\beta}\right)^2 - \alpha\beta Q_R^2\,\omega_n^3 k^2\left(\omega_n^2 - \frac{1}{\alpha\beta}\right)}{\omega_n^2 + Q_R^2\,\alpha\beta\,\left(\omega_n^2 - \frac{1}{\alpha\beta}\right)^2} \tag{4.5}$$

Usually the WPTSs are designed in order to have the same resonant frequency for the transmitter and the receiver and based on the above definitions it is equivalent to choose $\alpha\beta = 1$. With this choice, the normalized input impedance becomes:

$$\begin{aligned}\dot{Z}_{T,n} =& \frac{\omega_n^4\,k^2 Q_R}{\omega_N^2 + Q_R^2\,(\omega_n - 1)^2} + \\ &+ j\left\{\left(\frac{\omega_n^2 - 1}{\omega_n}\right)\left[\frac{Q_R^2\,(1-k^2)\,\omega_n^4 + (1-2Q_R^2)\,\omega_n^2 + Q_R^2}{\omega_N^2 + Q_R^2\,(\omega_n - 1)^2}\right]\right\}\end{aligned} \tag{4.6}$$

The reciprocal of (4.6) is the normalized input admittance $\dot{Y}_{T,n}$ of the circuit which equivalently can be considered as the normalized transmitting coil current. The normalized input admittance can be observed in Fig. 4.3, where it is plotted versus the normalized angular frequency for various quality factors (Fig. 4.3(a)) and for various coupling coefficients (Fig. 4.3(b)). It can be seen that both Q_R and k influence the input admittance. Furthermore, in the graphs it can be observed an interesting phenomenon called bifurcation [94] or pole-splitting [51]. In fact, when the quality factor moves from $Q_R = 1$ to $Q_R = 10$ (or the coupling coefficient shifts from $k = 0.10$ to $k = 0.30$), the resonant frequency that was centered at $\omega_n = 1$ for low quality factors (low coupling coefficients), splits into two. This is evident in the phase plots where the reactive part of the input admittance exhibits three zero crossings instead of just one.

Very often in WPTSs, the transmitting-side inverter is controlled not only by varying the phase-shift between the legs but also varying the switching frequency in the so called *dual control* [93]. Since it is very difficult to tune perfectly the system to the resonant frequency, a variable-frequency control adjusts the supply frequency to perform this task. The way the tuning is accomplished arises from the phase graphs of Fig. 4.3. Indeed, at $\omega_n = 1$ all the curves passes through zero. Hence, changing the supply frequency to maintain a Zero Phase Angle (ZPA) between the transmitting-side current and the fundamental of the inverter output voltage can be a good method for automatically tune the system. For such a control, the pole-splitting is undesired and this is because with bifurcation there are three possible frequencies where the phase of the input admittance is zero. It may happen that

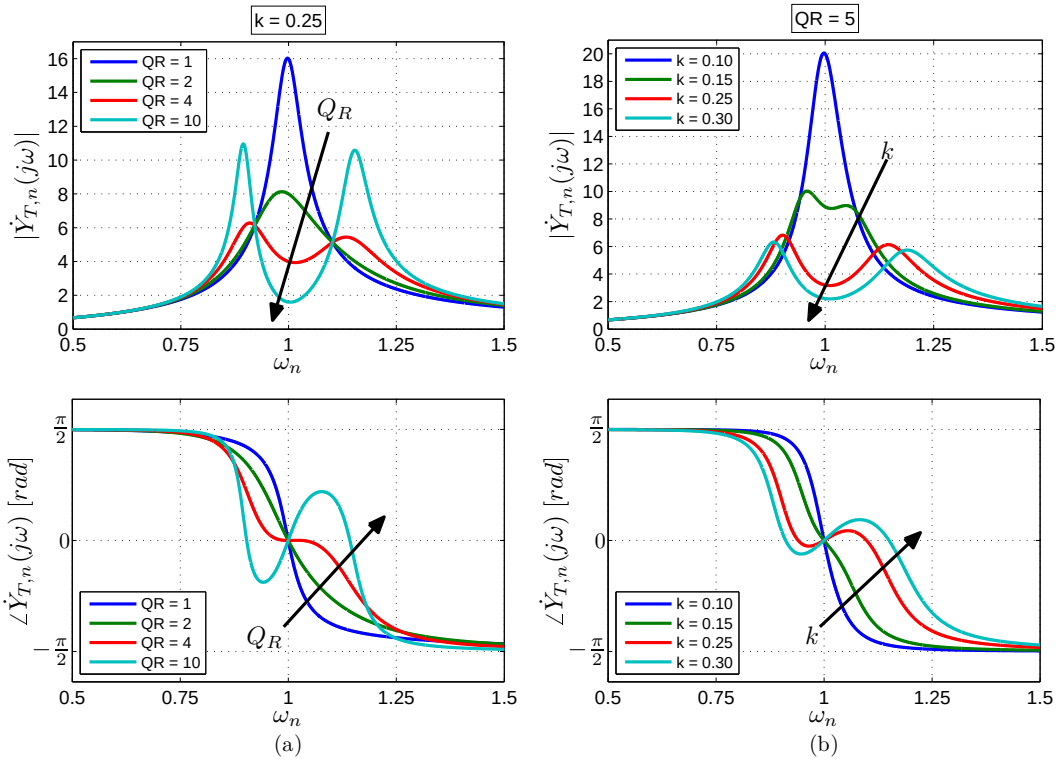

Fig. 4.3: Amplitude and phase of the normalized input admittance versus the normalized angular frequency for a SS WPTS. Figure (a) shows the curves with $k = 0.25$ and different Q_R, whereas figure (b) shows the curves with $Q_R = 5$ and different k.

the controller brings the system to work at a frequency different from $\omega_n = 1$ where the performance of the WPTS deviate from the ones for which the system is designed. For this reason it is very important to characterize the bifurcation to understand when it occurs.

For evaluating the frequencies at which the transmitting current is in phase with the inverter output voltage, it can be observed when the phase of the normalized input impedance becomes zero. The phase of the input impedance can be obtained from (4.6) and is given by:

$$\angle\dot{Z}_{T,n} = \arctan\left\{(\omega_n^2 - 1)\left[\frac{Q_R^2\,(1-k^2)\,\omega_n^4 + (1-2Q_R^2)\,\omega_n^2 + Q_R^2}{\omega_n^5 k^2 Q_R}\right]\right\} \tag{4.7}$$

The arctan(·) function is zero when its argument is zero. From (4.7), it is immediate to see that one of the frequencies that zeros the phase of the input impedance is just $\omega_n = 1$. When the SS WPTS is not operating under bifurcation, $\omega_n = 1$ is the only frequency that produces $\angle\dot{Z}_{T,n} = 0$. If the system bifurcates, the 4-th degree polynomial in ω_n which is the numerator of the rational function multiplied by $(\omega_n^2 - 1)$ in (4.7) has real roots. To study the roots of the bi-quartic polynomial it is convenient to replace ω_n with the variable u defined as $u = \omega_n^2$. The polynomial can be rewritten as:

$$n(u) = Q_R^2\,(1-k^2)\,u^2 + (1-2Q_R^2)\,u + Q_R^2 \tag{4.8}$$

The discriminant of (4.8) is given by:

$$\Delta = 4k^2\,Q_R^4 - 4Q_R^2 + 1 \tag{4.9}$$

When Δ is negative the roots of $n(u)$ and indirectly the ones of the original polynomial in ω_n are complex and the bifurcation is avoided. With some mathematical steps, it can be obtain that $\Delta < 0$ when:

$$Q_{R,1} < Q_R < Q_{R,2} \tag{4.10}$$

where

$$\begin{cases} Q_{R,1} = \frac{1}{2k}\left[\sqrt{1+k} - \sqrt{1-k}\right] \\ Q_{R,2} = \frac{1}{2k}\left[\sqrt{1+k} + \sqrt{1-k}\right] \end{cases} \tag{4.11}$$

Since in WPTS the coupling coefficient is small, the condition to have the discriminant (4.9) less than zero can be approximated as:

$$\frac{1}{2} < Q_R < \frac{1}{k} \tag{4.12}$$

When condition (4.12) is satisfied, the polynomial $n(u)$ in (4.8) does not have real roots. Consequently, the argument of the arctangent in (4.7) is zero only for $\omega_n = 1$. Condition (4.12) is too much restrictive. In fact, since $\omega_n = \sqrt{u}$, bifurcation does not occur even when the root of $n(u)$ are real but negative. The number of negative roots of the polynomial (4.8) can be assessed with the Descartes' rule of signs. Since $|k| < 1$ and $Q_R > 0$, the first and the third coefficient of the polynomial are always positive. Thus, if the second coefficient is also positive, since there are not sign variations, the roots of $n(u)$ (if real) are both negative. The second coefficient is positive when $Q_R < \frac{1}{\sqrt{2}}$ and so, by looking also at (4.12), when $Q_R < \frac{1}{2}$, the roots of $n(u)$ are negative. Then, the condition for the bifurcation avoidance can be extended in an approximated form as:

$$Q_R < \frac{1}{k} \tag{4.13}$$

It is easy to check the validity of this condition in the Fig. 4.3(a). The curve that corresponds to $Q_R = 4 = \frac{1}{k}$, in the phase plot is the curve that identifies the transition from the curves that have three zero-crossing to the curves with a single zero-crossing.

4.1.1 Resonant Condition: $\omega_n = 1$, $\alpha\beta = 1$

The inspection of the input admittance at the various supply frequencies has permitted to discover and define the bifurcation region. Usually, however, WPTSs are designed to work at the particular frequency that sets the transmitter and the receiver in resonance. This choice provides different benefits depending on the type of control that is implemented in the WPTS. If the transmitting-side current of a SS

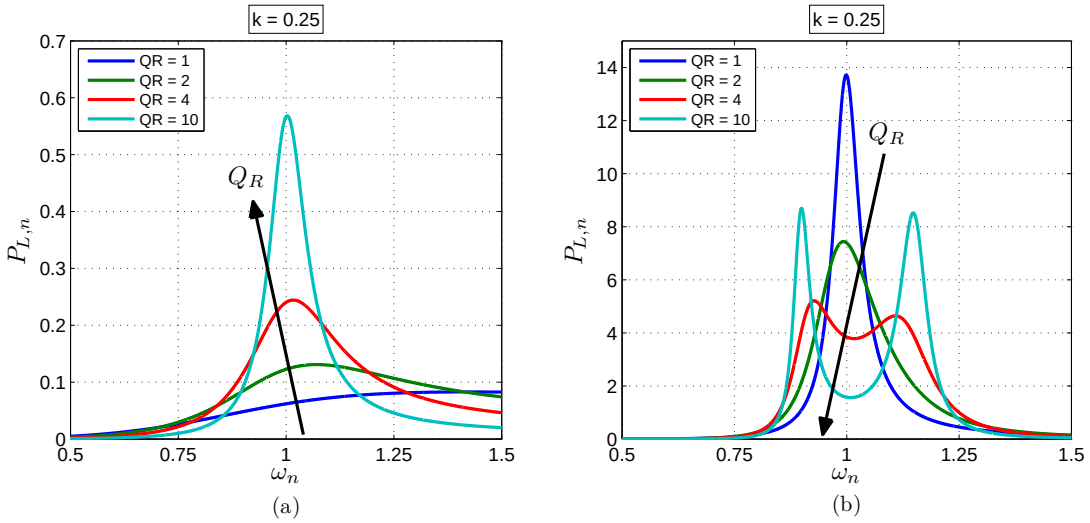

Fig. 4.4: Normalized output power of an SS-compensated WPTS with a constant transmitting-side current (a) and with a constant inverter output voltage (b) versus the normalized angular frequency.

WPTS is maintained constant, the profile of the load power versus the normalized angular frequency of the source can be seen in Fig. 4.4(a). The figure shows that, when the normalized transmitting-side current $\bar{I}_{T,n}$ is maintained constant and equal to 1, the load power of the SS WPTS is maximum at $\omega_n = 1$ (for the standard condition of having high value of Q_R). At this frequency, the less the load resistance R_L is, the higher is the power transferred. Thus, working at $\omega_n = 1$ permits the SS WPTS to deliver the maximum admissible power to the load (for a large load variation) and it permits the receiver to have the power characteristic typical of a voltage power supply.

A different situation arises when the inverter output voltage is maintained constant. In this case the frequency that allows the maximum power transfer is not always $\omega_n = 1$ (cf. Fig. 4.4(b)). Indeed, for high values of Q_R, the bifurcation phenomenon appears also in the power profile and the maximum power points are shifted slightly on the right and on the left with respect to the peak observable when Q_R is low. Nevertheless the best working point is still with the transmitter and the receiver in resonance. The reason for this choice comes from the efficiency plot. Whether the SS WPTS maintains a constant inverter output voltage or a constant transmitting coil current, the efficiency is the same and it is shown in Fig. 4.5 versus the normalized angular frequency[1]. It is easy to see that for high values of Q_R the maximum of the efficiency is obtained at $\omega_n = 1$.

Substantially, it is convenient to work with the transmitter and the receiver in resonance at the supply angular frequency $\omega_n = 1$ because it guarantees to transfer the power in the most efficient way for a broad range of loads. Furthermore, when a constant transmitting-side current is maintained, the choice $\omega_n = 1$ permits the

[1]To calculate the efficiency of the system (and also the powers of Fig. 4.4), the parasitic resistances of the coil have been added to the circuit of Fig. 4.2. The efficiency and the power profiles have been plotted considering the transmitting and the receiving coils with an identical quality factor of 200.

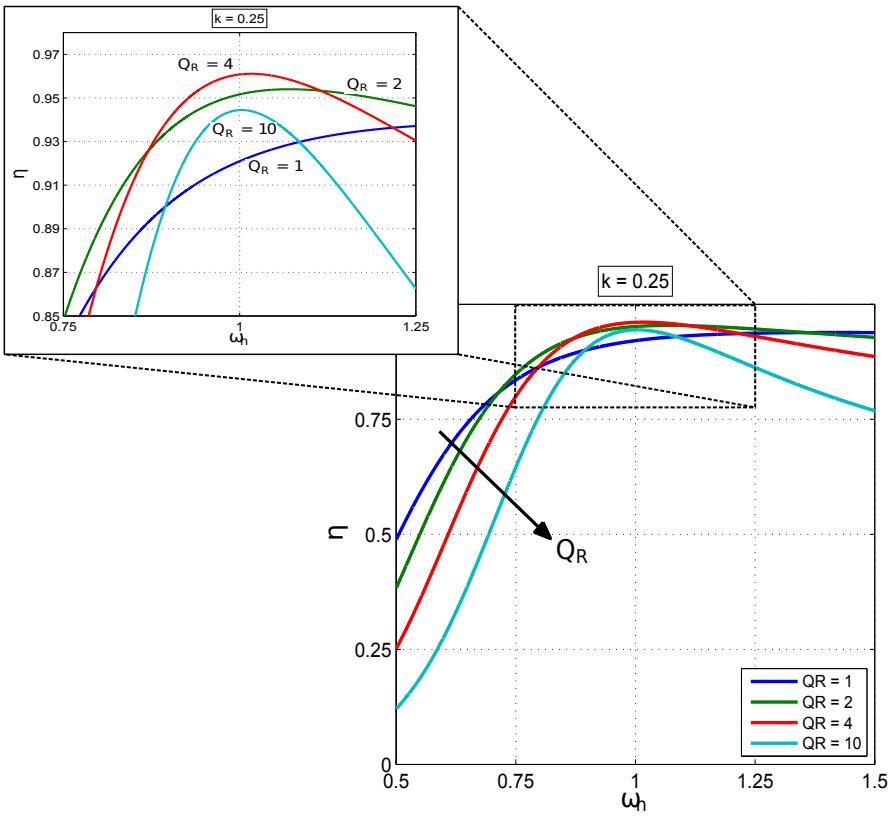

Fig. 4.5: Efficiency versus the normalized angular frequency of an SS-compensated WPTS. In the calculation of the efficiency two identical coil quality factors have been considered ($Q_{L,T} = Q_{L,R} = 200$).

WPTS to transfer the highest possible power. Therefore, it is useful to investigate the capabilities of the system at this particular frequency.

When $\omega_n = 1$, the reactive parts of both the transmitting and the receiving impedance become zero. For this reason, looking at the receiver side of Fig. 4.2, it can be stated immediately that $\dot{Z}_{R,n} = R_{L,n}$. The reflected impedance, under resonant conditions, is pure resistive and it is given by:

$$\dot{Z}_{ref,n} = R_{ref,n} = \frac{k^2\alpha}{R_{L,n}} \tag{4.14}$$

Since in the transmitting side the reactances of the inductance and of the capacitor cancel out, the normalized transmitting-side impedance is exactly equal to the reflected resistance. This permits the transmitting-side current to be found as:

$$\bar{I}_{T,n} = \frac{1}{\dot{Z}_{T,n}} = \frac{R_{L,n}}{k^2\alpha} = \frac{1}{k^2\,Q_R} \tag{4.15}$$

The normalized receiving-side induced voltage is given by:

$$\bar{E}_{R,n} = jk\sqrt{\alpha}\,\bar{I}_{T,n} = j\sqrt{\alpha}\,\frac{1}{k\,Q_R} \tag{4.16}$$

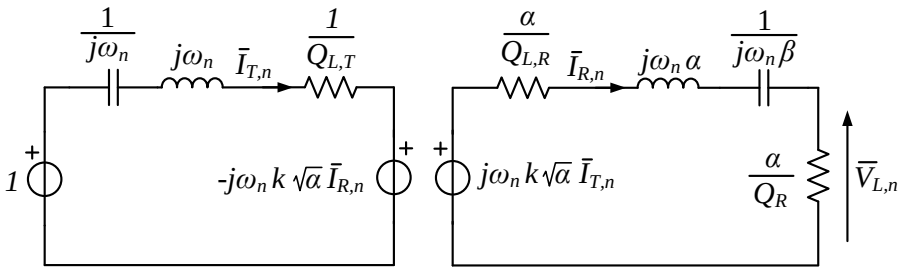

Fig. 4.6: Circuit for the calculation of the efficiency of an SS-compensated WPTS.

which, divided by the normalized load resistance, gives the normalized receiving-side current:

$$\bar{I}_{R,n} = \frac{\bar{E}_{R,n}}{\frac{\alpha}{Q_R}} = j\,\frac{1}{\sqrt{\alpha}}\,\frac{1}{k} \tag{4.17}$$

The normalized load voltage $\bar{V}_{L,n}$ coincides with $\bar{E}_{R,n}$ and its magnitude permits the voltage gain G_V of the SS WPTS to be found as:

$$G_V = \frac{V_{L,n}}{V_{s,n}} = V_{L,n} = \frac{\sqrt{\alpha}}{k\,Q_R} \tag{4.18}$$

It is easy to see that the voltage gain of the system depends on the load (depends on Q_R). A control system that wants to maintain the voltage on the load constant needs to change the inverter output voltage to cope with the load variations. With a constant coupling coefficient, if $V_{L,n}$ and consequently $E_{R,n}$ are controlled to be constant, the transmitting-side current remains constant (see the first equality of (4.16)). For this reason, a constant load voltage control falls within a constant transmitting-side current control.

The normalized load power that can be transferred with an SS-compensated WPTS is given by:

$$P_{L,n} = R_{L,n}\,I_{R,n}^2 = \frac{1}{k^2\,Q_R} \tag{4.19}$$

which is directly proportional to the load resistance $R_{L,n}$ and inversely proportional to the square of the coupling coefficient.

The same procedure employed in this section can be followed step by step to derive the relations for the real quantities of the circuit in Fig. 4.1. The various equations for the SS-compensated WPTS under resonant conditions are summarized in Tab. 4.1.

Another interesting thing to examine when the SS-compensated WPTS works in resonant conditions is the efficiency. To calculate the efficiency of the system, the circuit of Fig. 4.2 needs to be modified with the insertion of the normalized coil resistances. The resulting scheme is illustrated in Fig. 4.6[2].

[2]The circuit of Fig. 4.6 is the one employed for the derivation of the figures 4.4 and 4.5.

Tab. 4.1: Equations of the SS-compensated WPTS in resonant conditions.

Normalized	$\dot{Z}_{ref,n} = k^2\, Q_R$	(4.20)
	$\dot{Z}_{T,n} = k^2\, Q_R$	(4.21)
	$\bar{I}_{T,n} = \dfrac{1}{k^2\, Q_R}$	(4.22)
	$\bar{I}_{R,n} = j\, \dfrac{1}{\sqrt{\alpha}}\, \dfrac{1}{k}$	(4.23)
	$\bar{E}_{T,n} = 1$	(4.24)
	$\bar{E}_{R,n} = j\, \dfrac{\sqrt{\alpha}}{kQ_R}$	(4.25)
	$\bar{V}_{L,n} = j\, \dfrac{\sqrt{\alpha}}{kQ_R}$	(4.26)
	$G_V = \dfrac{\sqrt{\alpha}}{kQ_R}$	(4.27)
	$P_{L,n} = \dfrac{1}{k^2\, Q_R}$	(4.28)
Not Normalized	$\dot{Z}_{ref} = \dfrac{\omega_o^2 M^2}{R_L}$	(4.29)
	$\dot{Z}_T = \dfrac{\omega_o^2 M^2}{R_L}$	(4.30)
	$\bar{I}_T = \bar{V}_s\, \dfrac{R_L}{\omega_o^2 M^2}$	(4.31)
	$\bar{I}_R = j\, \dfrac{\bar{V}_s}{\omega_o M}$	(4.32)
	$\bar{E}_T = \bar{V}_s$	(4.33)
	$\bar{E}_R = j\, \bar{V}_s\, \dfrac{R_L}{\omega_o M}$	(4.34)
	$\bar{V}_L = j\, \bar{V}_s\, \dfrac{R_L}{\omega_o M}$	(4.35)
	$P_L = \dfrac{V_s^2}{\omega_o^2 M^2}\, R_L$	(4.36)

The efficiency of the system can be calculated with the following formula:

$$\eta = \frac{P_{L,n}}{P_{L,n} + P_{loss,n}} = \frac{1}{1 + \frac{P_{loss,n}}{P_{L,n}}} = \frac{1}{1+\lambda} \tag{4.37}$$

where $P_{loss,n}$ are the normalized power dissipated in the coil resistances and the quantity λ is the *loss factor* [51]. Since the losses of the system can be separated into the losses of the transmitter and the losses of receiver, the loss factor can be split as well. With the analysis of the circuit in Fig. 4.6 the loss factor of the receiver can be immediately found as:

$$\lambda_R = \frac{P_{loss,R,n}}{P_{L,n}} = \frac{\frac{\alpha}{Q_{L,R}} I_{R,n}^2}{\frac{\alpha}{Q_R} I_{R,n}^2} = \frac{Q_R}{Q_{L,R}} \tag{4.38}$$

To evaluate the losses of the transmitter with respect to the load power it is necessary to write the transmitting coil current in terms of receiving coil current. The resonance between the coil inductance and the capacitor in the receiving stage of the circuit in Fig. 4.6 allows us to write the following equality:

$$j\, k\sqrt{\alpha}\, \bar{I}_{T,n} = \left(\frac{\alpha}{Q_{L,R}} + \frac{\alpha}{Q_R} \right) \bar{I}_{R,n} \tag{4.39}$$

and consequently the normalized transmitting current is found to be:

$$\bar{I}_{T,n} = -j\, \frac{\sqrt{\alpha}}{k} \left(\frac{1}{Q_{L,R}} + \frac{1}{Q_R} \right) \bar{I}_{R,n} \tag{4.40}$$

The loss factor of the transmitter is given by:

$$\lambda_T = \frac{P_{loss,T,n}}{P_{L,n}} = \frac{\frac{1}{Q_{L,T}} I_{T,n}^2}{\frac{\alpha}{Q_R} I_{R,n}^2} = \frac{Q_R}{Q_{L,T}} \frac{1}{k^2} \left(\frac{1}{Q_{L,R}} + \frac{1}{Q_R} \right)^2 \tag{4.41}$$

where (4.40) has been used to calculate $I_{T,n}$.

The sum of (4.38) and (4.41) gives the total loss factor which can be written as:

$$\lambda = \lambda_T + \lambda_R = \frac{Q_R}{Q_{L,T}} \frac{1}{k^2} \left(\frac{1}{Q_{L,R}} + \frac{1}{Q_R} \right)^2 + \frac{Q_R}{Q_{L,R}} \tag{4.42}$$

It can be noticed from (4.42) that λ depends on the load quality factor. The total loss factor is minimum for

$$Q_R = \frac{Q_{L,R}}{\sqrt{1 + k^2\, Q_{L,T} Q_{L,R}}} \tag{4.43}$$

when it is equal to

$$\lambda_{min} = \frac{2}{k^2\, Q_{L,T} Q_{L,R}} \left(\sqrt{1 + k^2\, Q_{L,T} Q_{L,R}} + 1 \right) \tag{4.44}$$

Since with well-designed coils is not difficult to achieve coil quality factors greater than 200 at 85 kHz [39], usually $k^2\, Q_{L,T} Q_{L,R}$ is much greater than 1 and the previous expressions can be approximated. The minimum loss factor becomes:

$$\lambda_{min} \approx \frac{2}{k\sqrt{Q_{L,T}Q_{L,R}}} \tag{4.45}$$

which is found when the approximated quality factor is:

$$Q_R \approx \frac{1}{k}\sqrt{\frac{Q_{L,R}}{Q_{L,T}}} \tag{4.46}$$

It is interesting to see that equations (4.46) and (4.45) are identical to (3.88) and (3.89) derived in the previous chapter with a general method.

According to (4.37) and using (4.45), the maximum efficiency can be approximated in the form:

$$\eta_{max} \approx \frac{1}{1+\frac{2}{k\sqrt{Q_{L,T}\,Q_{L,R}}}} \tag{4.47}$$

The above equations can be used to better understand the plot of Fig. 4.5. That graph shows the efficiency of a SS-compensated WPTS with two equal quality factors for the transmitting and the receiving coil. It is easy to ascertain that the maximum efficiency is achieve when $Q_R = 4 = \frac{1}{k}$ (cf. (4.46)). Substituting $Q_{L,T} = Q_{L,R} = 200$ in (4.47) with the coupling coefficient $k = 0.25$, the maximum efficiency is found to be about 96%.

4.1.2 Design Procedure

The design of a WPTS consists in finding the values for the components that provide the desired performance to the system. For an SS-compensated WPTS the design task is fulfilled when the values of the coil inductances and of the resonant capacitors are found. In this section it will be illustrated a simple (and not comprehensive) way that can be used as a starting point to design the system. A detailed design procedure can be found in [50].

The design of a WPTS starts from the following specifications:

- P_{Nom} nominal power that has to be transferred;
- V_{DC} voltage of the dc bus at the input of the transmitting-side inverter;
- V_o voltage of the dc bus at the output of the receiving-side rectifier[3];
- ω working angular frequency;
- k_{Nom} nominal coupling coefficient.

The nominal power P_{Nom} and the voltage V_o come from the battery characteristics, whereas V_{DC} is defined by the PFC design. The working angular frequency nowadays is a standard established by SAE and fixed to 85 kHz. The nominal coupling coefficient k_{Nom} is set to a feasible value which for a WPTS ranges from 0.1 to

[3]In this design procedure the voltage at the output of the receiving-side rectifier is considered constant because it is controlled by adjusting the inverter output voltage.

0.3. Once the values for the coils inductances have been acquired from the design process, their magnetic design can start. It consists in finding the coils geometries and parameters that permit the designer to obtain inductance values closer to the ones achieved in the previous design step. This design phase is usually carried out with the aid of FEM codes which can be used, among other things, to calculate the coupling coefficient between the coils. Then, the value of the coupling coefficient obtained via software can be compared with the hypothetical k_{Nom} set as starting point. If the two values are similar the design procedure can be considered completed, otherwise the new value for k can be used as a new starting point to redo step by step the design. Such an iterative process is quite common while designing WPTSs.

From the specifications listed above some others quantities can be immediately found. The nominal equivalent resistance at the rectifier input terminals is:

$$R_{L,Nom} = \frac{8}{\pi^2}\frac{V_o^2}{P_{Nom}} \tag{4.48}$$

Since usually P_{Nom} coincides with the maximum power that has to be transmitted, the nominal resistance $R_{L,Nom}$ is also the minimum load resistance.

Using (2.52), the rms of the fundamental of the inverter output voltage can be written in terms of V_{DC} as:

$$V_{s,Nom} = \frac{2\sqrt{2}}{\pi}V_{DC}\sin\left(\frac{\alpha_{Nom}}{2}\right) \tag{4.49}$$

where the nominal phase-shift angle α_{Nom} is a degree of freedom of the design. It can be chosen equal to π to guarantee a large ZVS region for the inverter switches (cf. Sec. 2.5.1) and the maximum controllability of the system. In fact, in nominal conditions the inverter phase-shift angle is at its maximum and it is reduced in partial load conditions. If $\alpha_{Nom} = \pi$, it means that for a fixed V_{DC} the rms of the inverter output voltage can be set within the largest possible range. Another interesting choice for α_{Nom} is $\frac{2}{3}\pi$ that permits the harmonic content of the inverter output voltage to be reduced [100].

Let us choose $\alpha_{Nom} = \pi$. With this choice, it is easy to obtain the voltage gain of the ac stage from the specifications:

$$G_{V,Spec} = \frac{V_L}{V_{s,Nom}} = \frac{\frac{2\sqrt{2}}{\pi}V_o}{\frac{2\sqrt{2}}{\pi}V_{DC}} = \frac{V_o}{V_{DC}} \tag{4.50}$$

where the rectifier input voltage V_L has been calculated according to (2.47). The inherent voltage gain of the system is given by (4.27) which in nominal conditions is:

$$G_{V,Nom} = \frac{\sqrt{\alpha}}{k_{Nom}\,Q_{R,Nom}}^{4} \tag{4.51}$$

[4] In this formula α is the ratio between the inductances L_R and L_T and it does not have to be confused with the phase-shift angle.

With the assumption of having $Q_{L,T} = Q_{L,R}$, namely to be able to design coils with the same quality factor, the relation (4.46) to achieve the maximum efficiency when the system is working in nominal conditions becomes:

$$Q_{R,Nom} \approx \frac{1}{k_{Nom}} \tag{4.52}$$

Relation (4.52) can be used in (4.51) and the nominal voltage gain of the SS WPTS can be written as:

$$G_{V,Nom} = \sqrt{\alpha} = \sqrt{\frac{L_R}{L_T}} \tag{4.53}$$

By equating (4.53) and (4.50), a relation for the coil inductances is obtained:

$$L_T = L_R \left(\frac{V_{DC}}{V_o}\right)^2 \tag{4.54}$$

The receiving-side inductance can be obtained from (4.52) using the definition of the receiving-side quality factor:

$$L_R = \frac{R_{L,Nom}}{\omega\, k_{Nom}} \tag{4.55}$$

The value for the transmitting-side inductance can be easily attained from (4.54). According to this equation, when the dc-bus voltage of the transmitting side and dc-bus voltage of the receiving side are much different, the two inductances can have very different values as well. To decrease this mismatch, one can decide to choose either a small nominal phase-shift angle, loosing the ZVS of the first leg of the inverter, or an higher value for $Q_{R,Nom}$, accepting a lower efficiency. However, as stated in Ch. 3, the quality factor of the receiving stage cannot be too high to limit the receiving coil rating and to permit an easy tuning of the receiver. Practically, the receiving-side quality factor can be restricted to values less than 10.

So far, the values of the coil inductances have been assigned. It remains to define the values for the resonant capacitors. Since it has been proved that the best design is achieved when both the transmitter and the receiver are in resonance, the transmitting-side and the receiving-side capacitors can be obtained with the following formula:

$$C_i = \frac{1}{\omega_o^2 L_i} \tag{4.56}$$

where ω_o is the resonant frequency of the system which is equal to ω that comes from the specifications. The index $i = T, R$ is used to indicate transmitter and receiver, respectively.

To select the proper components it is necessary to know also the voltage and/or current ratings. The equations of Tab. 4.1 can be used for this task bearing in mind that to have a constant voltage V_o, a variable inverter output voltage is needed. The inverter output voltage that maintains the output voltage constant can be calculated from (4.35) and it is found to be:

$$\bar{V}_s = -j\,\frac{\omega_o M}{R_L}\,\frac{2\sqrt{2}}{\pi}V_o \tag{4.57}$$

In (4.57), the phasor $\bar{V}_L = \frac{2\sqrt{2}}{\pi}V_o$ has been used as reference for the phases. Substituting (4.57) into (4.31) and (4.32) the current ratings for the coils and the capacitors are found to be:

$$I_T = \frac{2\sqrt{2}}{\pi}V_o\frac{1}{\omega_o M} = \frac{2\sqrt{2}}{\pi}V_o\frac{1}{\omega_o k\sqrt{L_T L_R}} \tag{4.58}$$

$$I_R = \frac{2\sqrt{2}}{\pi}\frac{V_o}{R_L} \tag{4.59}$$

It is worth to note that the transmitting current is inversely proportional to the coupling coefficient k. The transmitting-side coil and the transmitting-side capacitor have to be rated for a current calculated with $k = k_{min}$, corresponding to the minimum admissible coupling coefficient. The receiving-side current is inversely proportional to the load resistance. Since the nominal load resistance is also the smallest one, the maximum receiving-side current is also the nominal one. Thus, the rated current for the receiving-side components corresponds to the nominal current.

From (4.58) and (4.59), the voltage rating for the transmitting-side and the receiving-side capacitors can be derived:

$$V_{CT} = \frac{1}{\omega_o C_T}I_T = \omega_o L_T I_T = \frac{2\sqrt{2}}{\pi}V_o\frac{1}{k}\sqrt{\frac{L_T}{L_R}} \tag{4.60}$$

$$V_{CR} = \frac{1}{\omega_o C_R}I_R = \omega_o L_R I_R = \frac{2\sqrt{2}}{\pi}V_o\frac{\omega_o L_R}{R_L} \tag{4.61}$$

With the analysis of the circuit in Fig. 4.1 and the above equations, the voltage ratings for the coils can be obtained as follows:

$$V_T = \frac{2\sqrt{2}}{\pi}\frac{V_o}{k}\sqrt{\frac{L_T}{L_R}}\sqrt{1 + k^4\frac{\omega_o^2 L_R^2}{R_L^2}} \tag{4.62}$$

$$V_R = \frac{2\sqrt{2}}{\pi}V_o\sqrt{1 + \frac{\omega_o^2 L_R^2}{R_L^2}} \tag{4.63}$$

Considering that k is low and the maximum voltage across the coil is achieved with $R_{L,Nom}$, equations (4.62) and (4.63) can be approximated with:

$$V_T \approx \frac{2\sqrt{2}}{\pi}\sqrt{\frac{L_T}{L_R}}\frac{V_o}{k} \tag{4.64}$$

$$V_R \approx \frac{2\sqrt{2}}{\pi}V_o\frac{\omega_o L_R}{R_L} \tag{4.65}$$

The ratio between the product of the transmitting coil rated current and voltage and the product of the receiving coil rated current and voltage ($\frac{V_T I_T}{V_R I_R}$) can be used to prove (3.85).

4.2 LC-Compensated Transmitter in WPTSs

One of the major drawback of the SS compensation for the WPTSs is that the transmitting coil current depends on both the load and the coupling coefficient (cf. (4.31)). It has been shown that to maintain the receiving-side dc-bus voltage constant it is necessary to control the transmitting-side current to be almost constant. Even though the coupling coefficient is nonfluctuating, to fulfill this task it is necessary to rely on a control system that acts on the inverter output voltage, since the load resistance varies a lot during the charging stage.

This shortcoming is exacerbated in applications such as dynamic charging where the coupling coefficient is anything but constant. Here, the current source characteristic of the transmitting side is desirable not only for achieving a constant receiving-side dc-bus voltage but also to guarantee the same power transfer capability for each pickups that are traveling over the track. Even if some researchers employed SS compensation in dynamic WPTSs [22], [63], this topology makes the control of the system challenging. The reason for that is because the SS compensation does not have an intrinsic transmitting-side constant current.

An alternative solution to the SS compensation arises for example from the employment of the parallel compensation in the transmitting side [19], [94]. In Sec. 3.2, it has been demonstrated the current source capability of the parallel compensation, whether it is utilized in either the transmitting or in the receiving side. However, it has been also shown that the phase angle of the input impedance of the circuit where this compensation topology is used is not zero and in general depends on the load (cf. (3.41)). When the parallel compensation is employed in the transmitting side, the input impedance of the system is affected also by the coupling coefficient and so it is difficult to design the system for achieving a large ZVS zone for the inverter[5].

To meet the requirements of having a constant transmitting current and a ZPA of the input impedance, researchers from Auckland introduced what they have called LCL compensation [28]. In [28], an LC network is connected in between the inverter output terminals and the transmitting coil to form an LCL circuit. Given the advantages brought by this topology, numerous others research contributions that study the LC compensation and its variants have proliferated, especially in the dynamic battery charging field [32], [62], [86], [101], [102].

In Sec. 3.3, the operation of the LCL circuit has been presented in a general way, but with an analysis mainly oriented at the receiving-side compensation. Indeed, a pure resistive load of the circuit has been considered, which has been envisaged as the equivalent receiving-side rectifier input resistance. When the LC compensation is used in the transmitting side the load connected to the LCL circuit (formed by

[5] In addition to the disadvantage caused by the difficult to achieve a ZPA of the input impedance, the parallel compensation is inadvisable because it requires to be supplied with a current-fed inverter.

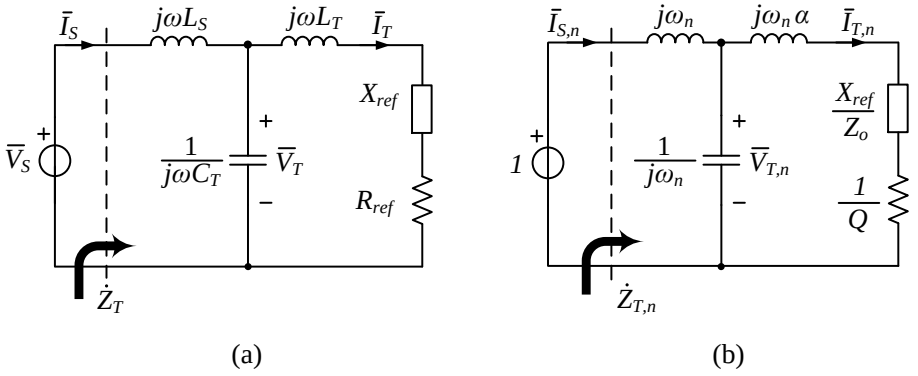

Fig. 4.7: Transmitting-side circuit of a WPTS with an LC compensation (a) and its normalized version (b).

the LC network and the transmitting coil) is the reflected impedance. Even though the receiver is perfectly tuned, the reflected impedance is not always constituted only by the resistive part. For this reason, to understand the behaviors of the LC compensating network in the transmitting side it is necessary to study the circuit in Fig. 4.7, where the load is represented by a generic impedance $\dot{Z}_{ref} = R_{ref} + j\, X_{ref}$.

In the circuit of Fig. 4.7(a) the phasors of the real quantities are involved, whereas the circuit of Fig. 4.7(b) is used to find the relations between the normalized phasors. The rules that allow the normalized circuit to be obtained are analogous to the ones utilized in the previous section. The parameters introduced here are:

- $\alpha = \frac{L_T}{L_s}$ ratio between the transmitting-side and the inverter-side inductances;
- $\omega_o = \frac{1}{\sqrt{L_s C_T}}$ resonant frequency of the transmitter;
- $\omega_n = \frac{\omega}{\omega_o}$ normalized angular frequency;
- $Z_o = \omega_o L_s$ characteristic impedance of the transmitting-side circuit;
- $Q = \frac{Z_o}{R_{ref}}$ quality factor of the transmitting-side circuit.

and the base quantities for the normalization process are:

- $V_b = V_s$
- $Z_b = Z_o$
- $I_b = \frac{V_b}{Z_b}$
- $P_b = \frac{V_b^2}{Z_b}$

From the analysis of the circuit in Fig. 4.7(b) the normalized transmitting current $\bar{I}_{T,n}$ is found to be:

$$I_{T,n} = \frac{1}{\frac{1}{Q}\left(1-\omega_n^2\right) + j\,\omega_n\left[1+\alpha\left(1+\frac{X_{ref}}{\alpha\,\omega_n Z_o}\right)\left(1-\omega_n^2\right)\right]} \tag{4.66}$$

It is easy to see that when $\omega_n = 1$ the normalized transmitting-side current becomes independent from Q (it does not depend on R_{ref}) and it can be written as:

$$I_{T,n} = -j \tag{4.67}$$

Equation (4.67) shows that when the inverter-side inductance resonates with the capacitor C_T ($\omega_n = 1$), the transmitting coil current is constant against the variations of R_{ref} and this is valid for every value of the reflected reactance X_{ref}. In other words, equation (4.67) proves that the current source behavior provided to the transmitting side by the LC network is always achieved irrespective of the reflected impedance. Although X_{ref} does not have any influence on the transmitting coil current, it affects the inverter-side current and consequently the input impedance. For instance, its angle is given by:

$$\angle\dot{Z}_{T,n} = \angle\dot{Z}_T = \arctan\left\{Q\left(1-\alpha\right) + Q\,\frac{X_{ref}}{Z_o}\right\} \tag{4.68}$$

Even when the inverter-side inductance and the transmitting coil inductance are equal ($\alpha = 1$), the angle of the input impedance does not becomes zero, as it would happen if the reflected impedance were pure resistive. If the reflected impedance is well-known and does not change during the WPTS operation it is possible to choose α in order to maintain the inverter output current in phase with the fundamental of the inverter output voltage. However, usually, $\dot{Z}_{ref}$ depends on the load resistance and on the coupling coefficient and a variable α is needed to have $\angle\dot{Z}_T = 0$. The solution of changing either L_T or L_s during the WPTS operation seems unfeasible and thus the ZPA cannot be guaranteed when the reflected impedance comprises also a reactive part.

The formulae for the other quantities of both Fig. 4.7(a) and Fig. 4.7(b) can be found in appendix A under the section A.2.

4.2.1 LC-Series WPTS

When an LC-compensated transmitter is coupled with a series-compensated receiver, it gives rise to the LC-Series WPTS. This solution provides the good features expected from the LC compensation in the transmitting side, while keeping the receiver compensation as simple as possible[6]. It is worth remembering that the receiver has to be installed on-board the EV and so simplicity and small size are two favorable things.

[6]Another simple solution is the LCL-parallel WPTS which has been studied in Sec. A.2. A thorough analysis that compares the two topologies can be done to assess the best solution. This analysis though, is beyond the scope of this thesis.

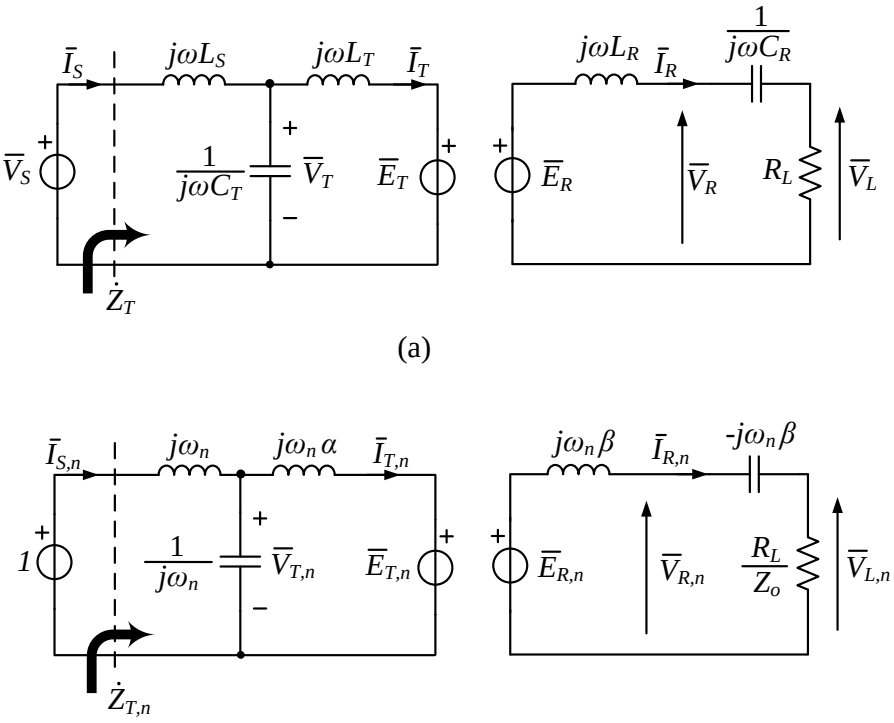

Fig. 4.8: Circuits for the analysis of the LC-Series WPTS under steady-state with normal (a) and normalized (b) quantities.

The circuits for the analysis of the LC-Series WPTS under steady-state with both normal and normalized quantities are shown in Fig. 4.8. For the normalized circuit of Fig. 4.8(b), the same parameters and the same base quantities employed in the derivation of the normalized circuit 4.7(b) have been used. In addition here, the parameter $\beta = \frac{L_R}{L_s}$ is introduced. The normalized circuit refers to a situation where the receiver is always in resonance[7]. When the receiver is perfectly tuned, the impedance reflected towards the transmitting side $\dot{Z}_{ref}$ is a resistance as it happens with the SS compensation. For the above considerations, with the LC-Series compensation it is possible to have a ZPA of the input impedance for every load and coupling condition (cf. (4.68)). The ZVS of the transmitting-side inverter can be attained when the transmitter is in resonance ($\omega_n = 1$) and simultaneously the transmitting coil inductance and the inverter-side inductance are equal ($\alpha = 1$).

A general analysis of the LC-Series WPTS has been carried out in appendix A. Using the results found in A.1 for $\omega_n = 1$ (or equivalently for $\omega = \omega_o$ in case of normal quantities) and substituting the condition $\alpha = 1$, the desired equations are obtained. They are collected in Tab. 4.2, where in all the equations, the quality factor of the receiving circuit $Q_R = \frac{\omega_o L_R}{R_L}$ is highlighted. It can be demonstrated

[7] To achieve this result the receiving-side capacitor C_R needs to be adjusted for each considered angular frequency of the voltage source. This is not a practical solution but it is just a theoretical way to simplify the analysis considering the receiver perfectly tuned.

that in resonant condition and with $\alpha = 1$, the receiving-side quality factor Q_R can be related to the transmitting-side quality factor $Q = \frac{Z_o}{R_{ref}}$ through the following equation:

$$Q_R = \frac{1}{k^2 Q} \tag{4.69}$$

From the analysis of the LC-Series WPTS some interesting considerations can be done:

1. as expected the transmitting coil current is constant irrespective of the load and the coupling coefficient (cf. (4.81));
2. the inverter output current i_s is in phase with the fundamental of the inverter output voltage (cf. (4.80));
3. because of the resonance in the series-compensated receiver, the voltage across the load is equal to the voltage induced into the receiving coil. For this reason, the amplitude of the phasor $\bar{E}_{R,n}$ in (4.75) coincides with the voltage gain of the system. Equation (4.75) shows that for an LC-Series WPTS the voltage gain does not depend on the load.

The advantages brought by the introduction of the LC compensation in place of the series compensation are clear. However, it is necessary to better understand how much is the efficiency reduction caused by the addition of a second inductor. The circuit that allows the efficiency of an LC-Series WPTS to be evaluated is shown in Fig. 4.9. It is build under the hypothesis of having the inverter-side inductance equivalent to the transmitting coil inductance. Furthermore, the coil quality factors for the three inductances are considered the same and equal to Q_L.

To derive an equation for the efficiency of the circuit, it is possible to proceed as for the SS WPTS calculating the loss factor $\lambda = \frac{P_{loss,n}}{P_{L,n}}$. Again, it is convenient to separate the loss factor into three contributions associated to the three sources of losses. The losses caused by the parasitic resistances of the transmitting and the receiving coils are the same as for Series-Series and their related loss factor can be written as in 4.41 and in 4.38, respectively[8]. An additional term contributes to the total loss factor of the LC-Series WPTS and it is λ_s associated to the losses in the parasitic resistance of the inductance L_s. To find it, it is useful to express $\bar{I}_{s,n}$ in terms of $\bar{I}_{R,n}$. From the circuit of Fig. 4.9(b), it is easy to derive the equation:

$$\bar{I}_{s,n} = j \left(R_{ref,n} + \frac{1}{Q_L} \right) \bar{I}_{T,n} \tag{4.88}$$

which links the phasor of the normalized inverter output current to the phasor of the normalized transmitting coil current. With the aid of the circuit of Fig. 4.9(a), the normalized transmitting coil current can be related to the normalized receiving coil current with a relation similar to (4.40):

$$\bar{I}_{T,n} = -j \frac{\sqrt{\beta}}{k} \left(\frac{1}{Q_L} + \frac{1}{Q_R} \right) \bar{I}_{R,n} \tag{4.89}$$

[8]The notation Q_L in place of $Q_{L,T}$ and $Q_{L,R}$ should be used.

Tab. 4.2: Equations of the LC-Series WPTS in resonant conditions and with $\alpha = 1$.

Normalized	$\dot{Z}_{T,n} = \dfrac{1}{k^2 Q_R}$	(4.70)
	$\bar{I}_{s,n} = k^2 Q_R$	(4.71)
	$\bar{I}_{T,n} = -j$	(4.72)
	$\bar{I}_{R,n} = \dfrac{1}{\sqrt{\beta}}\, k Q_R$	(4.73)
	$\bar{E}_{T,n} = -j\, k^2 Q_R$	(4.74)
	$\bar{E}_{R,n} = k\sqrt{\beta}$	(4.75)
	$\bar{V}_{T,n} = 1 - j\, k^2 Q_R$	(4.76)
	$\bar{V}_{R,n} = k\sqrt{\beta}\,(1 - j\, Q_R)$	(4.77)
	$P_{L,n} = k^2 Q_R$	(4.78)
Not Normalized	$\dot{Z}_T = \dfrac{R_L}{k^2 \beta}$	(4.79)
	$\bar{I}_s = \bar{V}_s \dfrac{k^2 \beta}{R_L}$	(4.80)
	$\bar{I}_T = \dfrac{\bar{V}_s}{j\omega_o L_s}$	(4.81)
	$\bar{I}_R = \dfrac{\bar{V}_s}{R_L}\, k\sqrt{\beta}$	(4.82)
	$\bar{E}_T = -j\, \bar{V}_s\, k^2 Q_R$	(4.83)
	$\bar{E}_R = \bar{V}_s\, k\sqrt{\beta}$	(4.84)
	$\bar{V}_T = \bar{V}_s\,(1 - j\, k^2 Q_R)$	(4.85)
	$\bar{V}_R = \bar{V}_s\, k\sqrt{\beta}\,(1 - j\, Q_R)$	(4.86)
	$P_L = \dfrac{V_s^2}{R_L}\, k^2 \beta$	(4.87)

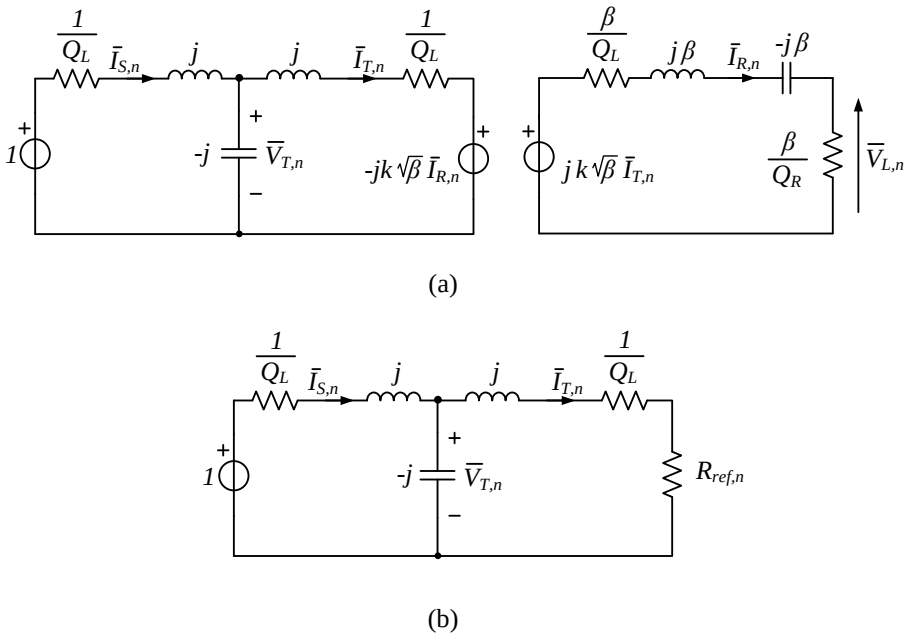

Fig. 4.9: Normalized circuit of an LC-Series WPTS used for the efficiency calculation (a). Its equivalent transmitting-side circuit (b).

Combining (4.88) and (4.89), the inverter-side current can be written in terms of receiving-side current and it is given by:

$$\begin{aligned}\bar{I}_{s,n} &= \left(R_{ref,n} + \frac{1}{Q_L}\right)\frac{\sqrt{\beta}}{k}\left(\frac{1}{Q_L}+\frac{1}{Q_R}\right)\bar{I}_{R,n} \\ &= \frac{\sqrt{\beta}}{k}\left[k^2 + \frac{1}{Q_L}\left(\frac{1}{Q_L}+\frac{1}{Q_R}\right)\right]\bar{I}_{R,n}\end{aligned} \tag{4.90}$$

where in the last equation the normalized reflected resistance has been replaced with its definition:

$$R_{ref,n} = \frac{k^2}{\left(\frac{1}{Q_L}+\frac{1}{Q_R}\right)} \tag{4.91}$$

Using (4.90), the loss factor λ_s is found to be:

$$\lambda_s = \frac{P_{loss,s,n}}{P_{L,n}} = \frac{\frac{1}{Q_L} I_{s,n}^2}{\frac{\beta}{Q_R} I_{R,n}^2} = \frac{Q_R}{Q_L}\frac{1}{k^2}\left[k^2 + \frac{1}{Q_L}\left(\frac{1}{Q_L}+\frac{1}{Q_R}\right)\right]^2 \tag{4.92}$$

and thus the total loss factor is given by:

$$\lambda = \lambda_R + \lambda_T + \lambda_s = \frac{Q_R}{Q_L}\left\{1 + \frac{1}{k^2}\left(\frac{1}{Q_L}+\frac{1}{Q_R}\right)^2 + \frac{1}{k^2}\left[k^2 + \frac{1}{Q_L}\left(\frac{1}{Q_L}+\frac{1}{Q_R}\right)\right]^2\right\} \tag{4.93}$$

Since Q_L is much greater than Q_R, equation (4.93) can be approximated as follows:

$$\lambda \approx \frac{Q_R}{Q_L}\left(1+\frac{1}{k^2Q_R^2}+k^2+\frac{2}{Q_LQ_R}\right) \tag{4.94}$$

It is easy to prove that when the receiving-side quality factor Q_R is equal to

$$Q_R = \frac{1}{k\sqrt{1+k^2}} \tag{4.95}$$

the loss factor is minimum and roughly equal to:

$$\lambda_{min} = \frac{2}{kQ_L}\left(\sqrt{1+k^2}+\frac{k}{Q_L}\right) \approx \frac{2}{kQ_L}\sqrt{1+k^2} \tag{4.96}$$

A comparison between (4.96) and (4.45) allows us to see that the minimum loss factor of the LC-Series WPTS differs by a factor $\sqrt{1+k^2}$ with respect to the minimum loss factor of a SS WPTS. Since $k \ll 1$, the loss factors of the two systems are almost the same. So, the introduction of the LC network in the transmitting side gives the above mentioned benefits to the system, without impairing the overall efficiency.

Design Procedure

The simple design procedure that will be presented in this section has the scope of giving a rough idea on how to define the parameters of an LC-Series dynamic WPTS.

In a dynamic WPTS the coupling coefficient varies a lot with the EV motion [103]. For this reason the coupling coefficient profile along the EV moving direction has a key role in the WPTS design. The profile of the coupling coefficient considered in this section is illustrated in Fig. 4.10. This trapezoidal shape can be considered as an approximation of the coupling coefficient profiles achieved in [13], [104]. They are obtained with a lumped track structure but placing the track coils very close one each other. In this situation, if the car moves straight on without a lateral misalignment, the coupling coefficient maintains the maximum allowable value k_{max} for a long time during the EV travel. The track coils can be energized immediately before the can arrival, in a sequential way[9].

The specifications from which the design process has to start can be given as follows:

- P_{Nom} nominal power required by the battery;
- V_{DC} voltage of the dc bus at the input of the transmitting-side inverter;
- $V_o = [V_{o,min}, V_{o,max}]$ dc/dc converter admissible input voltage range;

[9] A coupling coefficient profile similar to the one in Fig. 4.10 is shown in [105]. Here the authors achieve that profile of coupling for each coil of the track that are considered sufficiently far away not to interact each other. For this reason, the coupling coefficient remains at its maximum for a smaller amount of time, thus producing a pulsating transferred power. Such kind of systems require a design procedure more accurate than the one presented here.

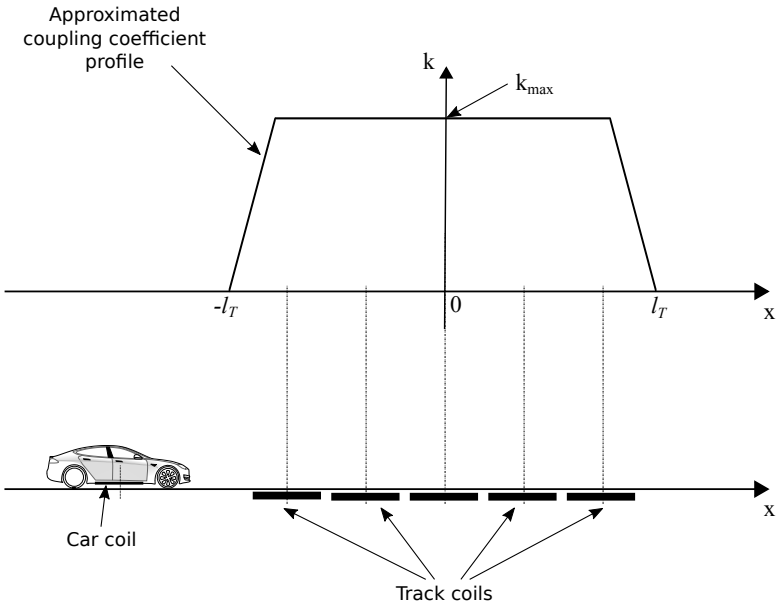

Fig. 4.10: Coupling coefficient profile along the EV moving direction.

- k_{max} maximum achievable coupling coefficient.

The coupling coefficient profile of Fig. 4.10 is an ideal profile. In fact, it is very difficult for a driver who is traveling at a medium speed to maintain the car carefully aligned to follow an ideal trajectory. If the system is designed to transfer the nominal power P_{Nom} when the coupling coefficient is k_{max}, as soon as the EV deviates from the ideal trajectory the output power reduces. It is more feasible to accept a certain amount of misalignment and design the system so that it is able to transfer the nominal power when $k = k_{min}$. It will be a task of the dc/dc converter downstream the rectifier to control the power to coincide with the actual battery demand even when the coupling coefficient is different from the one used to design the WPTS.

Since the LC network fed by a fixed inverter output voltage $V_s = \frac{2\sqrt{2}}{\pi} V_{DC}$ produces a constant track current, the induced receiving-side voltage and consequently the load voltage V_L is proportional to k (cf. (4.84)). The load voltage is proportional to the rectifier output voltage which coincides with the dc/dc converter input voltage. For this reason, the ratio between the maximum and the minimum voltage at the input of the dc/dc converter is equal to $\frac{k_{max}}{k_{min}}$. This fact can be considered for defining the minimum admissible coupling coefficient from the dc/dc converter input voltage range specification. This specification depends not only on the nominal voltage of the battery but also on the type of dc/dc converter. If the dc/dc converter is a step-down converter it is necessary to have $V_{o,min}$ greater or equal than the maximum battery voltage. To permit the proper operation of the dc/dc converter if it is a step-up converter, it is necessary to have $V_{o,max}$ less or equal than the minimum battery voltage.

The specification on the minimum admissible voltage at the input of the dc/dc converter can be used to find the value of β. In fact, from $V_{o,min}$ it is easy to find

the minimum rms value for the voltage at the rectifier input that is given by:

$$V_{L,min} = \frac{2\sqrt{2}}{\pi} V_{o,min} \tag{4.97}$$

Equating (4.97) and (4.84), we can write:

$$\begin{gathered} V_s\, k_{min} \sqrt{\beta} = V_{L,min} \\ \Downarrow \\ \beta = \frac{L_R}{L_T} = \left(\frac{V_{L,min}}{V_s}\right)^2 \frac{1}{k_{min}^2} \end{gathered} \tag{4.98}$$

The value for the receiving-side inductance L_R can be found from (4.95) which permits the power to be transferred with the maximum efficiency. Let us choose to have the maximum efficiency when the WPTS is delivering the nominal power to the battery and the coupling coefficient is $k_{avg} = \frac{k_{min}+k_{max}}{2}$. Under these conditions, the load resistance is given by:

$$R_L = \frac{V_{avg}^2}{P_{Nom}} = \frac{V_{L,min}^2}{P_{Nom}} \left(\frac{k_{avg}}{K_{min}}\right)^2 \tag{4.99}$$

Equation (4.99) is used to calculate the pickup quality factor in (4.95) from which the receiving-side inductance is found in the form:

$$L_R = \frac{1}{\omega_o} \frac{1}{k_{avg}\sqrt{1+k_{avg}^2}} R_L \approx \frac{1}{\omega_o} \frac{1}{k_{avg}} R_L \tag{4.100}$$

Once the value for L_R is computed, the value of the transmitting coil inductance and the inverter-side inductance ($\alpha = 1$) can be calculated from (4.98). They have to resonate with the capacitor C_T and the inductance L_R has to resonate with C_R. For this reason, the rated value for the capacitors can be obtained with an equation similar to (4.56).

This incomplete example highlights how much complicated is the design of a dynamic WPTS and how the coupling coefficient profile, thus the track coils deployment, greatly affects the system performance.

Chapter 5

WPTSs Dynamic Modeling

To control the power transmitted by a WPTS it is necessary to adjust some quantities on both the transmitting and the receiving circuits to follow a desired reference. This task is usually performed by means of control loops, where some regulators provide the controlling signals for the WPTS (e.g. the phase-shift angle for the transmitting-side inverter) according to the errors between the actual values of the controlled quantities and the references. The design of effective regulators requires a good dynamic model of the WPTS, i.e. to find how some observable quantities evolve from a steady-state condition as a consequence of the variation of other quantities, how they are influenced by some quantities internal to the system (for example quantities that cannot be measured), how much they are sensible to the variation of the parameters of the system, and so on. An accurate dynamic model is mandatory in particular for dynamic WPTSs, where the large coil coupling variation can pose severe stability issues.

This chapter reviews the main methods useful for modeling WPTSs: the Generalized State-Space Averaging (GSSA) and the Laplace Phasor Transform (LPT). Furthermore, a novel modeling method, called Modulated Variable Laplace Transform (MVLT) and proposed for this Ph.D. thesis, is introduced. The three methods are firstly explained using a simple series resonant tank circuit as an example. Afterwards, they are employed to find the dynamic model of a series-compensated receiving-side circuit of a WPTS.

5.1 Modeling Methods

Considerable efforts have been made into the development of suitable mathematical models for power electronics converters, among which the State-Space Averaging (SSA) method developed by Middlebrook and Ćuk appears the most successful [106]. By neglecting the ripple of the state variables, SSA method models the dynamics of the average values of the converters quantities. This simplification provides better physical insight into the system behavior and SSA is usually very accurate since in case of (well-designed) traditional converters the ripple of the state variables is significantly smaller than their average values taken over a switching period. The effectiveness of the SSA method for PWM converters is that it captures the dynamics of the low-frequency averaged signals which dominate the

transient behavior instead of inspecting the actual waveforms whose spectrum can contain high-frequency components. In addition, this technique of averaging permits the engineers to get rid of the intrinsic *switching* behavior of the converters and treat them as single time-invariant systems that are usually nonlinear. However, since average values change slowly over time, the *averaged* systems are easily linearizable and this operation leads to the so called *small-signal* models. One of the major assumptions for the validity of the SSA method is that the state variables of the converter should be slowly time-varying compared with the switching frequencies [107].

The transmitting power stage of a WPTS can be envisaged as a resonant converter. In resonant converters the quantities in the resonant tanks exhibit predominantly oscillatory behavior. In particular in WPTSs, the quantities involved in compensating networks are alternated signals pulsating at the inverter switching frequency. In other words, the switching period is equal to the natural time constant of the system. For this reason, SSA method applied to WPTSs and in general to resonant converters is not able to yield a useful dynamic model. In fact, SSA provides some relations, expressed in terms of state-space equations, between the average values of the state variables. When the state variables involved in the compensating networks of a WPTS are averaged over a switching period, the outcome of the operation produces null signals and the relations between them become totally useless.

The benefits of having a model that involves slow time-varying state variables are straightforward. First of all, as it has been mentioned earlier for SSA, such kind of model can be linearized more easily. Secondly, the transients of the converters are usually governed by time constants that are much longer than the switching periods. A further advantage in the use of an averaged model arises from the purpose of the dynamic model itself. In fact, the ultimate goal of developing a dynamic model is to obtain the converter input-to-output relation and based on it the proper control strategy can be implemented. If the average system behavior can be controlled with a slow input signal, it is not necessary to push the control system performance very high. In particular, this is useful for the digitally controlled converters where the control signal for the system typically comes from a microcontroller. The value of the control signal instant by instant is the outcome of an algorithm carried out in the digital controller. This requires an execution time for the algorithm computation less than the sampling period which, according to Nyquist-Shannon theorem, should be less than $\frac{1}{2B}$, where B is the bandwidth of the quantities involved in the control system. For this reason, a dynamic model which involves very fast signals is not helpful, since it may require microcontrollers with performance well beyond their capabilities.

From the above considerations it is easy to understand that a dynamic model which uses slowly varying state variables is advisable also for resonant converters and in particular for the transmitting power stage of a WPTS. The approach for developing such kind of model is suggested by the waveforms of the electrical quantities in the resonant tanks. They can be considered as high-frequency sinusoidal signals with a variable amplitude during the transient periods (similar to the signal of Fig. 3.6). In other words, the ac signals in the compensating networks of a WPTS can be conceived as amplitude-modulated signals with an high-frequency

sinusoidal carrier and with a modulating signal (also called *envelope*) that varies much slower than the carrier. So, the envelopes of the ac quantities can be used as the state variables for the *averaged* model[1]. The high-frequency components in the WPTS quantities are lost in the *averaging* process but, since the sinusoidal waveform of the carriers of voltages and currents are forced by the filtering action of the compensating networks, the only knowledge of the modulating signals is enough to reconstruct the full waveforms.

The two main techniques that model the systems through the envelopes (or signals proportional to the envelopes) of the real quantities are the Generalized State-Space Averaging (GSSA) [108] and the Laplace Phasor Transform (LPT) [109]. These methods have been used in [110]–[113] to model various types of WPTS. A model of a series-series WPTS has been obtained in [114] with a particular case of the GSSA method, called Extended Describing Function (EDF) method.

5.1.1 Generalized State-Space Averaging (GSSA) Method

The Generalized State-Space Averaging (GSSA) method, proposed by Sanders *et al.*, is based on the fact that any signal $x(\tau)$ on the time interval $[t-T, t]$ can be expressed as [115]:

$$x(\tau) = \sum_{k=-\infty}^{\infty} \langle x \rangle_k (t)\, e^{jk\omega\tau} \qquad \text{for } \tau \in [t-T, t]. \tag{5.1}$$

where T is an arbitrarily chosen time period and $\omega = \frac{2\pi}{T}$. The quantity $\langle x \rangle_k (t)$ is a complex time-varying signal which is given by:

$$\langle x \rangle_k (t) = \frac{1}{T} \int_{t-T}^{t} x(\tau)\, e^{-jk\omega\tau}\, d\tau \tag{5.2}$$

For a fixed time instant $t = t_0$, equation (5.1) is simply the complex Fourier series expansion of the periodic signal $x_{ext}^{t_0}(t)$ and (5.2) defines the Fourier coefficients. The signal $x_{ext}^{t_0}(t)$ has a period T and it is obtained by the periodic repetition of $x(\tau)$ when τ spans in the interval $[t_0 - T, t_0]$. If $x(t)$ is periodic with period T, the signal $x_{ext}^{t_0}(t)$, also known as periodic extension of $x(t)$, does not depend on the particular point t_0 and coincides precisely with $x(t)$. For this reason, also the Fourier coefficients in (5.2) would be time-independent. However, in general $x(t)$ can be non-periodic and (5.2) produces different sets of coefficients depending on the particular time instant considered. Instead of considering a discrete set of time instants it is possible to move the interval $[t-T, t]$ along the time axis seamlessly. This interval of length T can be envisaged as a sliding window. Doing so, each coefficient in (5.2) becomes a time-function. Figure 5.1 can clarify the situation.

The rationale behind the GSSA transformation is to determine a state-space model in which the coefficients (5.2) are the state variables. In can be observed

[1] In case of quantities with a predominant sinusoidal behavior as the ones involved in the compensating networks of WPTSs, the envelopes are proportional to the rms of the signals. The rms operation can be considered as a *generalized mean*. A dynamic model which uses the envelopes as state variables can be envisaged again as an *averaged* model.

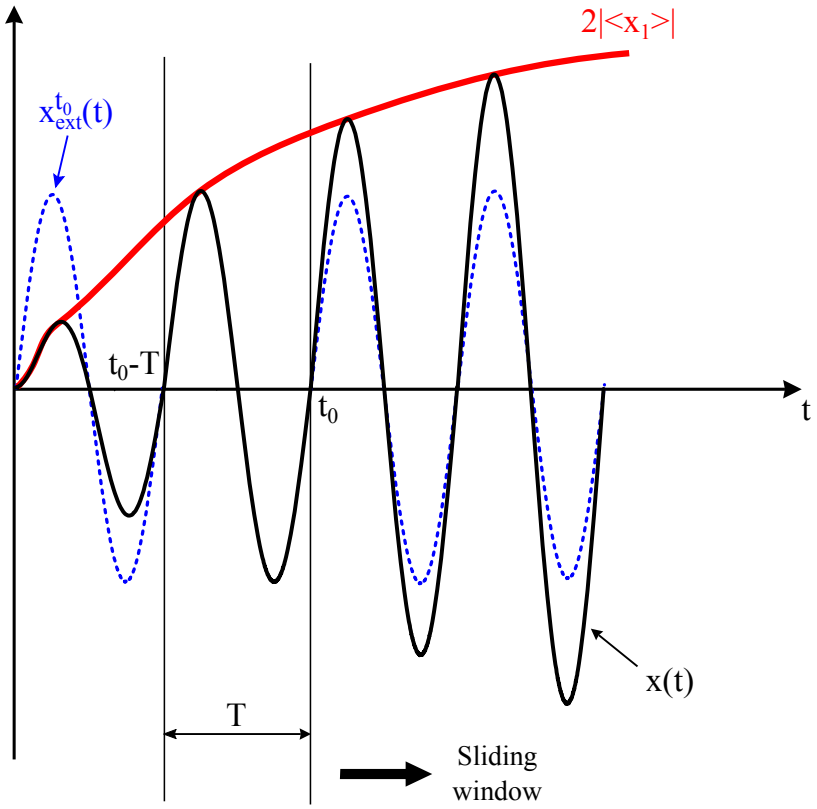

Fig. 5.1: Graphical explanation of the GSSA transformation.

from (5.1) that to reconstruct the signal $x(t)$ from the new state variables $\langle x \rangle_k$ in general an infinite number of terms are necessary. In practice, only one or two coefficients will be sufficient to represent the dominant components and the real time waveforms. In fact, the quantities in the compensating networks of a WPTS are quasi-sinusoidal, therefore, if the period T of the sliding window is chosen to be equal to or near the oscillation period of a waveform, the first Fourier coefficients approximate $x(t)$ very well. Under this hypothesis, equation (5.1) can be written as:

$$x(\tau) = \langle x \rangle_{-1} \, e^{-j\omega\tau} + \langle x \rangle_1 \, e^{j\omega\tau} \tag{5.3}$$

Since $\langle x \rangle_{-1}$ is equal to the complex conjugate of $\langle x \rangle_1$, equation (5.3) can be rewritten in terms of only one state variable:

$$\begin{aligned} x(\tau) &= \langle x \rangle_1^* \, (e^{j\omega\tau})^* + \langle x \rangle_1 \, e^{j\omega\tau} = 2\,\Re\{\langle x \rangle_1 \, e^{j\omega\tau}\} = \\ &= 2|\langle x \rangle_1| \cos(\omega\tau + \varphi) \end{aligned} \tag{5.4}$$

In (5.4), $(\cdot)^*$ is the complex conjugate and $\Re\{\cdot\}$ indicates the real part operator. From (5.4) it is easy to recognize that the high-frequency signal $x(t)$ can be completely reconstructed by only $\langle x \rangle_1$ and then it can be used as the unique state variable. The phase $\varphi(t)$ of the first Fourier coefficient gives the phase of carrier with respect to a certain reference, whereas its amplitude is proportional

the envelope of $x(t)$. This fact can be seen also in Fig. 5.1, where one can verify that $\langle x \rangle_1$ varies slower with respect to $x(t)$.

For the quantities that show a dominant dc component, for example the quantities downstream the receiving-side rectifier, only the 0-th coefficient is sufficient to model their dynamics. The coefficient of index 0 for a generic signal $x(t)$ is given by:

$$\langle x \rangle_0 (t) = \frac{1}{T} \int_{t-T}^{t} x(\tau)\, d\tau \tag{5.5}$$

Equation (5.5) is simply the average value of the signal $x(t)$. The classical SSA method can be obtained as a particular case of the GSSA method considering only the 0-th coefficient of the quantities.

The starting point for the GSSA method application is the state-space representation of the system. In general, a resonant converter can be represented through a set of non-linear Ordinary Differential Equations (ODEs). Each ODE can be written as:

$$\frac{d}{dt} x_i(t) = f(x_1, \dots, x_{i-1}, x_i, x_{i+1}, \dots, u_1, u_2, \dots) \tag{5.6}$$

where x_i is the i-th state variable of the system, $u_j\,(j = 1, 2, \dots)$ is the j-th input and $f(\cdot, \dots, \cdot)$ is a generic scalar function of its arguments. The generalized averaging consists in applying the transformation (5.2) to the equation (5.6) (and to all the other state equations) both on the left-hand side and on the right-hand side. This operation results in:

$$\left\langle \frac{d}{dt} x_i(t) \right\rangle_k = \langle f(x_1, \dots, x_{i-1}, x_i, x_{i+1}, \dots, u_1, u_2, \dots) \rangle_k \tag{5.7}$$

To derive a useful expression of the left-hand side, it is necessary to exploit the rule for computing the derivative of the k-th coefficient which can be obtained directly by the definition (5.2):

$$\frac{d}{dt} \langle x_i \rangle_k (t) = \left\langle \frac{d}{dt} x_i \right\rangle_k (t) - jk\omega \langle x_i \rangle_k (t) \quad [2] \tag{5.8}$$

A general rule for simplifying the right-hand side of (5.7) does not exist. However, usually for resonant converters, the function $f(\cdot)$ is polynomial. In this case, each addend of the polynomial function can be treated separately and this can be done for the linearity of (5.2). To compute the transformation for each individual term of the polynomial, the following convolutional property can be helpful:

$$\langle x\, y \rangle_k = \sum_{i=-\infty}^{\infty} \langle x \rangle_{k-i} \langle y \rangle_i \tag{5.9}$$

where the time argument t has been dropped to make the notation more clear. Property (5.9) has been obtained using both (5.2) and (5.1). An example of the

[2] In the derivation of this identity, the Leibniz Integral Rule should be applied. It is easier to apply this rule using the equivalent formula found in [108] for the transformation (5.2).

GSSA method application and thus the explanation of how (5.8) and (5.9) can be used will be given in the following sections.

5.1.2 Laplace Phasor Transform (LPT) Method

Laplace Phasor Transform method has been proposed by Rim and Cho in [109], where they modeled the dynamics of a series resonant converter. The transformation upon which the LPT method is based can be envisaged as an extension of the phasor transform to the transient case. Considering a phasor as a complex time-varying signal instead of a simple complex number, a signal $x(t)$ can be written as:

$$x(t) = \Re\{\bar{x}(t)\, e^{j\omega t}\} \ ^{3} \tag{5.10}$$

None of the signal $x(t)$ and ω must be sinusoidal or constant, however, the signal $\bar{x}(t)$ can be slowly time-varying only when $x(t)$ is almost sinusoidal with a frequency ω. In such case, it can be advantageous to discard from the analysis the high-frequency components present in the spectrum of $x(t)$ and study only the behavior of the signal $\bar{x}(t)$. The original signal can be easily derived from (5.10) that can be further expanded as:

$$x(t) = \Re\{\bar{x}(t)\, e^{j\omega t}\} = |\bar{x}(t)| \cos(\omega t + \varphi) \tag{5.11}$$

As can be seen from (5.11), the amplitude of the *dynamic phasor* $\bar{x}(t)$ identifies the envelope of the modulated signal $x(t)$ which has a sinusoidal carrier oscillating with an angular frequency ω. This carrier is shifted by the phase of the dynamic phasor $\varphi(t)$ which is time-varying. When the transient is extinguished, the variable $x(t)$ becomes pure sinusoidal and the complex signal $\bar{x}(t)$ becomes just the conventional phasor.

The analogy between (5.11) and (5.4) allows us to state that the Laplace phasor transformation is equivalent (apart from the coefficient 2) to the generalized averaging transformation when only the 1-st Fourier coefficients are retained. However, the main difference of the two methods lies on the way they are applied. The GSSA method applies the transformation to the state-space equations of the system, whereas the LPT method is based on transformations at circuit level. In fact, with the LPT method all the components of the original circuit that involves the high-frequency signals are transformed to obtain another circuit valid to describe the relationships between the dynamic phasors. Let us consider for example an inductor. Its v-i characteristic is given by:

$$v_L(t) = L \frac{d}{dt} i_L(t) \tag{5.12}$$

The current i_L and the voltage v_L can be written in terms of their dynamic phasors using (5.10):

[3] The original transformation was $x(t) = \Re\{\sqrt{2}\bar{x}(t)\, e^{j\omega t}\}$, which differs from (5.10) by the presence of $\sqrt{2}$ that multiplies the complex signal $\bar{x}(t)$. The transformation (5.10) has been used in [116] to model the low frequency components of both an amplitude-modulated and a frequency-modulated signal.

$$v_L(t) = \Re\{\bar{v}_L\, e^{j\omega t}\} \tag{5.13}$$
$$i_L(t) = \Re\{\bar{i}_L\, e^{j\omega t}\} \tag{5.14}$$

Substituting (5.13) and (5.14) into (5.12), the inductor v-i characteristic becomes:

$$\Re\{\bar{v}_L\, e^{j\omega t}\} = L\,\frac{d}{dt}\Big[\Re\{\bar{i}_L\, e^{j\omega t}\}\Big] \tag{5.15}$$

This equation can be further expanded considering that $\frac{d}{dt}\big[\Re\{\cdot\}\big] = \Re\big\{\frac{d}{dt}[\cdot]\big\}$ and it becomes:

$$\Re\{\bar{v}_L\, e^{j\omega t}\} = \Re\left\{L\left[\frac{d\,\bar{i}_L}{dt} + j\omega\,\bar{i}_L\right] e^{j\omega t}\right\} \tag{5.16}$$

It can be proved [117] that the real parts of the dynamic phasors in (5.16) are equal if and only if the dynamic phasors themselves are equal. For this reason, equation (5.16) is equivalent to:

$$\bar{v}_L(t) = L\,\frac{d\,\bar{i}_L(t)}{dt} + j\omega L\,\bar{i}_L(t) \tag{5.17}$$

Equation (5.17) provides the relation between the dynamic phasor of the current that flows through and the dynamic phasor of the voltage across the inductance. It can be seen that with respect to the equation (5.12) which put in relation the real voltage and the real current of the inductance, equation (5.17) has an additional term $j\omega L\,\bar{i}_L$. In this term the phasor of the inductor current multiplies the quantity $j\omega L$ that can be envisaged as an imaginary resistance placed in series with the inductor L. In steady-state, when the derivative term becomes 0, equation (5.17) represents the conventional relationship between the current and the voltage of the inductance written in phasor domain. Summing up, an inductor in the real time domain can be transformed into an inductor with a complex resistance in series to model the dynamics of the slowly time-varying dynamic phasors (cf. Fig. 5.2).

With a procedure similar to the one used to attain (5.17), it is possible to obtain the transformed circuit for a capacitor. The time-domain v-i characteristic of a capacitor

$$i_C(t) = C\,\frac{d}{dt}\,v_C(t) \tag{5.18}$$

in dynamic phasor domain becomes:

$$\bar{i}_C(t) = C\,\frac{d\,\bar{v}_C(t)}{dt} + j\omega C\,\bar{v}_C(t) \tag{5.19}$$

As shown in Fig. 5.2, equation (5.19) governs the relations between the quantities of a circuit formed by a capacitor C with a complex resistance $\frac{1}{j\omega C}$ connected in parallel. Figure 5.2 also shows the dynamic phasor transform applied to a resistance R. It can be noticed that the resistance is invariant to the dynamic phasor transformation.

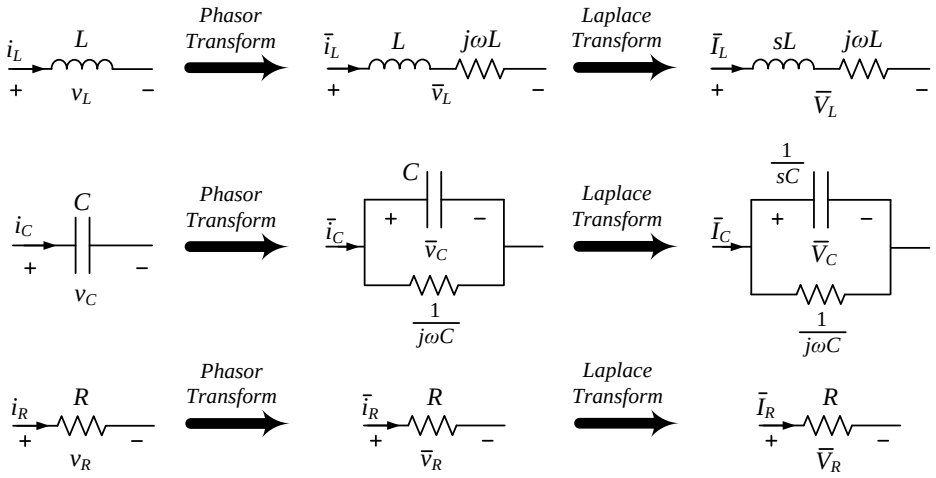

Fig. 5.2: Laplace Phasor Transform of the elementary circuital components.

The conventional phasor transform is a technique that permits an easy study of a circuit in sinusoidal steady-state by switching from a time domain to a frequency domain analysis. On the contrary, the transformation (5.10) produces a model in which the quantities are still in time domain (cf. (5.17) and (5.19)). The Laplace transform applied to the dynamic phasor domain equations of the various elementary components provides a way to understand the frequency behavior of these components as regards the dynamic phasors. The dynamic phasor transform followed by the Laplace transform gives rise to the Laplace phasor transform. It is worth noting that the Laplace transform is applied to complex signals [118] and the resulting components transfer functions are rational functions in s with complex coefficients. For instance, the transfer function of a capacitor that links the dynamic phasor of the voltage to the dynamic phasor of the current is given by:

$$\frac{\bar{V}_C(s)}{\bar{I}_C(s)} = \frac{1}{sC + j\omega C} \tag{5.20}$$

The transfer functions for the other elementary components can be derived looking at the last column of Fig. 5.2.

The application of the LPT method starts with the conversion of the original circuit substituting all the elementary components with their respective Laplace phasor transformed counterparts. From the transformed circuit then, it is easy to evaluated all the desired transfer functions. Some examples of the LPT method application will be introduced in the next sections.

5.1.3 Modulated Variable Laplace Trasform Method

The Modulated Variable Laplace Transform (MVLT) is a novel method proposed in this thesis and published in [119] for modeling the dynamics of the envelopes of the quantities involved in the compensating networks of a WPTS. This

method provides a direct link between the transfer functions for the real quantities of the WPTS and the transfer functions for the envelopes. The MVLT method is based on the fact that an amplitude modulated signal $x(t)$ can be written with the introduction of the dynamic phasor $\bar{x}(t)$ as in (5.11)[4]. If the spectrum of $\bar{x}(t)$ encompasses frequencies much lower than the angular frequency of the carrier ω and the signal $x(t)$ is provided as input of a linear system with transfer function $G(s)$, the output signal $y(t)$ can be written in a similar way as in (5.11). The relation between the Laplace transform of the complex signals $\bar{x}\, e^{j\omega t}$ and $\bar{y}\, e^{j\omega t}$ is then

$$\mathcal{L}\{\bar{y}\, e^{j\omega t}\}(s) = G(s)\, \mathcal{L}\{\bar{x}\, e^{j\omega t}\}(s) \tag{5.21}$$

where $\mathcal{L}\{\cdot\}$ indicates the Laplace transform of the argument. Using the "frequency shifting" property of the Laplace transform, equation (5.21) can be written as:

$$\bar{Y}(s - j\omega) = G(s)\, \bar{X}(s - j\omega) \tag{5.22}$$

which, with a variable substitution, becomes:

$$\bar{Y}(s) = G(s + j\omega)\, \bar{X}(s) \tag{5.23}$$

In (5.22) and (5.23), the quantities $\bar{X}(s)$ and $\bar{Y}(s)$ are the Laplace transforms of the complex signals $\bar{x}(t)$ and $\bar{y}(t)$, respectively. Equation (5.23) states that the transfer function which links the complex modulating signals (the dynamic phasors) is simply the real transfer function of the system $G(s)$ mapped into $s' = s + j\omega$ [5].

As it happens with the LPT method the transfer function for the dynamic phasors is a rational function in s with complex coefficients. However, engineers are used to work with transfer functions in which the coefficients are real. Fortunately, it is always possible to write $G(s + j\omega)$ as follows:

$$G(s + j\omega) = G_{Re}(s) + jG_{Im}(s) \tag{5.24}$$

where G_{Re} and G_{Im} are two rational functions in s in which the numerators and the denominators have real coefficients[6].

The transfer function (5.24) provides the relationship between $\bar{x}(t)$ and $\bar{y}(t)$, but the target of the MVLT method is to obtain the relation between the envelopes. The envelope of the output signal $y(t)$ is the amplitude of $\bar{y}(t)$ (see (5.11)) which is given by:

$$y_{env}(t) = |\bar{y}(t)| = \sqrt{y_{Re}^2(t) + y_{Im}^2(t)} \tag{5.25}$$

where $y_{Re}(t)$ and $y_{Im}(t)$ are the real and the imaginary parts of $\bar{y}(t)$. Since (5.25) is nonlinear, a transfer function between the envelope of the input $x_{env}(t)$ and $y_{env}(t)$ cannot be achieved. However, a small-signal model can be attained by linearizing (5.25) around a working point. This operation leads to:

[4] Ref. [120] demonstrates that (5.11) can be used also for phase modulated signals.
[5] This can be a proof for the qualitative results found in [116].
[6] The way for splitting $G(s + j\omega)$ into the $G_{Re}(s)$ and $G_{Im}(s)$ will be explained later on.

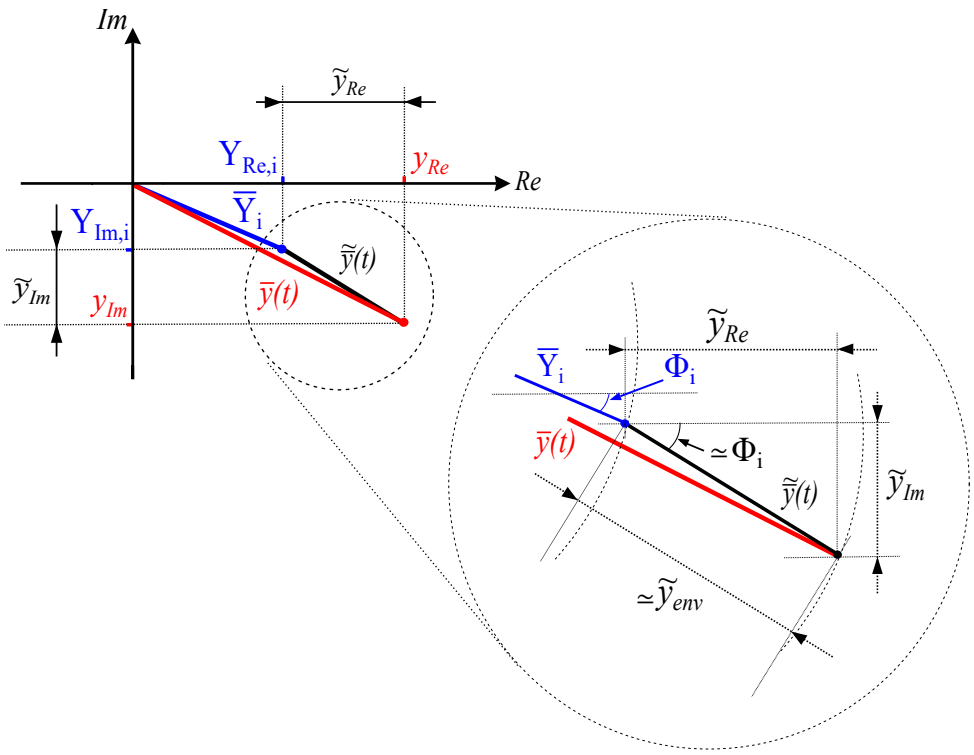

Fig. 5.3: Graphical explanation of the linearization process for the equation (5.25).

$$\begin{aligned} \tilde{y}_{env}(t) &\approx \frac{Y_{Re,i}}{\sqrt{Y_{Re,i}^2 + Y_{Im,i}^2}}\,\tilde{y}_{Re}(t) + \frac{Y_{Im,i}}{\sqrt{Y_{Re,i}^2 + Y_{Im,i}^2}}\,\tilde{y}_{Im}(t) \\ &\approx \quad \cos(\phi_i) \quad \tilde{y}_{Re}(t) + \quad \sin(\phi_i) \quad \tilde{y}_{Im}(t) \end{aligned} \tag{5.26}$$

In (5.26), $Y_{Re,i}$ and $Y_{Im,i}$ are the real and the imaginary part of $\bar{Y}_i = Y_i e^{j\phi_i}$ which coincides with the conventional phasor of the output $y(t)$ in the initial working point. After a system perturbation, the dynamic phasor $\bar{y}(t)$ moves from $\bar{Y}_i$ to reach the final point corresponding to $\bar{Y}_f$. If the perturbation is not so large, the dynamic phasor $\bar{y}(t)$ prior to becoming constant and equal to $\bar{Y}_f$ can be written as $\bar{Y}_i + \tilde{\bar{y}}(t)$, where $\tilde{\bar{y}}(t) = \tilde{y}_{Re} + j\tilde{y}_{Im}$ identifies its small variation around $\bar{Y}_i$ in the complex plane. Figure 5.3 exemplifies the situation.

Figure 5.3 is useful also to understand the meaning of the linearization of (5.25). In fact, if the angle of $\tilde{\bar{y}}(t)$ remains almost constant (so almost equal to ϕ_i), its amplitude can be approximated with (5.26). This means that the small variation $\tilde{y}_{env}(t)$ of the envelopes of $y(t)$ with respect to the initial envelope can be assessed through $|\tilde{\bar{y}}(t)|$.

The application of the Laplace transform to (5.26) leads to:

$$Y_{env}(s) = \cos(\phi_i)\, Y_{Re}(s) + \sin(\phi_i)\, Y_{Im}(s) \tag{5.27}$$

where the meaning of the definitions $Y_{env}(s)$, $Y_{Re}(s)$ and $Y_{Im}(s)$ are immediately

recognizable from (5.26) [7].

Starting from (5.27), it remains to link the Laplace transforms $Y_{Re}(s)$ and $Y_{Im}(s)$ to (the Laplace transform of) the small-signal input. Let us consider the carrier of the signal $\tilde{x}(t)$ as the reference for the phases. In this case, the dynamic phasor $\tilde{\tilde{x}}(t)$ which in general is given by $\tilde{\tilde{x}}(t) = \tilde{x}_{Re}(t) + j\tilde{x}_{Im}(t)$, consists only in the real signal. With this frame of reference, the real part of $\tilde{\tilde{x}}(t)$ coincides also with its envelope. In s-domain it is possible to write then $X_{env}(s) = X_{Re}(s)$.

The dynamic phasor $\tilde{\tilde{y}}(t)$ is obtained as the output of $G(s + j\omega)$ when $\tilde{\tilde{x}}(t) = \tilde{x}_{Re}(t)$ is applied as the input. Being the input of $G(s + j\omega)$ real, the real part of $\tilde{\tilde{y}}(t)$ is just the output of $G_{Re}(s)$ and the imaginary part is just the output of $G_{Im}(s)$. From this considerations, equation (5.27) can be written as:

$$Y_{env}(s) = \left[\cos(\phi_i)\, G_{Re}(s) + \sin(\phi_i)\, G_{Im}(s)\right]\, X_{env}(s) \tag{5.28}$$

Considering that the function inside the square brackets of (5.28) can be written as $\Re\{G(s+j\omega)e^{-j\phi_i}\}$ (provided that s is assumed real), the transfer function which links the envelopes can be finally written in terms of the transfer function $G(s)$:

$$G_{env}(s) = \frac{Y_{env}(s)}{X_{env}(s)} = \Re\{G(s + j\omega)e^{-j\phi_i}\} \tag{5.29}$$

It is interesting to note that the angle ϕ_i of the phasor $\bar{Y}_i$ is also the phase of $G(j\omega)$.

Relation Between the Real System Transfer Function and the MVLT Transfer Function

Equation (5.29) shows that for obtaining the transfer function which links the envelopes, it is necessary to extract the real part of the complex transfer function $G(s + j\omega)e^{-j\phi_i}$. Even though this operation is not an easy task, a direct relation between the poles of $G(s)$ and the ones of $G_{env}(s)$ exists. The first thing to do is to understand how to extract the real part of $G(s + j\omega)e^{-j\phi_i}$. According to (5.28), this scope is accomplished once the transfer function $G(s + j\omega)$ is split into $G_{Re}(s)$ and $G_{Im}(s)$. Let us consider $G(s)$ as a rational function given by $\frac{n(s)}{d(s)}$. So, the transfer function that links the dynamic phasors can be written as:

$$G(s + j\omega) = \frac{n(s + j\omega)}{d(s + j\omega)} = \frac{p(s)}{q(s)} \tag{5.30}$$

In (5.30), $p(s)$ and $q(s)$ are respectively the numerator and the denominator of $G(s + j\omega)$ which are polynomials in s with complex coefficients. A generic polynomial $a(s)$ such as $p(s)$ and $q(s)$ can be always written as $a(s) = a_{Re}(s) + ja_{Im}(s)$, where $a_{Re}(s)$ and $a_{Im}(s)$ are polynomials in s with real coefficients. By writing $p(s)$ and $q(s)$ in this way, the equation (5.30) becomes:

$$G(s + j\omega) = \frac{p_{Re}(s) + jp_{Im}(s)}{q_{Re}(s) + jq_{Im}(s)} \tag{5.31}$$

[7] The tildes have been dropped from the small-signal Laplace transformed quantities to lighten the notation.

Let us define the polynomial $\hat{q}(s) = q_{Re}(s) - jq_{Im}(s)$ which has the same structure of $q(s)$ but with respect to this one it has the coefficients that are complex conjugate. Multiplying the numerator and the denominator of $G(s + j\omega)$ by $\hat{q}(s)$, equation (5.31) becomes:

$$G(s+j\omega) = \frac{p(s)}{q(s)}\frac{\hat{q}(s)}{\hat{q}(s)} = \frac{p_{Re}\, q_{Re}(s) + p_{Im}\, q_{Im}(s)}{q^2_{Re}(s) + q^2_{Im}(s)} + j\,\frac{p_{Im}\, q_{Re}(s) - p_{Re}\, q_{Im}(s)}{q^2_{Re}(s) + q^2_{Im}(s)} \tag{5.32}$$

Equation (5.32) is the desired result since $G(s+j\omega)$ is written it the form (5.24). It can be observed that the denominators of $G_{Re}(s)$ and of $G_{Im}(s)$ are equal and their degree is twice the degree of $q(s)$ which coincides with the degree of $d(s)$ [8]. Since the envelope transfer function is a linear combination of $G_{Re}(s)$ and $G_{Im}(s)$ (cf. (5.28)), also the denominator of $G_{env}(s)$ has a degree that is twice the degree of $d(s)$. This implies that the order of the model that involves the envelopes is doubled with respect to the model for the real high-frequency signals.

Let us try now to find the relation between the poles of $G(s)$ and the ones of $G_{env}(s)$. For the above discussions, this problem is equivalent to find the relation between the zeros of $d(s)$ and the ones of the polynomial $q(s)\,\hat{q}(s)$. Lets us suppose to know the zeros $\dot{z}_{q,i}$ $i = [1, 2, \ldots, n]$ (n is the degree of $d(s)$) of $q(s)$. Consequently, it can be written as:

$$q(s) = \prod_{i=1}^{n}(s - \dot{z}_{q,i}) \tag{5.33}$$

The roots of $\hat{q}(s)$ are related to the ones of $q(s)$. Indeed, the roots of $\hat{q}(s)$ can be defined through the following equation:

$$\hat{q}(s) = 0 \quad \Rightarrow \quad q_{Re}(s) - j\, q_{Im}(s) = 0 \tag{5.34}$$

By applying the complex conjugate operator to both the left-hand side and the right-hand side of (5.34), we obtain:

$$\begin{gathered} \left[q_{Re}(s) - j\, q_{Im}(s)\right]^* = 0 \\ \Downarrow \\ q_{Re}(s^*) + jq_{Im}(s^*) = 0 \quad \Rightarrow \quad q(s^*) = 0 \end{gathered} \tag{5.35}$$

Equation (5.35) shows that the roots of $\hat{q}(s)$ are the complex conjugate of the roots of $q(s)$. Therefore, the polynomial $q(s)\,\hat{q}(s)$ can be written as:

$$q(s)\,\hat{q}(s) = \prod_{i=1}^{n}(s - \dot{z}_{q,i})(s - \dot{z}^*_{q,i}) = \prod_{i=1}^{n}\left(s^2 - 2\,\Re\{\dot{z}_{q,i}\}\,s + |\dot{z}_{q,i}|^2\right) \tag{5.36}$$

To simplify the notation, the roots of $q(s)$ can be written as $\dot{z}_{q,i} = \sigma_i + j\omega_i$ and (5.36) becomes:

[8] The degree of the polynomial that is the product between two polynomials is the sum of the degrees of the individual polynomials. The degree of the polynomial that is the sum between two polynomials is the maximum between the degrees of the individual polynomials.

$$q(s)\,\hat{q}(s) = \prod_{i=1}^{n}\left[s^2 - 2\,\sigma_i\,s + (\sigma_i^2 + \omega_i^2)\right] \tag{5.37}$$

To link the poles of $G(s)$ with those of of $G_{env}(s)$ it remains to find the relation between the zeros of $d(s)$ and the zeros of $q(s)$. Let us write the zeros of $d(s)$ in a general form as $\dot{z}_{d,i} = \alpha_i + j\beta_i$ $i = [1, 2, \ldots, n]$. From the definition $q(s) = d(s + j\omega)$ (cf. (5.30)), it is immediate to state that the zeros $\dot{z}_{q,i}$ of $q(s)$ can be associated to $\dot{z}_{d,i}$ through the following relation:

$$\dot{z}_{q,i} = \dot{z}_{d,i} - j\omega = \alpha_i + j(\beta_i - \omega) \tag{5.38}$$

The real part σ_i of the zeros of $q(s)$ is exactly equal to the real part α_i of the zeros of $d(s)$. The imaginary part ω_i of the zeros of $q(s)$ instead is shifted from β_i by a quantity ω, namely by the angular frequency of the carriers of the modulated signals. Substituting these results into (5.37), the relation between the poles of $G(s)$ and the ones of $G_{env}(s)$ is obtained:

$$q(s)\,\hat{q}(s) = \prod_{i=1}^{n}\left[s^2 - 2\,\alpha_i\,s + \alpha_i^2 + (\beta_i - \omega)^2\right] \tag{5.39}$$

Each term of the product (5.39) is produced by the complex conjugate zero pair $\dot{z}_i = \alpha_i \pm j\,|\omega - \beta_i|$. Based on this fact it is possible to state that:

- A pole in the origin $s = 0$ in $G(s)$ becomes an imaginary conjugate poles pair $s = \pm j\omega$ in $G_{env}(s)$;
- A real pole $s = \alpha$ in $G(s)$ is associated to the complex conjugate poles pair $s = \alpha \pm j\omega$ in $G_{env}(s)$;
- A complex conjugate poles pair $s = \alpha \pm j\beta$ in $G(s)$ produces two complex conjugate poles pairs in $G_{env}(s)$: one is given by $s = \alpha \pm j|\omega - \beta|$ and the other by $s = \alpha \pm j(\omega + \beta)$. It should be noted that if the imaginary part β of the poles of $G(s)$ coincides with the angular frequency ω of the input carrier, one pair is no more given by two complex conjugate poles but instead it is formed by two real poles $s = \alpha$ in $G_{env}(s)$.

Equations (5.39) provides the straightforward link between the poles of the real system transfer function and the envelope transfer function. Such an easy relation cannot be found for the zeros of the transfer functions.

5.2 Methods Application

The previous section has introduced the three modeling methods, illustrating the theoretical background behind each of them. To better understand how the three methods actually work and how they can be used, it is easier to apply them to a practical example. Let us consider the series resonant tank of Fig. 3.1 (reported for simplicity in Fig. 5.4) as study case. The circuit is supplied with a sinusoidal

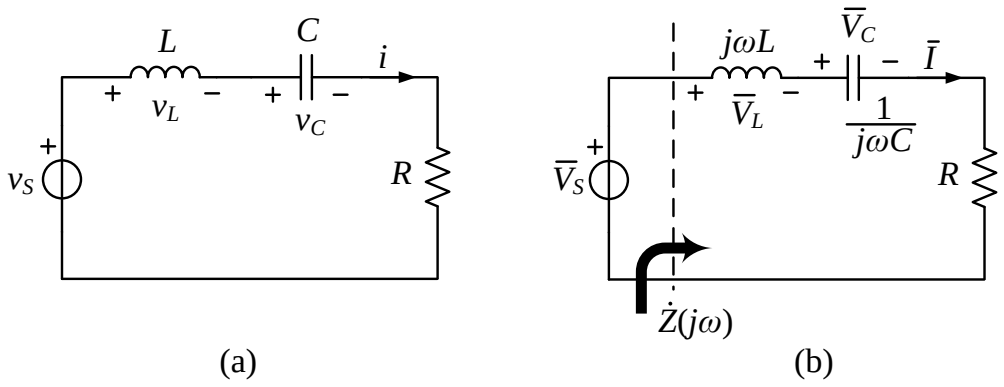

Fig. 5.4: Series resonant tank circuit. Circuit for modeling the dynamics of the high-frequency modulated signals (a) and circuit for the steady-state analysis (b).

voltage source v_s which has a slowly (with respect to the period $\frac{2\pi}{\omega}$ of the cosine wave) time-varying amplitude. It can be written as:

$$v_s(t) = v_{s,env}(t)\cos(\omega t) \tag{5.40}$$

In addition, let us suppose for simplicity that the angular frequency ω coincides with the resonant frequency of the LCR circuit.

5.2.1 GSSA Method Application

The starting requirement of the GSSA method is the state space model which involves the high-frequency signals of the circuit. For a series resonant tank it is easily derivable from the circuit of Fig. 5.4(a) and it is given by:

$$\begin{cases} \frac{di}{dt} = -\frac{R}{L}\, i - \frac{1}{L}\, v_C + \frac{1}{L}\, v_s \\ \frac{dv_C}{dt} = \frac{1}{C}\, i \end{cases} \tag{5.41}$$

To find the model which involves the complex Fourier coefficients $\langle\cdot\rangle_1$ it is necessary to apply the transformation (5.2) (with $k = 1$) at both the sides of the ODEs in (5.41). Doing so, and using the property (5.8) for the left-hand side, we obtain:

$$\begin{cases} \frac{d}{dt}\,\langle i\rangle_1 = -j\omega\,\langle i\rangle_1 - \frac{R}{L}\,\langle i\rangle_1 - \frac{1}{L}\,\langle v_C\rangle_1 + \frac{1}{L}\,\langle v_s\rangle_1 \\ \frac{d}{dt}\,\langle v_C\rangle_1 = -j\omega\,\langle v_C\rangle_1 + \frac{1}{C}\,\langle i\rangle_1 \end{cases} \tag{5.42}$$

The quantities $\langle i\rangle_1(t)$ and $\langle v_C\rangle_1(t)$ are the complex slowly time-varying signals whose magnitudes give the envelope of the resonant tank current and the envelope of the voltage across the capacitor C, respectively. To calculate the envelopes, the real and the imaginary parts of the complex Fourier coefficients are necessary and so each equation of (5.42) needs to be split accordingly. Using the following definitions:

$$\begin{cases} \langle i \rangle_1 (t) = i_{Re}(t) + j\, i_{Im}(t) \\ \langle v_C \rangle_1 (t) = v_{C,Re}(t) + j\, v_{C,Im}(t) \end{cases} \tag{5.43}$$

The complex model (5.42) turns into a model which involves real quantities:

$$\begin{cases} \frac{d\, i_{Re}}{dt} = \omega\, i_{Im} - \frac{R}{L}\, i_{Re} - \frac{1}{L}\, v_{C,Re} + \frac{1}{L}\, v_{s,Re} \\ \frac{d\, i_{Im}}{dt} = -\omega\, i_{Re} - \frac{R}{L}\, i_{Im} - \frac{1}{L}\, v_{C,Im} + \frac{1}{L}\, v_{s,Im} \\ \frac{d\, v_{C,Re}}{dt} = \omega\, v_{C,Im} + \frac{1}{C}\, i_{Re} \\ \frac{d\, v_{C,Im}}{dt} = -\omega\, v_{C,Re} + \frac{1}{C}\, i_{Im} \end{cases} \tag{5.44}$$

The quantities $i_{Re}(t)$, $i_{Im}(t)$, $v_{C,Re}(t)$ and $v_{C,Im}(t)$ are the state variables of the GSSA model that can be collected together in the vector $\mathbf{x}$. As it happens with the LPT and with the MVLT methods, the order of the system which involves the envelopes of the high-frequency modulated signals is twice the order of the original system (cf. (5.44) and (5.41)).

The inputs of the system (5.44) ($v_{s,Re}(t)$ and $v_{s,Im}(t)$) can be obtained applying (5.2) to (5.40). Under the hypothesis that $v_{env}(t)$ is much slower than the carrier $\cos(\omega t)$ of $v_s(t)$, it can be considered almost constant inside the period of integration $T = \frac{2\pi}{\omega}$. Taking into account this assumption, the inputs are given by:

$$\begin{cases} v_{s,Re}(t) = \frac{v_{env}(t)}{2} \\ v_{s,Im}(t) = 0 \end{cases} \tag{5.45}$$

The model (5.44) can be then expressed in matrix form as:

$$\frac{d\mathbf{x}(t)}{dt} = \mathbf{A}\,\mathbf{x} + \mathbf{b}\, v_{env}(t) \tag{5.46}$$

where

$$\mathbf{A} = \begin{bmatrix} -\frac{R}{L} & \omega & -\frac{1}{L} & 0 \\ -\omega & -\frac{R}{L} & 0 & -\frac{1}{L} \\ \frac{1}{C} & 0 & 0 & \omega \\ 0 & \frac{1}{C} & -\omega & 0 \end{bmatrix}, \qquad \mathbf{b} = \begin{bmatrix} \frac{1}{2}\frac{1}{L} \\ 0 \\ 0 \\ 0 \end{bmatrix} \tag{5.47}$$

To completely define the GSSA state space model, the output matrix remains to be found. Let us consider the envelope of the current i as the output quantity. According to (5.4), it is given by the following nonlinear function:

$$y = i_{env}(t) = 2\,|\langle i \rangle_1 (t)| = 2\sqrt{i_{Re}^2(t) + i_{Im}^2(t)} \tag{5.48}$$

To use the powerful tools of the linear algebra, equation (5.48) has to be linearized around the working point $\mathbf{X_0}$ and this operation leads to an equation similar to (5.26):

$$\begin{aligned} \tilde{y}(t) = \tilde{i}_{env}(t) &\approx 2\,\frac{I_{Re,i}}{\sqrt{I_{Re,i}^2 + I_{Im,i}^2}}\,\tilde{i}_{Re}(t) + 2\,\frac{I_{Im,i}}{\sqrt{I_{Re,i}^2 + I_{Im,i}^2}}\,\tilde{i}_{Im}(t) \\ &\approx 2\,\cos(\phi_i)\,\tilde{i}_{Re}(t) + 2\,\sin(\phi_i)\,\tilde{i}_{Im}(t) \end{aligned} \tag{5.49}$$

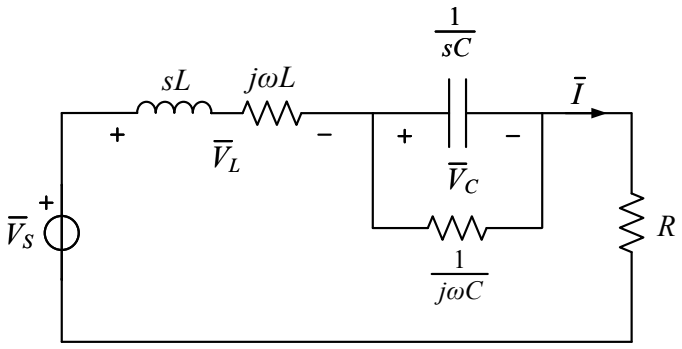

Fig. 5.5: LPT method application to the circuit of Fig. 5.4(a).

In (5.49), the capital letters indicates the steady-state values of the respective quantities and ϕ_i is the steady-state angle of $\langle i \rangle_1$ with respect to the angle of $\langle v_s \rangle_1$ which by definition is 0. It has been shown in Ch. 3 that, when the series resonant tank is fed with a voltage source tuned to the resonant frequency of the system, the current $i(t)$ is in phase with $v_s(t)$. For this reason, $\phi_i = 0$ and (5.49) can be simplified as:

$$\tilde{y}(t) = \tilde{i}_{env}(t) \approx 2\,\tilde{i}_{Re}(t) \tag{5.50}$$

Equation (5.50) can be written as:

$$\tilde{y}(t) = \mathbf{c}\,\tilde{\mathbf{x}} \qquad \text{with} \quad \mathbf{c} = \begin{bmatrix} 2 & 0 & 0 & 0 \end{bmatrix} \tag{5.51}$$

where $\tilde{\mathbf{x}}$ indicates the small-variation of the state vector around $\mathbf{X}_0$.

The transfer function which links the envelope of the resonant tank current to the envelope of the input voltage source can be found with the usual equation:

$$G_{i,GSSA}(s) = \mathbf{c}\,(s\,\mathbf{I} - \mathbf{A})^{-1}\,\mathbf{b} \tag{5.52}$$

where $\mathbf{I}$ is the identity matrix.

5.2.2 LPT Method Application

While the GSSA method utilizes the transformation (5.2) on the state space equations of the circuit of Fig. 5.4(a), the LPT method works directly on it. Applying the transformations of Fig. 5.2 to each element that forms the series resonant tank, the Laplace phasor transformed circuit of Fig. 5.5 is found. All the quantities shown in the scheme represent the Laplace transforms of the complex phasors whose amplitudes are the envelopes for the signals of the circuit of Fig. 5.4(a).

The relation between the Laplace transform of the complex phasor $\bar{i}(t)$ and the Laplace transform of $\bar{v}_s$ can be easily obtained once the input impedance of the circuit is found. It is given by:

$$\begin{aligned} Z_s(s) &= R + sL + j\,\omega L + \frac{1}{sC + j\,\omega C} \\ &= \frac{1 - \omega^2 LC + sRC + s^2 LC + j\,\omega\,(RC + s\,2LC)}{sC + j\,\omega C} \end{aligned} \tag{5.53}$$

The transfer function which links the complex phasors is then given by:

$$G_{i,phas}(s) = \frac{\bar{I}(s)}{\bar{V}_s(s)} = \frac{1}{Z_s(s)} = \frac{sC + j\,\omega C}{1 - \omega^2 LC + sRC + s^2 LC + j\,\omega\,(RC + s\,2LC)} \tag{5.54}$$

To find the transfer function which links the envelope of the current i to the envelope of the input voltage source v_s, it is possible to proceed in the same way as with the MVLT method. The first thing to do is to split the transfer function (5.54) into the real and the imaginary parts ($G_{i,phas}(s) = G_{Re}(s) + j\,G_{Im}(s)$). The desired transfer function can be obtained then through an equation similar to (5.28). Under the hypotheses made for this study case, the current i of the resonant tank is always in phase with the voltage source v_s. For this reason, the angle ϕ_i in (5.28) is 0 and the envelope transfer function coincides with $G_{Re}(s)$:

$$G_{i,LPT}(s) = \frac{I_{env}(s)}{V_{s,env}(s)} = \frac{sC\,(1 - \omega^2 LC + sRC + s^2 LC) + \omega^2 C\,(RC + s\,2LC)}{(1 - \omega^2 LC + sRC + s^2 LC)^2 + \omega^2\,(RC + s\,2LC)^2} \tag{5.55}$$

The real part of the transfer function $G_{i,phas}(s)$ is obtained through (5.32).

5.2.3 MVLT Method Application

The reason for the introduction of a new modeling method is that with both the GSSA and the LPT methods the direct link between the "instantaneous model" and the "envelope model" is lost. This link is maintained by the MVLT method which thus can provide better insight into the envelope model.

The starting point of the MVLT method application is the transfer function which links the real quantities of the resonant tank. In particular, the transfer function which links the current to the input voltage source is given by (3.13) and here is rewritten for simplicity:

$$G(s) = \frac{I(s)}{V_s(s)} = \frac{sC}{1 + sRC + s^2 LC} \tag{5.56}$$

The second step is to calculate $G(s + j\,\omega)$:

$$G(s + j\omega) = \frac{(s + j\omega)\,C}{1 + (s + j\omega)\,RC + (s + j\omega)^2\,LC} \tag{5.57}$$

A comparison between (5.57) and (5.54) shows that the two complex transfer functions are identical. For this reason, the application of (5.29) to find the transfer function for the envelopes $G_{i,MVLT}(s)$ produces the same result of the LPT method (see (5.55)).

Tab. 5.1: Parameters of the series resonant tank implemented in Simulink.

Parameter	Symbol	Value
Voltage source angular frequency	ω	$2\pi\,85000\,\frac{\text{rad}}{\text{s}}$
Inductance	L	$120\,\mu\text{H}$
Capacitance	C	$29\,\text{nF}$
Load resistance	R	$7\,\Omega$

5.2.4 Methods Comparison

The envelope transfer functions ($G_{i,GSSA}(s)$, $G_{i,LPT}(s)$ and $G_{i,MVLT}(s)$) carried out with the three modeling methods applied to the series resonant tank are equivalent. Equations (5.52) and (5.55) (which is the same for the MVLT method) result in the same expression given by:

$$G_{env}(s) = \frac{I_{env}(s)}{V_{env}(s)} = \frac{1}{R}\,\frac{1 + \frac{2L}{R}\,s + \frac{1}{\omega^2}\,s^2 + \frac{L}{R}\frac{1}{\omega^2}\,s^3}{1 + \frac{4L}{R}\,s + \left(\frac{1}{\omega^2} + 4\frac{L^2}{R^2}\right)\,s^2 + \frac{L}{R}\frac{1}{\omega^2}\,s^3 + \frac{L^2}{R^2}\frac{1}{\omega^2}\,s^4} \tag{5.58}$$

To validated the model, the transfer function (5.58) has been imported in Simulink where the step response has been obtained. In the same environment, with the aid of SimPowerSystems, the system of Fig. 5.4(a) with the parameters found in Tab. 5.1 has been simulated and the real waveform of the current has been acquired[9].

The input of the series resonant tank implemented in Simulink is a sinusoidal signal whose amplitude has been changed during the simulation (cf. (5.40)). The variation in the amplitude has been made with a step (at 20 ms) equal to the one used as the input of the envelope model (5.58) (the amplitude of the step is 65 V) and which has been superposed to the steady-state amplitude of $300V$. The output of the real system and the output of the envelope model (superposed to the steady-state value of the resonant tank current) have been plotted in Fig. 5.6.

The figure shows that the output of the model (the blue thick line) corresponds with good agreement to the envelope of the resonant tank current, plotted in Fig. 5.6 with a black thin line. This result is the proof of the validity of the three modeling methods.

According to the value of Tab. 5.1 and using the technique described in [38, p. 289], the zeros and the poles of the envelope transfer function can be roughly obtained. The transfer function (5.58) can be approximated as follows:

$$G_{env}(s) \approx \frac{1}{R}\,\frac{\left(1 + \frac{R}{4L}\frac{1}{\omega^2}\,s + \frac{1}{2\omega^2}\,s^2\right)}{\left(1 + 2\frac{L}{R}\,s\right)\,\left(1 + \frac{1}{4}\frac{R}{L}\frac{1}{\omega^2}\,s + \frac{1}{4\omega^2}\,s^2\right)} \tag{5.59}$$

in which a zero-pole cancellation $\left(1 + 2\frac{L}{R}\,s\right)$ has occurred. Equation (5.59) can be used to roughly validate the analysis done regarding the relation between the poles of the real transfer function and the ones of the envelope transfer function.

[9] The real waveform of the current could be obtained also as the output of the transfer function (5.56).

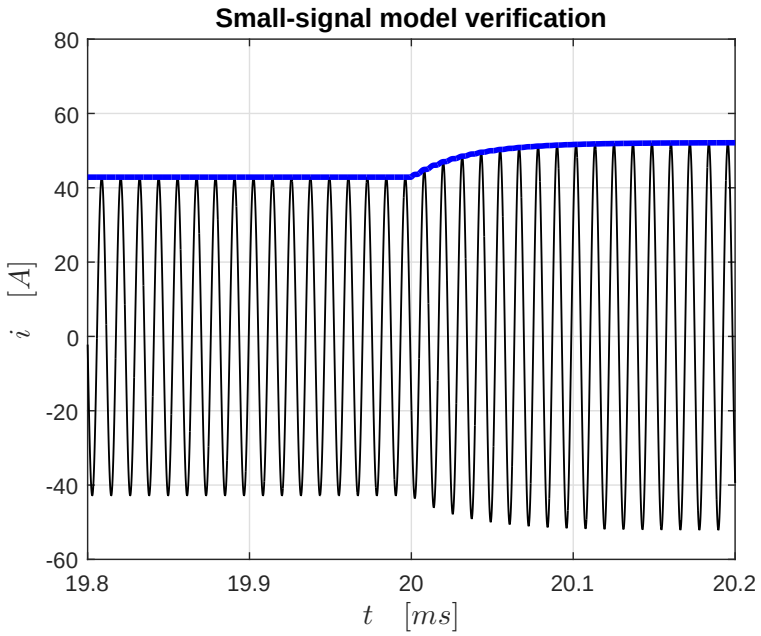

Fig. 5.6: Validation of the envelope model (5.58).

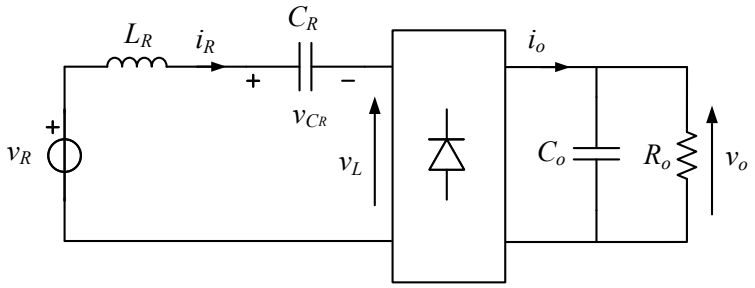

Fig. 5.7: Series-compensated receiving stage of a WPTS.

5.3 Application of the Modeling Methods to the Receiving Stage of a WPTS

The series resonant tank has been a simple example to well understand how the various modeling methods can be applied. Let us try now to model the dynamic behavior of a series-compensated receiving stage of a WPTS. The circuit is shown in Fig. 5.7, where the box with a diode depicted represents a diode rectifier. The main difference between this circuit and the series resonant tank (at least for what concerns the modeling purpose) is the non-linearity of the series-compensated receiver caused by the presence of the rectifier.

For the analysis it is assumed that the diode rectifier works in CCM and the capacitor C_o is large enough to make the ripple of the output voltage v_o negligible. Furthermore the quality factor of the resonant tank is high to force the current i_R to be almost sinusoidal. This is a valid assumption in particular because the voltage v_R induced into the receiver is considered a modulated signal with a sinusoidal

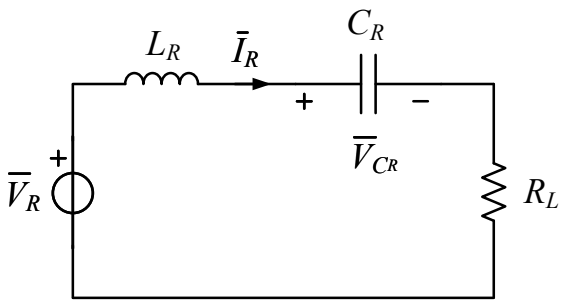

Fig. 5.8: Circuit for the study of the steady-state operation of the series-compensated receiver of Fig. 5.7.

carrier. The frequency of the carrier is equal to the natural frequency of the resonant tank. These hypotheses entail the following consequences:

- The rectifier input voltage v_L is a square wave that is always in phase with the sinusoidal current $i_R(t)$;
- the rectifier output current $i_o(t)$ is equal to the absolute value of the current $i_R(t)$;
- only the dc component of the current $i_o(t)$ significantly contributes to the dynamic behavior of the rectifier output voltage $v_o(t)$.

As it has been shown in the previous sections, to linearize the various models, the steady-state operation of the real system is required. The steady-state for the series-compensated receiver of Fig. 5.7 can be assessed from the circuit of Fig. 5.8. The figure shows that the steady-state operation of the series-compensated receiver is equivalent to the one of the series resonant tank where, as explained in Ch. 2, the resistance R_L is related to the load resistance R_o through the relation $R_L = \frac{8}{\pi^2} R_o$. Since the frequency of the sinusoidal voltage source is equal to the resonant frequency of the series resonant tank (for hypothesis), the steady-state values for the state variables of the circuit in Fig. 5.7 can be obtained with (3.4) that here is modified to fit this particular nomenclature:

$$\begin{cases} \bar{I}_R = \frac{\bar{V}_R}{R_L} \\ \bar{V}_{C_R} = -j\frac{1}{\omega C_R}\bar{I}_R = -j\frac{1}{\omega C_R}\frac{\bar{V}_R}{R} \end{cases} \tag{5.60}$$

In particular what it is necessary to know is that the current i_R, in steady-state conditions, is in phase with the induced voltage v_R.

5.3.1 GSSA Model

The starting point of the GSSA method is always the state space model of the real system. The state space model of the series-compensated receiver of Fig. 5.7 can be written as:

$$\begin{cases} \frac{di_R}{dt} = -\frac{1}{L_R}\, v_o\, \mathrm{sgn}(i_R) - \frac{1}{L_R}\, v_{C_R} + \frac{1}{L_R}\, v_R \\ \frac{dv_{C_R}}{dt} = \frac{1}{C_R}\, i_R \\ \frac{dv_o}{dt} = \frac{1}{C_o}\, \mathrm{sgn}(i_R)\, i_R - \frac{1}{R_o C_o}\, v_o \end{cases} \tag{5.61}$$

where $\mathrm{sgn}(\cdot)$ indicates the signum function[10]. As can be seen, this function introduces some non-linearities into the real system. Since the current i_R is sinusoidal, it is not possible to find a reasonable working point around which linearize the real system. This is one of the reason that led to the development of the "average" models. The "average" model with the GSSA method is obtained using the transformation (5.2). This operator applied to the state space model (5.61) produces:

$$\begin{cases} \frac{d}{dt}\langle i_R\rangle_1 = -j\omega\, \langle i_R\rangle_1 - \frac{1}{L_R}\, \langle v_o\, \mathrm{sgn}(i_R)\rangle_1 - \frac{1}{L_R}\, \langle v_{C_R}\rangle_1 + \frac{1}{L_R}\, \langle v_R\rangle_1 \\ \frac{d}{dt}\langle v_{C_R}\rangle_1 = -j\omega\, \langle v_{C_R}\rangle_1 + \frac{1}{C_R}\, \langle i_R\rangle_1 \\ \frac{d}{dt}\langle v_o\rangle_0 = \frac{1}{C_o}\, \langle \mathrm{sgn}(i_R)\, i_R\rangle_0 - \frac{1}{R_o C_o}\, \langle v_o\rangle_0 \end{cases} \tag{5.62}$$

in which the property (5.8) has already been applied. One should note that, in the first two state equations, the complex 1-st Fourier coefficients of the current i_R and of the voltage across the capacitor v_{C_R} have been considered as the new state variables for the average model. On the contrary, since the dc component of v_o dominates its behavior, only the real 0-th coefficient has been taken into account for the rectifier output voltage.

To find a useful expression for the $\langle \mathrm{sgn}(i_R)\, v_o\rangle_1$ and $\langle \mathrm{sgn}(i_R)\, i_R\rangle_0$ terms in (5.62), property (5.9) has to be used. Since the function $\mathrm{sgn}(i_R)$ is a square wave of unitary amplitude in phase with the current i_R, its dominant Fourier coefficient is the 1-st and it is given by:

$$\langle \mathrm{sgn}(i_R)\rangle_1 = \frac{2}{\pi} e^{j\varphi_{i_R}} \tag{5.63}$$

where $\varphi_{i_R}(t)$ is the phase of the complex signal $\langle i_R\rangle_1$ with respect to the phase of $\langle v_R\rangle_1$. Retaining only the significant terms in the convolution sum of (5.9), the required expressions can be written as:

$$\langle \mathrm{sgn}(i_R)\, v_o\rangle_1 \cong \langle \mathrm{sgn}(i_R)\rangle_1\, \langle v_o\rangle_0 \tag{5.64}$$

$$\begin{aligned} \langle \mathrm{sgn}(i_R)\, i_R\rangle_0 &\cong \langle \mathrm{sgn}(i_R)\rangle_1^*\, \langle i_R\rangle_1 + \langle \mathrm{sgn}(i_R)\rangle_1\, \langle i_R\rangle_1^* = \\ &= 2\Re\{\langle \mathrm{sgn}(i_R)\rangle_1^*\, \langle i_R\rangle_1\} \end{aligned} \tag{5.65}$$

Since the complex signals $\langle \mathrm{sgn}(i_R)\rangle_1$ and $\langle i_R\rangle_1$ are always in phase, the expression in (5.65) inside the curly brackets is real and $\langle \mathrm{sgn}(i_R)\, i_R\rangle_0$ becomes:

$$\langle \mathrm{sgn}(i_R)\, i_R\rangle_0 = 2\, |\langle \mathrm{sgn}(i_R)\rangle_1| \cdot |\langle i_R\rangle_1| = \frac{2}{\pi}\, 2|\langle i_R\rangle_1| \tag{5.66}$$

[10] It is worth noting that the function $\mathrm{sgn}(i_R)\, i_R$ in (5.61) is nothing else but the absolute value of $i_R(t)$.

Apart from the mathematical derivation, from the physical point of view (5.66) represents the average value of the current i_o if the current i_R would be pure sinusoidal.

Substituting (5.66) and (5.64) into (5.62), we obtain:

$$\begin{cases} \frac{d}{dt}\langle i_R\rangle_1 = -j\omega\,\langle i_R\rangle_1 - \frac{1}{L_R}\,\langle v_o\rangle_0\,\frac{2}{\pi}\,e^{j\varphi_{i_R}} - \frac{1}{L_R}\,\langle v_{C_R}\rangle_1 + \frac{1}{L_R}\,\langle v_R\rangle_1 \\ \frac{d}{dt}\langle v_{C_R}\rangle_1 = -j\omega\,\langle v_{C_R}\rangle_1 + \frac{1}{C_R}\,\langle i_R\rangle_1 \\ \frac{d}{dt}\langle v_o\rangle_0 = \frac{1}{C_o}\,\frac{4}{\pi}|\,\langle i_R\rangle_1\,| - \frac{1}{R_oC_o}\,\langle v_o\rangle_0 \end{cases} \tag{5.67}$$

Using a notation similar to the one employed in the derivation of the GSSA model for the series resonant tank, the complex Fourier coefficients in (5.67) can be split into real and imaginary part:

$$\begin{cases} \frac{d\,i_{R,Re}}{dt} = \omega\,i_{R,Im} - \frac{1}{L_R}\,\frac{2}{\pi}\,\cos(\varphi_{i_R})\,\langle v_o\rangle_0 - \frac{1}{L_R}\,v_{C_{R,Re}} + \frac{1}{L_R}\,v_{R,Re} \\ \frac{d\,i_{R,Im}}{dt} = -\omega\,i_{R,Re} - \frac{1}{L_R}\,\frac{2}{\pi}\,\sin(\varphi_{i_R})\,\langle v_o\rangle_0 - \frac{1}{L_R}\,v_{C_{R,Im}} + \frac{1}{L_R}\,v_{R,Im} \\ \frac{d\,v_{C_{R,Re}}}{dt} = \omega\,v_{C_{R,Im}} + \frac{1}{C_R}\,i_{R,Re} \\ \frac{d\,v_{C_{R,Im}}}{dt} = -\omega\,v_{C_{R,Re}} + \frac{1}{C_R}\,i_{R,Im} \\ \frac{d}{dt}\langle v_o\rangle_0 = \frac{1}{C_o}\,\frac{4}{\pi}\sqrt{i_{R,Re}^2 + i_{R,Im}^2} - \frac{1}{R_oC_o}\,\langle v_o\rangle_0 \end{cases} \tag{5.68}$$

where

$$\cos(\varphi_{i_R}) = \frac{i_{R,Re}}{\sqrt{i_{R,Re}^2 + i_{R,Im}^2}} \tag{5.69}$$

$$\sin(\varphi_{i_R}) = \frac{i_{R,Im}}{\sqrt{i_{R,Re}^2 + i_{R,Im}^2}} \tag{5.70}$$

As can be seen, the system (5.68) is still non-linear. However, now it can be linearized according to the steady-state values of the state variables found in (5.60). Considering also that the voltage v_R is of the form (5.40), the small-signal GSSA model for the series-compensated receiver of Fig. 5.7 can be obtained:

$$\begin{cases} \frac{d\,\tilde{i}_{R,Re}}{dt} = \omega\,\tilde{i}_{R,Im} - \frac{1}{L_R}\,\tilde{v}_{C_{R,Re}} - \frac{1}{L_R}\,\frac{2}{\pi}\,\langle\tilde{v}_o\rangle_0 + \frac{1}{2L}\,\tilde{v}_{env} \\ \frac{d\,\tilde{i}_{R,Im}}{dt} = -\omega\,\tilde{i}_{R,Re} - \frac{1}{L_R}\,\frac{8}{\pi^2}R_o\,\tilde{i}_{R,Im} - \frac{1}{L_R}\,\tilde{v}_{C_{R,Im}} \\ \frac{d\,\tilde{v}_{C_{R,Re}}}{dt} = \omega\,\tilde{v}_{C_{R,Im}} + \frac{1}{C_R}\,\tilde{i}_{R,Re} \\ \frac{d\,\tilde{v}_{C_{R,Im}}}{dt} = -\omega\,\tilde{v}_{C_{R,Re}} + \frac{1}{C_R}\,\tilde{i}_{R,Im} \\ \frac{d}{dt}\langle\tilde{v}_o\rangle_0 = \frac{1}{C_o}\,\frac{4}{\pi}\,\tilde{i}_{R,Re} - \frac{1}{R_oC_o}\,\langle\tilde{v}_o\rangle_0 \end{cases} \tag{5.71}$$

Once again, the tilde indicates the small-signal quantities.

Considering the envelope of the current i_R as the output of the model and linearizing the respective equation as it has been done with (5.48), the state matrix

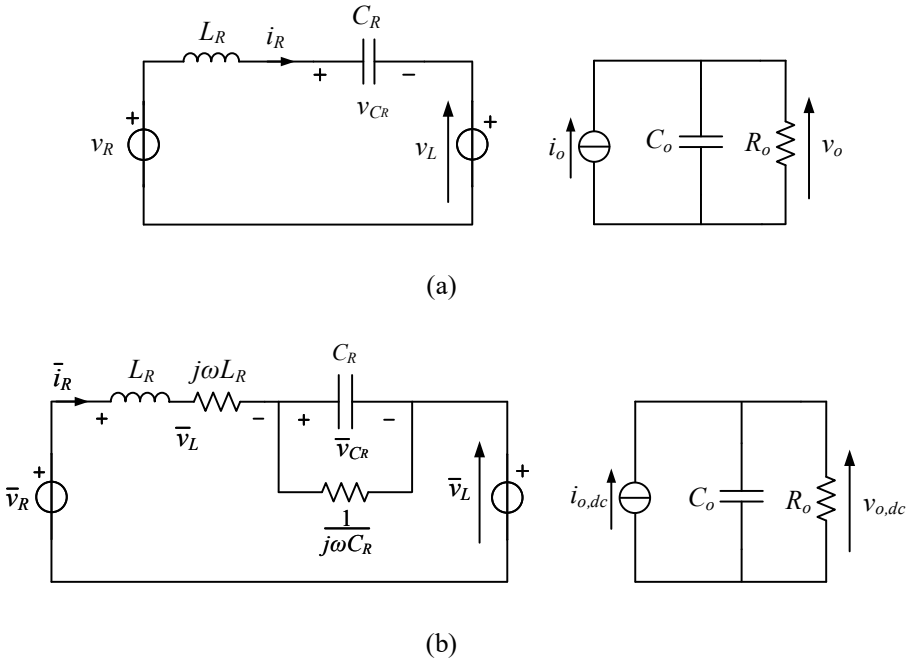

Fig. 5.9: Equivalent circuit of the series-compensated receiver of Fig. 5.7 (a) and circuit after the application of the phasor transform (b).

A, the input vector **b** and the output vector **c** of the GSSA model for the series-compensated receiver are found to be:

$$\mathbf{A} = \begin{bmatrix} 0 & \omega & -\frac{1}{L_R} & 0 & -\frac{1}{L_R}\frac{2}{\pi} \\ -\omega & -\frac{1}{L_R}R_L & 0 & -\frac{1}{L_R} & 0 \\ \frac{1}{C_R} & 0 & 0 & \omega & 0 \\ 0 & \frac{1}{C_R} & -\omega & 0 & 0 \\ \frac{1}{C_o}\frac{4}{\pi} & 0 & 0 & 0 & -\frac{1}{R_o C_o} \end{bmatrix}, \quad \mathbf{b} = \begin{bmatrix} \frac{1}{2}\frac{1}{L_R} \\ 0 \\ 0 \\ 0 \\ 0 \end{bmatrix} \tag{5.72}$$

$$\mathbf{c} = \begin{bmatrix} 2 & 0 & 0 & 0 & 0 & 0 \end{bmatrix}$$

The transfer function between the envelope of the induced voltage v_R and the envelope of the current i_R can be obtained with (5.52).

5.3.2 LPT Model

Due to the presence of the diode rectifier, the application of the LPT to the circuit of Fig. 5.7 is not so trivial. To deal with the rectifier it is more convenient to consider the circuit of Fig. 5.9(a). It is perfectly equivalent to the one of Fig. 5.7, but it highlights the circuit for the ac quantities and the circuit for the dc quantities.

The LPT for the single components (illustrated in Fig. 5.2) has a physical reason only if it is applied to the elements of the ac circuit. In fact it simplifies the modeling of the circuit by replacing the relations between the high-frequency

quantities with the ones between the slowly time-varying complex phasors. For the quantities in the dc circuit it is not necessary to introduce the phasor transform, since the modeling can be simplified by just considering their dc components.

The phasor transform applied to the ac circuit of Fig. 5.9(a) leads to the circuit of Fig. 5.9(b). In the figure, the phasor transformed circuit is drawn together with the circuit downstream the rectifier in which only the dc components of the quantities have been retained.

The phasor transformed circuit and the dc circuit of Fig. 5.9(b) are not independent one each other. In fact, the rectifier output current i_o is the absolute value of the current i_R. Since, with the hypotheses made, the current i_R can be considered a sinusoidal signal with a slowly variable amplitude, the average value of the current i_o can be written as:

$$i_{o,dc} = \int_{t-T}^{t} |i_R(t)|\, dt = \frac{2}{\pi}\, i_{R,env} \tag{5.73}$$

The envelope of the current i_R is related to the complex phasor $\bar{i}_R$ through (5.11) and so (5.73) can be rewritten as:

$$i_{o,dc} = \frac{2}{\pi}\, |\bar{i}_R| = \frac{2}{\pi}\, \bar{i}_R\, e^{-j\,\varphi_{i_R}} \tag{5.74}$$

where $\varphi_{i_R}(t)$ is the instantaneous phase of the dynamic phasor $\bar{i}_R$ with respect to the phase of $\bar{v}_R$.

Equation (5.74) links the dc circuit to the ac circuit. In the same way, there is an influence of the dc circuit on the ac stage. Indeed, the complex phasor $\bar{v}_L$ depends on (the average value of) the rectifier output voltage v_o ($v_{o,dc}$) as follows:

$$\bar{v}_L = \frac{4}{\pi}\, v_{o,dc}\, e^{j\,\varphi_{i_R}} \tag{5.75}$$

Equation (5.75) descends from the fact that the voltage v_L is a square wave in phase with the current i_R. For the modeling purpose, the square wave v_L can be replaced with its fundamental $v_{L,1}$ due to the good filtering action of the resonant tank. The application of the phasor transform (5.10) to $v_{L,1}$ leads to (5.75).

It can be noticed that neither (5.74) nor (5.75) are linear and this is caused by the presence of $\varphi_{i_R}(t)$ that is function of the state variable $\bar{i}_R$. As a consequence, the equations that describe both the ac and the dc circuits are non-linear. An attempt to use the Laplace transform on the circuit of Fig. 5.9(b) does not bring any benefit. It is necessary to find a sort of small-signal circuit before shifting the analysis in s-domain.

The linearization of the circuit of Fig. 5.9(b) can be done considering that, if the variations of the quantities involved in the receiver are not so large, the angle of the complex phasor $\bar{i}_R$ is likely to remain almost constant[11]. This assumption can be proved simulating the behavior of the circuit after a small perturbation of the envelope of the voltage v_R. The result can be observed in Fig. 5.10. The upper graph of the figure shows the normalized value of the current i_R together with the normalized value of the voltage v_R. It can be seen that at $t = 20\,ms$ the

[11] This can be not true if the quantities involved in the circuit are frequency-modulated.

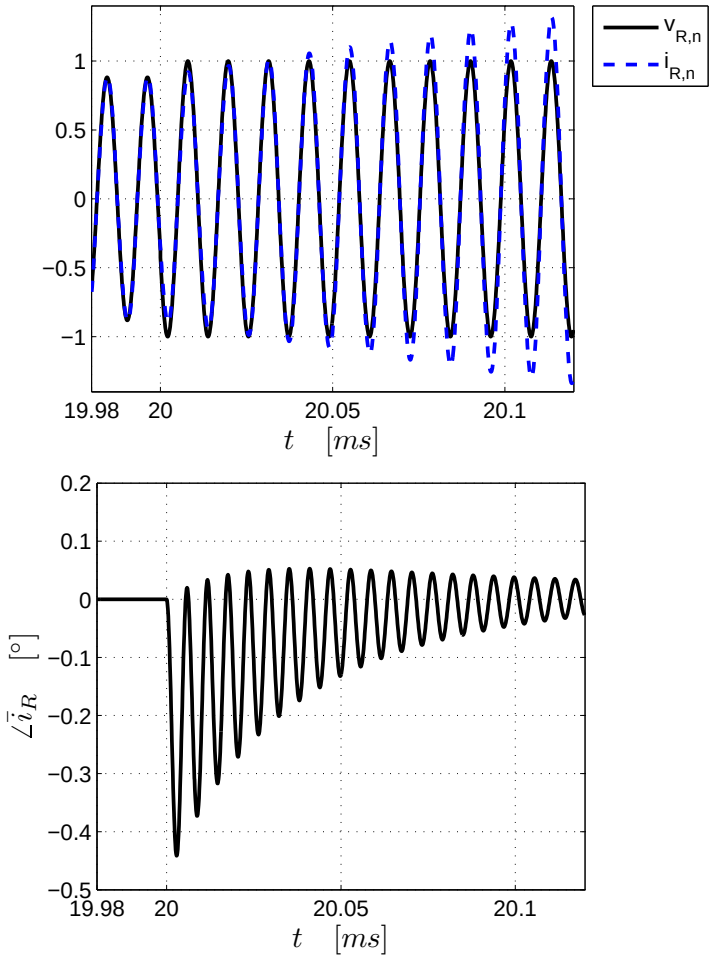

Fig. 5.10: Current i_R (normalized) after a small perturbation of the voltage v_R (normalized) at 20 ms (upper plot). Phase of the current i_R with respect to the phase of the voltage v_R under the transient condition (lower plot).

amplitude of v_R has been changed with a step. In the successive instants, a rapid increment of the amplitude of i_R is observed. Nevertheless, the current i_R remains almost in phase with the voltage v_R for all the transient period. This fact, can be verified looking at the lower graph of Fig. 5.10, where the phase $\varphi_{i_R}(t)$ of the current i_R (which coincides with the phase of $\bar{i}_R$) is displayed. The phase variation is contained within an interval less than 1°. The result obtained in Fig. 5.10 with a particular choice for the parameters of the circuit of Fig. 5.9(a) can be generalized.

In the light of the above achievements, it is possible to state that in the small-signal versions of the equations (5.75) and (5.74), the variable φ_{i_R} can be considered constant and in general equal to ϕ_{i_R}. Now it is convenient to use the Laplace transform, which applied to (5.74) results in:

$$I_o(s) = \frac{2}{\pi}\,\bar{I}_R(s)\,e^{-j\,\phi_{i_R}} \tag{5.76}$$

where $I_o(s)$ and $\bar{I}_R(s)$ are the Laplace transforms of the small-signal $\tilde{i}_{o,dc}$ and $\tilde{\bar{i}}_R$, respectively.

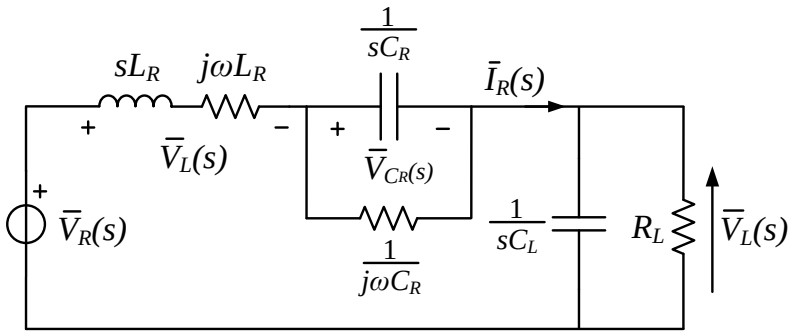

Fig. 5.11: LPT method applied to the small-signal version of the series-compensated receiver of Fig. 5.9(b).

By studying the dc circuit of Fig. 5.9(b) in s-domain and using (5.76), the Laplace transform $V_o(s)$ of the small-signal (dc component of the) rectifier output voltage $\tilde{v}_{o,dc}$ is found to be:

$$V_o(s) = \frac{2}{\pi} \frac{R_o}{1 + R_o C_o\, s} \bar{I}_R(s)\, e^{-j\,\phi_{i_R}} \tag{5.77}$$

Applying the Laplace transform to the small-signal version of (5.75) and substituting (5.77) for the Laplace transform of $\tilde{v}_{o,dc}$, the Laplace transform of $\tilde{\bar{v}}_L$ can be written as:

$$\bar{V}_L(s) = \frac{8}{\pi^2} \frac{R_o}{1 + R_o C_o\, s} \bar{I}_R(s) = \frac{R_L}{1 + R_L C_L\, s} \bar{I}_R(s) \tag{5.78}$$

where $C_L = \frac{\pi^2}{8} C_o$. The last equality of (5.78) shows that the small-signal complex phasor $\tilde{\bar{v}}_L$ can be obtained as the voltage across the parallel of the equivalent resistance R_L and the equivalent capacitor C_L when it is flown by the complex phasor $\tilde{\bar{i}}_R$. The LPT applied to the small-signal version of the ac circuit of Fig. 5.9(b) produces the circuit of Fig. 5.11.

The circuit of Fig. 5.11 can be studied as the one in Fig. 5.5 for the resonant tank, in order to obtain the transfer function $G_{i,phas}(s)$ that links the complex phasor of the current i_R to the complex phasor of v_R. The transfer function which links the envelope is then equal to $G_{Re}(s)$ (cf. (5.28)), since the steady-state value of the initial phase ϕ_i of complex phasor $\bar{i}_R$ around which the linearization is performed is 0.

5.3.3 MVLT Model

The modeling of the rectifier of Fig. 5.7 with the MVLT method is closely related to the modeling done with the LPT method.

With the MVLT method, the analysis is shifted from a framework where there are the high-frequency signals to one in which the slowly varying envelopes are involved, by simply calculating the transfer function of the system $G(s)$ in $s + j\,\omega$. Since the (dc components of the) quantities of the dc circuit of Fig. 5.9(a) are

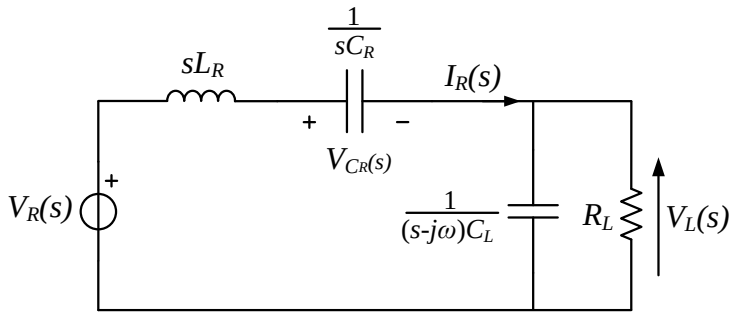

Fig. 5.12: Fictitious circuit for the derivation of $G(s)$ for the MVLT method application to the series-compensated receiver of Fig. 5.7.

already proportional to the envelope of some quantities of the ac circuit (cf. (5.74)), the Laplace transform applied to the ODE that governs this system does not have to be calculated in $s + j\,\omega$ (but simply in s). For this reason, it is necessary to introduce a fictitious circuit (see Fig. 5.12) from which a fictitious transfer function $G(s)$ can be obtained.

It can be noticed that in Fig. 5.12 the dc circuit (Laplace transformed) of Fig. 5.9(a) has been reflected into the ac circuit (Laplace transformed) by simply preprocessing the input-to-output transfer function of the capacitor C_o, which has been considered equal to $\frac{1}{(s-j\omega)C_L}$. Please note that in the ac side the capacitor C_o and the resistance R_o have become respectively C_L and R_L, with the definitions introduced before.

From the circuit of Fig. 5.12, the transfer function $G(s)$ can be derived. It is no more a transfer function with real coefficients as it happens in case of linear systems. Once $G(s)$ is calculated in $s + j\omega$ as indicated by the MVLT method, the obtained transfer function is identical to $G_{i,phas}(s)$ of the LPT method. Thus LPT and MVLT methods produce the same result.

5.3.4 Models comparison

It has been just shown that the models obtained with the LPT and with the MVLT methods are identical. Contrary to what happens in the series resonant tank study case, here the model obtained with the GSSA method is slightly different from them. One evidence of this is provided by the fact that the order of the three models are different. Indeed, the model obtained with the GSSA method (cf. matrices (5.72)) is of the 5-th order. This is simply because the complex Fourier coefficients introduce two state variables in the GSSA model (the real and the imaginary parts), whereas the 0-th real Fourier coefficient produces a single new state variable. The models achieved with the LPT and the MVLT methods instead, have an order equal to 6. This is due to the splitting of the transfer function $G_{i,phas}(s)$ (or equivalently $G(s + j\omega)$) into the real and the imaginary part.

An analytical expression for a 5-th order and for a 6-th order model is quite

Tab. 5.2: Values used in the numerical analysis for the parameters of the series-compensated receiver of Fig. 5.7.

Parameter	Symbol	Value
Induced voltage angular frequency	ω	$2\pi\,85000\,\frac{\text{rad}}{\text{s}}$
Resonant inductance	L_R	$120\,\mu\text{H}$
Resonant capacitance	C_R	$29\,\text{nF}$
Output capacitance	C_o	$300\,\mu\text{F}$
Load resistance	R_o	$7\,\Omega$

Tab. 5.3: Zeros, poles and gains of the transfer functions obtained with the GSSA and with the LPT methods.

	GSSA	LPT
Gain	0.176	0.176
Zeros	-476 $-1.181e4 \pm j\,7.576e5$	-476 $-0.0047 \pm j\,7.58e5$
Poles	$-238.1 \pm j\,3347$ $-1.181e4 \pm j\,1.07e6$	$-238.1 \pm j\,3352$ $-0.0047 \pm j\,1.07e6$

difficult to find. A better insight into the difference of the two models can be attained with a numerical analysis. The matrices (5.72) for the GSSA model have been inserted in MATLAB using the values found in Tab. 5.2 for the parameters that appear in them. The transfer function between the envelope of the current i_R and the envelope of the voltage v_R is then calculated using (5.52).

The transfer function for the LPT method has been computed with a procedure similar to the one used for the series resonant tank and through MuPAD, a tool of MATLAB for the manipulation of symbolic expressions[12]. Then, it has been imported in MATLAB with the same parameters of Tab. 5.2.

The resulting transfer functions have been expressed in the standard Bode form and their related gains, zeros and poles are shown in Tab. 5.3. Surprisingly, the number of the poles in the table is 4 for both the transfer functions and not 5 or 6 as expected. This is because of a real zero-pole cancellation in the GSSA transfer function and because of the cancellation of a complex-conjugate zero pair with a complex-conjugate pole pair in the LPT transfer function. In Tab. 5.3, it is possible to note also that the two transfer functions differ mostly for the real part of a complex zero and of a complex pole; the LPT method produces a model which is less dumped than the GSSA model.

Despite the difference in the structure of the two transfer functions, their step responses are almost indistinguishable (see Fig. 5.13).

In Fig. 5.13, besides the step responses of the two models (which have been superposed to a constant value of about 26.4 A), it is plotted also the real envelope

[12]The MVPT method will not be mentioned anymore in this chapter since its outcomes are perfectly equivalent to the ones of LPT method.

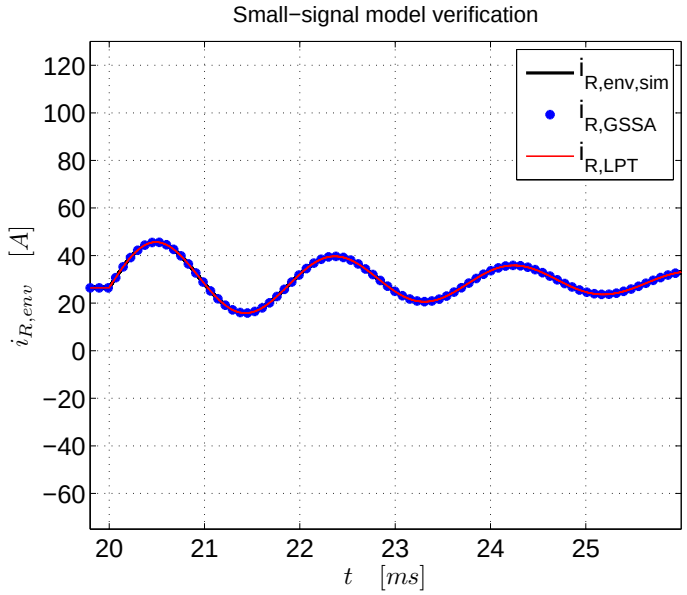

Fig. 5.13: Validation of the GSSA and the LPT model obtained for the series-compensated receiver of Fig. 5.7.

of the current i_R, obtained from the simulation of the circuit of Fig. 5.7. The simulated case refers to a situation where the amplitude of the induced voltage v_R has been changed with a step of 15 V at 20 ms. Before the step the steady-state amplitude of v_R was 150 V.

In Fig. 5.13 it can be observed how fine the step responses of the two models match the real envelope of the current i_R, given that the three curves are perfectly overlapped. However, a difference between the three curves exists if one carefully inspects the graph at a very tiny time scale [119].

Chapter 6

Modeling and Control of an LC-Compensated DWPTS

The purpose of this chapter is to implement a simple control scheme for the the track current of a lumped Dynamic Wireless Power Transfer System (DWPTS). The high working frequency of the DWPTS prevents its instantaneous control because of the fast processing that would be required for the track current, well beyond the capabilities of the modern microcontrollers. Therefore, the control of the DWPTS is carried out by acting on the envelope of the transmitting coil current on account of the fact that it has a sinusoidal waveform.

In this chapter, first of all, the envelope model of the DWPTS is attained through the MVLT method. Then, based on the obtained dynamic model, the regulator that controls the track current is designed through the Bode diagram of the envelope transfer function. At last, the performance of the arranged control system is tested by simulation.

6.1 LC-Compensated DWPTS

The DWPTS considered in this chapter has a lumped track structure (cf. Fig. 2.3). The lumped track DWPTSs can achieve higher efficiencies with respect to the stretched track DWPTSs. In addition, with the DWPTSs having a lumped track structure it is easier to limit the EMI emissions in order to comply with the ICNIRP guidelines. These advantages owned by the lumped track DWPTSs can be accomplished solely if the coils that form the track are selectively energized only when they are coupled with the pickup coil. To this end, it is necessary to adopt a strategy to detect the EVs along the track [121], [122]. When no EV is detected, the power supply should ideally be in the OFF state; no losses are incurred in this state. Upon detecting an incoming EV, the track coil should be rapidly energized at an appropriate time so that both the power transfer time and the operating efficiency are optimized. Continuous transfer of power to a moving EV may be achieved by turning ON and OFF the transmitters sequentially along its direction of travel. This situation is exemplified in Fig. 6.1.

The large variation of the coil coupling and the different levels of power required by the battery at various State Of Charge (SOC) make the control of DWPTSs a

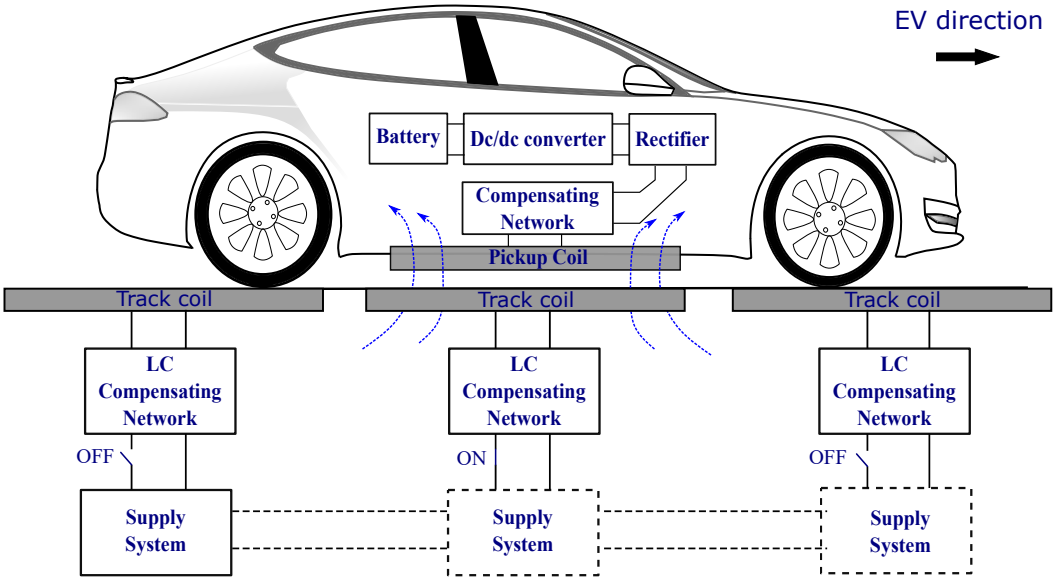

Fig. 6.1: Example of DWPTS. The coils of the track are selectively energized.

tough task. Among all the possible control strategies [81], the easiest and the most feasible seems to be the secondary-side control, also known as decoupling control [76]. In this control strategy, the current of the track coil directly coupled with the pickup is maintained constant, whereas a dc/dc converter in the receiving-side is responsible to perform the battery charging regulation. The controller that acts to maintain the track current constant does not use information regarding the receiver operation, thus eliminating the need for a feedback communication.

A solution that can relieve the task of the controller for the track current is to compensate the track with an LC network (see Fig. 6.1). Indeed, as it has been shown in Ch. 4, the transmitting coil current of an LC-compensated DWPTS is constant independently of the load and the coil coupling variations. However, this is true only in an ideal case (neglecting the parasitic resistances) and under steady-state conditions. A well-design feedback control system is still necessary to improve the dynamic behavior of track current and to make the system robust against the variation of the parameters. The track current should be reach its constant reference in the smallest amount of time and without overshoots.

The constants of the regulator that controls the track current can be set empirically, for example through Ziegler–Nichols method. However, a high-performance regulator (as the one required by DWPTSs) can be designed only on the basis of a dynamic model of the system. As explained in Ch. 5, the DWPTSs necessitate an envelope model that allows the control of the amplitudes to be implemented. Here, the transfer function which links the envelope of the track current to the envelope of the (fundamental of the) inverter output voltage is obtained through the MVLT method.

6.1.1 Electrical Scheme

The circuit analyzed in this chapter is shown in Fig. 6.2 and it constitutes the electrical scheme of the transmitting side for one of the track coil of the DWPTS

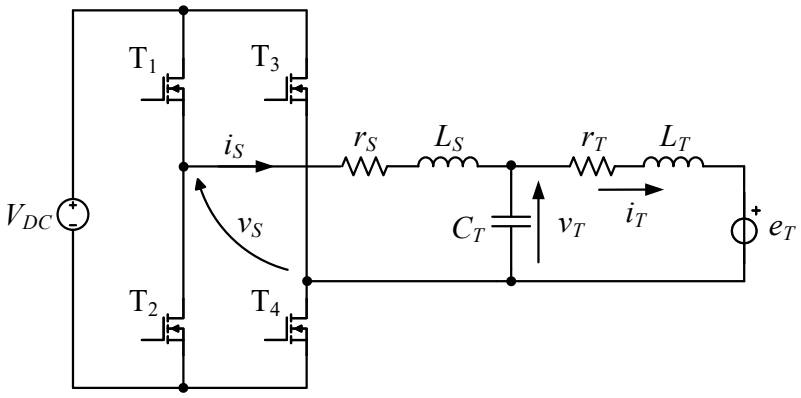

Fig. 6.2: Electrical scheme for the transmitting side circuitry of one track coil of the DWPTS illustrated in 6.1.

illustrated in Fig. 6.1. The simplification made in the circuit is to assume the voltage V_{DC} at the input of the inverter constant.

The purpose of this study is the design of a regulator which is able to settle the track current with good dynamic performance. To maximize the power transferred to the EV and to limit the losses and the magnetic field emissions, the transmitting power supply has to energize the track coil with a fast transient just before the car arrival. For this reason, in the scheme of Fig. 6.2 the pickup circuitry does not appear[1]. However, the influence of the pickup on the performance of the regulator when the EV is over the track coil can be assessed through the voltage e_T that the receiving coil induces in the track. In the derivation of the dynamic model, the induced voltage e_T is considered as a disturbance.

The inverter that supplies the track coil through the LC network regulates the track current by varying the fundamental of the feeding voltage v_s using the phase shift technique. The fundamental $v_{s,1}$ of the inverter output voltage is given by (2.52). The good filtering capability of the LC network allows the harmonics of the voltage v_s to be neglected, an so the inverter can be substituted with a sinusoidal voltage source with a time-variable amplitude. Both the steady-state and the transient analyses are greatly simplified by this approximation.

Under steady-state, the circuit of Fig. 6.2 can be envisaged as an LCL circuit fed by a sinusoidal voltage source whose phasor is given by $\bar{V}_s$ [2]. The steady-state analysis can be carried out as in Sec. 4.2. However, the situation here is slightly different because of the presence of the parasitic resistances r_s and r_T and since there is the induced voltage e_T in place of the reflected resistance. In this case, under the assumption that the track inductance L_T is equal to the inverter inductance L_s and both resonate with C_T, the phasor of the track current can be written as:

[1] The overall model and a more sophisticated control of a DWPTS with an LC-series compensation is proposed in [123].

[2] The phasor $\bar{V}_s$ is related to the fundamental $v_{s,1}$ of the inverter output voltage. For the sake of clarity, the subscript 1 has been disregarded from the phasor notation.

$$\bar{I}_T = \frac{\bar{V}_s}{j\omega\left(L_T + r_s R_T C_T\right)} - \frac{\bar{E}_T}{r_s + \frac{L_T}{C_T r_T}} \tag{6.1}$$

where $\bar{E}_T$ indicates the phasor of $e_T(t)$. Equation (6.1) shows that the presence of the parasitic resistances makes the track coil current become load dependent (it depends from e_T). If in (6.1), the approximation $r_s = r_T \approx 0$ is made, the track current returns to be equal to:

$$\bar{I}_T = \frac{\bar{V}_s}{j\omega L_T} \tag{6.2}$$

as in (4.81). For deriving the small-signal envelope model of the circuit in Fig. 6.2 it is interesting to see from (6.2) that the track current lags $v_{s,1}$ by 90°.

6.2 MVLT Model

To derive the envelope model through the MVLT method for the system of Fig. 6.2 it is necessary to start from the real transfer function, namely the transfer function that links the track current to the fundamental of the inverter output voltage. From the circuit it is easy to obtain the desired transfer function that is given by:

$$G_{I_T}(s) = \frac{1}{\left(r_s + r_T\right)\left[1 + \left(\frac{r_s r_T C_T + L_s + L_T}{r_s + r_T}\right) s + \left(\frac{r_T L_s C_T + r_s L_T C_T}{r_s + r_T}\right) s^2 + \left(\frac{L_s L_T C_T}{r_s + r_T}\right) s^3\right]} \tag{6.3}$$

From (6.3) it is possible to see the waveform of the track current immediately after the energization of the system. In fact, it can be obtained as the output of $G_{I_T}(s)$ when the square wave v_s corresponding to the inverter output voltage is given as the input. A practically equivalent result can be attained if the fundamental $v_{s,1}$ is considered as the input of (6.3) in place of the real square wave. The resulting track current is shown in Fig. 6.3, where the values of Tab. 6.1 have been considered for the parameters in (6.3). The amplitude of the sine given at the input of $G_{I_T}(s)$ can also be obtained from Tab. 6.1 and it is given by $V_s = \frac{4}{\pi} V_{DC} \approx 465\,V$. Figure 6.3 shows that the amplitude of i_T requires a certain amount of time to become constant (about 16 A) and during the transient the track current can reach values that approach to twice the steady-state value[3]. This results unacceptable and a regulator that improves the dynamic of the envelope of i_T is mandatory for a safe and fast start-up. This regulator can be designed around the MVLT transfer function $G_{i_T,env}$ that links the envelope of the track current to the envelope of $v_{s,1}$. This transfer function for the envelopes can be obtained from (6.3) using (5.29) or equivalently (5.28). From the steady-state analysis it has been shown that the current i_T lags the fundamental of the inverter output voltage by 90° and so the angle ϕ_i in (5.29) (or in (5.28)) is $-\frac{\pi}{2}$. For this reason, the transfer function $G_{i_T,env}(s)$ can be obtained with the following equation:

[3]For clarity reason, Fig. 6.3 does not show the complete transient which lasts about 1.5 ms.

Tab. 6.1: Values of the parameters considered for the various simulations of the circuit in Fig. 6.2.

Parameter	Symbol	Value
Voltage of the bus dc	V_{DC}	365 V
Voltage source angular frequency	ω	$2\pi\,85000\,\frac{\text{rad}}{\text{s}}$
Inverter side inductance	L_s	55 μH
Track coil inductance	L_T	55 μH
Inverter side resistance	r_s	0.5 Ω
Track coil resistance	r_T	0.5 Ω
Resonant capacitor	C_T	64 nF

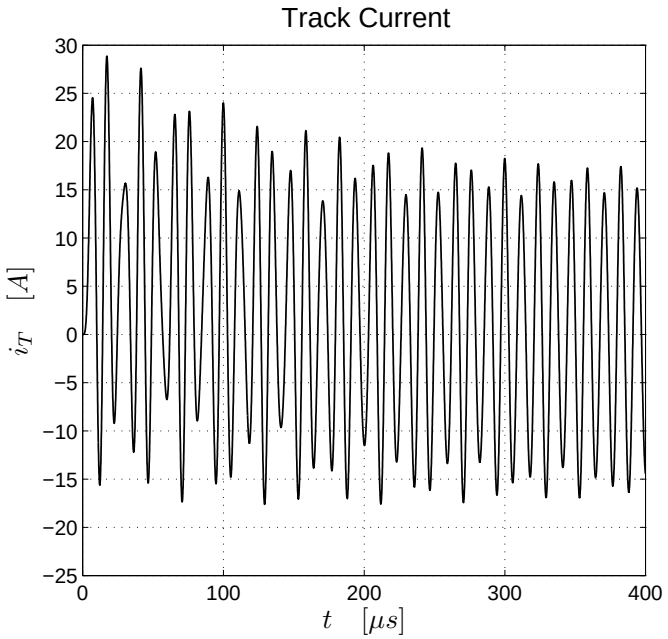

Fig. 6.3: Approximated waveform of the current i_T at the track coil start-up.

$$G_{I_T,env}(s) = \frac{I_{T,env}(s)}{V_{s,env}(s)} = -\Im\{G_{i_T}(s + j\omega)\} \tag{6.4}$$

where $\Im\{\cdot\}$ indicates the imaginary part of its argument, $I_{T,env}(s)$ is the Laplace transform of the envelope of i_T and $V_{s,env}(s)$ is the Laplace transform of the envelope of $v_{s,1}$. The analytical computation of (6.4) is too involved, but the MVLT method is easily implementable in a numerical computing environment like MATLAB. Using the values of Tab. (6.1), the transfer function $G_{i_T,env}(s)$ assumes the form

$$G_{I_T,env}(s) = k\,\frac{\prod_{j=1}^{2}(s - z_j)}{\prod_{i=1}^{6}(s - p_i)} \tag{6.5}$$

where $k = 8.3091 \cdot 10^{21}$ and the value of the zeros z_j and the poles p_i can be found in Tab. 6.2. The table reports also the zeros and the poles of the transfer

Tab. 6.2: Zeros and poles of the transfer functions $G_{i_T}(s)$ and $G_{i_T,env}(s)$.

	$\mathbf{G_{i_T}(s)}$	$\mathbf{G_{i_T,env}(s)}$
Zeros(z_j) $[*10^5]$	No zeros	$-0.0606 \pm j\,3.0833$
Poles(p_i) $[*10^5]$	$-0.0455 \pm j\,7.5528$	$-0.0455 \pm j\,12.893$ $-0.0455 \pm j\,2.212$
	-0.0909	$-0.0909 \pm j\,5.3407$

function $G_{i_T}(s)$. A comparison between the poles of the real transfer function and the poles of the envelope transfer function validates the analysis done in Sec. 5.1.3, since the imaginary parts of the poles of $G_{i_T,env}(s)$ are shifted by the angular frequency of the input voltage ($\omega \approx 534070\,\frac{\text{rad}}{\text{s}}$) from the the ones of the poles of $G_{i_T}(s)$.

The numerical analysis done for obtaining the the envelope transfer function is very accurate but it does not provide physical insight. To understand the meaning of the poles and the zeros of the real and the envelope transfer functions it is possible to make an approximation and consider the parasitic resistances negligible. With this assumption, equation (6.3) becomes:

$$G_{I_T}(s) = \frac{1}{(L_s + L_T)\,s\left(1 + s^2 \frac{L_s L_T}{L_s + L_T} C_T\right)} = \frac{1}{(L_s + L_T)\,s\left[1 + \left(\frac{s}{\omega_r}\right)^2\right]} \tag{6.6}$$

The transfer function $G_{i_T}(s)$ has a pole in the origin and two imaginary conjugate poles pair $s = \pm j\,\omega_r$, where $\omega_r = \sqrt{\frac{2}{L_s C_T}} = \sqrt{2}\,\omega$ if the inverter inductance and the track coil inductance are equal. From (6.6), the envelope transfer function is obtained as follows:

$$G_{I_T,env}(s) = -\Im\{G_{i_T}(s + j\omega)\} = \frac{3\,\omega^3}{L_s} \frac{\left(s^2 + \frac{\omega_r^2 - \omega^2}{3}\right)}{(s^2 + \omega^2)\left[s^2 + (\omega - \omega_r)^2\right]\left[s^2 + (\omega + \omega_r)^2\right]} \tag{6.7}$$

Equation (5.32) has been used to find the imaginary part of $G_{i_T}(s + j\omega)$. When $L_s = L_T$, equation (6.7) becomes:

$$G_{I_T,env}(s) \approx \frac{3\,\omega^3}{L_s} \frac{\left[s^2 + (0.577\,\omega)^2\right]}{(s^2 + \omega^2)\left[s^2 + (0.414\,\omega)^2\right]\left[s^2 + (2.414\,\omega)^2\right]} \tag{6.8}$$

The zeros and the poles of (6.8) are in good agreement with the ones shown in Tab. (6.2) [4].

[4] The poles of (6.8) just do not have the real part which produces a damping. As expected neglecting the resistances, the envelope transfer function as well as the real transfer function become undamped.

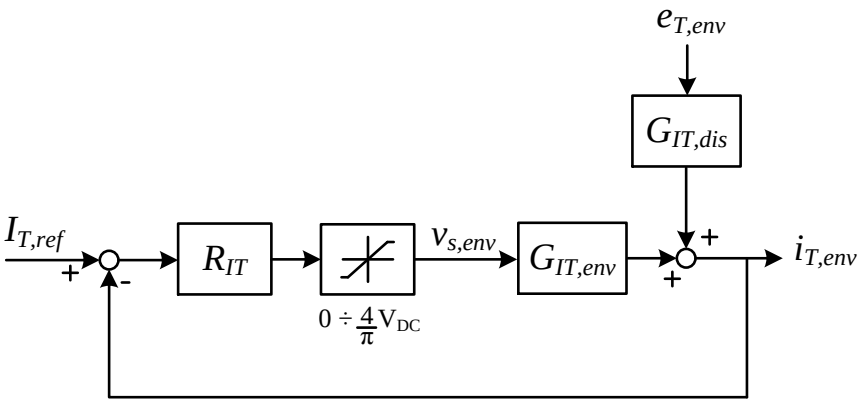

Fig. 6.4: Block diagram for the control loop of the track current.

Tab. 6.3: Zeros, poles and gain of the transfer function $G_{i_T,dis}(s)$.

	$\mathbf{G_{i_T,dis}(s)}$
Gain	$-5.79 \cdot 10^{-4}$
Zeros (p_i) $[*10^5]$	$-0.0430 \pm j\,11.4064$ $-0.0706 \pm j\,3.5363$ -0.0455
Poles(p_i) $[*10^5]$	$-0.0455 \pm j\,12.893$ $-0.0455 \pm j\,2.212$ $-0.0909 \pm j\,5.3407$

6.3 Regulator Design

The track current regulator R_{i_T} provides the reference for the envelope of $v_{s,1}$ according to the error between the reference value $I_{T,ref}$ and the actual value of $i_{T,env}$. The block diagram of the control loop is illustrated in Fig. 6.4. Besides the track current control loop, the figure shows also the disturbance for the envelope of the track current caused by the envelope of the induced voltage e_T. The transfer function $G_{i_T,dis}(s)$ which links the envelope of the track current to $e_{T,env}$ can be obtained with a procedure similar to the one used to attain (6.5). The gain, the zeros and the poles of $G_{i_T,dis}(s)$ expressed in Bode form are listed in Tab. 6.3.

The regulator for the track current is designed according to the Bode diagram of the transfer function $G_{i_T,env}(s)$ which is shown in the left part of Fig. 6.5. The specification for the control loop of Fig. 6.4 are:

- Bandwidth around 1 kHz;
- good stability;
- good disturbance rejection capabilities.

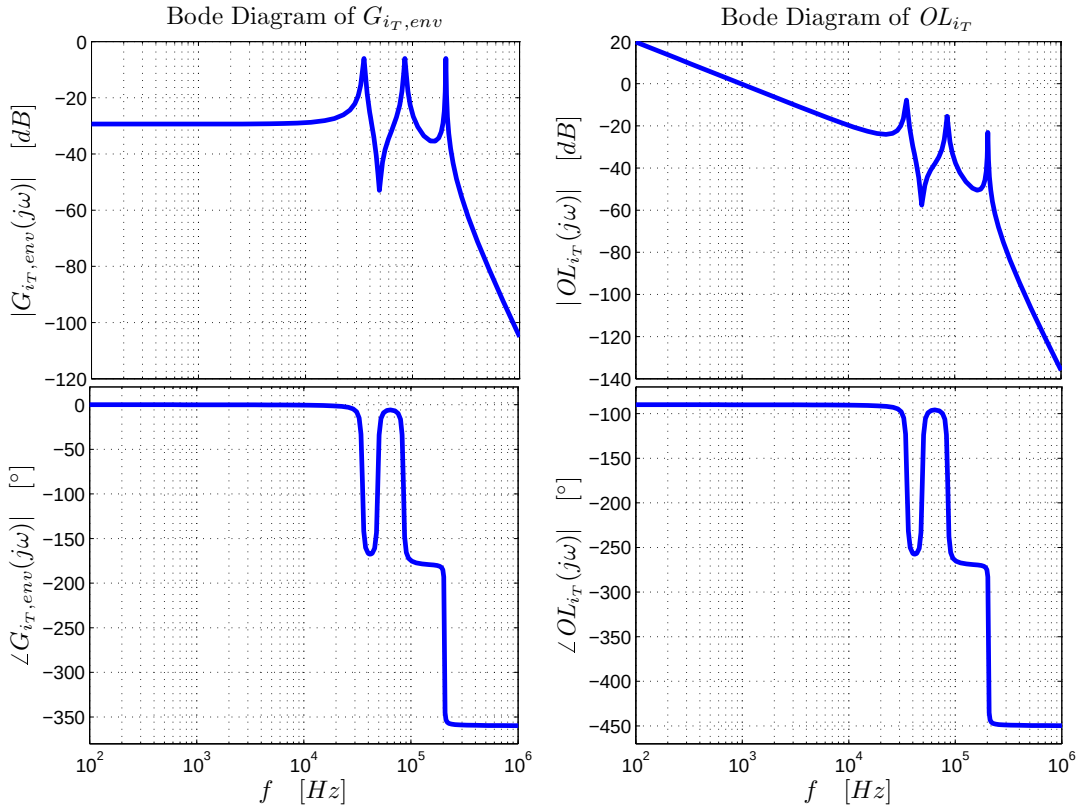

Fig. 6.5: Bode diagram of the envelope transfer function $G_{i_T,env}(s)$ (left graphs). Bode diagram of the open-loop transfer function $OL_{i_T}(s)$ (right graphs).

The frequency-domain analysis of the open-loop transfer function $OL_{i_T}(s) = R_{I_T}(s)\, G_{I_T,env}(s)$ has been carried out for satisfying the requirements. Using SISO Design Tool of MATLAB, the current regulator has been designed as follows:

$$R_{i_T}(s) = \frac{180000}{s} \tag{6.9}$$

It consists in a pure integrator that sets the crossover frequency of the open-loop transfer function L_{i_T}(s) at about 950 kHz with a phase margin of 90° (cf. the right graphs of Fig. 6.5). This choice for the regulator allows for a fast and overdamped start-up of the track current. In addition to the good dynamic performance, the regulator should also provide rejection for the disturbance caused by the induced voltage on the track current. To check this capability, the disturbance-to-output transfer function is calculated as follows:

$$W_{I_T,dis}(s) = G_{i_T,dis}(s)\, \frac{1}{1 + R_{i_T} G_{i_T,env}(s)} \tag{6.10}$$

and its Bode diagram is plotted in Fig. 6.6. In the figure, it can be seen that the gain of the magnitude of $W_{I_T,dis}(j\omega)$ for $\omega \to 0$ tends to $-\infty$ [dB]. This entails that, even though the envelope of e_T is applied to the system of Fig. 6.2 as a step, under steady-state conditions this disturbance does not have any influence of the track current.

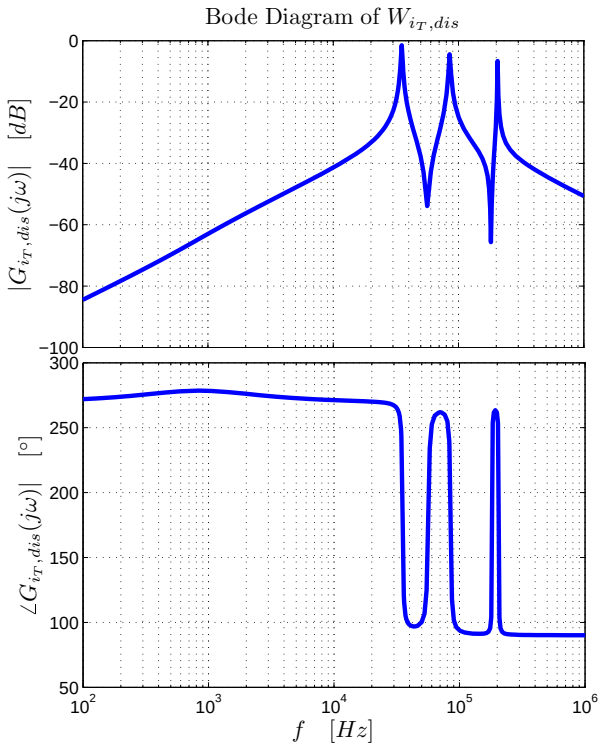

Fig. 6.6: Bode diagram of the closed-loop disturbance-to-output transfer function $W_{i_T,dis}(s)$.

Both the regulator design and the MVLT model of the system (6.2) have been tested through simulations. The current loop in Fig. 6.4 has been implemented in Simulink with the disturbance set to 0. In the same program, the system of Fig. 6.7 has been simulated. Also in this case the voltage e_T has been disregarded. The peak detector block of Fig. 6.7 has been implemented through the Fourier block of Simulink. In both the circuit of Fig. 6.7 and the control system of Fig. 6.4 build around the MVLT model, the current reference $I_{T,ref}$ has been set to 10 A. The current $i_{T,env}$ obtained as the output of the closed-loop input-to-output transfer function of Fig. 6.4 has been plotted together with the current i_T measured in the circuit of Fig. 6.7. The result is shown in Fig. 6.8. The first thing that can be observed from the plot is that the output of the model matches well with the envelope of the current obtained from the simulation of the circuit 6.7. This happens even though the transfer function $G_{i_T,env}(s)$ is valid only for a small variation of the track current around a steady-state value. The linearization of the MVLT model which involves only the output relation and not the system itself does not impair so much the model accuracy, even in presence of large variations of the signals.

In Fig. 6.8, it can be seen also that in 600 µs the current i_T has almost reached the reference value with an overdamped response. By considering a car with a speed of 27.78 $\frac{\text{m}}{\text{s}}$ (100 $\frac{\text{km}}{\text{h}}$) and the length of a coil of the track equals to 1 m, the pickup coil (1 m long) remains coupled with the transmitting coil for about 36 ms. This means that, if the track coils are selectively energized only when the car is arriving in proximity of them, only the 1.7 % of the time that the pickup spends over the transmitting coil is needed for the start-up. In addition, since the car,

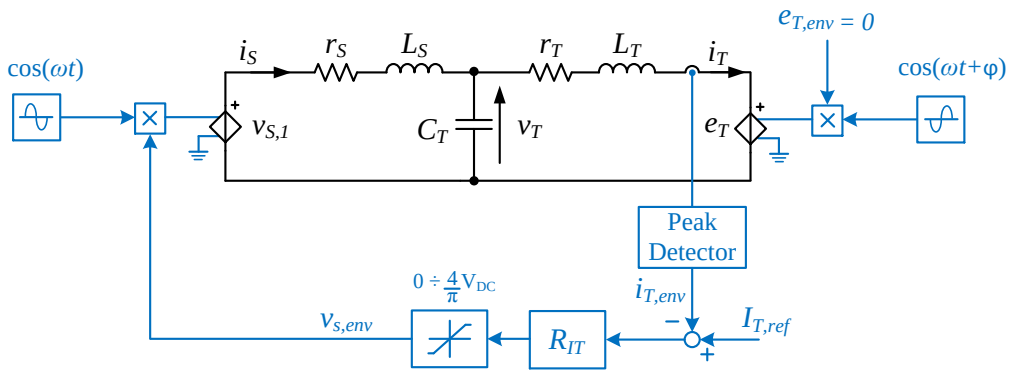

Fig. 6.7: Track current loop set up around a simplified version of the circuit of Fig. 6.2.

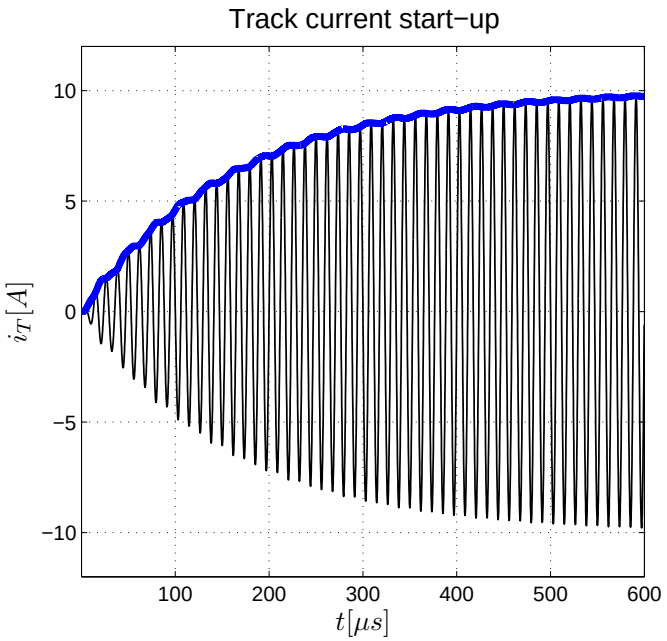

Fig. 6.8: Track current at the start-up of the circuit of Fig. 6.7 (black thin line). Output of the block diagram of Fig. 6.4 (blue thick line).

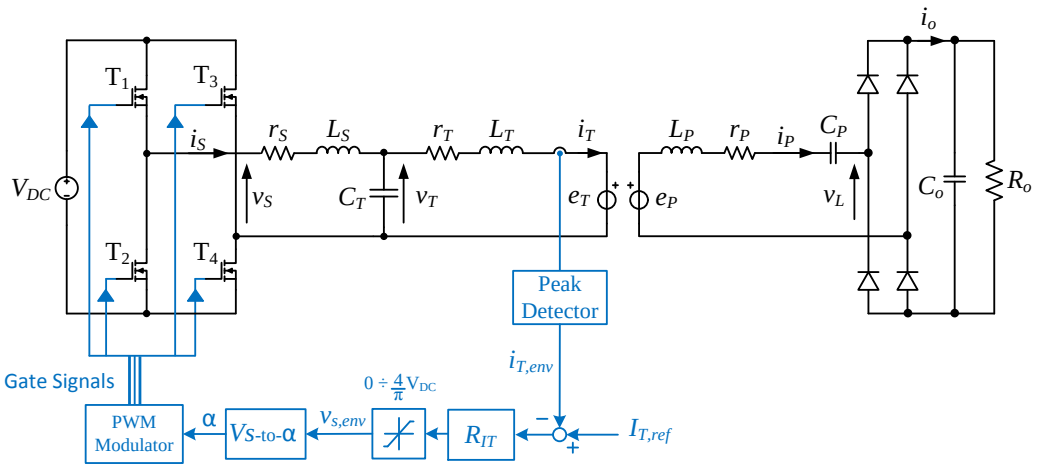

Fig. 6.9: Electrical scheme of the DWPTS simulated in PSIM.

with a speed of 27.78 $\frac{\text{m}}{\text{s}}$, covers 1.7 cm in 600 µs and the pickup coil is presumably not installed in the front of the vehicle chassis, when the flux produced by the track coil starts to link the pickup, the track current has already reached the steady-state condition.

6.4 Simulation Results

In the previous section, the design of the regulator has been carried out on the basis of the MVLT model of the system of Fig. 6.2. Although the validity of the model in (6.5) has been verified comparing the output of the closed-loop response with the envelope of the current obtained from the circuit of Fig. 6.7, it is still approximated for the following main reasons:

- It considers only the 1st-harmonic of the various quantities;
- the non-linear relation between the amplitude of the fundamental of the input voltage and the phase-shift angle α of the inverter (see (2.52)) has not considered;
- the influence of the pickup coil in the transmitting system when the EV is over the track coil is modeled with a simple voltage source with a constant amplitude.

From these considerations, it arises that the regulator has to be tested, implementing a feedback loop around the real DWPTS taken as case of study. For this purpose, the circuit in Fig. 6.9 have been simulated in PSIM. Here, it can be analyzed the real influence of the pickup circuitry on the track current, since the induced voltages e_T and e_R have been defined as:

$$\begin{cases} e_T = -M \frac{di_R}{dt} \\ e_R = M \frac{di_T}{dt} \end{cases} \tag{6.11}$$

where the mutual inductance M has been considered as a step with amplitude 11 µH at 10 µs. This step is used to simulate an abrupt car entrance.

The values for the pickup inductance L_P, the pickup capacitor C_P and the pickup coil resistance r_P are the same as L_T, C_T and r_T, respectively. The capacitance of C_o has been chosen equal to 100 µF and a value of 1 Ω has been considered for the load resistance.

The peak detector block of Fig. 6.9 is implemented through an analog circuit which is designed in order to not affect the control feedback loop. The V_s-to-α block converts the reference for the envelope of $v_{s,1}$ into the phase-shift angle α of the inverter. This is a non linear block obtained inverting (2.52) and it is described by the following relation:

$$\alpha = 2 \arcsin\left(\frac{\pi}{4}\frac{v_{s,env}}{V_{DC}}\right) \tag{6.12}$$

To have a steady-state envelope for the track current equal to 10 A, the envelope of the inverter output voltage has to be about 294 V (cf. (6.2)). From (6.12) it is possible to find the steady-state value of α that is equal to 1.368 rad (about 78°)[5].

The PWM modulator block of Fig. 6.9 provides the correct signals to the gates of the inverter MOSFETs according to the phase-shift angle obtained from the V_s-to-α block.

The start-up transient of the track current for the circuit simulated in PSIM is shown in Fig. 6.10. In the figure, the track current is plotted together with the envelope obtained from the peak detector block. The startup operation is in good agreement with the theoretical analysis and the envelope of the track current during the transient period is very similar to the waveform shown in Fig. 6.8 valid for the linear circuit of Fig. 6.7.

The current of Fig. 6.10 is the start-up current of the track that is obtained when the pickup coil has not reached the track coil yet. The capabilities of the regulator to reject the disturbance caused to the track current by the pickup coil can be observed through Fig. 6.11. The figure illustrates the track current with its envelope and the phase-shift angle α obtained from the V_s-to-α block, immediately after the application of the mutual inductance as a step in the equations for the induced voltages e_T and e_R. It can be seen that the the envelope of the track current practically returns to the set point value in about 200 μs even if the transient lasts about 500 μs. The simulation confirms that the track current remains under control even in case of an abrupt change of the coupling coefficient between a coil of the track and the pickup coil. This situation never happens in the reality, since the real coupling coefficient variation is smoother. Figure 6.11 shows that even in case of this severe condition, the regulator works as expected.

In the lower plot of Fig. 6.11 it can be observed that, contrarily to the result expected from (6.2) and (6.12), the phase-shift angle changes when the pickup coil is over the track coil. This is due to the presence of the parasitic resistances. Furthermore, the steady-state value of α, that was calculated to be about 1.368 rad, is equal to 1.45 rad. This is caused not only by the resistance r_s and r_T, but also by the fact that the envelope of the track current, obtained from the analog peak

[5] This value is approximated since (6.2) does not take into account the parasitic resistances.

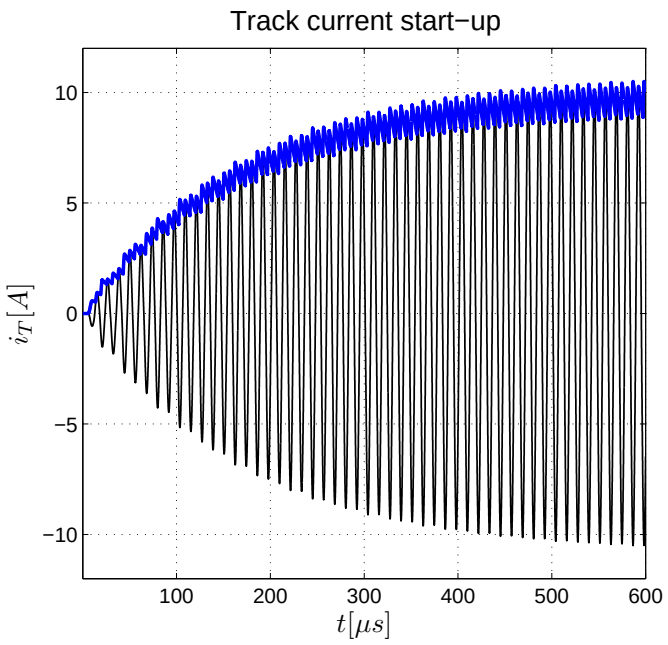

Fig. 6.10: Start-up transient of the track current for the circuit of Fig. 6.9.

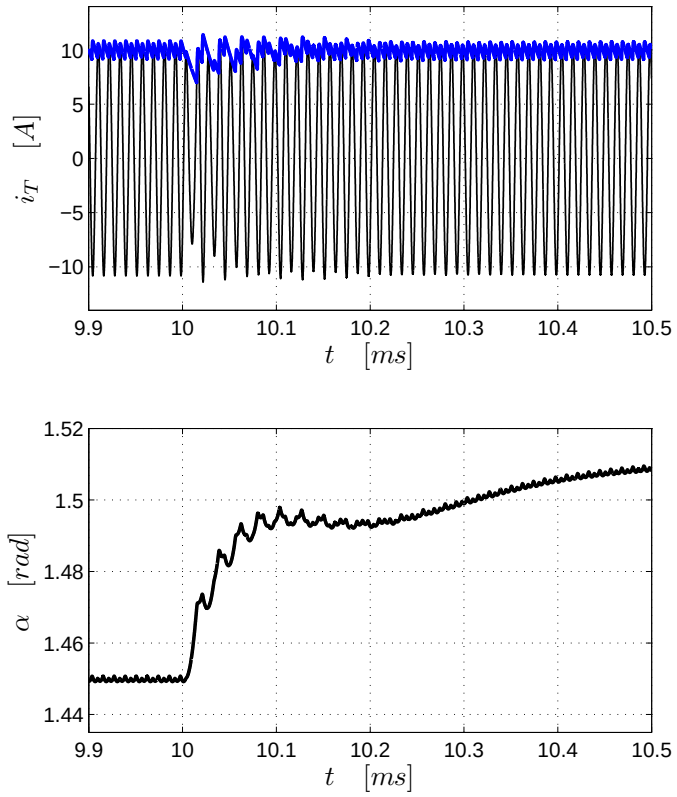

Fig. 6.11: Regulator performance: track current (upper plot) and phase-shift angle (lower plot), after an abrupt pickup coil entrance at 10 ms.

detector, is not sharp (it has a saw-toothed shape). The peak detector can be improved reducing the ripple of the obtained envelope and this lead to a phase-shift angle close to 1.368 rad. However, this reduces the dynamic performance of the regulator. The parameters of the peak detector have to be design according to this compromise.

Chapter 7

A Modified LCC-Compensated Pickup Topology for DWPTSs

This chapter proposes an unconventional pickup topology employed in the dynamic battery charging of electric vehicles. The pickup reactive power compensation is performed through a modified LCC network that permits the continuous conduction mode operation of the rectifier for a wide range of working conditions. The dc/dc converter that controls the battery charging process requires a small value of dc inductance for the proper operation. The proposed control strategy for the switch in the dc/dc conversion stage maintains the pickup input power factor close to one for large variations of the charging power. In this chapter, at first the operation of the proposed topology and its related control strategy are introduced and then a design procedure for the modified LCC network parameters is presented. The pickup topology is implemented in PSIM and the outcomes of the simulations corroborate the analytical analysis.

7.1 Pickup Topologies

While the previous chapters focused mostly on the track side, in this chapter a particular topology for the pickup circuitry is presented. Usually, papers regarding the pickup topology treat either the compensating networks or the dc/dc converters responsible for the battery charging, but few of them study both the topics together. However, especially in case of DWPTSs, the study of the compensating networks in the pickup side has to take into account also the operation of the dc/dc converter because it can affect the overall pickup performance. In addition, the type of dc/dc converter installed downstream the rectifier depends on the passive network employed to compensate the pickup reactive power.

The common solutions adopted for the pickup topology are the series compensation joined with a buck converter (see Fig. 7.1(a)) and the parallel compensation with a downstream boost converter (cf. Fig. 7.1(b)). Both the buck and the boost converters rely on a large dc inductance L_{CH} for the proper operation[1].

[1] In Fig. 7.1, a smaller inductance should be present in series with the battery to ensure a good filtering of the current I_B. For the sake of simplicity, this component has not been depicted here.

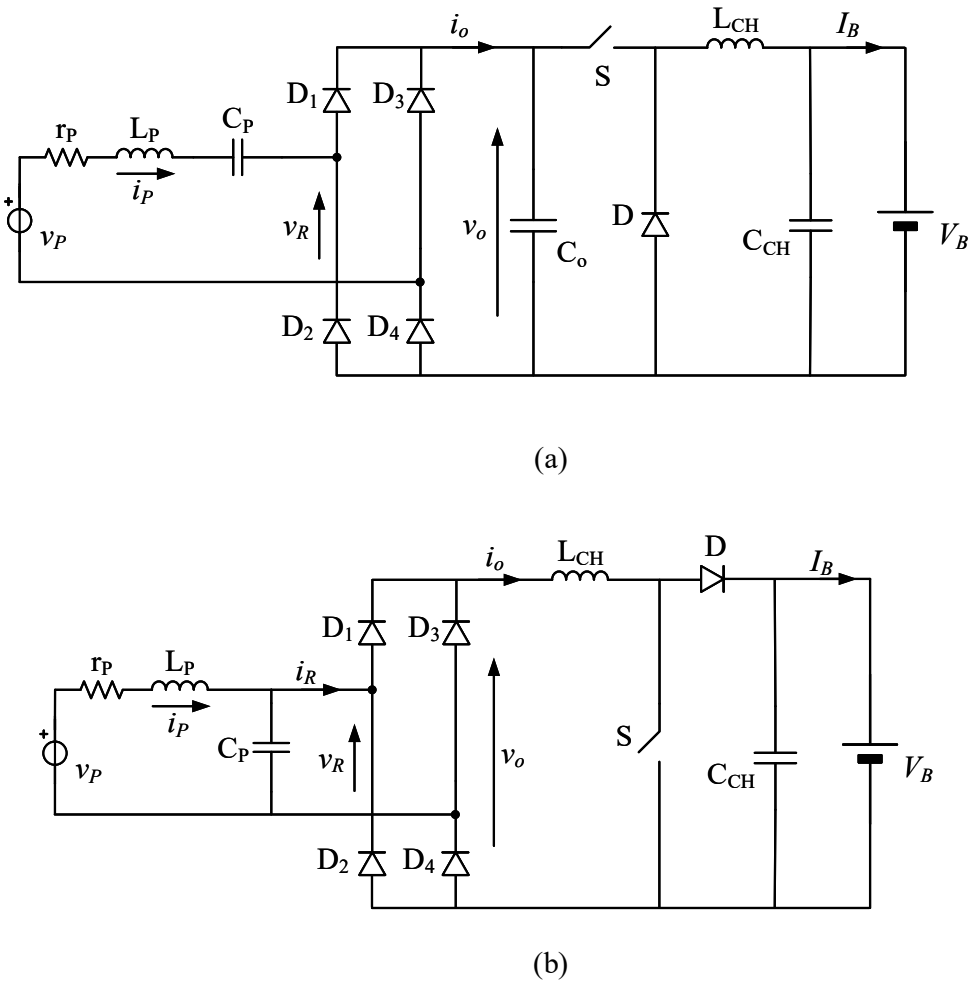

Fig. 7.1: Common pickup topologies: series compensation with buck converter (a), parallel compensation with boost converter (b).

This bulky component can be eliminated or at least significantly reduced using a full bridge rectifier and implementing the power regulation at this stage [78]. However, when the bidirectional power flow is not necessary, this solution adds complexity and cost. In [82], the receiving-side control is implemented by employing a semi-active rectifier. With the control method proposed by the authors, the two switches are softly commutated, but the phase displacement between the receiving voltage and current depends on the switch control angle and, in the case of a DWPTS, a Unity Power Factor (UPF) cannot be guaranteed. In [124], the authors introduce an LC-compensated pickup with a low-frequency switch inserted directly after the diode bridge without the need for the dc inductance typical of the parallel compensation used to sustain the rectifier output current. Such a controller, valid for material handling systems, does not have the high-speed performance required in a DWPTS. In this chapter the topology presented in [124] is revised and a different control strategy is proposed in order to fulfill the stringent requirements of a DWPTS. The particular control strategy allows a UPF to be maintained at the

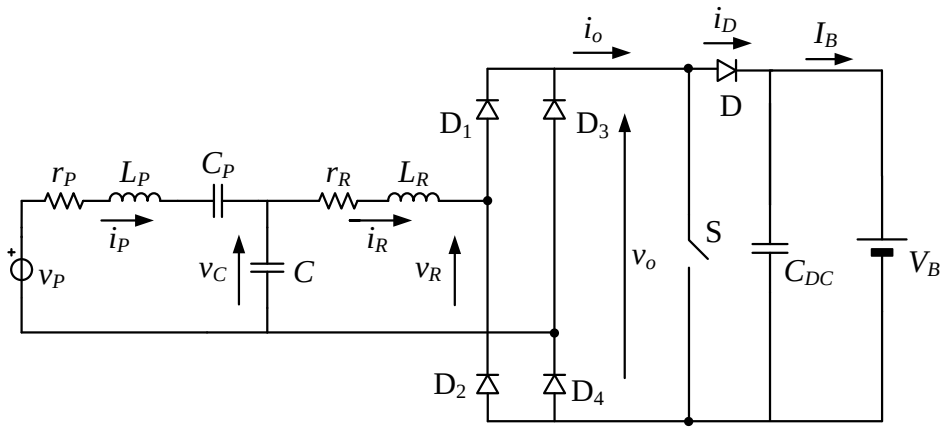

Fig. 7.2: Proposed pickup topology.

input of the receiver for a wide range of the operating conditions, thus improving the pickup sizing factor.

7.2 LCC-Compensated Pickup

The pickup topology considered in this chapter is shown in Fig. 7.2. It consists of an LCC-compensated pickup [32] cascaded by a passive diode bridge that is used to rectify the voltage v_R to properly supply the battery V_B. Between them the switch S is inserted to control the charging battery current I_B. When the switch S is open, the rectifier output current i_o flows through the diode D and then is filtered by the capacitor C_{DC} prior to charging the battery. When the switch is closed it forms a short circuit at the rectifier output terminals and the resonating current i_R flows into it through the diodes D_1 and D_4 when it is positive, in diodes D_3 and D_2, alternatively. During this period, the battery current is provided by the capacitor C_{DC}. The situation is illustrated in Fig. 7.3.

The rectifier output can be shorted through the switch S because of the current-source characteristic of the LCC network. As regards the resonant tank, it is formed by the capacitor C_P in series with the pickup inductance L_P, by the rectifier-side inductance L_R and by the capacitor C. The capacitor C_P has the twofold purpose of:

1. compensate part of the inductance L_P;
2. block the dc-component that can arise in the current i_P, thus avoiding the possible saturation of the ferrite core of the pickup coil.

The inductance L_P is not fully compensated and so the LCC network behaves like an LCL circuit. The inductance L_R is set to be equal to the equivalent series inductance of the "P" branch and both resonate with the capacitor C. The resistances r_P and r_R account for the losses in the compensation network. The pickup circuitry is fed by the voltage v_P that is induced by the track current.

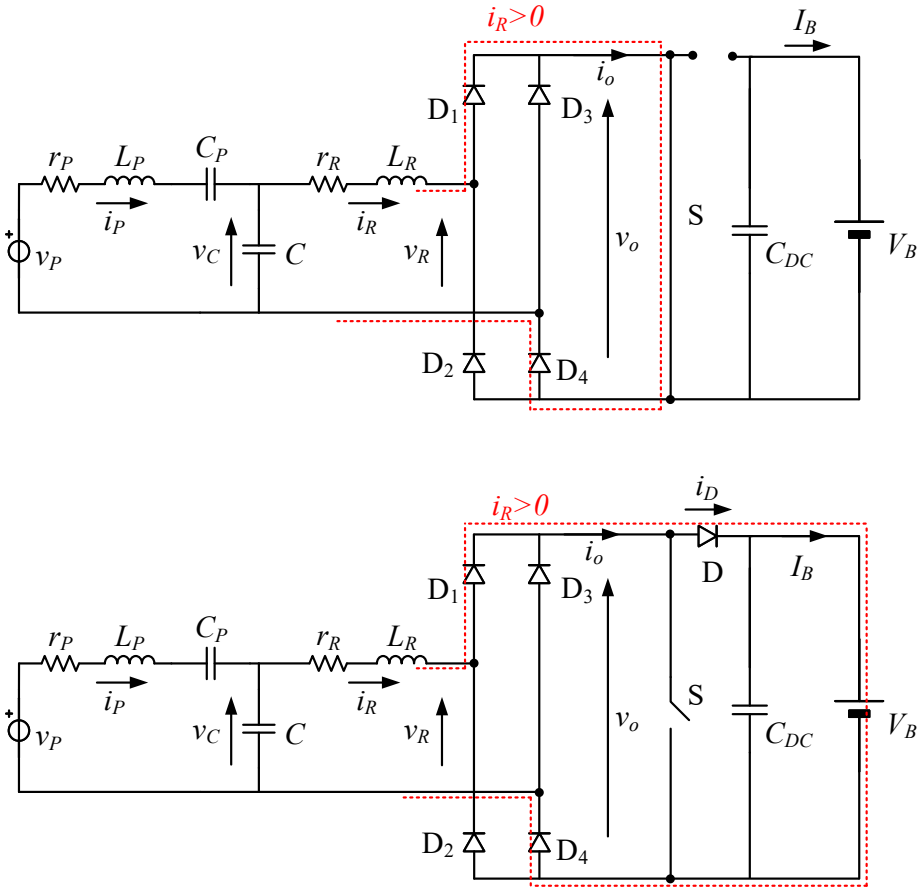

Fig. 7.3: Path of the rectifier output current i_o depending on the state of the switch S.

Since the track current is sinusoidal with a controlled amplitude, the voltage v_P is also sinusoidal and its amplitude is given by:

$$V_P = \omega M I_T = \omega k \sqrt{L_T L_P}\, I_T \tag{7.1}$$

where ω and I_T are, respectively, the angular frequency and the magnitude of the track current. In the second equality of (7.1) the mutual inductance M has been replaced according to the definition (2.11). From (7.1), it is easy to see that when the angular frequency and the magnitude of the track current are fixed, the magnitude of pickup induced voltage is proportional to k, provided that the track inductance L_T and the pickup inductance L_P remain unaffected by the variation of their relative position.

7.3 Pickup Operation

To study the operation of the circuit in Fig. 7.2, it is assumed that the rectifier works in CCM. Under this assumption, the FHA analysis can provide good insight into the resonant LCC circuit operation. FHA considers the ac quantities of the

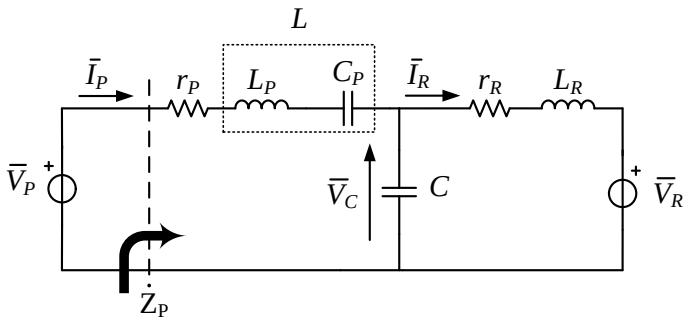

Fig. 7.4: LCC compensating network.

resonant tank as purely sinusoidal so that the circuit can be studied in the phasor-domain.

7.3.1 LCC Compensating Network

The previous considerations lead to rely on the circuit in Fig. 7.4 to study the behavior of the compensating network of the proposed pickup topology.

Under the sinusoidal steady-state condition, the series of the pickup inductance and the capacitance C_P can be conceived as an equivalent inductor whose inductance is given by:

$$L = L_P - \frac{1}{\omega^2 C_P} \tag{7.2}$$

From the steady-state point of view, the LCC compensation is nothing else but the LCL circuit. Since the capacitor C resonates with L at the chosen operating frequency, the current phasor $\bar{I}_R$ can be written in a similar way as in (6.2):

$$\bar{I}_R = \frac{\bar{V}_P}{j\omega L} \tag{7.3}$$

To derive (7.3), the parasitic resistance r_P and r_R have been neglected.

If the rectifier-side inductance L_R is equal to the inductance L, the LCL network becomes symmetrical and, with the same hypotheses done in the derivation of (7.3), the phasor $\bar{I}_P$ of the pickup current can be obtained as:

$$\bar{I}_P = -\frac{\bar{V}_R}{j\omega L} \tag{7.4}$$

It is worth to note that pickup current is originated only by the voltage v_R. Since v_R depends mainly on the load, ideally, when there is no load, the pickup current vanishes. An important requirement to satisfy in the pickup design is to achieve the UPF between the voltage v_P and the current i_P. This limits the pickup sizing factor and increases the system efficiency. The phase displacement between the pickup current and voltage can be assessed from the phase of the pickup input impedance $\dot{Z}_P$ (see Fig. 7.4) which, from (7.4), can be written as:

$$\dot{Z}_P = \frac{\bar{V}_P}{\bar{I}_P} = -j\omega L \frac{\bar{V}_P}{\bar{V}_R} \tag{7.5}$$

Voltage v_P and current i_P are in phase when $\dot{Z}_P$ is real, i.e. when the load seen by the voltage source V_P is resistive. Equation (7.5) states that the angle of $\dot{Z}_P$ is zero if $\bar{V}_R$ lags $\bar{V}_P$ by 90°. By (7.3), this condition implies that $\bar{V}_R$ should be in phase with $\bar{I}_R$ to achieve the UPF of the pickup; the rectifier, the switch S with its control strategy and the battery of Fig. 7.2 have to appear as a resistance to the resonant tank.

7.3.2 Proposed Control Strategy

Although the amplitude of the phasor $\bar{I}_R$ can be directly derived from the phasor of the sinusoidal voltage induced in the pickup coil, as expected from (7.3), the computation of (7.4) requires the knowledge of the phasor $\bar{V}_R$ related to the fundamental $v_{R,1}$ of the rectifier input voltage v_R. The voltage v_R is influenced by the rectifier functioning that, in turn, depends on the battery operation and on the control strategy of the switch S. The rectifier input voltage for the circuit in Fig. 7.2 is neither sinusoidal nor a square wave, as it normally happens for the conventional pickup topologies, thus a time-domain analysis of the rectifier operation is required.

The time-domain analysis of the rectifier operation is based on the assumption that i_R is sinusoidal. The waveforms of the quantities affected by the proposed control strategy are ideally depicted in Fig. 7.5. The control signal v_g provided to the gate of the switch S is synchronized with the current i_R. For this reason, in Fig. 7.5 the origin of the angular coordinate θ, has been chosen in order to coincide with the negative to positive zero-crossing of the rectifier input current. In this reference system and with the above assumption, the rectifier input current can be written as:

$$i_R = I_R \sin(\theta) \tag{7.6}$$

From Fig. 7.5, it can be seen that in the interval $[0, \alpha]$ the switch S is on. During this period the rectifier output current i_o, obtained from the rectification of the current i_R, flows entirely through S and consequently, the current in the diode D is zero. The battery current I_B is provided by the capacitor C_{DC}. At $\theta = \alpha$, the switch S is turned off, the diode D starts conducting and the battery current is sustained by current i_D conveniently filtered. This situation persists until θ reaches the value $(2\pi - \alpha)$ when the switch S is turned on. During the interval $[(2\pi - \alpha), 2\pi]$, the current in the switch S, the current in the diode D and the battery current flow as in the period $[0, \alpha]$.

From the last graph of Fig. 7.5, it can be noticed that the battery current I_B is almost constant and it is obtained by filtering the current i_D. For this reason, the value of the constant I_B can be assessed from the average value of the current i_D which is given by:

$$I_D = I_B = \frac{1}{\pi} \int_{\alpha}^{\pi} I_R \sin(\theta)\, d\theta = \frac{2}{\pi} I_R \cos^2\left(\frac{\alpha}{2}\right) \tag{7.7}$$

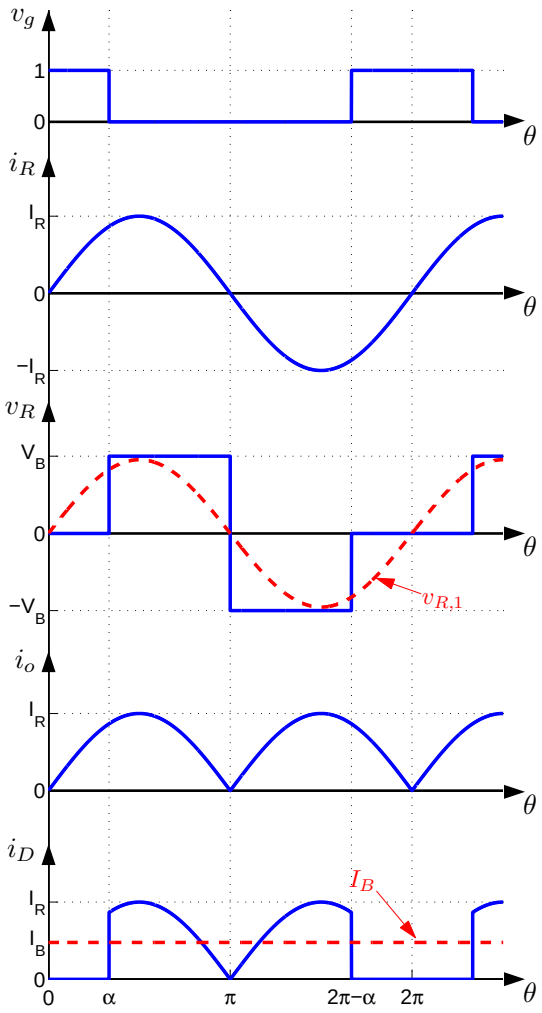

Fig. 7.5: Ideal waveforms of the quantities affected by the proposed control strategy. From top to bottom: i) gate signal of the switch S, ii) rectifier input current i_R, iii) rectifier input voltage v_R and its fundamental $v_{R,1}$, iv) rectifier output current i_o, v) current i_D in the diode D and battery current I_B.

In (7.7), the particular symmetry of the current i_D and the fact that it coincides with the current i_R in the interval $[\alpha, \pi]$ have been exploited. Equation (7.7) states that the battery charging current is independent from the battery voltage and it can be controlled by changing α, i.e. by changing the fraction of the overall period 2π in which the switch S is in the on-state. In other words, this pickup topology acts as a controlled current source, as long as the higher order harmonics in the rectifier current can be neglected.

As regards the voltage v_R, it can be noticed from the third plot of Fig. 7.5 that when the switch S is in the on-state, the voltage across the rectifier input terminals is clamped to zero. This is true provided that the voltage drops across the diodes of the rectifier and across the switch S are neglected. When the switch S is off the voltage v_R depends on the sign of i_R: it is equal to $+V_B$ when i_R is positive, to $-V_B$ conversely. In the third plot of Fig. 7.5, it is also shown that with the proposed control strategy the fundamental of the rectifier input voltage, depicted

with the red dashed line, is ideally in phase with the current i_R. The amplitude of $v_{R,1}$ can be obtained from the Fourier series expansion of the signal v_R or more conveniently from power considerations. Considering the diode rectifier, the switch, the power diode and the capacitor C_{DC} lossless components, the battery charging power should be equal to the ac active power seen by the rectifier input. The battery charging power is simply given by the battery current (7.7) multiplied by the battery voltage V_B and results:

$$P_B = V_B I_B = \frac{2}{\pi} V_B I_R \cos^2\left(\frac{\alpha}{2}\right) \tag{7.8}$$

The active power seen by the rectifier input is given by:

$$P_R = \frac{1}{2}\,\Re\{\bar{V}_R \bar{I}_R^*\} = \frac{1}{2} V_R I_R \tag{7.9}$$

where the operator $\Re\{\cdot\}$ extracts the real part from the complex number $V_R I_R^*$, which is the product between the phasor of the fundamental of v_R and the complex conjugate of the phasor $\bar{I}_R$. The second equality of (7.9) is derived from the fact that $v_{R,1}$ is in phase with i_R. In case of ideal components, the battery charging power P_B is the same as P_R and, from (7.8) and (7.9), the amplitude of the fundamental of v_R can be obtained in the form:

$$V_R = \frac{4}{\pi}\, V_B \cos^2\left(\frac{\alpha}{2}\right) \tag{7.10}$$

Since with the proposed control method the voltage $v_{R,1}$ is always in phase with the current i_R, namely 90° lagging the voltage v_P, the impedance seen by the pickup voltage source expressed by (7.5) is pure resistive and this entails that the pickup does not have to cope with the reactive power.

7.4 Pickup Design

The design of the pickup topology presented here concerns with the sizing of the parameters of the LCC compensating network. Since the pickup inductance is essentially defined by geometrical constraints during the coil coupling design, the capacitor C_P allows a degree of freedom in the choice of L in order to adapt the rectifier output current to the battery demands. In fact, combining (7.3) and (7.7), the current that the converter is able to provide to charge the battery without the switching operation, i.e. with α equal to 0, can be written as:

$$I_D = I_o = \frac{2}{\pi}\frac{V_P}{\omega L} \tag{7.11}$$

It is easy to note that the average value of the rectifier output current I_o depends on the value of the inductance L and assumes the shape of the amplitude of the pickup induced voltage profile. With a constant amplitude and frequency of the track current and with a fixed value of the inductances L_T and L_P, from (7.1) it can be noticed that the pickup voltage profile depends on the coupling coefficient k, namely depends on the track and pickup structures and on their relative position. To assess the performance of the proposed pickup topology, the trapezoidal coil

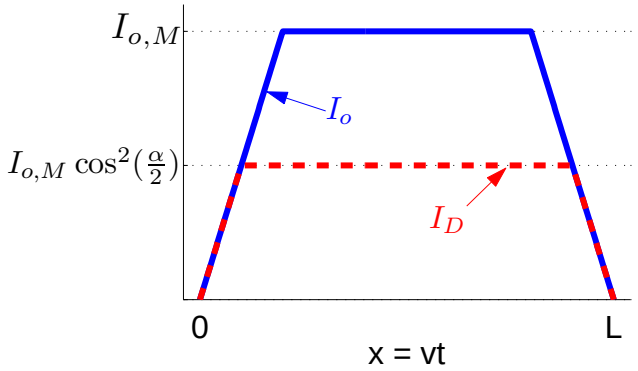

Fig. 7.6: Profile of the currents I_o and I_D when the pickup coil passes over a track segment.

coupling profile of Fig. 4.10 is considered. For this reason, from (7.11) and (7.1), one can deduce that the shape of the average value of the rectifier output current is trapezoidal as well as the coupling coefficient profile. This profile is depicted in Fig. (7.6). In addition to the current I_o, Fig. (7.6) illustrates also the average value of the power diode current I_D, obtained operating the switch S in order to feed the battery with the proper current. Both the waveforms are plotted versus the relative position between the pickup coil and the track segment. This position is expressed through the variable x that starts from 0 when the pickup is approaching the track and is equal to the track length L when the car is leaving. If the car equipped with the pickup moves with constant speed, the x-axis can be also envisaged as the time variable. It is worth noting that the time scale of the plot in Fig. (7.6) is much greater than the period of the track current, i.e. the period of the waveforms of Fig. 7.5. For this reason, the equations found in the previous section are still valid.

From Fig. 7.6, it is easy to see an advantage of the LCC topology with respect to the series compensation in the pickup side. Indeed, at very low k, even though the current I_o at the rectifier output is less than the maximum current $I_{o,M}$ achievable when the pickup coil is well coupled with the track segment, it never ceases. Contrarily, in a series compensated pickup, when there is an high misalignment between the track and the pickup, the rectifier output current is discontinuous and the power transfer becomes intermittent [105].

When the battery is charging with the nominal current $I_{B,N}$, a good design of the LCC network makes the control operate with the minimum angle α, ideally 0. This is achieved forcing the quantity $I_{o,M}$, obtained with (7.1) and (7.11) when k is set to the maximum value k_M, to be equal to the battery nominal current. This yields the value for the inductance L:

$$L = \frac{2}{\pi}\frac{1}{\omega}\frac{V_{P,M}}{I_{B,N}} \tag{7.12}$$

where $V_{P,M}$ is the maximum value of the amplitude of the pickup induced voltage, which gives rise to the maximum value $I_{o,M}$ for the average value of the rectifier output current. The value of the inductance in (7.12) has to be used to size L_R. It can happen that this value is too small to mitigate the harmonics in

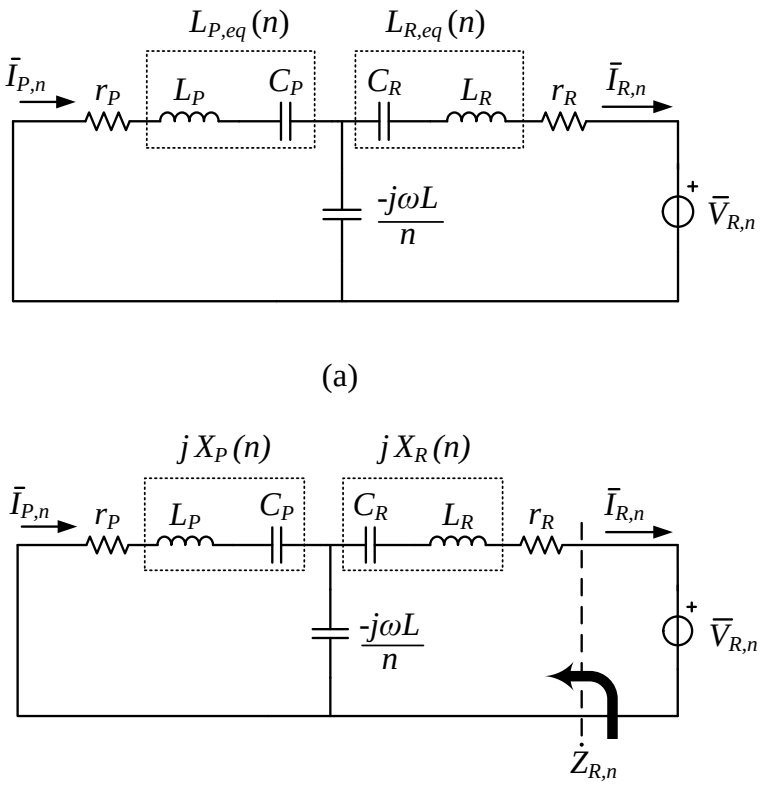

Fig. 7.7: Modified LCC compensation network. Circuit for the analysis of the fundamental quantities (a) and for the n-th order harmonics (b). $n = 2, 3, 4 \ldots$

the current i_R introduced by the voltage v_R. To face this problem, the inductance L_R can be replaced with the series of an inductor and a capacitor; the inductor has a value higher than the one obtained with (7.12) and the capacitor is designed to partially compensate it in order to see an equivalent inductance whose value is L at the supply frequency. The resulting modified LCC circuit is sketched in Fig. 7.7(a). The inductance L_R can be designed in order to fix the maximum value of the 2-nd order harmonic $I_{R,2}$ of the current i_R as a percentage of the fundamental I_R. To find the value of $I_{R,2}$, the scheme in Fig. 7.7(b) can be examined. It is used to assess the relations between the n-th harmonics of the quantities in the compensating network of the proposed topology; for this reason, the pure sinusoidal pickup voltage does not appear in it. All the reactances of Fig. 7.7(b) are expressed as function of the harmonic order n. For example, the reactance associated to the capacitor C at frequencies multiple of the nominal one ω is given by:

$$X_{C,n} = -\frac{1}{n\omega C} = -\frac{\omega L}{n} \tag{7.13}$$

in which the last equality holds because the capacitor C is designed to resonate with L at the nominal frequency. The equivalent reactances X_P and X_R have a similar expression which is found to be:

$$X_{i,n} = n\omega L_i - \frac{1}{n\omega C_i} = \left(\frac{n^2-1}{n}\right)\omega L_i + \frac{\omega L}{n} \tag{7.14}$$

where the subscript $i = P, R$ indicates either the "P" or the "R" branch. In the derivation of (7.14) the expression (7.2) has been exploited to substitute for C_P. An equivalent equation holds for C_R. . The n-th harmonic of the current i_R is given by:

$$I_{R,n} = \frac{V_{R,n}}{Z_{R,n}} \tag{7.15}$$

where the quantity $V_{R,n}$ is the amplitude of the n-th harmonic of v_R and $Z_{R,n}$ is the magnitude of the output impedance indicated in Fig. 7.7(b). The calculation of the impedance $\dot{Z}_{R,n}$ can be approximated considering $|X_{C,n}|$ small with respect to the reactance $X_{P,n}$; this is a valid approximation because usually L_P is greater that L. With this hypothesis, the harmonics of the current i_R do not flow in the "P" branch and, neglecting the small resistance r_R, the impedance $\dot{Z}_{R,n}$ becomes:

$$\dot{Z}_{R,n} \approx j(X_{R,n} + X_{C,n}) = j\left(\frac{n^2-1}{n}\right)\omega L_R \tag{7.16}$$

To calculate the 2-nd order harmonic of the current i_R, it is necessary to know $V_{R,2}$ that can be evaluated from the absolute value of the relative Fourier coefficient of the voltage v_R shown in the third plot of Fig. 7.5. It is given by:

$$V_{R,2} = \left|\frac{2}{\pi}\int_{\alpha}^{\pi} V_B \sin(2\theta)\, d\theta\right| = \frac{2}{\pi} V_B \sin^2(\alpha) \tag{7.17}$$

From (7.17), it can be noticed that the maximum value of the 2-nd harmonic of the rectifier input voltage is achieved when α is equal to $\frac{\pi}{2}$ and its value is $\frac{2}{\pi}V_{B,M}$ where $V_{B,M}$ is the maximum battery voltage. Substituting $n = 2$ in (7.16) and using (7.15) and (7.17), the maximum value of the 2-nd order harmonic of the current i_R is:

$$I_{R,2} = \frac{4}{3\pi}\frac{V_{B,M}}{\omega L_R} \tag{7.18}$$

The value of L_R can be obtained by imposing that the ratio between the amplitudes of the 2-nd harmonic and the fundamental of i_R is equal to a small fraction, for example 0.1. This leads to the equation:

$$\frac{I_{R,2}}{I_R} = 0.1 \quad \Rightarrow \quad L_R = 10\,\frac{4}{3\pi}\frac{V_{B,M}}{V_{P,M}}\,L \tag{7.19}$$

In the derivation of (7.19), the current I_R has been obtained using (7.3) with the maximum induced pickup voltage. It is worth to note that the harmonic content of the current i_R depends on the ratio $\frac{V_B}{V_{P,M}}$ that cannot be too high to avoid an oversizing of the inductance L_R.

Based on these considerations the design of the parameters of the modified LCC compensating network can be summarized as follow:

- Given the maximum pickup induced voltage $V_{P,M}$ and the nominal battery current $I_{B,N}$, the value for the inductance L can be found with (7.12).
- The capacitor C that resonates with L at the nominal frequency is given by $C = \frac{1}{\omega^2 L}$.
- With a given maximum battery voltage, the inductance L_R can be calculated according to (7.19).
- The capacitance C_P is derived from (7.2) and an equivalent equation is used for sizing C_R.

7.5 Simulation Results

To validate the theoretical analysis, the circuit of Fig. 7.2 with the modified LCC compensating network of Fig. 7.7(a) has been simulated in the PSIM environment. Together with the pickup power circuit, the control loop that regulates the battery charging has been implemented as well. The overall simulated system is depicted in Fig. 7.8. The DWPTS, intended to charge a battery with a nominal current $I_{B,N}$ of 25 A and a nominal voltage $V_{B,N}$ of 296 V, has been designed around the specifications listed in the upper part of Tab. 7.1 and according to the procedure explained in the previous section. The resulting components ratings can be found in the lower part of Tab. 7.1. The selection of the capacitor C_{DC} has been based on considerations regarding voltage and current ripple attenuation. The inductance L of Tab. 7.1 has been chosen less than 19 µH, value given by (7.12). This safety margin guarantees the battery charging with the nominal current $I_{B,N}$ even with the presence of the resistances r_P and r_R, neglected in the theoretical analysis. With this selection of L, the output current I_o expected from (7.11) is about 28 A.

The pickup circuit of Fig. 7.8 is supplied by an high-frequency sinusoidal voltage whose amplitude has a trapezoidal shape. As concern the control loop, it constitutes the inner loop used to perform the CC/CV charging process explained in Sec. 2.3. It is simply a current loop that utilizes the sensed battery current as a negative feedback and compares it with a current reference $I_{B,ref}$. Usually, this current reference is given by an outer voltage loop, but the implementation of the outer loop is not crucial for the analysis of the proposed control strategy. The current error feeds a PI regulator in which the gain and the time constant have been set to -0.05 rad/A and 40 µs, respectively[2]. The output of the regulator, conveniently bounded into the interval $0 \div \pi$, provides the reference of the duty-cycle α for the switch S. The nominal control angle α_N, which would have been 0 in ideal conditions if the outcome of (7.12) had used to design L, from (7.7) is found to be around 0.67 rad and 0.57 rad from simulation (a similar value can be obtained employing cumbersome equations that take into account r_P and r_R). In the control system of Fig. 7.8 the duty-cycle α is compared with a triangular wave which has an amplitude equal to π and it is in phase with the rectifier input

[2]The gain of the regulator is negative because the system is such that for a small increment of the control angle α corresponds a small reduction of the battery current.

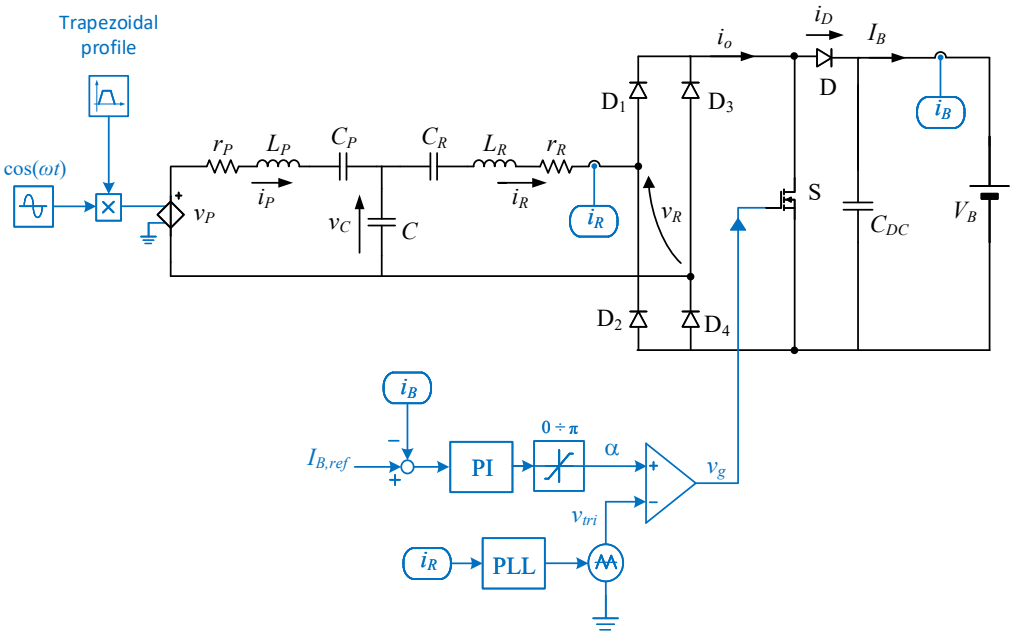

Fig. 7.8: Proposed pickup topology and control strategy simulated in PSIM.

Tab. 7.1: Specifications and components ratings for the simulated circuit.

Specifications		
Parameter	**Symbol**	**Value**
Maximum pickup induced voltage	$V_{P,M}$	400 V
Angular frequency	ω	$2\pi \cdot 85000\ \frac{\text{rad}}{\text{s}}$
Battery current	I_B	2.5 ÷ 25A
Battery voltage	V_B	240 ÷ 336V
Components ratings		
Resonant inductance	L	17 μH
Pickup coil inductance	L_P	120 μH
Rectifier-side inductance	L_R	60 μH
Resonant capacitance	C	206 nF
Pickup-side capacitance	C_P	34 nF
Rectifier-side capacitance	C_R	82 nF
Output capacitance	C_{DC}	300 μF
Pickup coil resistance	r_P	0.2 Ω
Rectifier-side resistance	r_R	0.1 Ω

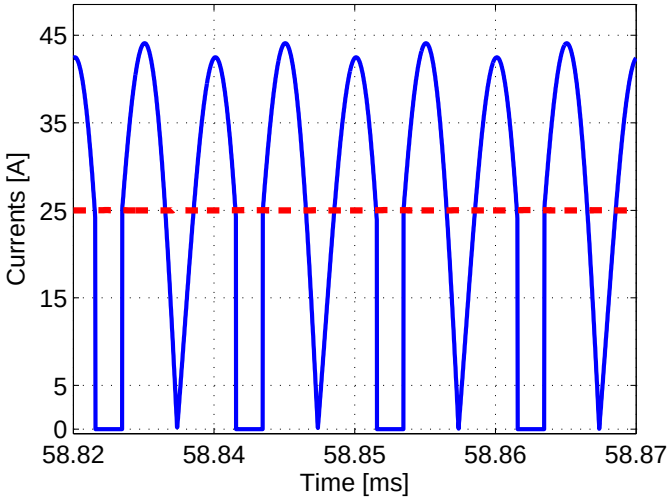

Fig. 7.9: Current i_D (blue solid) and i_B (red dashed) in nominal conditions obtained from simulation.

current. The phase of the rectifier input current has been obtained through a PLL. The output of the comparator is the gate signal v_g for the switch S which is in accordance with the signal shows in the first plot of Fig. 7.5.

To confirm the analysis done in Sec. 7.3, Fig. 7.9 reports the currents i_D and I_B obtained simulating the circuit of Fig. 7.8 under nominal conditions and when the coupling coefficient is maximum (in the flat zone of the amplitude of v_P). The waveforms of Fig. 7.9 are in good agreement with the last plot of Fig. 7.5 apart from the small variations in the amplitude of current i_D that are caused by the harmonics introduced in the LCC network by the voltage v_R. These harmonics are emphasized during the CV charging mode, for example when the battery absorbs half of the maximum power. In this situation, the battery charging current is 12.5 A with an ideal control angle α equal to 1.68 rad obtained from (7.7). These harmonics affect a little bit the phase displacement between the pickup induced voltage and the pickup current, as can be seen from Fig. 7.10. The pickup current (red line marked with crosses) is leading the voltage v_P (blue line without marks) by a small angle. As a comparison, the topology and the control strategy introduced in [82] have been simulated with the same parameters and under the half-load condition. The resulting pickup current is shown in Fig. 7.10 with a black line marked with dots. In this case, the current lags the voltage of about 47° and its amplitude is about 40% higher with respect to the amplitude of the pickup current obtained with the circuit proposed here. The amplitude of the currents can be a valid evidence on the superiority of the proposed topology in terms of efficiency.

In conclusion, in this chapter a new topology for the dc/dc converter downstream a modified version of an LCC-compensated pickup for DWPTSs has been proposed. The proposed topology gets rid of the large dc inductance used for the proper operation of the traditional pickup circuits. This solution leads to a reduction of the pickup size. Since the pickup circuitry has to be installed into the EVs, the power density (W/dm^3) of the on-board power electronics equipment is a crucial parameter. The adopted control strategy for the switch of the dc/dc converter

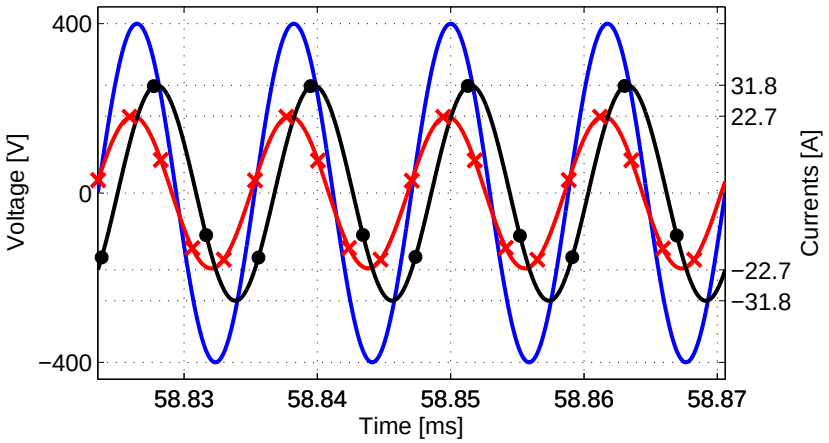

Fig. 7.10: Pickup voltage v_P (blue without marks) and current i_P (red marked with crosses) from the simulation of the half-load condition. For the same condition, the current i_P (black marked with dots) obtained with the topology and the control strategy presented in [82].

responsible for the battery charging process allows a UPF to be maintained at the pickup ac input stage. With the same transferred power, a pickup power factor close to one allows the pickup coil current to be minimum and thus this solution maximizes the pickup efficiency reducing its VA sizing. Having an high efficiency is another key feature for the pickup circuitry since the losses cannot be easily dissipated on-board the EVs.

Chapter 8

Conclusions

This thesis investigates the WPTSs employed in the dynamic EV battery charging. In particular, dynamic WPTSs with a lumped track structure are faced in this work. Although these systems are much more complicated to realize, they have better characteristics in terms of efficiency and magnetic field containment with respect to the stretched track dynamic WPTSs. Dynamic WPTSs can be employed in urban environments, for instance in proximity of the traffic lights. For this reason, it is very important that they comply with the ICNIRP guidelines. With stretched track systems it is very difficult to limit the magnetic field emissions that can be harmful for the pedestrians moving in proximity of the track.

This thesis starts with an introduction of the reasons that have lead the researchers to think about WPT for the EV application. Among them, convenience, reduction of the electrical shock risks and possibility to automate the charging process for the so called opportunity charging make the WPT a interesting alternative to the traditional wired chargers. These are the benefits brought by static WPTSs, but the real advantage of using the WPT technology comes from the dynamic EV wireless charging. In fact, by wirelessly transferring the charging and/or the traction power from an external stationary grid to the EVs, the size of the on-board batteries can be significantly reduced. The implementation of a compact network of chargers deployed under the urban roads allows the batteries to remain always charged thus increasing the range of the EVs and reducing the necessity of long stops at the charging stations.

In the first part of the thesis, the fundamental principles of the WPT technology and the key parts of a WPTS are carefully investigated with the aim of introducing the readers to the topic. The arguments are presented in a general manner valid both for static and for dynamic WPTSs. The possible ways of modeling the coil coupling and the steps needed for attaining the models are analyzed in detail. This work is helpful for clarifying the situation since a literature review can generate some confusion because various feasible coil coupling models are used.

The purpose of the compensating networks is explained, whether they are employed in the transmitting side or in the receiving side of a WPTS. For a WPTS in which the transmitting coil current is maintained constant, the receiving-side compensation is needed to increase the power transfer capabilities and the efficiency of the system. Despite the different topologies of compensating networks, a common equation is obtained both for the transferred power and for the power transfer

efficiency. The transmitting-side compensating networks are used to reduce the VA power rating of the inverter. Furthermore, they can be used to provide the transmitting coil with the current-source capability which is advisable in case of dynamic WPTSs.

The steady-state operation and the design procedure of various WPTSs are addressed in this work. The series-series compensation is demonstrated to be inadequate for the lumped track dynamic WPTSs since when the coil coupling becomes low, the track coil current tends to increase enormously. The best solution for such systems is the employment of the LC network (or similar networks derived from it) for the track compensation. This network inherently maintains a constant track current, thus relieving the task of the current regulator. This fact has been proved studying the steady-state equations of an LC-series, an LC-parallel and an LC-LC compensated WPTS.

The main contribution of this work is in the modeling of the dynamic of WPTSs. Since in WPTSs as well as in resonant converters the inverter switching frequency is equal or close to the operating frequency of the involved quantities, the conventional SSA technique cannot be applied to model such systems. For them, it is necessary to introduce a different method that models the systems considering the envelopes of the alternating quantities and the average values of the dc signals. The proposed MVLT as well as the GSSA and the LPT, available from the literature, are methods that are based on this fact. The reason for the introduction of a new modeling method is that with both the GSSA and the LPT methods the direct link between the "instantaneous model" and the "envelope model" is lost. This link is maintained by the MVLT method which thus can provide better insight into the envelope model. The validity of the models obtained with the MVLT method has been verified through some simulations. One of the considered test case is the series-compensated receiving-side circuit of a WPTS.

The MVLT method is used in this work for modeling the dynamic of (the envelope of) the quantities involved in the track side of an LC-compensated dynamic WPTS. The track current of an LC-compensated dynamic WPTS can be conceived as a high-frequency sinusoidal signal whose amplitude can be modulated by changing the amplitude of the (fundamental of the) inverter output voltage. The MVLT method is used to obtain the transfer function between the envelope of the inverter output voltage and the envelope of the track current. Based on the Bode diagram of this transfer function, a regulator is designed with the target of maintaining the track current under control. It is found that a pure integrator is enough to attain the desired bandwidth for the feedback loop and to maintain the system stability. The regulator allows for a fast and a safe star-up of the track current and in addition it is robust against the coil coupling coefficient variations typical of a lumped track dynamic WPTS.

Another important result of this thesis is the introduction of an unconventional topology for the pickup compensating network and for the on-board dc/dc converter. Contrarily to the common pickup topology, the proposed one does not rely on a bulky dc inductance for the proper operation of the dc/dc converter. The selected topology for the compensating network has been the LCC, which behaves in a similar way as the LC compensation. The current source characteristic of the LCC network allows the insertion of a switch connected directly in parallel

to the rectifier output terminals. A theoretical analysis is performed to find the mathematical expression of the relation between the command signal of the switch, which is operated at the supply voltage frequency, and the current injected in the battery. The control signal for the switch is synchronized with the rectifier input current and the control strategy is carefully selected in order to maintain a unity power factor between the pickup induced voltage and the pickup coil current. With the same transferred power, a pickup power factor close to one allows the pickup coil current to be minimum and thus this solution maximizes the pickup efficiency reducing its VA sizing. A time-domain analysis of this novel topology with the particular control strategy is carried out to understand the operating mode of the pickup. This theoretical analysis is based on the hypothesis of having the rectifier input current purely sinusoidal. This assumption and the analytical results have been checked through a comparison with the outcomes of some PSIM simulations where the novel topology and the control strategy have been implemented.

This Ph.D. work can be carry on with several others research activities. Among them, the ones that are immediately correlated with the main achievements seem to be the most interesting. First of all, some minor adjustments in the mathematical formalism should be done to make the MVLT method widespread accepted. Secondly, since all the performed theoretical analyses have been validated only through computer simulations, they could be verified also experimentally. To this end, a test rig for the LC-compensated dynamic WPTS and for the novel pickup topology should be arranged. Experimental tests can strengthen the quality of the theoretical analyses.

Appendix A

WPTSs Design: Formulary

This appendix constitutes a useful formulary for designing WPTSs that has LC compensating network in the transmitting side. All the equations shown in this chapter are derived based on the hypothesis that the receiver is always in resonance. This implies that for a fixed receiver side inductance, the capacitance changes its value at the various supply frequencies.

A.1 LC-Series

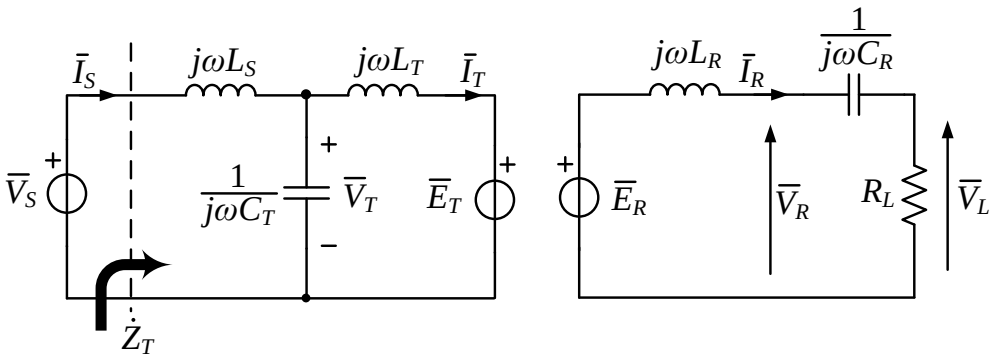

Fig. A.1: Fundamental Harmonic Approximation (FHA) scheme of an LC-series Wireless Power Transfer System (WPTS).

Hypothesis:

- Receiver in resonance

Definitions:

- $L_T = \alpha\, L_s$
- $L_R = \beta\, L_s$
- $R_{ref} = \frac{\omega^2\, k^2\, \alpha\beta\, L_s^2}{R_L}$
- $\omega_o = \frac{1}{\sqrt{L_s C_T}}$

General Case

$$B = R_{ref}\,(1-\omega^2\,L_sC_T) + j\,\omega L_s\,(1+\alpha-\alpha\,\omega^2 L_sC_T) \tag{A.1}$$

$$\dot{Z}_T = \frac{B}{1-\alpha\,\omega^2 L_sC_T + j\,\omega C_T R_{ref}} \tag{A.2}$$

$$\bar{I}_s = \bar{V}_s\,\frac{1-\alpha\,\omega^2 L_sC_T + j\,\omega C_T R_{ref}}{B} \tag{A.3}$$

$$\bar{V}_T = \frac{\bar{V}_s}{B}\,(R_{ref} + j\,\omega\,\alpha L_s) \tag{A.4}$$

$$\bar{I}_T = \frac{\bar{V}_s}{B} \tag{A.5}$$

$$\bar{E}_R = \bar{V}_s\,\frac{j\,\omega\,k\sqrt{\alpha\beta}\,L_s}{B} \tag{A.6}$$

$$\bar{I}_R = \frac{\bar{V}_s}{R_L}\,\frac{j\,\omega\,k\sqrt{\alpha\beta}\,L_s}{B} \tag{A.7}$$

$$\bar{V}_R = \bar{V}_s\,\frac{j\,\omega\,k\sqrt{\alpha\beta}\,L_s}{B}\left(1-j\,\frac{\omega L_s\beta}{R_L}\right) \tag{A.8}$$

$$\bar{E}_T = \bar{V}_s\,\frac{\omega^2\,k^2\,\alpha\beta\,L_s^2}{B\,R_L} \tag{A.9}$$

$$P_t = R_{ref}\,\frac{|\bar{V}_s|^2}{R_{ref}^2\,(1-\omega^2\,L_sC_T)^2 + \omega^2 L_s^2\,(1+\alpha-\alpha\,\omega^2 L_sC_T)^2} \tag{A.10}$$

Case: $\omega = \omega_o$

$$\dot{Z}_T = \frac{j\,\omega_o L_s}{\left[(1-\alpha) + j\,\frac{\omega_o L_s k^2\alpha\beta}{R_L}\right]} \tag{A.11}$$

$$\bar{I}_s = \frac{\bar{V}_s}{j\,\omega_o L_s}\,\left[(1-\alpha) + j\,\frac{\omega_o L_s k^2\alpha\beta}{R_L}\right] \tag{A.12}$$

$$\bar{V}_T = \bar{V}_s\,\left(\alpha - j\,\frac{\omega_o k^2\alpha\beta L_s}{R_L}\right) \tag{A.13}$$

$$\bar{I}_T = \frac{\bar{V}_s}{j\,\omega_o L_s} \tag{A.14}$$

$$\bar{E}_R = \bar{V}_s\,k\sqrt{\alpha\beta} \tag{A.15}$$

$$\bar{I}_R = \frac{\bar{V}_s}{R_L}\,k\sqrt{\alpha\beta} \tag{A.16}$$

$$\bar{V}_R = \bar{V}_s\,k\sqrt{\alpha\beta}\left(1-j\,\frac{\omega_o L_s\beta}{R_L}\right) \tag{A.17}$$

$$\bar{E}_T = \bar{V}_s\,\frac{-j\,\omega_o L_s}{R_L}\,k^2\alpha\beta \tag{A.18}$$

$$P_t = \frac{|\bar{V}_s|^2}{R_L}\,k^2\alpha\beta \tag{A.19}$$

Normalized Value Analysis

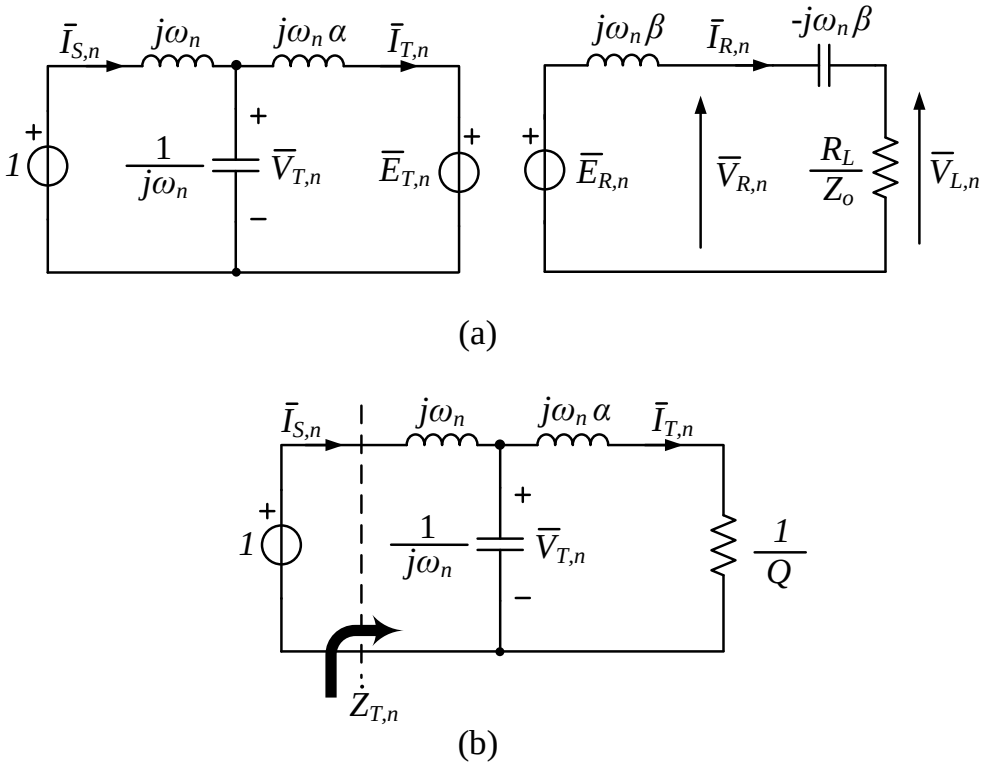

Fig. A.2: Fundamental Harmonic Approximation (FHA) scheme with normalized values of an LC-series Wireless Power Transfer System (WPTS) (a). Transmitting-side equivalent circuit (b).

Definitions:

- $\alpha = \frac{L_T}{L_s}$
- $\beta = \frac{L_R}{L_s}$
- $\omega_o = \frac{1}{\sqrt{L_s C_T}}$
- $Z_o = \sqrt{\frac{L_s}{C_T}}$
- $M = kL_s\sqrt{\alpha\beta}$
- $R_{ref} = \frac{\omega_n^2\,\omega_o^2\,k^2\alpha\beta L_s^2}{R_L}$
- $Q = \frac{Z_o}{R_{ref}} = \frac{R_L}{\omega_n^2\,\omega_o\,k^2\alpha\beta L_s}$

Base quantities:

- $V_b = V_s$

- $Z_b = Z_o$
- $I_b = \frac{V_b}{Z_o}$
- $P_b = \frac{V_b^2}{Z_o}$

General case

$$A = (1 - \omega_n^2) + j\,\omega_n\,Q(1 + \alpha - \omega_n^2\alpha) \tag{A.20}$$

$$\dot{Z}_{T,n} = \frac{A}{Q(1 - \omega_n^2\,\alpha) + j\,\omega_n} \tag{A.21}$$

$$\bar{I}_{s,n} = \frac{Q\,(1 - \omega_n^2\,\alpha) + j\,\omega_n}{A} \tag{A.22}$$

$$\bar{V}_{T,n} = \frac{1 + j\,\omega_n\,\alpha\,Q}{A} \tag{A.23}$$

$$\bar{I}_{T,n} = \frac{Q}{A} \tag{A.24}$$

$$\bar{E}_{R,n} = j\,\omega_n\,k\,\sqrt{\alpha\beta}\,\frac{Q}{A} \tag{A.25}$$

$$\bar{I}_{R,n} = j\,\omega_n\,k\,\sqrt{\alpha\beta}\,\frac{Q}{A}\,\frac{Z_o}{R_L} \tag{A.26}$$

$$\bar{V}_{R,n} = j\,\omega_n\,k\,\sqrt{\alpha\beta}\,\frac{Q}{A}\,\left(1 - j\,\omega_n\beta\,\frac{Z_o}{R_L}\right) \tag{A.27}$$

$$\bar{E}_{T,n} = \omega_n^2\,k^2\,\alpha\beta\,\frac{Q}{A}\frac{Z_o}{R_L} \tag{A.28}$$

$$P_{t,n} = \frac{Q}{|A|^2} \tag{A.29}$$

And the phase of the input impedance:

$$\angle\,\dot{Z}_{T,n} = \arctan\left\{\omega_n\left[Q\,(1 + \alpha - \omega_n^2\,\alpha)\,(1 - \omega_n^2\,\alpha) - \frac{1}{Q}\,(1 - \omega_n^2)\right]\right\} \tag{A.30}$$

Or:

$$\angle\,\dot{Z}_{T,n} = \arctan\left\{\frac{\omega_n Q\,(1 + \alpha - \omega_n^2\alpha)}{1 - \omega_n^2}\right\} - \arctan\left\{\frac{\omega_n}{Q(1 - \omega_n^2\alpha)}\right\} \tag{A.31}$$

Substituting Q to A.30:

$$\angle\,\dot{Z}_{T,n} = \arctan\left\{\omega_n\left[\frac{R_L}{\omega_n^2\,\omega_o\,k^2\alpha\beta L_s}\,(1 + \alpha - \omega_n^2\,\alpha)\,(1 - \omega_n^2\,\alpha) - \frac{\omega_n^2\,\omega_o\,k^2\alpha\beta L_s}{R_L}\,(1 - \omega_n^2)\right]\right\} \tag{A.32}$$

Case: $\omega_n = 1$

$$A = j\,Q \tag{A.33}$$

$$\dot{Z}_{T,n} = \frac{j\,Q}{Q\,(1-\alpha)+j} = \frac{Q + j\,Q^2\,(1-\alpha)}{Q^2\,(1-\alpha)^2+1} \tag{A.34}$$

$$\bar{I}_{s,n} = \frac{Q\,(1-\alpha)+j}{j\,Q} = \frac{1}{Q} - j\,(1-\alpha) \tag{A.35}$$

$$\bar{V}_{T,n} = \frac{1+j\,\alpha\,Q}{j\,Q} = \alpha - j\,\frac{1}{Q} \tag{A.36}$$

$$\bar{I}_{T,n} = \frac{1}{j} \tag{A.37}$$

$$\bar{E}_{R,n} = k\,\sqrt{\alpha\beta} \tag{A.38}$$

$$\bar{I}_{R,n} = k\,\sqrt{\alpha\beta}\,\frac{Z_o}{R_L} \tag{A.39}$$

$$\bar{V}_{R,n} = k\,\sqrt{\alpha\beta}\,\left(1 - j\,\beta\,\frac{Z_o}{R_L}\right) \tag{A.40}$$

$$\bar{E}_{T,n} = -j\;k^2\,\alpha\beta\,\frac{Z_o}{R_L} \tag{A.41}$$

$$P_{t,n} = \frac{1}{Q} \tag{A.42}$$

And the phase of the input impedance:

$$\angle\,\dot{Z}_{T,n} = \arctan\left\{Q\,(1-\alpha)\right\} = \arctan\left\{\frac{R_L}{\omega_o\,k^2\,\alpha\beta\,L_s}\,(1-\alpha)\right\} \tag{A.43}$$

A.2 LC-Parallel

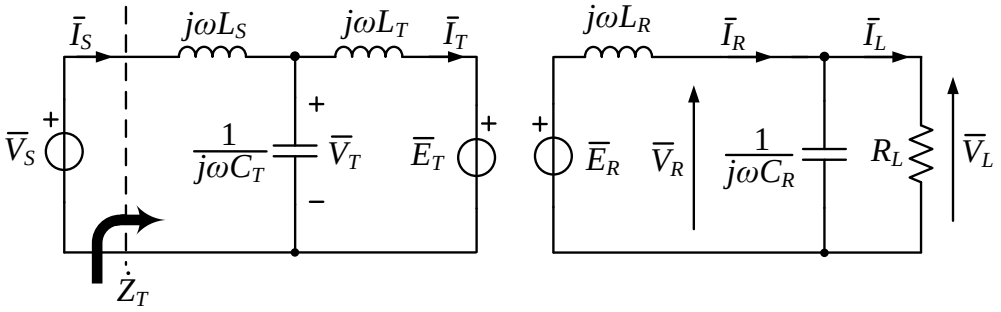

Fig. A.3: Fundamental Harmonic Approximation (FHA) scheme of an LC-parallel Wireless Power Transfer System (WPTS).

Hypothesis:

- Receiver in resonance

Definitions:

- $L_T = \alpha\, L_s$
- $L_R = \beta\, L_s$
- $R_{ref} = \frac{M^2}{L_R^2}\, R_L = \frac{\alpha}{\beta}\, R_L\, k^2$
- $X_{ref} = -\omega\, \frac{M^2}{L_R} = -\omega\, k^2\, \alpha L_s$
- $\omega_o = \frac{1}{\sqrt{L_s C_T}}$

General Case

$$B = R_{ref}\,(1 - \omega^2\, L_s C_T) + j\,\omega L_s\, \left[1 + \alpha\, \left(1 + \frac{X_{ref}}{\omega\, \alpha L_s}\right) - \omega^2 L_s C_T\, \alpha\, \left(1 + \frac{X_{ref}}{\omega\, \alpha L_s}\right)\right] \tag{A.44}$$

$$\dot{Z}_T = \frac{B}{1 - \omega^2 L_s C_T\, \alpha\, \left(1 + \frac{X_{ref}}{\omega\, \alpha L_s}\right) + j\,\omega C_T R_{ref}} \tag{A.45}$$

$$\bar{I}_s = \bar{V}_s\, \frac{1 - \omega^2 L_s C_T\, \alpha\, \left(1 + \frac{X_{ref}}{\omega\, \alpha L_s}\right) + j\,\omega C_T R_{ref}}{B} \tag{A.46}$$

$$\bar{V}_T = \frac{\bar{V}_s}{B}\, \left[R_{ref} + j\,\omega\, \alpha L_s\, \left(1 + \frac{X_{ref}}{\omega\, \alpha L_s}\right)\right] \tag{A.47}$$

$$\bar{I}_T = \frac{\bar{V}_s}{B} \tag{A.48}$$

$$\bar{E}_R = \bar{V}_s\, \frac{j\,\omega\, k\sqrt{\alpha\beta}\, L_s}{B} \tag{A.49}$$

$$\bar{I}_L = k\sqrt{\frac{\alpha}{\beta}}\, \frac{\bar{V}_s}{B} \tag{A.50}$$

$$\bar{V}_R = k\sqrt{\frac{\alpha}{\beta}}\, \frac{\bar{V}_s}{B}\, R_L \tag{A.51}$$

$$\bar{I}_R = \frac{\bar{V}_s}{B}\, \left[\sqrt{\frac{\alpha}{\beta}}\, k + j\, \frac{1}{\beta} \sqrt{\frac{\alpha}{\beta}}\, \frac{k}{\omega L_s}\, R_L\right] \tag{A.52}$$

$$\bar{E}_T = \frac{\bar{V}_s}{B}\, (R_{ref} + jX_{ref}) \tag{A.53}$$

$$P_t = R_{ref}\, \frac{|\bar{V}_s|^2}{R_{ref}^2\, (1 - \omega^2\, L_s C_T)^2 + \omega^2 L_s^2\, \left[1 + \alpha\, (1 + \frac{X_{ref}}{\omega\, \alpha L_s}) - \omega^2 L_s C_T\, \alpha (1 + \frac{X_{ref}}{\omega\, \alpha L_s})\right]^2} \tag{A.54}$$

Substituting R_{ref} and X_{ref}:

$$B = \frac{\alpha}{\beta}\, k^2\, R_L\, (1 - \omega^2\, L_s C_T) + j\, \omega L_s\, [1 + \alpha\, (1 - k^2) - \omega^2\, C_T L_s \alpha\, (1 - k^2)] \tag{A.55}$$

$$\dot{Z}_T = \frac{B}{1 - \omega^2 L_s C_T\, \alpha(1 - k^2) + j\, \omega C_T \frac{\alpha}{\beta}\, k^2\, R_L} \tag{A.56}$$

$$\bar{I}_s = \frac{\bar{V}_s}{B}\, \left[1 - \omega^2 L_s C_T\, \alpha(1 - k^2) + j\, \omega C_T \frac{\alpha}{\beta}\, k^2\, R_L\right] \tag{A.57}$$

$$\bar{V}_T = \frac{\bar{V}_s}{B}\, \left[\frac{\alpha}{\beta}\, k^2\, R_L + j\, \omega L_s\, \alpha(1 - k^2)\right] \tag{A.58}$$

$$\bar{I}_T = \frac{\bar{V}_s}{B} \tag{A.59}$$

$$\bar{E}_R = \bar{V}_s\, \frac{j\, \omega\, k \sqrt{\alpha\beta}\, L_s}{B} \tag{A.60}$$

$$\bar{I}_L = k \sqrt{\frac{\alpha}{\beta}}\, \frac{\bar{V}_s}{B} \tag{A.61}$$

$$\bar{V}_R = k \sqrt{\frac{\alpha}{\beta}}\, \frac{\bar{V}_s}{B}\, R_L \tag{A.62}$$

$$\bar{I}_R = \frac{\bar{V}_s}{B}\, \left[\sqrt{\frac{\alpha}{\beta}}\, k + j\, \frac{1}{\beta} \sqrt{\frac{\alpha}{\beta}} \frac{k}{\omega L_s}\, R_L\right] \tag{A.63}$$

$$\bar{E}_T = \frac{\bar{V}_s}{B}\, \left(\frac{\alpha}{\beta}\, k^2\, R_L - j\omega k^2 \alpha L_s\right) \tag{A.64}$$

$$P_t = \frac{\alpha}{\beta}\, k^2\, R_L\, \frac{|\bar{V}_s|^2}{\left(\frac{\alpha}{\beta}\right)^2 k^4\, R_L^2\, (1 - \omega^2\, L_s C_T)^2 + \omega^2 L_s^2\, [1 + \alpha\, (1 - k^2) - \omega^2 L_s C_T\, \alpha(1 - k^2)]^2} \tag{A.65}$$

Case $\omega = \omega_o$

$$B = j\, \omega_o L_s \tag{A.66}$$

$$\dot{Z}_T = \frac{j\, \omega_o L_s}{1 - \ \alpha(1 - k^2) + j\, \omega_o C_T \frac{\alpha}{\beta}\, k^2\, R_L} \tag{A.67}$$

$$\bar{I}_s = \frac{\bar{V}_s}{j\, \omega_o L_s}\, \left[1 - \ \alpha(1 - k^2) + j\, \omega_o C_T \frac{\alpha}{\beta}\, k^2\, R_L\right] \tag{A.68}$$

$$\bar{V}_T = \frac{\bar{V}_s}{j\, \omega_o L_s}\, \left[\frac{\alpha}{\beta}\, k^2\, R_L + j\, \omega_o L_s\, \alpha(1 - k^2)\right] \tag{A.69}$$

$$\bar{I}_T = \frac{\bar{V}_s}{j\, \omega_o L_s} \tag{A.70}$$

$$\bar{E}_R = \bar{V}_s\, k \sqrt{\alpha\beta} \tag{A.71}$$

$$\bar{I}_L = \frac{\bar{V}_s}{j\, \omega_o L_s}\, k \sqrt{\frac{\alpha}{\beta}} \tag{A.72}$$

$$\bar{V}_R = \frac{\bar{V}_s}{j\,\omega_o L_s}\, k \sqrt{\frac{\alpha}{\beta}}\, R_L \tag{A.73}$$

$$\bar{I}_R = \frac{\bar{V}_s}{j\,\omega_o L_s} \left[\sqrt{\frac{\alpha}{\beta}}\, k + j\, \frac{1}{\beta} \sqrt{\frac{\alpha}{\beta}} \frac{k}{\omega_o L_s}\, R_L \right] \tag{A.74}$$

$$\bar{E}_T = \frac{\bar{V}_s}{j\,\omega_o L_s} \left(\frac{\alpha}{\beta}\, k^2\, R_L - j\omega_o k^2 \alpha L_s \right) \tag{A.75}$$

$$P_t = \frac{|\bar{V}_s|^2}{\omega_o^2 L_s^2}\, \frac{\alpha}{\beta}\, k^2\, R_L \tag{A.76}$$

Normalized Value Analysis

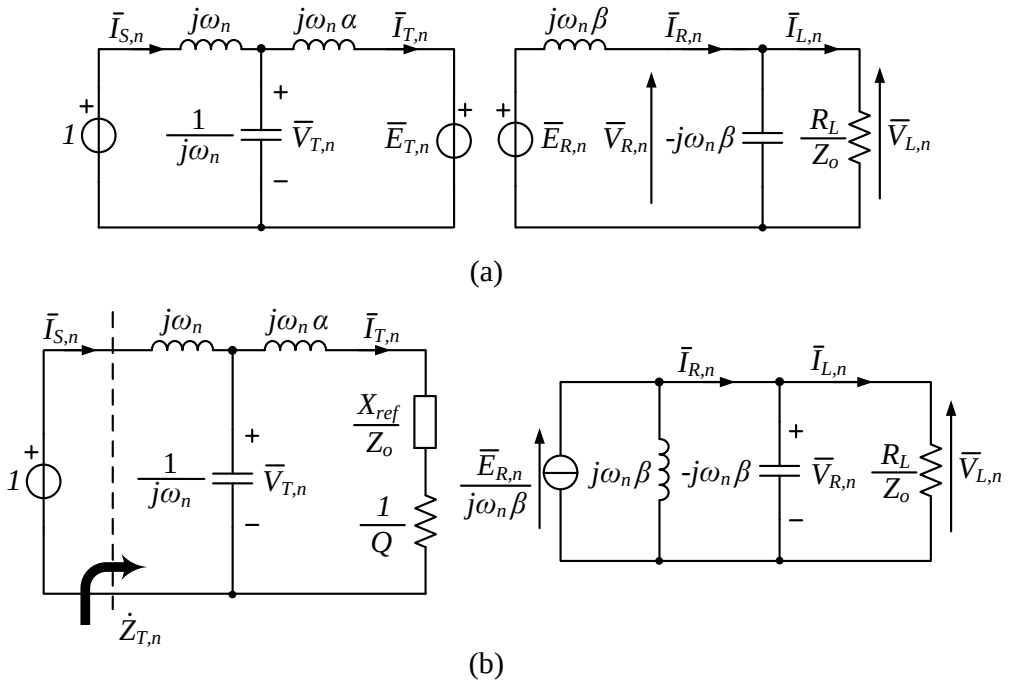

Fig. A.4: Fundamental Harmonic Approximation (FHA) scheme with normalized values of an LC-parallel Wireless Power Transfer System (WPTS) (a). Equivalent circuits (b).

Definitions:

- $\alpha = \frac{L_T}{L_s}$
- $\beta = \frac{L_R}{L_s}$
- $\omega_o = \frac{1}{\sqrt{L_s C_T}}$
- $Z_o = \sqrt{\frac{L_s}{C_T}}$

- $M = kL_s\sqrt{\alpha\beta}$
- $R_{ref} = \frac{M^2}{L_R^2} R_L = \frac{\alpha}{\beta} R_L\, k^2$
- $X_{ref} = -\omega_n\omega_o \frac{M^2}{L_R} = -\omega_n\alpha\, k^2\, Z_o$
- $Q = \frac{Z_o}{R_{ref}} = \frac{\omega_o L_s}{R_L \frac{\alpha}{\beta} k^2}$

Base quantities:

- $V_b = V_s$
- $Z_b = Z_o$
- $I_b = \frac{V_b}{Z_o}$
- $P_b = \frac{V_b^2}{Z_o}$

General case

$$A = 1 - \omega_n^2 + j\,\omega_n Q \left[1 + \alpha\left(1 + \frac{X_{ref}}{\alpha\,\omega_n Z_o}\right)\left(1 - \omega_n^2\right)\right] \tag{A.77}$$

$$\dot{Z}_{T,n} = \frac{A}{Q\left[1 - \omega_n^2\,\alpha\left(1 + \frac{X_{ref}}{\alpha\,\omega_n Z_o}\right)\right] + j\,\omega_n} \tag{A.78}$$

$$\bar{I}_{s,n} = \frac{Q\left[1 - \omega_n^2\,\alpha\left(1 + \frac{X_{ref}}{\alpha\,\omega_n Z_o}\right)\right] + j\,\omega_n}{A} \tag{A.79}$$

$$\bar{V}_{T,n} = \frac{1 + j\,\omega_n\, Q\alpha\left(1 + \frac{X_{ref}}{\alpha\,\omega_n Z_o}\right)}{A} \tag{A.80}$$

$$\bar{I}_{T,n} = \frac{Q}{A} \tag{A.81}$$

$$\bar{E}_{R,n} = \frac{j\,\omega_n k\,\sqrt{\alpha\beta}\,Q}{A} \tag{A.82}$$

$$\bar{I}_{L,n} = k\sqrt{\frac{\alpha}{\beta}}\frac{Q}{A} \tag{A.83}$$

$$\bar{V}_{R,n} = \frac{1}{k}\sqrt{\frac{\beta}{\alpha}}\frac{1}{A} \tag{A.84}$$

$$\bar{I}_{R,n} = k\sqrt{\frac{\alpha}{\beta}}\frac{Q}{A} + j\,\frac{1}{\sqrt{\alpha\beta}}\frac{1}{k}\frac{1}{A}\frac{1}{\omega_n} \tag{A.85}$$

$$\bar{E}_{T,n} = \frac{1 - j\,\omega_n\, k^2\alpha Q}{A} \tag{A.86}$$

$$P_{t,n} = \frac{Q}{|A|^2} \tag{A.87}$$

Substituting R_{ref} and X_{ref}:

$$A = 1 - \omega_n^2 + j\,\omega_n Q\,\left[1 + \alpha\,(1-k^2)(1-\omega_n^2)\right] \tag{A.88}$$

$$\dot{Z}_{T,n} = \frac{A}{Q\,[1 - \omega_n^2\,\alpha\,(1-k^2)] + j\,\omega_n} \tag{A.89}$$

$$\bar{I}_{s,n} = \frac{Q\,[1 - \omega_n^2\,\alpha\,(1-k^2)] + j\,\omega_n}{A} \tag{A.90}$$

$$\bar{V}_{T,n} = \frac{1 + j\,\omega_n\,Q\,\alpha\,(1-k^2)}{A} \tag{A.91}$$

$$\bar{I}_{T,n} = \frac{Q}{A} \tag{A.92}$$

$$\bar{E}_{R,n} = \frac{j\,\omega_n k\,\sqrt{\alpha\beta}\,Q}{A} \tag{A.93}$$

$$\bar{I}_{L,n} = k\sqrt{\frac{\alpha}{\beta}}\,\frac{Q}{A} \tag{A.94}$$

$$\bar{V}_{R,n} = \frac{1}{k}\sqrt{\frac{\beta}{\alpha}}\,\frac{1}{A} \tag{A.95}$$

$$\bar{I}_{R,n} = k\sqrt{\frac{\alpha}{\beta}}\,\frac{Q}{A} + j\,\frac{1}{\sqrt{\alpha\beta}}\,\frac{1}{k}\,\frac{1}{A}\,\frac{1}{\omega_n} \tag{A.96}$$

$$\bar{E}_{T,n} = \frac{1 - j\,\omega_n\,k^2\alpha Q}{A} \tag{A.97}$$

$$P_{t,n} = \frac{Q}{(1-\omega_n^2)^2 + \omega_n^2 Q^2\,\left[1 + \alpha\,(1-k^2)(1-\omega_n^2)\right]^2} \tag{A.98}$$

And the angle of the input impedance is:

$$\angle\,\dot{Z}_{T,n} = \arctan\left\{\omega_n Q\left[1 + \alpha(1-k^2) - \omega_n^2\,\alpha(1-k^2))\right]\left[1 - \omega_n^2\,\alpha(1-k^2)\right] - \frac{1}{Q}\,\omega_n(1-\omega_n^2)\right\} \tag{A.99}$$

Case $\omega_n = 1$

$$A = j\,Q \tag{A.100}$$

$$\dot{Z}_{T,n} = \frac{j\,Q}{Q\,[1 - \alpha\,(1-k^2)] + j\,1} \tag{A.101}$$

$$\bar{I}_{s,n} = \frac{1}{Q} - j\,[1 - \alpha\,(1-k^2)] \tag{A.102}$$

$$\bar{V}_{T,n} = \alpha\,(1-k^2) - j\,\frac{1}{Q} \tag{A.103}$$

$$\bar{I}_{T,n} = \frac{1}{j} \tag{A.104}$$

$$\bar{E}_{R,n} = k\sqrt{\alpha\beta} \tag{A.105}$$

$$\bar{I}_{L,n} = -j\,k\sqrt{\frac{\alpha}{\beta}} \tag{A.106}$$

$$\bar{V}_{R,n} = -j\,\frac{1}{k}\sqrt{\frac{\beta}{\alpha}}\,\frac{1}{Q} \tag{A.107}$$

$$\bar{I}_{R,n} = \frac{1}{Q}\,\frac{1}{\sqrt{\alpha\beta}}\,\frac{1}{k} - j\,k\sqrt{\frac{\alpha}{\beta}} \tag{A.108}$$

$$\bar{E}_{T,n} = -k^2\alpha - j\,\frac{1}{Q} \tag{A.109}$$

$$P_{t,n} = \frac{1}{Q} \tag{A.110}$$

And the phase of the input impedance:

$$\angle\,\dot{Z}_{T,n} = \arctan\left\{Q[1-\alpha\,(1-k^2)]\right\} \tag{A.111}$$

A.3 LC-CL

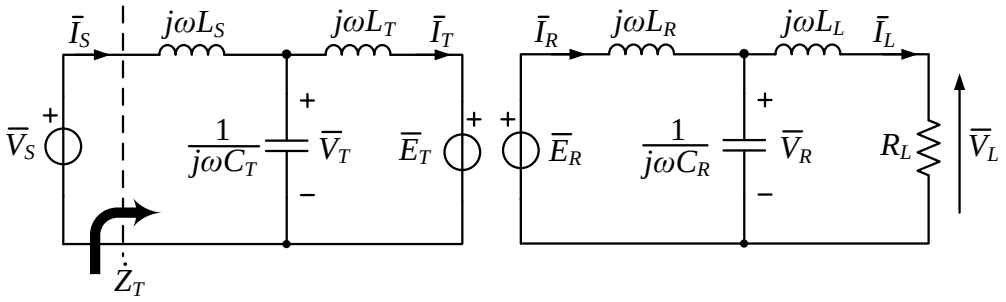

Fig. A.5: Fundamental Harmonic Approximation (FHA) scheme of an LC-LC Wireless Power Transfer System (WPTS).

Hypotheses:

- L_R and C_R in resonance
- $L_L = L_R$

Definitions:

- $L_T = \alpha\,L_s$
- $L_R = \beta\,L_s$

- $R_{ref} = \frac{\alpha}{\beta} R_L k^2$
- $X_{ref} = 0$
- $\omega_o = \frac{1}{\sqrt{L_s C_T}}$

General Case

$$B = \frac{\alpha}{\beta} R_L k^2 (1 - \omega^2 L_s C_T) + j \omega L_s (1 + \alpha - \alpha \omega^2 L_s C_T) \tag{A.112}$$

$$\dot{Z}_T = \frac{B}{1 - \alpha \omega^2 L_s C_T + j \omega C_T \frac{\alpha}{\beta} R_L k^2} \tag{A.113}$$

$$\bar{I}_s = \frac{\bar{V}_s}{B} \left[1 - \alpha \omega^2 L_s C_T + j \omega C_T \frac{\alpha}{\beta} R_L k^2\right] \tag{A.114}$$

$$\bar{V}_T = \frac{\bar{V}_s}{B} (\frac{\alpha}{\beta} R_L k^2 + j \omega \alpha L_s) \tag{A.115}$$

$$\bar{I}_T = \frac{\bar{V}_s}{B} \tag{A.116}$$

$$\bar{E}_R = \bar{V}_s \frac{j \omega k \sqrt{\alpha\beta} L_s}{B} \tag{A.117}$$

$$\bar{I}_R = j \frac{\bar{V}_s}{B} \sqrt{\frac{\alpha}{\beta}} \frac{k}{\omega L_s \beta} R_L \tag{A.118}$$

$$\bar{V}_R = \frac{\bar{V}_s}{B} \sqrt{\frac{\alpha}{\beta}} k \, [R_L + j \omega L_s \beta] \tag{A.119}$$

$$\bar{I}_L = \frac{\bar{V}_s}{B} \sqrt{\frac{\alpha}{\beta}} k \tag{A.120}$$

$$\bar{E}_T = \frac{\bar{V}_s}{B} \frac{\alpha}{\beta} R_L k^2 \tag{A.121}$$

$$\bar{V}_L = \frac{\bar{V}_s}{B} \sqrt{\frac{\alpha}{\beta}} k R_L \tag{A.122}$$

$$P_t = \frac{\alpha}{\beta} R_L k^2 \frac{|\bar{V}_s|^2}{(\frac{\alpha}{\beta} R_L k^2)^2 (1 - \omega^2 L_s C_T)^2 + \omega^2 L_s^2 (1 + \alpha - \alpha \omega^2 L_s C_T)^2} \tag{A.123}$$

Case $\omega = \omega_o$

$$B = j \omega_o L_s \tag{A.124}$$

$$\dot{Z}_T = \frac{j \omega_o L_s}{1 - \alpha + j \omega_o C_T \frac{\alpha}{\beta} R_L k^2} \tag{A.125}$$

$$\bar{I}_s = \frac{\bar{V}_s}{j \omega_o L_s} \left[1 - \alpha + j \omega_o C_T \frac{\alpha}{\beta} R_L k^2\right] \tag{A.126}$$

$$\bar{V}_T = \frac{\bar{V}_s}{j \omega_o L_s} (\frac{\alpha}{\beta} R_L k^2 + j \omega_o \alpha L_s) \tag{A.127}$$

$$\bar{I}_T = \frac{\bar{V}_s}{j\,\omega_o L_s} \tag{A.128}$$

$$\bar{E}_R = \bar{V}_s\,k\,\sqrt{\alpha\beta} \tag{A.129}$$

$$\bar{I}_R = \frac{\bar{V}_s}{\omega_o^2 L_s^2}\,\frac{1}{\beta}\,\sqrt{\frac{\alpha}{\beta}}\,R_L \tag{A.130}$$

$$\bar{V}_R = \bar{V}_s\,\sqrt{\frac{\alpha}{\beta}}\,k\,\left[\beta - j\,\frac{R_L}{\omega_o L_s}\right] \tag{A.131}$$

$$\bar{I}_L = \frac{\bar{V}_s}{j\,\omega_o L_s}\,\sqrt{\frac{\alpha}{\beta}}\,k \tag{A.132}$$

$$\bar{E}_T = \frac{\bar{V}_s}{j\,\omega_o L_s}\,\frac{\alpha}{\beta}\,R_L\,k^2 \tag{A.133}$$

$$\bar{V}_L = \frac{\bar{V}_s}{j\,\omega_o L_s}\,\sqrt{\frac{\alpha}{\beta}}\,k\,R_L \tag{A.134}$$

$$P_t = \frac{|\bar{V}_s|^2}{\omega_o^2 L_s^2}\,\frac{\alpha}{\beta}\,k^2\,R_L \tag{A.135}$$

Normalized Value Analysis

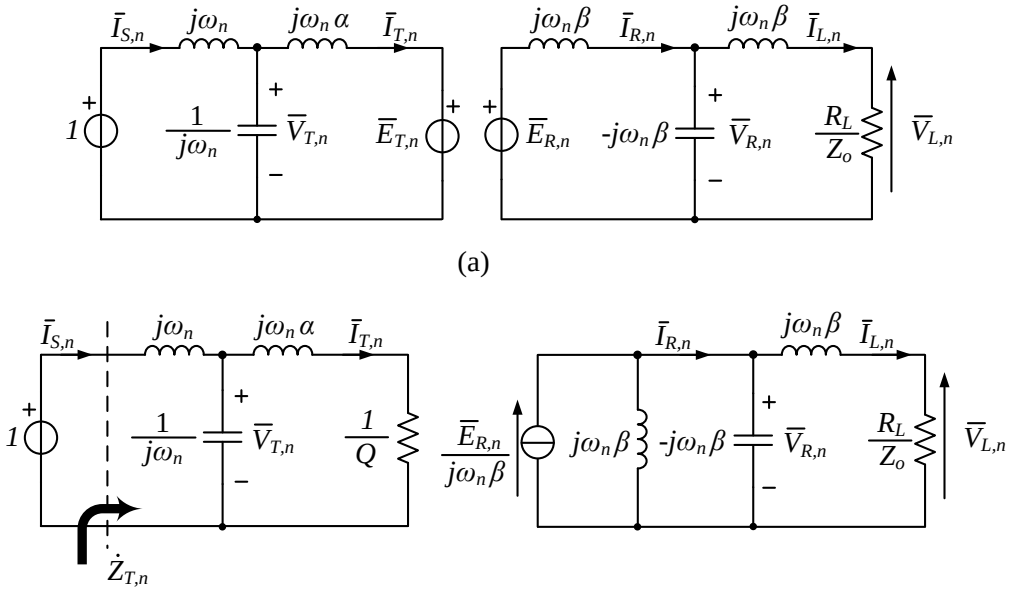

Fig. A.6: Fundamental Harmonic Approximation (FHA) scheme with normalized values of an LC-LC Wireless Power Transfer System (WPTS) (a). Equivalent circuits (b).

Definitions:

- $\alpha = \frac{L_T}{L_s}$
- $\beta = \frac{L_R}{L_s}$
- $\gamma = \frac{L_2}{L_R}$
- $\omega_o = \frac{1}{\sqrt{L_s C_T}}$
- $Z_o = \sqrt{\frac{L_s}{C_T}}$
- $M = kL_s\sqrt{\alpha\beta}$
- $R_{ref} = \frac{\alpha}{\beta} R_L k^2$
- $X_{ref} = 0$
- $Q = \frac{Z_o}{R_{ref}} = \frac{\omega_o L_s}{R_L \frac{\alpha}{\beta} k^2}$

Hypothesis:

- $\gamma = 1$

Base quantities:

- $V_b = V_s$
- $Z_b = Z_o$
- $I_b = \frac{V_b}{Z_o}$
- $P_b = \frac{V_b^2}{Z_o}$

General case

$$A = 1 - \omega_n^2 + j\,\omega_n Q(1 + \alpha - \alpha\omega_n^2) \tag{A.136}$$

$$\dot{Z}_{T,n} = \frac{A}{Q\,(1 - \omega_n^2\alpha) + j\,\omega_n} \tag{A.137}$$

$$\bar{I}_{s,n} = \frac{Q\,(1 - \omega_n^2\alpha) + j\,\omega_n}{A} \tag{A.138}$$

$$\bar{V}_{T,n} = \frac{1 + j\,\omega_n Q\alpha}{A} \tag{A.139}$$

$$\bar{I}_{T,n} = \frac{Q}{A} \tag{A.140}$$

$$\bar{E}_{R,n} = j\,\omega_n k\,\sqrt{\alpha\beta}\,\frac{Q}{A} \tag{A.141}$$

$$\bar{I}_{R,n} = j\,\frac{1}{k\omega_n}\,\frac{1}{\sqrt{\alpha\beta}}\,\frac{1}{A} \tag{A.142}$$

$$\bar{V}_{R,n} = \frac{1}{A}\sqrt{\frac{\beta}{\alpha}}\frac{1}{k}\left[1 + j\,\omega_n\beta\,\frac{Z_o}{R_L}\right] \tag{A.143}$$

$$\bar{I}_{L,n} = \frac{1}{A}\sqrt{\frac{\beta}{\alpha}}\frac{1}{k}\frac{Z_o}{R_L} \tag{A.144}$$

$$\bar{E}_{T,n} = \frac{1}{A} \tag{A.145}$$

$$\bar{V}_{L,n} = \frac{1}{A}\sqrt{\frac{\beta}{\alpha}}\frac{1}{k} \tag{A.146}$$

$$P_t = \frac{Q}{|A|^2} \tag{A.147}$$

And the angle of the input impedance:

$$\angle\,\dot{Z}_{T,n} = \arctan\left\{\omega_n\left[Q\,(1+\alpha-\omega_n^2\,\alpha)\,(1-\omega_n^2\,\alpha) - \frac{1}{Q}\,(1-\omega_n^2)\right]\right\} \tag{A.148}$$

Case $\omega_n = 1$

$$A = j\,Q \tag{A.149}$$

$$\dot{Z}_{T,n} = \frac{j\,Q}{Q\,(1-\alpha)+j} = \frac{1}{Q^2(1-\alpha)^2+1}\,[Q + j\,Q^2(1-\alpha)] \tag{A.150}$$

$$\bar{I}_{s,n} = \frac{Q\,(1-\alpha)+j}{j\,Q} = \frac{1}{Q} - j\,(1-\alpha) \tag{A.151}$$

$$\bar{V}_{T,n} = \frac{1+j\,Q\alpha}{j\,Q} = \alpha - j\,\frac{1}{Q} \tag{A.152}$$

$$\bar{I}_{T,n} = \frac{1}{j} \tag{A.153}$$

$$\bar{E}_{R,n} = k\,\sqrt{\alpha\beta} \tag{A.154}$$

$$\bar{I}_{R,n} = k\,\frac{1}{\beta}\sqrt{\frac{\alpha}{\beta}}\,\frac{R_L}{Z_o} \tag{A.155}$$

$$\bar{V}_{R,n} = k\,\sqrt{\alpha\beta} - j\,k\,\sqrt{\frac{\alpha}{\beta}}\,\frac{R_L}{Z_o} \tag{A.156}$$

$$\bar{I}_{L,n} = -j\,k\,\sqrt{\frac{\alpha}{\beta}} \tag{A.157}$$

$$\bar{E}_{T,n} = -j\,\frac{R_L}{Z_o}\,\frac{\alpha}{\beta}\,k^2 \tag{A.158}$$

$$\bar{V}_{L,n} = -j\,k\,\sqrt{\frac{\alpha}{\beta}}\,\frac{R_L}{Z_o} \tag{A.159}$$

$$P_t = \frac{R_L}{Z_o}\,\frac{\alpha}{\beta}\,k^2 \tag{A.160}$$

And the angle of the input impedance:

$$\angle \dot{Z}_{T,n} = \arctan\left\{Q(1-\alpha)\right\} \tag{A.161}$$

Bibliography

[1] National Aeronautics and Space Administration (NASA). (Sep. 2018). Global climate change, [Online]. Available: https://climate.nasa.gov/evidence/ (cit. on p. 1).

[2] International Energy Agency (IEA). (Nov. 2015). World energy outlook 2015, [Online]. Available: https://webstore.iea.org/world-energy-outlook-2015 (cit. on p. 1).

[3] M. Ehsani, Y. Gao, S. Gay, and A. Emadi, *Modern Electric, Hybrid Electric, and Fuel Cell Vehicles: Fundamentals, Theory, and Design*, ser. Power Electronics and Applications Series. CRC Press, 2004, ISBN: 9781420037739 (cit. on p. 1).

[4] S. Sorrell, J. Speirs, R. Bentley, A. Brandt, and R. Miller, "Global oil depletion: A review of the evidence," *Energy Policy*, vol. 38, no. 9, pp. 5290–5295, 2010 (cit. on p. 1).

[5] International Energy Agency (IEA). (May 2018). Global EV outlook 2018, [Online]. Available: https://webstore.iea.org/global-ev-outlook-2018 (cit. on p. 1).

[6] S. Li and C. C. Mi, "Wireless power transfer for electric vehicle applications," *IEEE J. Emerg. Sel. Topics Power Electron.*, vol. 3, no. 1, pp. 4–17, Mar. 2015 (cit. on pp. 1, 10, 12, 35).

[7] G. Berckmans, M. Messagie, J. Smekens, N. Omar, L. Vanhaverbeke, and J. Van Mierlo, "Cost projection of state of the art lithium-ion batteries for electric vehicles up to 2030," *Energies*, vol. 10, no. 9, pp. 1–20, 2017. [Online]. Available: https://EconPapers.repec.org/RePEc:gam:jeners:v:10:y:2017:i:9:p:1314-:d:110631 (cit. on p. 2).

[8] M. Shirk and J. Wishart, "Effects of electric vehicle fast charging on battery life and vehicle performance," in *SAE 2015 World Congress & Exhibition*, SAE International, Apr. 2015. [Online]. Available: https://doi.org/10.4271/2015-01-1190 (cit. on p. 2).

[9] F. Lu, H. Zhang, H. Hofmann, and C. Mi, "A double-sided LCLC-compensated capacitive power transfer system for electric vehicle charging," *IEEE Trans. Power Electron.*, vol. 30, no. 11, pp. 6011–6014, Nov. 2015 (cit. on p. 2).

[10] R. Bosshard and J. W. Kolar, "Inductive power transfer for electric vehicle charging: Technical challenges and tradeoffs," *IEEE Power Electron. Mag.*, vol. 3, no. 3, pp. 22–30, Sep. 2016 (cit. on pp. 2, 26).

[11] S. Lukic and Z. Pantic, "Cutting the cord: Static and dynamic inductive wireless charging of electric vehicles," *IEEE Electrific. Mag.*, vol. 1, no. 1, pp. 57–64, Sep. 2013 (cit. on p. 2).

[12] Z. Pantic, S. Bai, and S. M. Lukic, "Inductively coupled power transfer for continuously powered electric vehicles," in *Proc. 2009 IEEE Vehicle Power and Propulsion Conference*, Dearborn, MI, USA, Sep. 2009, pp. 1271–1278 (cit. on p. 3).

[13] A. Zaheer, M. Neath, H. Z. Z. Beh, and G. A. Covic, "A dynamic EV charging system for slow moving traffic applications," *IEEE Trans. Transport. Electrific.*, vol. 3, no. 2, pp. 354–369, Jun. 2017 (cit. on pp. 4, 99).

[14] B. Singh, B. N. Singh, A. Chandra, K. Al-Haddad, A. Pandey, and D. P. Kothari, "A review of single-phase improved power quality AC-DC converters," *IEEE Trans. Ind. Electron.*, vol. 50, no. 5, pp. 962–981, Oct. 2003 (cit. on p. 9).

[15] O. Garcia, J. A. Cobos, R. Prieto, P. Alou, and J. Uceda, "Single phase power factor correction: A survey," *IEEE Trans. Power Electron.*, vol. 18, no. 3, pp. 749–755, Jun. 2003 (cit. on p. 9).

[16] G. A. Covic, J. T. Boys, M. L. G. Kissin, and H. G. Lu, "A three-phase inductive power transfer system for roadway-powered vehicles," *IEEE Trans. Ind. Electron.*, vol. 54, no. 6, pp. 3370–3378, Dec. 2007 (cit. on p. 10).

[17] A. W. Green and J. T. Boys, "10 kHz inductively coupled power transfer-concept and control," in *Proc. 1994 Fifth International Conference on Power Electronics and Variable-Speed Drives*, London, UK, Oct. 1994, pp. 694–699 (cit. on p. 10).

[18] J. T. Boys, G. A. Covic, and A. W. Green, "Stability and control of inductively coupled power transfer systems," *IEE Proc. - Electr. Power Appl.*, vol. 147, no. 1, pp. 37–43, Jan. 2000 (cit. on pp. 10, 36, 42).

[19] C.-S. Wang, O. H. Stielau, and G. A. Covic, "Design considerations for a contactless electric vehicle battery charger," *IEEE Trans. Ind. Electron.*, vol. 52, no. 5, pp. 1308–1314, Oct. 2005 (cit. on pp. 10, 42, 92).

[20] SAE International. (Nov. 2017). Wireless power transfer for light-duty plug-in/electric vehicles and alignment methodology, [Online]. Available: https://saemobilus.sae.org/content/J2954_201711 (cit. on p. 10).

[21] Systems Control Technology, Inc, "Roadway powered electric vehicle project track construction and testing program phase 3D," Jan. 1994 (cit. on p. 10).

[22] S. Y. Choi, B. W. Gu, S. Y. Jeong, and C. T. Rim, "Advances in wireless power transfer systems for roadway-powered electric vehicles," *IEEE J. Emerg. Sel. Topics Power Electron.*, vol. 3, no. 1, pp. 18–36, Mar. 2015 (cit. on pp. 10, 14, 15, 92).

[23] S. Chopra and P. Bauer, "Analysis and design considerations for a contactless power transfer system," in *Proc. 2011 IEEE 33rd International Telecommunications Energy Conference (INTELEC)*, Amsterdam, NLD, Oct. 2011, pp. 1–6 (cit. on p. 10).

[24] C.-S. Wang, O. H. Stielau, and G. A. Covic, "Load models and their application in the design of loosely coupled inductive power transfer systems," in *Proc. International Conference on Power System Technology*, vol. 2, Perth, WA, AUS, 2000, 1053–1058 vol.2 (cit. on p. 10).

[25] W. Zhang, S. C. Wong, C. K. Tse, and Q. Chen, "Design for efficiency optimization and voltage controllability of series-series compensated inductive power transfer systems," *IEEE Trans. Power Electron.*, vol. 29, no. 1, pp. 191–200, Jan. 2014 (cit. on p. 10).

[26] Y. H. Sohn, B. H. Choi, E. S. Lee, G. C. Lim, G. H. Cho, and C. T. Rim, "General unified analyses of two-capacitor inductive power transfer systems: Equivalence of current-source SS and SP compensations," *IEEE Trans. Power Electron.*, vol. 30, no. 11, pp. 6030–6045, Nov. 2015 (cit. on pp. 10, 77).

[27] K. Aditya and S. S. Williamson, "Comparative study of series-series and series-parallel topology for long track EV charging application," in *Proc. 2014 IEEE Transportation Electrification Conference and Expo (ITEC)*, Dearborn, MI, USA, Jun. 2014, pp. 1–5 (cit. on p. 10).

[28] C.-S. Wang, G. A. Covic, and O. H. Stielau, "Investigating an LCL load resonant inverter for inductive power transfer applications," *IEEE Trans. Power Electron.*, vol. 19, no. 4, pp. 995–1002, Jul. 2004 (cit. on pp. 10, 92).

[29] W. Zhang and C. C. Mi, "Compensation topologies of high-power wireless power transfer systems," *IEEE Trans. Veh. Technol.*, vol. 65, no. 6, pp. 4768–4778, Jun. 2016 (cit. on pp. 10, 28).

[30] J. L. Villa, J. Sallan, J. F. S. Osorio, and A. Llombart, "High-misalignment tolerant compensation topology for ICPT systems," *IEEE Trans. Ind. Electron.*, vol. 59, no. 2, pp. 945–951, Feb. 2012 (cit. on p. 10).

[31] Y. Wang, Y. Yao, X. Liu, and D. Xu, "S/CLC compensation topology analysis and circular coil design for wireless power transfer," *IEEE Trans. Transport. Electrific.*, vol. 3, no. 2, pp. 496–507, Jun. 2017 (cit. on p. 10).

[32] S. Li, W. Li, J. Deng, T. D. Nguyen, and C. C. Mi, "A double-sided LCC compensation network and its tuning method for wireless power transfer," *IEEE Trans. Veh. Technol.*, vol. 64, no. 6, pp. 2261–2273, Jun. 2015 (cit. on pp. 10, 28, 92, 149).

[33] X. Qu, Y. Jing, H. Han, S. C. Wong, and C. K. Tse, "Higher order compensation for inductive-power-transfer converters with constant-voltage or constant-current output combating transformer parameter constraints," *IEEE Trans. Power Electron.*, vol. 32, no. 1, pp. 394–405, Jan. 2017 (cit. on p. 10).

[34] M. Budhia, G. Covic, and J. Boys, "A new IPT magnetic coupler for electric vehicle charging systems," in *Proc. 36th Annual Conference on IEEE Industrial Electronics Society (IECON)*, Glendale, AZ, USA, Nov. 2010, pp. 2487–2492 (cit. on pp. 11, 19, 20).

[35] J. T. Boys and G. A. Covic, "The inductive power transfer story at the university of Auckland," *IEEE Circuits Syst. Mag.*, vol. 15, no. 2, pp. 6–27, Secondquarter 2015 (cit. on pp. 11, 17).

[36] G. A. Covic and J. T. Boys, "Modern trends in inductive power transfer for transportation applications," *IEEE J. Emerg. Sel. Topics Power Electron.*, vol. 1, no. 1, pp. 28–41, Mar. 2013 (cit. on pp. 11, 20, 22).

[37] R. Bosshard and J. W. Kolar, "Multi-objective optimization of 50 kW/85 kHz IPT system for public transport," *IEEE J. Emerg. Sel. Topics in Power Electron.*, vol. 4, no. 4, pp. 1370–1382, Dec. 2016 (cit. on p. 12).

[38] W. R. Erickson and D. Maksimovic, *Fundamentals of Power Electronics, Second Edition*. Dordrecht: Kluwer, 2001, ISBN: 0792372700 (cit. on pp. 12, 25, 44, 68, 120).

[39] G. A. Covic and J. T. Boys, "Inductive power transfer," *Proc. IEEE*, vol. 101, no. 6, pp. 1276–1289, Jun. 2013 (cit. on pp. 12, 71, 87).

[40] International Commission on Non-Ionizing Radiation Protection (ICNIRP), "Guidelines for limiting exposure to time-varying electric, magnetic and electromagnetic fields (up to 300 GHz)," *Health Phys.*, vol. 74, no. 4, pp. 494–522, 1998 (cit. on p. 13).

[41] ——, "Guidelines for limiting exposure to time-varying electric and magnetic (1 Hz – 100 kHz)," *Health Phys.*, vol. 99, no. 6, pp. 818–836, 2010 (cit. on p. 13).

[42] M. Budhia, J. T. Boys, G. A. Covic, and C. Y. Huang, "Development of a single-sided flux magnetic coupler for electric vehicle IPT charging systems," *IEEE Trans. Ind. Electron.*, vol. 60, no. 1, pp. 318–328, Jan. 2013 (cit. on pp. 13, 20).

[43] S. Choi, J. Huh, W. Y. Lee, S. W. Lee, and C. T. Rim, "New cross-segmented power supply rails for roadway-powered electric vehicles," *IEEE Trans. Power Electron.*, vol. 28, no. 12, pp. 5832–5841, Dec. 2013 (cit. on p. 14).

[44] K. Lee, Z. Pantic, and S. M. Lukic, "Reflexive field containment in dynamic inductive power transfer systems," *IEEE Trans. Power Electron.*, vol. 29, no. 9, pp. 4592–4602, Nov. 2014 (cit. on pp. 14, 23).

[45] S. Lee, J. Huh, C. Park, N. S. Choi, G. H. Cho, and C. T. Rim, "On-line electric vehicle using inductive power transfer system," in *Proc. 2010 IEEE Energy Conversion Congress and Exposition (ECCE)*, Atlanta, GA, USA, Oct. 2010, pp. 1598–1601 (cit. on p. 14).

[46] S. Y. Choi, B. W. Gu, S. Y. Jeong, and C. T. Rim, "Trends of wireless power transfer systems for roadway powered electric vehicles," in *Proc. IEEE 79th Vehicular Technology Conference (VTC Spring)*, Seoul, South Korea,ROK, Jun. 2014, pp. 1–5 (cit. on p. 15).

[47] C. C. Mi, G. Buja, S. Y. Choi, and C. T. Rim, "Modern advances in wireless power transfer systems for roadway powered electric vehicles," *IEEE Trans. Ind. Electron.*, vol. 63, no. 10, pp. 6533–6545, Oct. 2016 (cit. on pp. 15, 28).

[48] H. Sakamoto, K. Harada, S. Washimiya, K. Takehara, Y. Matsuo, and F. Nakao, "Large air-gap coupler for inductive charger [for electric vehicles]," *IEEE Trans. Magn.*, vol. 35, no. 5, pp. 3526–3528, Sep. 1999 (cit. on p. 17).

[49] ——, "Large air gap coupler for inductive charger," in *Proc. IEEE International Magnetics Conference*, Kyongju, Korea, ROK, Jun. 1999, AS10–AS10 (cit. on p. 17).

[50] G. Buja, M. Bertoluzzo, and K. N. Mude, "Design and experimentation of WPT charger for electric city car," *IEEE Trans. Ind. Electron.*, vol. 62, no. 12, pp. 7436–7447, Dec. 2015 (cit. on pp. 18, 88).

[51] R. Bosshard, J. W. Kolar, J. Mühlethaler, I. Stevanović, B. Wunsch, and F. Canales, "Modeling and η - α -Pareto optimization of inductive power transfer coils for electric vehicles," *IEEE J. Emerg. Sel. Topics Power Electron.*, vol. 3, no. 1, pp. 50–64, Mar. 2015 (cit. on pp. 18, 25, 80, 87).

[52] M. Budhia, G. A. Covic, and J. T. Boys, "Design and optimization of circular magnetic structures for lumped inductive power transfer systems," *IEEE Trans. Power Electron.*, vol. 26, no. 11, pp. 3096–3108, Nov. 2011 (cit. on p. 18).

[53] R. Bosshard, U. Iruretagoyena, and J. W. Kolar, "Comprehensive evaluation of rectangular and double-d coil geometry for 50 kW/85 kHz IPT system," *IEEE J. Emerg. Sel. Topics Power Electron.*, vol. 4, no. 4, pp. 1406–1415, Dec. 2016 (cit. on pp. 20, 25).

[54] J. Sallan, J. L. Villa, A. Llombart, and J. F. Sanz, "Optimal design of ICPT systems applied to electric vehicle battery charge," *IEEE Trans. Ind. Electron.*, vol. 56, no. 6, pp. 2140–2149, Jun. 2009 (cit. on p. 20).

[55] G. R. Nagendra, G. A. Covic, and J. T. Boys, "Determining the physical size of inductive couplers for IPT EV systems," *IEEE J. Emerg. Sel. Topics Power Electron.*, vol. 2, no. 3, pp. 571–583, Sep. 2014 (cit. on p. 20).

[56] A. Zaheer, D. Kacprzak, and G. A. Covic, "A bipolar receiver pad in a lumped ipt system for electric vehicle charging applications," in *Proc. 2012 IEEE Energy Conversion Congress and Exposition (ECCE)*, Raleigh, NC, USA, Sep. 2012, pp. 283–290 (cit. on p. 22).

[57] M. Guarnieri, *Elementi di elettrotecnica circuitale*. Padova: Edizioni Progetto, 2010, (in Italian), ISBN: 9788896477052 (cit. on p. 23).

[58] K. Aditya and S. S. Williamson, "A review of optimal conditions for achieving maximum power output and maximum efficiency for a series-series resonant inductive link," *IEEE Trans. Transport. Electrific.*, vol. 3, no. 2, pp. 303–311, Jun. 2017 (cit. on p. 23).

[59] T. Diekhans and R. W. D. Doncker, "A dual-side controlled inductive power transfer system optimized for large coupling factor variations and partial load," *IEEE Trans. Power Electron.*, vol. 30, no. 11, pp. 6320–6328, Nov. 2015 (cit. on pp. 23, 39, 42).

[60] D. J. Thrimawithana, U. K. Madawala, and M. Neath, "A synchronization technique for bidirectional IPT systems," *IEEE Trans. Ind. Electron.*, vol. 60, no. 1, pp. 301–309, Jan. 2013 (cit. on pp. 23, 39).

[61] S. Raabe, "Inductive power transfer pickups for high demand applications," PhD thesis, University of Auckland, Auckland, NZ, 2011. [Online]. Available: https://researchspace.auckland.ac.nz/handle/2292/8312 (cit. on p. 23).

[62] W. Li, H. Zhao, J. Deng, S. Li, and C. C. Mi, "Comparison study on SS and double-sided LCC compensation topologies for EV/PHEV wireless chargers," *IEEE Trans. Veh. Technol.*, vol. 65, no. 6, pp. 4429–4439, Jun. 2016 (cit. on pp. 23, 92).

[63] J. Huh, S. W. Lee, W. Y. Lee, G. H. Cho, and C. T. Rim, "Narrow-width inductive power transfer system for online electrical vehicles," *IEEE Trans. Power Electron.*, vol. 26, no. 12, pp. 3666–3679, Dec. 2011 (cit. on pp. 25, 92).

[64] K. Hata, T. Imura, and Y. Hori, "Efficiency maximization of wireless power transfer based on simultaneous estimation of generalized two parameters," in *Proc. IEEE 2nd Annual Southern Power Electronics Conference (SPEC)*, Auckland, NZ, Dec. 2016, pp. 1–6 (cit. on pp. 26, 39).

[65] S. Chopra and P. Bauer, "Driving range extension of EV with on-road contactless power transfer - a case study," *IEEE Trans. Ind. Electron.*, vol. 60, no. 1, pp. 329–338, Jan. 2013 (cit. on p. 26).

[66] Y. H. Sohn, B. H. Choi, G. H. Cho, and C. T. Rim, "Gyrator-based analysis of resonant circuits in inductive power transfer systems," *IEEE Trans. Power Electron.*, vol. 31, no. 10, pp. 6824–6843, Oct. 2016 (cit. on p. 26).

[67] R. Bosshard, "Multi-objective optimization of inductive power transfer systems for EV charging," PhD thesis, ETH Zürich, Zürich, CH, 2015. [Online]. Available: https://www.research-collection.ethz.ch/handle/20.500.11850/117204 (cit. on pp. 26, 43).

[68] M. P. Kazmierkowski and A. J. Moradewicz, "Unplugged but connected: Review of contactless energy transfer systems," *IEEE Ind. Electron. Mag.*, vol. 6, no. 4, pp. 47–55, Dec. 2012 (cit. on p. 28).

[69] A. E. Fitzgerald, C. Kingsley, and S. D. Umans, *Electric Machinery*. New York: McGraw-Hill, 2003, ISBN: 0073660094 (cit. on p. 29).

[70] O. Tremblay and L. A. Dessaint, "Experimental validation of a battery dynamic model for EV applications," *World Electric Vehicle Journal*, vol. 3, May 2009 (cit. on p. 33).

[71] Z. M. Salameh, M. A. Casacca, and W. A. Lynch, "A mathematical model for lead-acid batteries," *IEEE Trans. Energy Convers.*, vol. 7, no. 1, pp. 93–98, Mar. 1992 (cit. on p. 33).

[72] L. Gao, S. Liu, and R. A. Dougal, "Dynamic lithium-ion battery model for system simulation," *IEEE Trans. Compon. Packag. Technol.*, vol. 25, no. 3, pp. 495–505, Sep. 2002 (cit. on p. 33).

[73] J. Deng, S. Li, S. Hu, C. C. Mi, and R. Ma, "Design methodology of LLC resonant converters for electric vehicle battery chargers," *IEEE Trans. Veh. Technol.*, vol. 63, no. 4, pp. 1581–1592, May 2014 (cit. on p. 34).

[74] M. Fu, C. Ma, and X. Zhu, "A cascaded boost-buck converter for high-efficiency wireless power transfer systems," *IEEE Trans. Ind. Informat.*, vol. 10, no. 3, pp. 1972–1980, Aug. 2014 (cit. on pp. 35, 37).

[75] Z. Pantic and S. M. Lukic, "Framework and topology for active tuning of parallel compensated receivers in power transfer systems," *IEEE Trans. Power Electron.*, vol. 27, no. 11, pp. 4503–4513, Nov. 2012 (cit. on p. 35).

[76] H. H. Wu, A. Gilchrist, K. D. Sealy, and D. Bronson, "A high efficiency 5 kW inductive charger for EVs using dual side control," *IEEE Trans. Ind. Informat.*, vol. 8, no. 3, pp. 585–595, Aug. 2012 (cit. on pp. 36, 42, 134).

[77] L. Zhao, D. J. Thrimawithana, and U. K. Madawala, "A comparison of LCL and LC bi-directional inductive power transfer systems," in *Proc. 2014 International Power Electronics and Application Conference and Exposition*, Shanghai, China, Nov. 2014, pp. 766–771 (cit. on p. 39).

[78] U. K. Madawala and D. J. Thrimawithana, "A bidirectional inductive power interface for electric vehicles in V2G systems," *IEEE Trans. Ind. Electron.*, vol. 58, no. 10, pp. 4789–4796, Oct. 2011 (cit. on pp. 39, 148).

[79] ——, "Current sourced bi-directional inductive power transfer system," *IET Power Electron.*, vol. 4, no. 4, pp. 471–480, Apr. 2011 (cit. on p. 39).

[80] D. J. Thrimawithana and U. K. Madawala, "A generalized steady-state model for bidirectional IPT systems," *IEEE Trans. Power Electron.*, vol. 28, no. 10, pp. 4681–4689, Oct. 2013 (cit. on p. 39).

[81] G. Lovison, M. Sato, T. Imura, and Y. Hori, "Secondary-side-only simultaneous power and efficiency control for two converters in wireless power transfer system," in *Proc. 41st Annual Conference of the IEEE Industrial Electronics Society (IECON 2015)*, Yokohama, JP, Nov. 2015, pp. 004 824–004 829 (cit. on pp. 39, 134).

[82] C. Y. Huang, J. T. Boys, and G. A. Covic, "LCL pickup circulating current controller for inductive power transfer systems," *IEEE Trans. Power Electron.*, vol. 28, no. 4, pp. 2081–2093, Apr. 2013 (cit. on pp. 39, 148, 160, 161).

[83] E. S. Lee, B. G. Choi, J. S. Choi, D. T. Nguyen, and C. T. Rim, "Wide-range adaptive IPT using dipole-coils with a reflector by variable switched capacitance," *IEEE Trans. Power Electron.*, vol. 32, no. 10, pp. 8054–8070, Oct. 2017 (cit. on p. 39).

[84] J. M. Miller, C. P. White, O. C. Onar, and P. M. Ryan, "Grid side regulation of wireless power charging of plug-in electric vehicles," in *Proc. 2012 IEEE Energy Conversion Congress and Exposition (ECCE)*, Sep. 2012, pp. 261–268 (cit. on p. 39).

[85] W. Li, H. Zhao, S. Li, J. Deng, T. Kan, and C. C. Mi, "Integrated *LCC* compensation topology for wireless charger in electric and plug-in electric vehicles," *IEEE Trans. Ind. Electron.*, vol. 62, no. 7, pp. 4215–4225, Jul. 2015 (cit. on p. 39).

[86] Q. Zhu, L. Wang, Y. Guo, C. Liao, and F. Li, "Applying LCC compensation network to dynamic wireless EV charging system," *IEEE Trans. Ind. Electron.*, vol. 63, no. 10, pp. 6557–6567, Oct. 2016 (cit. on pp. 39, 92).

[87] H. H. Wu, G. A. Covic, J. T. Boys, and D. J. Robertson, "A series-tuned inductive-power-transfer pickup with a controllable AC-voltage output," *IEEE Trans. Power Electron.*, vol. 26, no. 1, pp. 98–109, Jan. 2011 (cit. on p. 39).

[88] M. T. Outeiro, G. Buja, and D. Czarkowski, "Resonant power converters: An overview with multiple elements in the resonant tank network," *IEEE Ind. Electron. Mag.*, vol. 10, no. 2, pp. 21–45, Summer 2016 (cit. on p. 39).

[89] A. Safaee and K. Woronowicz, "Time-domain analysis of voltage-driven series-series compensated inductive power transfer topology," *IEEE Trans. Power Electron.*, vol. 32, no. 7, pp. 4981–5003, Jul. 2017 (cit. on p. 40).

[90] J. T. Boys, G. A. Covic, and Y. Xu, "DC analysis technique for inductive power transfer pick-ups," *IEEE Power Electron. Lett.*, vol. 1, no. 2, pp. 51–53, Jun. 2003 (cit. on p. 41).

[91] H. H. Wu, J. T. Boys, and G. A. Covic, "An AC processing pickup for IPT systems," *IEEE Trans. Power Electron.*, vol. 25, no. 5, pp. 1275–1284, May 2010 (cit. on p. 41).

[92] G. S. Buja and G. B. Indri, "Optimal pulsewidth modulation for feeding ac motors," *IEEE Trans. Ind. Appl.*, vol. IA-13, no. 1, pp. 38–44, Jan. 1977 (cit. on p. 42).

[93] R. Bosshard, U. Badstübner, J. W. Kolar, and I. Stevanović, "Comparative evaluation of control methods for inductive power transfer," in *Proc. 2012 International Conference on Renewable Energy Research and Applications (ICRERA)*, Nov. 2012, pp. 1–6 (cit. on pp. 42, 80).

[94] C.-S. Wang, G. A. Covic, and O. H. Stielau, "Power transfer capability and bifurcation phenomena of loosely coupled inductive power transfer systems," *IEEE Trans. Ind. Electron.*, vol. 51, no. 1, pp. 148–157, Feb. 2004 (cit. on pp. 42, 80, 92).

[95] N. Mohan, T. M. Undeland, and W. P. Robbins, *Power Electronics. Converters, Applications and Design*, third. John Wiley and Sons, Inc, 2003, ISBN: 9780471226932 (cit. on p. 44).

[96] M. Kasper, R. M. Burkart, G. Deboy, and J. W. Kolar, "ZVS of power MOSFETs revisited," *IEEE Trans. Power Electron.*, vol. 31, no. 12, pp. 8063–8067, Dec. 2016 (cit. on p. 46).

[97] M. Borage, S. Tiwari, and S. Kotaiah, "Analysis and design of an LCL-T resonant converter as a constant-current power supply," *IEEE Trans. Ind. Electron.*, vol. 52, no. 6, pp. 1547–1554, Dec. 2005 (cit. on p. 64).

[98] Z. Pantic, S. Bai, and S. M. Lukic, "ZCS *LCC*-compensated resonant inverter for inductive-power-transfer application," *IEEE Trans. Ind. Electron.*, vol. 58, no. 8, pp. 3500–3510, Aug. 2011 (cit. on p. 70).

[99] R. K. Jha, G. Buja, M. Bertoluzzo, S. Giacomuzzi, and K. N. Mude, "Performance comparison of the one-element resonant EV wireless battery chargers," *IEEE Trans. Ind. Appl.*, vol. 54, no. 3, pp. 2471–2482, May 2018 (cit. on p. 77).

[100] L. Chen, G. R. Nagendra, J. T. Boys, and G. A. Covic, "Double-coupled systems for IPT roadway applications," *IEEE J. Emerg. Sel. Topics Power Electron.*, vol. 3, no. 1, pp. 37–49, Mar. 2015 (cit. on p. 89).

[101] B. Esteban, M. Sid-Ahmed, and N. C. Kar, "A comparative study of power supply architectures in wireless EV charging systems," *IEEE Trans. Power Electron.*, vol. 30, no. 11, pp. 6408–6422, Nov. 2015 (cit. on p. 92).

[102] H. Feng, T. Cai, S. Duan, J. Zhao, X. Zhang, and C. Chen, "An LCC-compensated resonant converter optimized for robust reaction to large coupling variation in dynamic wireless power transfer," *IEEE Trans. Ind. Electron.*, vol. 63, no. 10, pp. 6591–6601, Oct. 2016 (cit. on p. 92).

[103] G. Buja, M. Bertoluzzo, and H. K. Dashora, "Lumped track layout design for dynamic wireless charging of electric vehicles," *IEEE Trans. Ind. Electron.*, vol. 63, no. 10, pp. 6631–6640, Oct. 2016 (cit. on p. 99).

[104] F. Lu, H. Zhang, H. Hofmann, and C. C. Mi, "A dynamic charging system with reduced output power pulsation for electric vehicles," *IEEE Trans. Ind. Electron.*, vol. 63, no. 10, pp. 6580–6590, Oct. 2016 (cit. on p. 99).

[105] M. Bertoluzzo, G. Buja, and H. K. Dashora, "Design of DWC system track with unequal DD coil set," *IEEE Trans. Transport. Electrific.*, vol. 3, no. 2, pp. 380–391, Jun. 2017 (cit. on pp. 99, 155).

[106] R. D. Middlebrook and S. Cuk, "A general unified approach to modelling switching-converter power stages," in *Proc. 1976 IEEE Power Electronics Specialists Conference*, Cleveland, OH, USA, Jun. 1976, pp. 18–34 (cit. on p. 103).

[107] D. Maksimovic, A. M. Stankovic, V. J. Thottuvelil, and G. C. Verghese, "Modeling and simulation of power electronic converters," *Proc. IEEE*, vol. 89, no. 6, pp. 898–912, Jun. 2001 (cit. on p. 104).

[108] S. R. Sanders, J. M. Noworolski, X. Z. Liu, and G. C. Verghese, "Generalized averaging method for power conversion circuits," *IEEE Trans. Power Electron.*, vol. 6, no. 2, pp. 251–259, Apr. 1991 (cit. on pp. 105, 107).

[109] C. T. Rim and G. H. Cho, "Phasor transformation and its application to the DC/AC analyses of frequency phase-controlled series resonant converters (SRC)," *IEEE Trans. Power Electron.*, vol. 5, no. 2, pp. 201–211, Apr. 1990 (cit. on pp. 105, 108).

[110] A. P. Hu, "Modeling a contactless power supply using GSSA method," in *Proc. 2009 IEEE International Conference on Industrial Technology*, Gippsland, Australia, AUS, Feb. 2009, pp. 1–6 (cit. on p. 105).

[111] H. Hao, G. A. Covic, and J. T. Boys, "An approximate dynamic model of LCL- T-based inductive power transfer power supplies," *IEEE Trans. Power Electron.*, vol. 29, no. 10, pp. 5554–5567, Oct. 2014 (cit. on p. 105).

[112] Y. Sun, W. Tao, J. Xia, and H. Zhang, "Dynamic phasor modeling of inductive power transfer system and its state feedback design," in *Proc. 2017 IEEE PELS Workshop on Emerging Technologies: Wireless Power Transfer (WoW)*, Chongqing, China,CHN, Jun. 2017, pp. 282–287 (cit. on p. 105).

[113] S. Lee, B. Choi, and C. T. Rim, "Dynamics characterization of the inductive power transfer system for online electric vehicles by laplace phasor transform," *IEEE Trans. Power Electron.*, vol. 28, no. 12, pp. 5902–5909, Dec. 2013 (cit. on p. 105).

[114] K. Aditya and S. S. Williamson, "Simplified mathematical modelling of phase-shift controlled series-series compensated inductive power transfer system," in *Proc. 2016 IEEE 25th International Symposium on Industrial Electronics (ISIE)*, Santa Clara, CA, USA, Jun. 2016, pp. 842–848 (cit. on p. 105).

[115] V. A. Caliskan, O. C. Verghese, and A. M. Stankovic, "Multifrequency averaging of DC/DC converters," *IEEE Trans.on Power Electron.*, vol. 14, no. 1, pp. 124–133, Jan. 1999 (cit. on p. 105).

[116] Y. Yin, R. Zane, J. Glaser, and R. W. Erickson, "Small-signal analysis of frequency-controlled electronic ballasts," *IEEE Trans. Circuits Syst. I, Fundam. Theory Appl.*, vol. 50, no. 8, pp. 1103–1110, Aug. 2003 (cit. on pp. 108, 111).

[117] C. T. Rim, "Unified general phasor transformation for AC converters," *IEEE Trans. Power Electron.*, vol. 26, no. 9, pp. 2465–2475, Oct. 2011 (cit. on p. 109).

[118] C. Park, S. Lee, G. H. Cho, and C. T. Rim, "Static and dynamic analyses of three-phase rectifier with LC input filter by Laplace phasor transformation," in *Proc. 2012 IEEE Energy Conversion Congress and Exposition (ECCE)*, Sep. 2012, pp. 1570–1577 (cit. on p. 110).

[119] **M. Forato**, M. Bertoluzzo, and G. Buja, "Modeling of the dynamics of a resonant wireless power transfer circuit," in *Proc. 2017 IEEE 26th International Symposium on Industrial Electronics (ISIE)*, Edinburgh, UK, Jun. 2017, pp. 472–477 (cit. on pp. 110, 131).

[120] L. Scandola, "Implementation and modeling of online efficiency optimization techniques for high-frequency dc-dc converters in automotive applications," PhD thesis, University of Padova, Padova, IT, 2016. [Online]. Available: http://paduaresearch.cab.unipd.it/9455/ (cit. on p. 111).

[121] G. R. Nagendra, L. Chen, G. A. Covic, and J. T. Boys, "Detection of EVs on IPT highways," *IEEE J. Emerg. Sel. Topics Power Electron.*, vol. 2, no. 3, pp. 584–597, Sep. 2014 (cit. on p. 133).

[122] A. Kamineni, M. J. Neath, A. Zaheer, G. A. Covic, and J. T. Boys, "Interoperable EV detection for dynamic wireless charging with existing hardware and free resonance," *IEEE Trans. Transport. Electrific.*, vol. 3, no. 2, pp. 370–379, Jun. 2017 (cit. on p. 133).

[123] **M. Forato**, M. Bertoluzzo, and G. Buja, "Dynamic EV charging WPT system control based on modulated variable Laplace transform," in *Proc. 2018 IEEE PELS Workshop on Emerging Technologies: Wireless Power Transfer (Wow)*, Montréal, QC, Canada, Jun. 2018, pp. 1–6 (cit. on p. 135).

[124] N. A. Keeling, G. A. Covic, and J. T. Boys, "A unity-power-factor IPT pickup for high-power applications," *IEEE Trans. Ind. Electron.*, vol. 57, no. 2, pp. 744–751, Feb. 2010 (cit. on p. 148).